

# Performance Evaluation of the SPS Scraping System in View of the High Luminosity LHC

A thesis submitted to the University of Manchester for the degree of  
Doctor of Philosophy  
in the Faculty of Engineering and Physical Sciences

2015

Alessio Mereghetti

School of Physics and Astronomy

# Contents

<b>Abstract</b>	<b>13</b>
<b>Declaration</b>	<b>15</b>
<b>Copyright</b>	<b>16</b>
<b>Acknowledgements</b>	<b>17</b>
<b>The Author</b>	<b>19</b>
<b>1 Introduction</b>	<b>20</b>
1.1 Colliding Beams . . . . .	22
1.2 The Large Hadron Collider and the CERN Accelerator Complex .	27
1.3 The High Luminosity LHC and the LHC Injectors Upgrade Projects	33
1.4 Machine Protection . . . . .	37
1.4.1 Machine Protection Needs . . . . .	38
1.4.2 Machine Protection Systems and Beam–Intercepting Devices	40
1.4.3 Interaction of Radiation with Matter . . . . .	41
1.4.4 Impedance and Wake Fields . . . . .	49
1.4.5 Design of Beam–Intercepting Devices . . . . .	57
1.4.6 An Example: the LHC Collimation System . . . . .	60
1.5 Thesis Purpose and Structure . . . . .	62
<b>2 The SPS Scraping System and Its Upgrade</b>	<b>67</b>
2.1 The SPS . . . . .	71
2.1.1 The Layout and the Optics . . . . .	72
2.1.2 Parameters of Longitudinal Beam Dynamics . . . . .	76
2.1.3 The Permanent Magnetic Bump in LSS1 . . . . .	77
2.1.4 The SPS Cycle . . . . .	79
2.2 The SPS Scraping System . . . . .	81
2.2.1 The Existing System . . . . .	83
2.2.2 The Upgraded System . . . . .	92
2.2.3 Comparison Between the Two Systems . . . . .	98
2.3 Conclusions . . . . .	102

<b>3 Simulation Tools</b>	<b>104</b>
3.1 FLUKA . . . . .	107
3.1.1 Overview of the Code . . . . .	108
3.1.2 Moving Portions of Geometry . . . . .	109
3.1.3 Simulation Settings . . . . .	110
3.2 SIXTRACK . . . . .	112
3.2.1 Overview of the Code . . . . .	113
3.2.2 Online Aperture Check . . . . .	113
3.2.3 Dynamic Kicks . . . . .	115
3.3 The Coupling Between FLUKA and SIXTRACK . . . . .	118
3.3.1 Implementation Details . . . . .	120
3.4 Ancillary Tools . . . . .	125
3.4.1 The Line Builder and the FLUKA Element DataBase . . .	126
3.4.2 Beam Sampling . . . . .	127
3.5 Conclusions . . . . .	131
<b>4 Characterisation of the Existing SPS Scraping System</b>	<b>134</b>
4.1 Overview of Past Investigations . . . . .	137
4.1.1 Simulation Settings . . . . .	139
4.1.2 Results . . . . .	141
4.1.3 Conclusions . . . . .	149
4.2 Analysis of the Existing System . . . . .	151
4.2.1 Simulation Settings . . . . .	153
4.2.2 Material of the Blade . . . . .	156
4.2.3 Permanent Bump in the LSS1 . . . . .	167
4.2.4 Energy Ramping . . . . .	176
4.2.5 Blade Tilting . . . . .	182
4.2.6 Conclusions . . . . .	188
4.3 The Burst Test and the Benchmark of the Simulation Tools . . .	194
4.3.1 Set–Up of the Burst Test . . . . .	197
4.3.2 SPS Monitors . . . . .	199
4.3.3 Outcomes of the Test . . . . .	203
4.3.4 Benchmark Against BCT Signals . . . . .	213
4.3.5 Benchmark Against BLM Signals . . . . .	234
4.3.6 Conclusions . . . . .	258
4.4 Conclusions . . . . .	262
<b>5 Characterisation of the Upgraded SPS Scraping System</b>	<b>267</b>
5.0.1 Simulation Settings . . . . .	271
5.1 Preliminary Studies . . . . .	273
5.1.1 Simulation Settings . . . . .	274
5.1.2 Results . . . . .	275
5.1.3 Conclusions . . . . .	282
5.2 Results with Dynamic Kicks . . . . .	283

5.2.1	Simulation Settings . . . . .	283
5.2.2	Results . . . . .	284
5.2.3	Conclusions . . . . .	287
5.3	Full Analysis . . . . .	289
5.3.1	Simulation Settings . . . . .	290
5.3.2	Results . . . . .	291
5.3.3	Conclusions . . . . .	299
5.4	Comparison with the Existing System . . . . .	300
5.4.1	Energy Deposition . . . . .	301
5.4.2	Profile of Beam Intensity . . . . .	303
5.4.3	Losses . . . . .	305
5.4.4	Additional Remarks . . . . .	306
<b>6</b>	<b>Conclusions</b>	<b>307</b>
<b>A</b>	<b>Notes on Linear Accelerator Physics</b>	<b>313</b>
A.1	Particle Coordinates, Motion and Optics Functions . . . . .	314
A.2	Statistical Quantities . . . . .	318
A.3	The Floquet's Transformations and the Normalised Phase Spaces	320
A.4	Normalised Emittance . . . . .	321
<b>B</b>	<b>Limits of Energy Deposition in Copper and Graphite</b>	<b>323</b>
B.1	Copper . . . . .	323
B.2	Graphite . . . . .	324
<b>C</b>	<b>Averaging BCT Signals</b>	<b>326</b>
C.1	Normalisation and Averaging of BCT Signals . . . . .	327
C.2	Amount of Scraped Beam . . . . .	331
C.3	Basic Statistics Formulae . . . . .	331
C.4	Basic Formulae for the Propagation of Uncertainties . . . . .	332
C.5	BCT Readouts . . . . .	332
<b>D</b>	<b>Amount of Scraped Beam</b>	<b>337</b>
D.1	Origin of Combined Betatron–Momentum Cleaning . . . . .	337
D.2	Expected Amount of Surviving Beam . . . . .	340
D.2.1	Reminder on Gaussian Distributions . . . . .	341
D.2.2	Pure Betatron Cleaning . . . . .	344
D.2.3	Combined Betatron–Momentum Cleaning . . . . .	344
<b>E</b>	<b>Collection of BLM Signals</b>	<b>350</b>
<b>Bibliography</b>		<b>361</b>

*Total word count: 69982*

# List of Tables

1.1	Energy of colliding beams and equivalent beam energy for fixed target experiments. . . . .	23
1.2	Beam particle, collision energy and peak luminosity of recent colliders. . . . .	26
1.3	Beam parameters for “nominal” LHC operation with protons. . . . .	29
1.4	Accelerator chain for proton injection into LHC . . . . .	32
1.5	Main beam parameters at extraction in the SPS. . . . .	37
1.6	Physical and nuclear properties of materials most commonly used in beam-intercepting devices. . . . .	49
2.1	Main parameters for the longitudinal beam dynamics in the SPS. . . . .	77
2.2	Displacement of quadrupoles, at the origin of the permanent magnetic bump in the SPS LSS1. . . . .	78
2.3	Optics functions, closed orbit and beam spot size at the three SPS scrapers. . . . .	88
2.4	Optics functions, closed orbit and rms beam dimensions at the absorbers of the upgraded SPS scrapers. . . . .	97
2.5	Nominal kicks for scraping the beam with magnetic bumps in LSS6. .	98
4.1	Beam parameters for the 2010 studies. . . . .	140
4.2	Ultimate limits of energy deposition in graphite and copper considered in the present work. . . . .	142
4.3	Beam parameters for the comparison of different blade materials. .	157
4.4	Beam parameters for assessing the effect of the permanent magnetic bump in the SPS LSS1. . . . .	168
4.5	Settings of the burst test. . . . .	199
4.6	Parameters of the BCT signals. . . . .	201
4.7	Calibration factors of the SPS BLMs and maximum signal allowed by the readout electronics. . . . .	203
4.8	Estimated porosity in the vertical blade of the scraper after test. .	210
4.9	Comparison of fitting parameters between the fits from Fig. 4.37 and Fig. 4.38. . . . .	218
4.10	Parameters used to sample the beam for the benchmark against the BCT readouts. . . . .	220

4.11	Speed and tilt angle of the scraper blades as reconstructed from the BCT signals. . . . .	225
4.12	Amount of beam scraped as estimated via the BCT signals and energy deposition expected in the blades during the burst test. . . . .	231
4.13	References for the algebra on BLM signals. . . . .	241
4.14	Amount of beam scraped as estimated via the BLM signals and energy deposition expected in the blades during the burst test. . . . .	249
4.15	Main characteristics of the region of active gas of the SPS BLMs as modelled in the FLUKA geometry. . . . .	252
4.16	Transverse positions in the FLUKA geometry and shifts for the sensitivity analysis on the BLM positions. . . . .	255
5.1	Comparison of the maximum energy deposition in the blade of the SPS scraping system presently installed and in the static absorber of the upgraded system. . . . .	302
C.1	Time intervals for computing the average beam intensity before and after scraping, and after dump. . . . .	329
C.2	Rules for the propagation of uncertainties. . . . .	332

# List of Figures

1.1	Lawrence's cyclotron and the CERN accelerator complex. . . . .	21
1.2	Layout of the LHC. . . . .	27
1.3	Timeline of the centre-of-mass energy and peak luminosity. . . . .	30
1.4	Critical curve of the LHC SC dipoles. . . . .	31
1.5	Schematic view of the CERN accelerator complex. . . . .	32
1.6	LHC baseline plan for the period 2012–2022 and beyond. . . . .	34
1.7	Evolution of peak and integrated luminosity of the HL-LHC. . . . .	35
1.8	Stopping power in different materials and straggling functions in silicon for 500 MeV pions. . . . .	43
1.9	Total and elastic cross sections of $pp$ and $pn$ reactions. . . . .	45
1.10	EM fields of an ultrarelativistic charged particle. . . . .	50
1.11	Parasitic modes in a pill box cavity. . . . .	52
1.12	RLC parallel circuit equivalent to a pill box cavity and qualitative time dependence of the generated wake fields. . . . .	53
1.13	Scheme of a pick-up electrode and its equivalent circuit. . . . .	56
1.14	Principle of the LHC multi-stage betatron collimation system. . . . .	61
2.1	Schematic layout of the SPS complex. . . . .	68
2.2	SPS optics. . . . .	74
2.3	SPS closed orbit with the permanent magnetic bump in LSS1. . . . .	79
2.4	SPS cycle when accelerating LHC beams. . . . .	80
2.5	The SPS scrapers. . . . .	84
2.6	Installation of the SPS scrapers in the LSS1. . . . .	85
2.7	Schematics of the SPS LSS1. . . . .	86
2.8	Schematics of the SPS LSS5. . . . .	87
2.9	Betatron cleaning obtained with the scrapers. . . . .	89
2.10	Operational schematics of the mechanical and upgraded scrapers. . . . .	92
2.11	Schematics of the SPS LSS6. . . . .	94
2.12	SPS closed orbit with the magnetic bumps of the upgraded scraping system. . . . .	95
3.1	Horizontal closed orbit at the absorber of the upgraded SPS scraping system, in case of an arbitrary modulation of the bumper kicks. . . . .	116
3.2	Typical cross section of a sextupole magnet, with the schematics of its polarisation. . . . .	118

3.3	Schematics of the SIXTRACK-FLUKA coupling. . . . .	120
3.4	Example of evolution of the horizontal position and total energy of a beam proton during scraping in the SPS. . . . .	124
3.5	3D rendering of the FLUKA geometry of the LHC LSS7. . . . .	126
4.1	Peak energy deposition in the SPS scraper blades as from the 2010 studies. . . . .	141
4.2	Total energy deposition in the SPS scraper blades as from the 2010 studies. . . . .	143
4.3	Scaling of maximum and total energy deposition with scraping position as from the 2010 studies. . . . .	145
4.4	Evolution of the beam intensity during scraping as from the 2010 studies. . . . .	146
4.5	Loss pattern in the SPS as from the 2010 studies. . . . .	148
4.6	Temperature rise in the SPS scraper blades as from the 2010 studies. . . . .	150
4.7	Energy deposition in the scraper blades for different materials. . . . .	159
4.8	3D rendering of the horizontal graphite blade of the SPS scrapers and energy deposition map. . . . .	160
4.9	Distribution of energy loss in different blade materials per single proton passage, according to the dominant event. . . . .	161
4.10	Evolution of the beam intensity and rate of intercepted protons for different blade materials. . . . .	163
4.11	Pattern of proton losses around the SPS ring for different blade materials. . . . .	164
4.12	Pattern of proton losses around the SPS ring, grouped according to the last event the lost proton underwent in the scraper blade, for different blade materials. . . . .	166
4.13	Evolution of the beam intensity and rate of intercepted protons in case the permanent magnetic bump in the SPS LSS1 is considered. . . . .	171
4.14	Energy deposition in the blades of the SPS scrapers in case the permanent magnetic bump in the SPS LSS1 is considered. . . . .	172
4.15	Pattern of proton losses around the SPS ring in case the permanent magnetic bump in the SPS LSS1 is considered. . . . .	174
4.16	Evolution of the beam intensity and rate of intercepted protons when scraping during the energy ramp. . . . .	178
4.17	Check of synchronisation between energy ramp and scraping time. . . . .	179
4.18	Energy deposition in the blades of the SPS scrapers when scraping during the energy ramp. . . . .	180
4.19	Pattern of proton losses around the SPS ring when scraping during the energy ramp. . . . .	181
4.20	Schematics of the tilting of the scraper blade. . . . .	182
4.21	Energy deposition in the blades of the SPS scrapers for different tilt angles. . . . .	184

4.22	3D rendering of the horizontal graphite blade of the SPS scrapers and energy deposition map, in case of a positive tilt angle about the longitudinal axis. . . . .	185
4.23	Evolution of the beam intensity for different tilt angles. . . . .	186
4.24	Schematics of the SPS scraper blade tilted by a positive angle about the longitudinal axis. . . . .	188
4.25	Pattern of proton losses around the SPS ring when the scraper blade is tilted about the longitudinal axis. . . . .	189
4.26	Pattern of proton losses around the SPS ring when the scraper blade is tilted about the vertical axis. . . . .	190
4.27	Pattern of proton losses around the SPS ring when the scraper blade is tilted about the horizontal axis. . . . .	191
4.28	Typical profile of the SPS beam obtained with the wire scanner. .	198
4.29	Main technical drawing of the SPS BLM. . . . .	202
4.30	BCT signals during the burst test of the SPS scraper blades. . . .	204
4.31	Time profile of the vacuum in the MKD dump kickers immediately upstream of the tested scrapers. . . . .	206
4.32	BLM readouts along the SPS ring recorded during the burst test of scraper blades. . . . .	207
4.33	Normalised and averaged BCT signals when performing regular scraping before and after the burst test of the scraper blades. . . .	208
4.34	Picture and SEM image of the vertical blade of the scraper after test. . . . .	209
4.35	Normalised BCT signals during the burst test compared to those obtained with low intensity beams. . . . .	212
4.36	Normalised and averaged BCT signals at low beam intensity. . . .	216
4.37	Beam scans performed with the operational scraper. . . . .	217
4.38	Scraper scans of the beam obtained with BCT measurements when setting up the burst test. . . . .	217
4.39	Time evolution of the beam intensity during scraping as predicted by the simulation and as from BCT signals. . . . .	223
4.40	Density of scraped protons in the $n_\beta$ – $n_\delta$ space in case of regular scraping, with aligned and tilted blades. . . . .	228
4.41	Beam distribution at the entrance of the scraper tank at the beginning and end of a FLUKA–SIXTRACK coupled simulation. . . .	230
4.42	Effect of a change in the porosity of the scraper blade on the profile of the beam intensity in case of regular scraping. . . . .	232
4.43	Schematics of a damaged blade, aligned and with a tilt angle about the longitudinal axis. . . . .	233
4.44	Qualitative comparison between the readouts from the BLMs along the SPS during the burst test and a beam loss map from simulation. .	239
4.45	Signals of BLMs in the SPS LSS1 for different scraping settings. .	243
4.46	Comparison between measured BLM signals and those reconstructed with the algebra on signals obtained with specific scraping settings.	247

4.47	Saturation in BLM signals measured during the burst test and the reconstructed pattern obtained with the algebra on signals with specific scraping settings. . . . .	248
4.48	3D rendering of the FLUKA geometry of the SPS LSS1. . . . .	250
4.49	3D rendering of the FLUKA geometry of the MKPA kicker and of the BLM. . . . .	251
4.50	Quantitative comparison of the signals in the BLMs located in the LSS1 between measurements and simulations. . . . .	254
4.51	Quantitative comparison of the signals in the BLMs located in the LSS1 between measurements and simulations with more realistic scraping settings and beam distribution. . . . .	257
5.1	Energy deposition in the static absorber block of the upgraded SPS scrapers, for the baseline, in case of a longer absorber, and in case of a faster rising of the bump. . . . .	276
5.2	Evolution of the beam intensity and rate of intercepted protons for the baseline of the upgraded SPS scrapers, in case of a longer absorber, and in case of a faster rising of the bump. . . . .	278
5.3	Sign convention for misalignment studies of the upgraded SPS scrapers. . . . .	279
5.4	Energy deposition in the static absorber block of the upgraded SPS scrapers for different impact angles. . . . .	280
5.5	Evolution of the beam intensity and rate of intercepted protons for the upgraded SPS scrapers in case of different impact angles. . . . .	281
5.6	Energy deposition in the static absorber block of the upgraded SPS scrapers when simulating the rising of the magnetic bump. . . . .	285
5.7	Schematics of the change in the closed orbit when rising the magnetic bump. . . . .	286
5.8	Evolution of the beam intensity and rate of intercepted protons for the upgraded SPS scrapers when simulating the rising of the magnetic bump. . . . .	288
5.9	Energy deposition in the static absorber block of the upgraded SPS scrapers as from full simulation. . . . .	292
5.10	Effect of sextupoles on the fluence of beam protons at the entrance face of the absorber of the vertical scraping system. . . . .	293
5.11	Energy loss in the static absorber block of the upgraded SPS scrapers as from full simulation. . . . .	294
5.12	Evolution of the beam intensity and rate of intercepted protons for the upgraded SPS scrapers as from full simulation. . . . .	295
5.13	Pattern of proton losses along the SPS ring for the upgraded SPS scrapers as from full simulation. . . . .	297
5.14	Pattern of proton losses along the SPS ring for the upgraded SPS scrapers as from full simulation, grouped according to the last event the lost proton underwent in the scraper blade. . . . .	298

5.15 Comparison of the pattern of proton losses along the SPS ring between the SPS scraping system presently installed and the upgraded one. . . . .	305
A.1 Curvilinear reference system and motion of beam particles in the transverse phase space. . . . .	314
B.1 Specific heat of copper as a function of temperature. . . . .	324
B.2 Specific heat of graphite as a function of temperature. . . . .	325
C.1 Example of SPS cycle with BCT timing explicitly indicated. . . . .	327
C.2 BCT signals when scraping at $-11$ mm with the horizontal blade. . . . .	333
C.3 BCT signals when scraping at $-11.5$ mm with the horizontal blade. . . . .	333
C.4 BCT signals when scraping at $-12.5$ mm with the horizontal blade. . . . .	333
C.5 BCT signals when scraping at $-13$ mm with the horizontal blade. . . . .	334
C.6 BCT signals at regular scraping with the horizontal blade before the burst test. . . . .	334
C.7 BCT signals at regular scraping with the horizontal blade after the burst test. . . . .	334
C.8 BCT signals when scraping at $6.2$ mm with the vertical blade. . . . .	335
C.9 BCT signals when scraping at $5.7$ mm with the vertical blade. . . . .	335
C.10 BCT signals when scraping at $5.6$ mm with the vertical blade. . . . .	335
C.11 BCT signals when scraping at $5.5$ mm with the vertical blade. . . . .	336
C.12 BCT signals at regular scraping with the vertical blade before the burst test. . . . .	336
C.13 BCT signals at regular scraping with the vertical blade after the burst test. . . . .	336
D.1 Schematics of combined betatron-momentum cleaning as seen in the $n_\beta$ - $n_\delta$ plane. . . . .	338
D.2 Fraction of beam stopped by an intercepting device as a function of its cleaning position $R \sigma_{z,\beta}$ . . . . .	349
E.1 BLM signals when no scraping is performed with a low intensity beam (i.e. $\sim 10^{12}$ protons). . . . .	351
E.2 BLM signals when no scraping is performed with a high intensity beam (i.e. $\sim 3 \cdot 10^{13}$ protons) (1). . . . .	352
E.3 BLM signals when no scraping is performed with a high intensity beam (2). . . . .	353
E.4 BLM signals when scraping with the horizontal blade at $-11$ mm (i.e. full beam scraping), with a low intensity beam. . . . .	354
E.5 BLM signals when scraping with the horizontal blade at $-11.5$ mm (i.e. $\sim 500 \mu\text{m}$ off the centre of the beam), with a low intensity beam. . . . .	355

E.6	BLM signals when scraping with the vertical blade at 5.7 mm (i.e. full beam scraping), with a low intensity beam. . . . .	356
E.7	BLM signals when scraping with the horizontal blade at $-13.2$ mm (i.e. regular scraping), with a high intensity beam, before the burst test of the blade. . . . .	357
E.8	BLM signals when scraping with the horizontal blade at $-13.2$ mm (i.e. regular scraping), with a high intensity beam, after the burst test of the blade. . . . .	358
E.9	BLM signals when scraping with the vertical blade at 3.5 mm (i.e. regular scraping), with a high intensity beam, before the burst test of the blade. . . . .	359
E.10	BLM signals when scraping with the vertical blade at 3.5 mm (i.e. regular scraping), with a high intensity beam, after the burst test of the blade. . . . .	360

# Abstract

Injection in the LHC is a delicate moment, since the LHC collimation system cannot offer adequate protection during beam transfer. For this reason, a complex chain of injection protection devices has been put in place. Among them, the SPS scrapers are the multi-turn cleaning system installed in the SPS aimed at halo removal immediately before injection in the LHC.

The upgrade in luminosity of the LHC foresees beams brighter than those currently available in machine, posing serious problems to the performance of the existing injection protection systems. In particular, the integrity of beam-intercepting devices is challenged by unprecedented beam parameters, leading to interactions potentially destructive. In this context, a new design of scrapers has been proposed, aimed at improved robustness and performance.

This thesis compares the two scraping systems, i.e. the existing one and the one proposed for upgrade. Unlike any other collimation system for regular halo cleaning, both are “fast” systems, characterised by the variation of the relative distance between the beam and the absorbing medium during cleaning, which enhances the challenge on energy deposition values. Assets / liabilities of the two systems are highlighted by means of numerical simulations and discussed, with particular emphasis on energy deposition in the absorbing medium, time evolution of the beam current during scraping and losses in the machine. Advantages of the system proposed for upgrade over the existing one are highlighted.

The analysis of the existing system takes into account present operational conditions and addresses the sensitivity to settings previously not considered, updating and extending past studies. The work carried out on the upgraded system represents the first extensive characterisation of a multi-turn cleaning system based on a magnetic bump.

Results have been obtained with the FLUKA-SIXTRACK coupling, developed during this PhD activity from its initial version to being a state-of-art tracking tool for cleaning studies in circular machines. Relevant contributions to the development involve the handling of time-varying impact conditions. An extensive benchmark against a test of the scraper blades with beam has been carried out, to verify the reliability of results. Effects induced in the tested blades confirm the high values of energy deposition predicted by the simulation. Moreover, the comparison with the time profile of the beam intensity measured during scraping allowed the reconstruction of the actual settings of the blades during the test.

Finally, the good agreement of the quantitative benchmark against readouts of beam loss monitors finally proves the quality of the analyses and the maturity of the coupling.

# Declaration

No portion of the work referred to in this thesis has been submitted in support of an application for another degree or qualification of this or any other university or other institution of learning.

Alessio Mereghetti  
School of Physics and Astronomy  
University of Manchester  
Oxford Road  
Manchester  
M13 9PL  
2015

# Copyright

The author of this thesis (including any appendices and/or schedules to this thesis) owns certain copyright or related rights in it (the “Copyright”) and s/he has given The University of Manchester certain rights to use such Copyright, including for administrative purposes.

Copies of this thesis, either in full or in extracts and whether in hard or electronic copy, may be made only in accordance with the Copyright, Designs and Patents Act 1988 (as amended) and regulations issued under it or, where appropriate, in accordance with licensing agreements which the University has from time to time. This page must form part of any such copies made.

The ownership of certain Copyright, patents, designs, trade marks and other intellectual property (the “Intellectual Property”) and any reproductions of copyright works in the thesis, for example graphs and tables (“Reproductions”), which may be described in this thesis, may not be owned by the author and may be owned by third parties. Such Intellectual Property and Reproductions cannot and must not be made available for use without the prior written permission of the owner(s) of the relevant Intellectual Property and/or Reproductions.

Further information on the conditions under which disclosure, publication and commercialisation of this thesis, the Copyright and any Intellectual Property and/or Reproductions described in it may take place is available in the University IP Policy (see <http://documents.manchester.ac.uk/DocuInfo.aspx?DocID=487>), in any relevant Thesis restriction declarations deposited in the University Library, The University Librarys regulations (see <http://www.manchester.ac.uk/library/aboutus/regulations>) and in The Universitys policy on presentation of Theses.

# Acknowledgements

My deepest gratitude goes to my PhD supervisors, Francesco Cerutti and Robert B. Appleby, who have been constant guidance and strong focussing in the lattice structure of this PhD. Francesco, all these years are an unforgettable experience of daily passion and commitment, and the miracle of a great human esteem happened, in addition to the professional one. Rob, it goes without saying that I would not be here without you.

Special thanks to Roberto Losito and Malika Meddahi. In addition to procurement and financing, always fundamental for an accelerator to translate from design to reality, they made this PhD real, and they were always supportive and a continuous source of precious advices.

An accelerator is not only what you get in simulations, but also the “real thing”. This PhD was the occasion to discover it; hence, I would like to thank all the people who took me by hand in this adventure: V. Kain, B. Goddard, O. Mete, C. Bracco, F.M. Velotti, E. Gianfelice-Wendt, C. Kornelis, E. Veyrun, L. Jensen, L. Drøsdal, who all unveiled different secrets of the SPS and its equipment.

Among the CERN colleagues, I cannot forget C. Maglioni, attentive work fellow on thermomechanics, and Y. Papaphilippou and H. Bartosik, for their constant help and advice with MADX.

A huge “thank you!” to all the FLUKA team, who never left me alone in all these years and who always showed me a more human side of CERN. I would like especially to mention all the people with whom I have been in close contact:

Alfredo, Vasilis, Anton, Carlo, Ruben, Thanasis, Ela, Vittorio, Christina, David and Pablo. Special mention to Gen, a real discovery of these years, and Luigi, always there for me. Maira, even if you are not based at CERN, you deserve a place here!

I cannot forget Vale Previtali and Marco Garattini, even if the time spent together was limited. Vale, thanks a lot for the days in the library!

How possible not to mention the office mates, daily pillars of this PhD activity: the “guru” (and Anna, of course!), Ketil, Elian, Philippo, Lef. Thanks for standing me all these years, even in the worst moments!

I could not make it without my friends, it is that simple: Tino, Ila and Giovannino, a real extension of my family, here in Geneva – and indeed you were on the point of fostering a PhD student! Elvis, Ema, Di, Betta, Simon, Lucio and Benny, Lucissimo, Delo, Francesca, Francesca, Cate, Luisella, Sguccioni (with Chiara and Gioele), Elly, Anas, Oscar, Martina: thanks for having always been there for me! These lines do not reflect the gratitude in my heart! A particular “thank you!” to the “PhD students on fire”, i.e. Fontolo, Lucia and Lemon, real day-by-day fellows in these last months of writing.

Finally, I owe the most to my family: dad and mom, Arianna and Grigna with my three wonderful nieces, i.e. Beatrice, Elena and Agnese. How to forget aunt Grazia? Thanks also for your constant support! You all have been the constant source of hope of these years of sacrifice, encouraging me at every difficult moment, and always bringing me back to equilibrium, to properly face every challenge in front of me.

# The Author

The Author completed the MSc in Nuclear Engineering at “Politecnico di Milano” in July 2007, with a final dissertation focussed on the activity carried out at CERN as technical student in the Radiation Protection group, under the supervision of dr. Marco Silari, about Monte Carlo (MC) simulations of concrete and iron shields for proton–therapy accelerators.

He spent three years at CERN working as fellow in the FLUKA Team, under the supervision of dr. Francesco Cerutti. The main activity was to perform MC simulations for beam–machine interaction studies, especially targeted to the LHC. Profiting from the experience gained in MC simulations, starting from 2011 he started the PhD activity on cleaning studies for collimation systems in circular accelerators, which is at present his main activity in the LHC Collimation Team at CERN.

# Chapter 1

## Introduction

Over the last century, physics has been investigating the elementary constituents of matter and the interactions between them. Starting from the Geiger–Marsden experiments between 1908 and 1913, which definitively ruled out Thomson’s plum pudding model of the atom in favour of the planetary model by Rutherford, the method has always been to use particles as probes to explore the secrets of matter. Beam particles are sent against a target, and the distribution of the secondary particles resulting from the interaction is detected, to be compared with the theoretical prediction to be verified.

At the beginning of the investigations, the only available sources of particles were radioactive nuclides occurring in nature. The need for higher energies and intensities, to explore new reactions, immediately triggered the development of tools for generating particle beams to be used as probes. Accelerators came soon into play, and the inexorable quest for improving beam characteristics went alongside of extending accelerator capabilities. In 80 years of history, it has been possible to move from small devices like Lawrence’s cyclotron to giant accelerator infrastructures like the one at CERN (see Fig. 1.1), with several experiments at different energies and physics reach served at the same time.

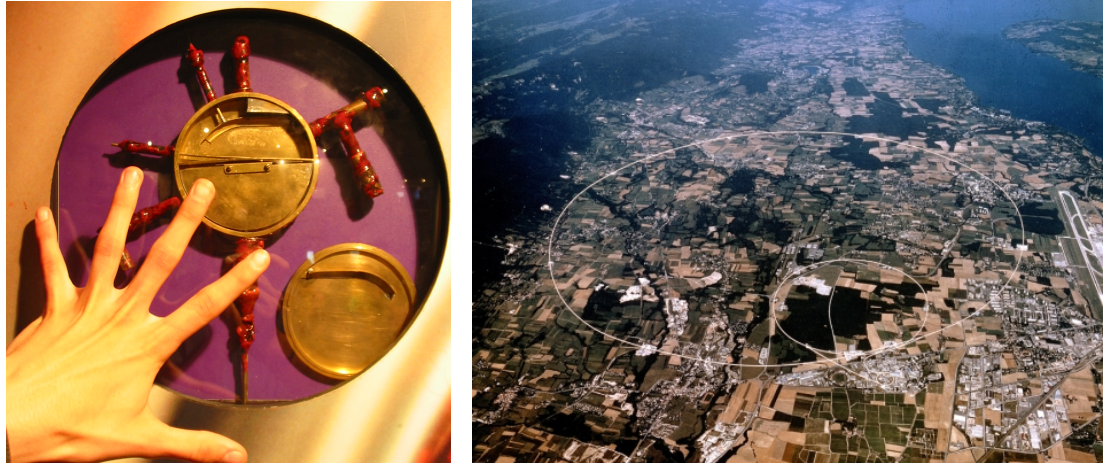


Figure 1.1: Left frame: a reproduction of Lawrence's cyclotron. Right frame: the CERN accelerator complex in the Geneva landscape.

Together with detector R&D, accelerator R&D is nowadays vital to high energy physics investigations. Technological advancements are important in all the systems involved in the accelerator operation: not only acceleration and magnetic guidance, but also beam controls and machine protection systems. These last ones have recently become more and more important, as beams become increasingly destructive with intensities and energies, and devices more and more expensive and fragile. In particular, the growing deployment of superconducting (SC) devices have tightened the requirements on safe machine operation.

Machine protection systems can reach high levels of complexity, involving different techniques of detecting equipment failures, sophisticated interlocks cross-checking different operational settings at the same time, and optimum design of beam-intercepting devices. The interaction of the lost particles with the protection device is the ultimately critical factor, as the beam characteristics may undermine the hardware integrity. Beam and impact parameters, together with material properties, are the factors ruling damage mechanisms. The analysis of faults and loss scenarios, and estimation of consequences on sensitive equipment through computer simulations are fundamental steps towards the design of a

machine protection system able to ensure the safe operation of the accelerator.

## 1.1 Colliding Beams

In high energy physics, the parameters most important to experiments are the energy available to new reactions, and the rate of useful events. The former coincides with the energy in the centre-of-mass reference system  $E_{\text{CM}}$ ; the latter leads to the definition of the instantaneous luminosity  $\mathcal{L}$  (see later). These two parameters are dramatically important whenever rare events, featured by small production cross sections, are under investigation. Moreover, they play a relevant role also in defining the typical scales and costs of the apparatus required for generating the necessary beams.

Starting from the kinematics of a moving particle and its four-vector momentum, the energy in the centre-of-mass reference system can be expressed in terms of the total energy  $E$  and momentum  $\vec{p}$  of the interacting particles as

$$E_{\text{CM}}^2 = (E_1 + E_2)^2 - (\vec{p}_1 + \vec{p}_2)^2.$$

It can be immediately seen that for a fixed-target experiment, in which one of the two particles is at rest, a relevant fraction of energy is lost due to the motion of the centre of mass. The first term on the right side of the expression profits from the contribution of the kinetic energy of only one interacting particle, and the second term, different from zero, further erodes energy, as  $\vec{p}_2 = \vec{0}$ . On the contrary, in case of colliding beams for which the collision point is at rest in the laboratory frame, the first term on the right side profits from the contribution of both beams and the second one is zero, as the momenta of the two particles are identical but opposite in sign. This case is called “head-on” collisions.

accelerator	particles	$E_{\text{coll}}$	$E_{\text{CM}}$	$E_{\text{FT}}$
ISR [1]	p p	28 GeV	56 GeV	1.67 TeV
SPS [2]	p p $^-$	315 GeV	630 GeV	212 TeV
ILC	e $^-$ e $^+$	500 GeV	1.0 TeV	0.98 EeV
Tevatron	p p $^-$	1.18 TeV	2.36 TeV	2.97 PeV
LHC	p p	7 TeV	14 TeV	104 PeV
FCC	p p	50 TeV	100 TeV	5.33 EeV

Table 1.1: Examples of total energy of colliding beams and beam energy required for performing fixed-target experiments with the same energy available in centre-of-mass reference system.

In the particular case of two particles with same rest mass  $m_0$  colliding head-on both with relativistic reduced energy at collision  $\gamma_{\text{coll}}$ ,  $E_{\text{CM}}$  can be re-written as

$$E_{\text{CM}} = 2\gamma_{\text{coll}} m_0 c^2.$$

On the contrary, in the case of a fixed-target experiment, where only one of the two identical particles is in motion with relativistic reduced energy  $\gamma_{\text{FT}}$ ,  $E_{\text{CM}}$  can be expressed as

$$E_{\text{CM}} = \sqrt{2(\gamma_{\text{FT}} + 1)} m_0 c^2.$$

While a linear dependence on the total energy of the colliding beams is found for the former expression, the latter is featured by the much slower growth with the square root. Finally, the required energy in fixed-target conditions to get the same energy in the centre-of-mass reference system as in the case of colliding beams is

$$\gamma_{\text{FT}} = 2\gamma_{\text{coll}}^2 - 1.$$

It can be immediately seen how convenient are colliders over fixed target experiments in the quest for the highest energies at the technological reach. Table 1.1 lists colliding beam energies, energy available in the centre-of-mass reference system and the beam energy required for performing the equivalent fixed-target

experiment with the same energy in the centre-of-mass reference system, for some colliders already shut-down, in operation or under design at the time of writing.

Proposals of machines for colliding high energy beams were first described in 1956 [3, 4]. The first machines to be built and operated [5] were the Ada storage ring in Frascati (Italy), colliding an electron and a positron beam, both at 250 MeV (1962<sup>1</sup>); the Princeton–Stanford CBX (USA), colliding two electron beams, both at 500 MeV (1963); and the VEP–1 storage ring in Novosibirsk (Russia), colliding two electron beams, both at 130 MeV (1963).

The rate of useful events  $dR/dt$  occurring in a high energy physics experiment depends on the cross section of the studied event  $\sigma$ , which represents the probability for a reaction to happen starting from the given collision, and the instantaneous luminosity  $\mathcal{L}$ , which describes the available rate of impacts, as

$$\frac{dR}{dt} = \mathcal{L} \sigma.$$

Expressing  $\sigma$  in  $\text{cm}^2$ , the units of measurement of the luminosity are  $\text{cm}^{-2} \text{ s}^{-1}$ . It can be useful to keep in mind that cross sections are measured in barn (equivalent to  $10^{-24} \text{ cm}^2$ ), with a mb being one of the most common sub-multiple. Similarly, it can be useful to express the luminosity in terms of inverse barn, i.e.  $10^{27} \text{ cm}^{-2} \text{ s}^{-1} = 1 \text{ mb}^{-1} \text{ s}^{-1}$ .

For a fixed target experiment, the luminosity can be calculated on the basis of the properties of both the impacting beam and the target which is hit. In case of a homogeneous material with constant density, it can be written as

$$\frac{dR}{dt} = \underbrace{\phi \rho l}_{\mathcal{L}_{\text{FT}}} \sigma,$$

---

<sup>1</sup>The reported year is the one when collisions started.

where  $\phi$  is the beam current (i.e. number of particles per second),  $\rho$  the density of the material and  $l$  the target length. When the target is much larger than the beam spot size, any dependence on the beam distribution can be neglected.

In the case of two colliding beams, both can be seen as beam and target at the same time, and as such the distributions must be taken into account in the calculation of the luminosity. In case of bunched beams with Gaussian profiles, the instantaneous luminosity can be expressed as follows

$$\mathcal{L} = \gamma \frac{n_b N_b^2 f_{\text{rev}}}{4\pi\beta^* \epsilon_n} R, \quad (1.1)$$

where  $\gamma$  is the relativistic reduced energy of the beam;  $n_b$  and  $N_b$  are the number of circulating bunches and bunch population, respectively;  $f_{\text{rev}}$  is the revolution frequency of the beam in the accelerator;  $\beta^*$  and  $\epsilon_n$  are the value of the optical  $\beta$ -function (see Sec. A.1) at the collision point and the normalised emittance of the beam (see Sec. A.4), both determining the transverse size of the beam (see Sec. A.2).  $R$  is a geometrical factor expressing how bunches cross, and in case of Gaussian profiles it can be written as

$$R = \frac{1}{\sqrt{1 + \left[ \frac{\theta_c \sigma_z}{2\sigma} \right]^2}},$$

where  $\sigma_z$  and  $\sigma$  are the longitudinal and transverse r.m.s. size of the bunches, respectively. The quantity  $\theta_c \sigma_z / 2\sigma$  is also known as the “Piwinski angle”, where  $\theta_c$  is the crossing angle.. For a more rigorous derivation of the expression of the luminosity, please refer to Ref. [6].

It can be immediately seen that for a collider the luminosity depends only on

Collider	Beams	Energy [GeV]	$\mathcal{L}_{\text{peak}}$ [ $10^{30} \text{ cm}^{-2} \text{ s}^{-1}$ ]
SPS	$p$ vs $\bar{p}$	315 vs 315	6
Tevatron	$p$ vs $\bar{p}$	1000 vs 1000	100 [7]
HERA	$e^+$ vs $p$	30 vs 920	40
LHC	$p$ vs $p$	7000 vs 7000	10000
LEP	$e^+$ vs $e^-$	105 vs 105	100
PEP	$e^+$ vs $e^-$	9 vs 3	8000 [7]
KEKB	$e^+$ vs $e^-$	8 vs 3.5	10000

Table 1.2: Beam particle, collision energy and peak luminosity of colliders recently built and operated [6]. LHC values refer to design parameters.

beam characteristics and collision conditions. While the instantaneous luminosity drops off with time due to burning beam particles (and other effects lowering the beam intensity), its peak value is determined by optimising the working conditions, and expresses the best that the accelerator can reach. Table 1.2 lists accelerated beams, collision energies and peak luminosity of colliders recently built and operated [6].

As the integral of the collision rate over time gives the statistics available to the analysis of experimental data, the integral over time of the instantaneous luminosity, i.e. the integrated luminosity  $\mathcal{L}_{\text{int}}$  [6], gives an indication of the useful collisions collected during a certain running period  $\Delta T$

$$\mathcal{L}_{\text{int}} = \int_0^{\Delta T} \mathcal{L}(t) dt. \quad (1.2)$$

The integrated luminosity is directly dependent on the machine availability.

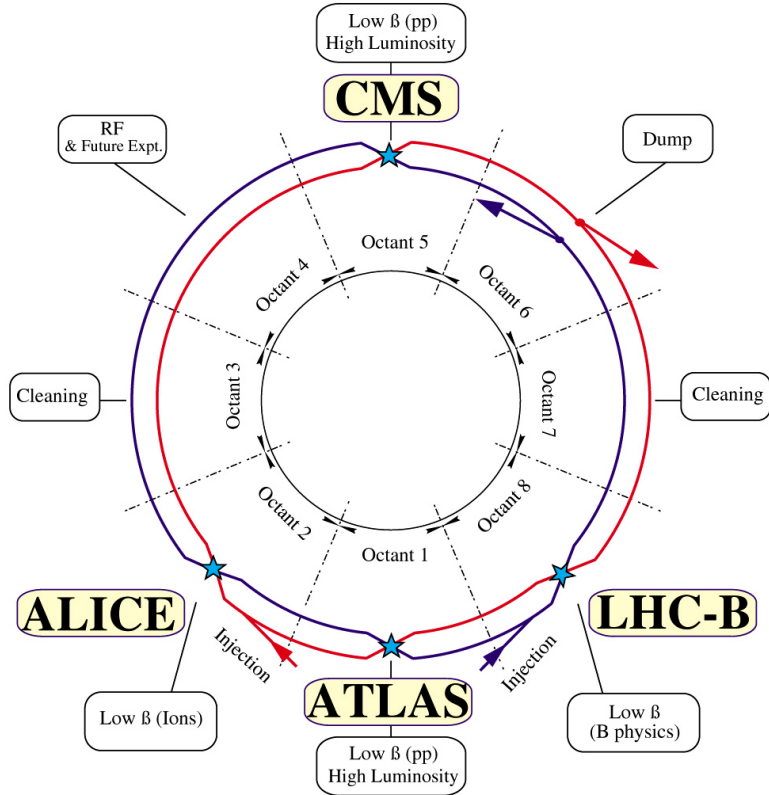


Figure 1.2: Layout of the LHC.

## 1.2 The Large Hadron Collider and the CERN Accelerator Complex

The CERN LHC is the largest and most powerful machine for research ever designed, built and operated so far. It extends for approximately 27 km underground the Geneva area, crossing the border between France and Switzerland. It is a synchrotron, where two counter-rotating hadron beams are accelerated and collided. It can be routinely operated with both proton and lead ion beams.

The LHC is segmented in eight arcs, keeping the beams on the circular orbit, and eight long straight sections (LSSs), where devices with dedicated tasks are installed (see Fig. 1.2). The part of each LSS hosting devices with specific tasks is called Insertion Region (IR) [8], and it is surrounded by matching sections

(MSs), responsible for the smooth transition between the specialised optics of the IR and the regular one of the arc. Finally, dispersion suppressors (DSs) are special strings of magnets at each end of the arcs, aimed at cancelling dispersion (see Sec. A.1) effects onto the IRs.

At the middle of four LSSs beams are crossed and giant detectors intercept and measure the collision products: ATLAS [9] (IR1) and CMS [10] (IR5) are two general purpose, high-luminosity detectors; ALICE [11] (IR2) is mainly devoted to study the quark-gluon plasma; LHCb [12] (IR8) hunts for measurable asymmetries between matter and antimatter. The other four LSSs are dedicated to the beam acceleration (IR4), to betatronic (IR7) and momentum collimation (IR3), and to the extraction and beam dump system (IR6). The injection of the two beams is performed upstream of the low-luminosity detectors, one per beam: Beam 1 (B1) is injected upstream of the ALICE detector, and B2 is injected upstream of the LHCb detector (see Fig. 1.2).

The IRs hosting the experimental detectors are equipped with special magnet strings, aimed at the final focussing of beams before collision. These are the last stage of the accelerator before each beam enters the experimental vacuum chamber, and they sit on both sides of each detector. They are composed by three quadrupoles in a row, and as such they are called the “inner triplet” (IT), even though the central magnet is split into two modules.

Table 1.3 lists some of the main beam parameters for “nominal” LHC operation with protons [8]. The so-called “ultimate” LHC operation is another set of beam parameters the LHC is expected to work with, in addition to the nominal ones. The aim is to double the peak luminosity increasing the bunch population up to  $1.7 \cdot 10^{11}$  protons per bunch [13]. As it can be seen, the LHC is a record-breaking machine; unprecedented values of beam intensity for the given emittance, beam kinetic energy at collision and stored energy per beam are

			Injection	Collision
Proton energy	$E_p$	[GeV]	450	7000
Number of particles per bunch	$N_b$		1.15 $10^{11}$	
Number of bunches per beam	$n_b$		2808	
Longitudinal emittance	$\epsilon_s$	[eV s]	1	2.5
Transverse normalised emittance	$\epsilon_n$	[ $\mu$ m]	3.5	3.75
Stored energy per beam	$E_T$	[MJ]	23.3	362
Peak Luminosity (ATLAS and CMS)	$\mathcal{L}_0$	[ $\text{cm}^{-2} \text{ s}^{-1}$ ] [ $\text{fb}^{-1} \text{ s}^{-1}$ ]		$10^{34}$ $10^{-5}$
Half crossing angle (ATLAS and CMS)	$\theta_c/2$	[ $\mu$ rad]		142.5
optical $\beta$ -function (ATLAS and CMS)	$\beta^*$	[m]	18	0.55
Revolution Frequency	$f_{\text{rev}}$	[kHz]		11.245

Table 1.3: Main beam parameters for “nominal” LHC operation with protons [8].

some of the parameters that make LHC unique in the world. For comparison, Fig. 1.3 [14] shows the evolution of the total energy available in the centre-of-mass reference system and the peak luminosity in the last half-century.

Thanks to its high values of beam energy and intensity, the LHC can explore the present frontier of high energy physics. The official announcement on July, 12<sup>th</sup> 2012 of the discovery of a new boson at a mass of approximately 125 GeV/c<sup>2</sup> [15, 16], the properties of which are in very good agreement with those of the long-awaited Higgs particle, is an intermediate step towards those experimental achievements that the LHC is expected to reach. Colliding beams in the multi-TeV region, the LHC is also supposed to give further insights into Beyond Standard Model (BSM) physics, including dark matter and super-symmetry.

Despite the large circumference, dipole fields of 8.3 T are required to keep protons at top energy on the circular orbit. As this value is much higher than the maximum magnetic field provided by warm dipoles, the arcs, and partially the LSSs, are equipped with SC magnets.

Superconductivity [18] is a property some materials have when cooled to very

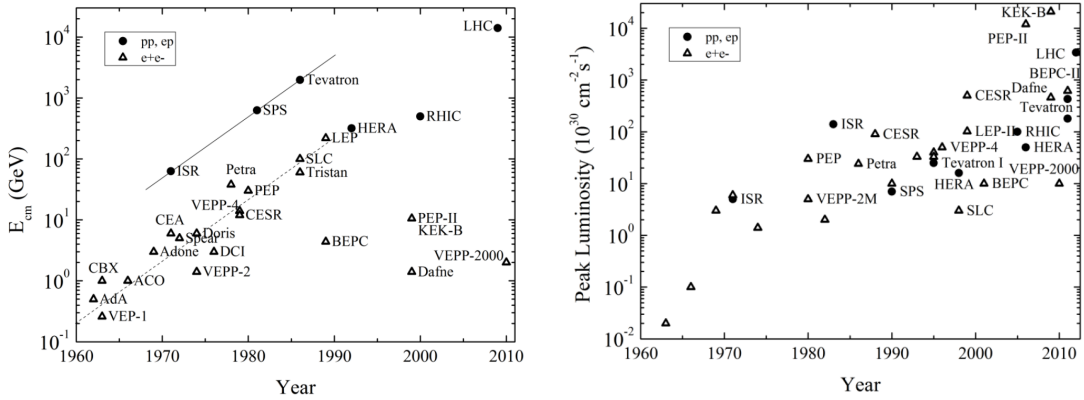


Figure 1.3: Recent evolution [14] of the total energy available in the centre-of-mass reference system (left frame) and of the peak luminosity (right frame).

low temperatures, and it enables the flow of currents with no dissipation by the Joule effect. In such a way, it is possible to let high current densities flow through wound conductors, and thus obtain high values of magnetic field. Figure 1.4 [17] shows the critical curve of Niobium–Titanium, the SC material chosen for the LHC dipoles. The critical curve identifies the surface in the phase diagram which separates the SC from the normal conducting state. The coils are kept SC if the working point identified by the operating temperature  $T$ , the applied magnetic induction  $B$  and the current density  $J$  stays below that curve. The blue dot in the picture identifies the working point of the LHC dipoles. If a local increase in temperature brings the working point above the curve, the coil locally loses the SC state for the normal conducting one, with further coil heating due to Joule effect and consequent spreading of the normal conducting zone. What is thus induced is the so-called magnet “quench”. Quenches should be avoided during LHC operation, not only to avoid any damage to the SC material in case of quenches rapidly evolving, but also because recovery is a lengthy process that reduces the time available to physics. Even small disturbances like heating from beam losses or friction between cables could bring the superconductors irreversibly over the critical curve in the phase diagram.

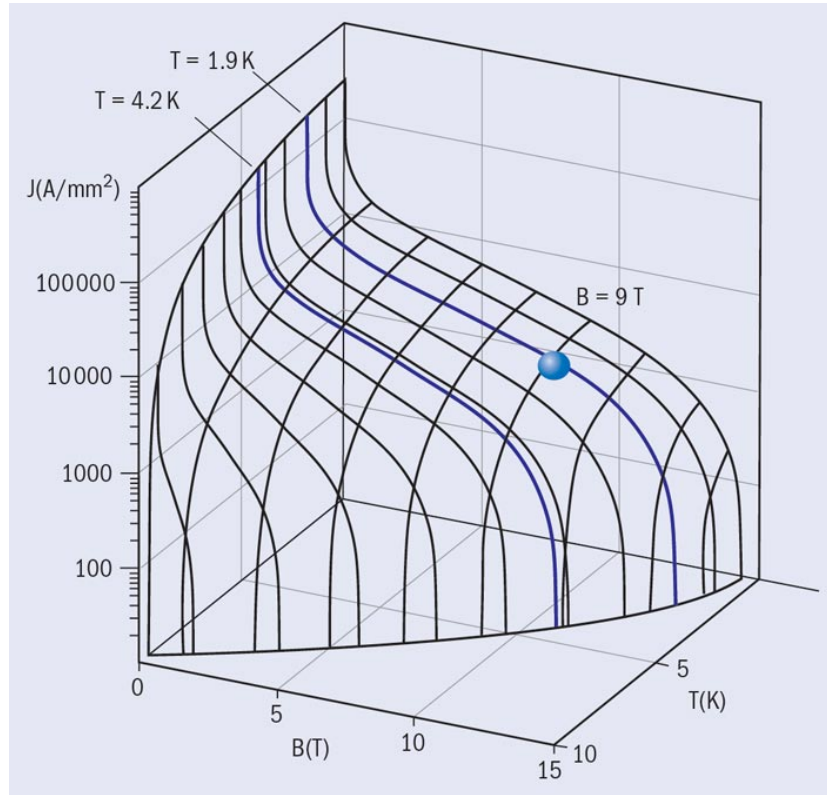


Figure 1.4: Critical curve of the LHC SC dipoles [17].

In addition to the LHC, CERN operates other accelerators, to complement its research activity with fixed-target experiments at lower energy scales. Being connected in series, they are used as successive stages of acceleration, and in particular as injectors to the LHC. Figure 1.5 shows the schematics of the CERN accelerator complex, including their main experimental apparatus, whereas Tab. 1.4 summarises the accelerator chain of protons [19], along with injection and extraction energies. While the LHC is a SC machine, all other accelerators and beam transfer lines are made up of warm magnets.

After being generated at approximately 100 keV in the Duoplasmatron, with a maximum current of 300 mA, protons are immediately bunched by a radio frequency quadrupole (RFQ). An RFQ is a combined-function straight device; with only one RF wave, it focusses, bunches and accelerates at the same time a continuous beam of charged particles with high efficiency and preserving the emittance.

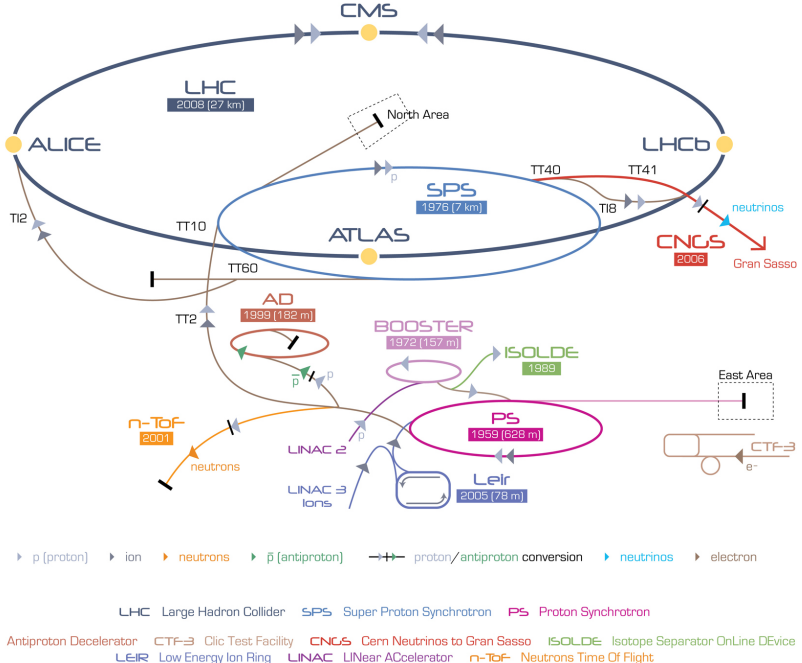


Figure 1.5: Schematic view of the CERN accelerator complex.

Accelerator	Inj. Energy	Ext. Energy
LINAC2	750.0 keV	50.0 MeV
PSB	50.0 MeV	1.4 GeV
PS	1.4 GeV	26.0 GeV
SPS	26.0 GeV	450.0 GeV

Table 1.4: Accelerator chain for proton injection into LHC, along with injection and extraction energies [19].

The CERN RFQ is capable of delivering an output current of 200 mA, with a high voltage between the electrodes of approximately 180 kV, at the frequency of 200 MHz. After the RFQ, protons are injected in the LINAC2, the first stage of acceleration. This is a 35 m long Alvarez linear accelerator, with a top energy of 50 MeV. After LINAC2, all other acceleration stages before the LHC are circular machines: the Proton Synchrotron (PS) with its Booster (PSB), and the Super Proton Synchrotron (SPS).

The PS is the oldest machine in operation at CERN; started in 1959, it delivers protons at 26 GeV/c. It has a circumference of 628 m, mainly filled with

combined–function magnets. It has undergone many modifications, and its proton intensity has grown a thousandfold.

Protons are not injected directly into the PS, but are pre–accelerated in the PSB up to an energy of 1.4 GeV. The low injection energy of 50 MeV limits the intensity the PS can accept, due to the tune spread induced by space–charge effects; the connection of the PSB in 1972 allowed the PS to boost its injected intensity by a factor of 10. After several upgrades of the PSB, which lead to increase the beam energy at flat top to the present value from the original one of 800 MeV, the intensity the PS can digest is 100 times bigger than the one at 50 MeV. The PSB is a quarter of the PS in size.

The SPS represents the last stage of acceleration before injection into the LHC. It is a 6.9 km long synchrotron, first switched on in 1976, at present accelerating protons up to 450 GeV/c. It has been operated not only as accelerator for fixed–target experiments, but also as proton–antiproton collider, leading to the Nobel prize–winning discovery of the  $W^\pm$  and  $Z^0$  bosons in 1983.

### 1.3 The High Luminosity LHC and the LHC Injectors Upgrade Projects

Since the first circulating beam at 450 GeV in 2010 and throughout Physics Run 1, the LHC performance has been continuously improved, in terms of both beam energy and peak luminosity. Only in 2012, the LHC delivered a total integrated luminosity of more than  $20 \text{ fb}^{-1}$  to the ATLAS and CMS detectors independently [20], in proton–proton collisions at 8 TeV energy in the centre–of–mass reference system. For comparison, all other hadron colliders in the world have so far produced a total integrated luminosity of approximately  $10 \text{ fb}^{-1}$  [13]. This remarkable result has been possible thanks to the high peak luminosity of

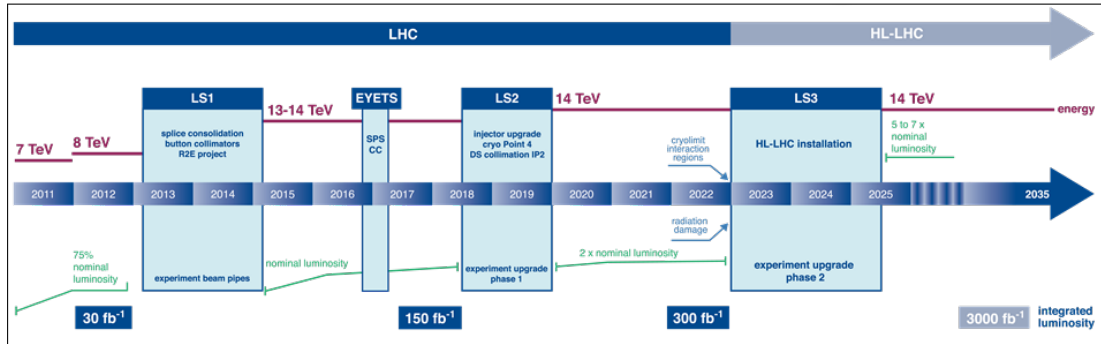


Figure 1.6: LHC baseline plan for the period 2012–2022 and beyond [21].

the LHC, and its steady improvement towards its nominal value.

Figure 1.6 shows the baseline plan of the LHC for the period 2012–2022 [22], as of November 2014. The Long Shut Down 1 (LS1), covering 2013 and 2014, should allow the LHC nominal operation, i.e. with a peak luminosity of  $10^{34} \text{ cm}^{-2} \text{ s}^{-1}$  in proton–proton collisions at 14 TeV centre-of-mass reference system. The LS2, expected to occur in 2018–2019, should enable LHC operation with ultimate beam parameters, i.e. doubling the peak luminosity for the same collision energy.

With such a schedule, the LHC should be able to deliver a total integrated luminosity of  $\sim 300 \text{ fb}^{-1}$  at best in its first 10 years of life (see Fig. 1.7). Key to this result are the high value of the peak luminosity, again, and the optimisation of the machine running time. Nevertheless, after 2019 the gain in statistics will become marginal without a considerable improvement in the peak luminosity.

The High Luminosity LHC (HL-LHC) project [13, 22, 23, 21] envisages a relevant upgrade of the LHC, aimed at a total integrated luminosity greater than  $3000 \text{ fb}^{-1}$  in approximately 12 years of operation. Such a high value can be achieved only with a significant increase in the instantaneous luminosity  $\mathcal{L}$ . The necessary hardware change and machine upgrade are planned for the LS3, in 2023–2025 (see Fig. 1.7).

In order to limit the peak energy deposition in the SC coils of the IT and the peak pile up in the detectors, the instantaneous luminosity will be kept at

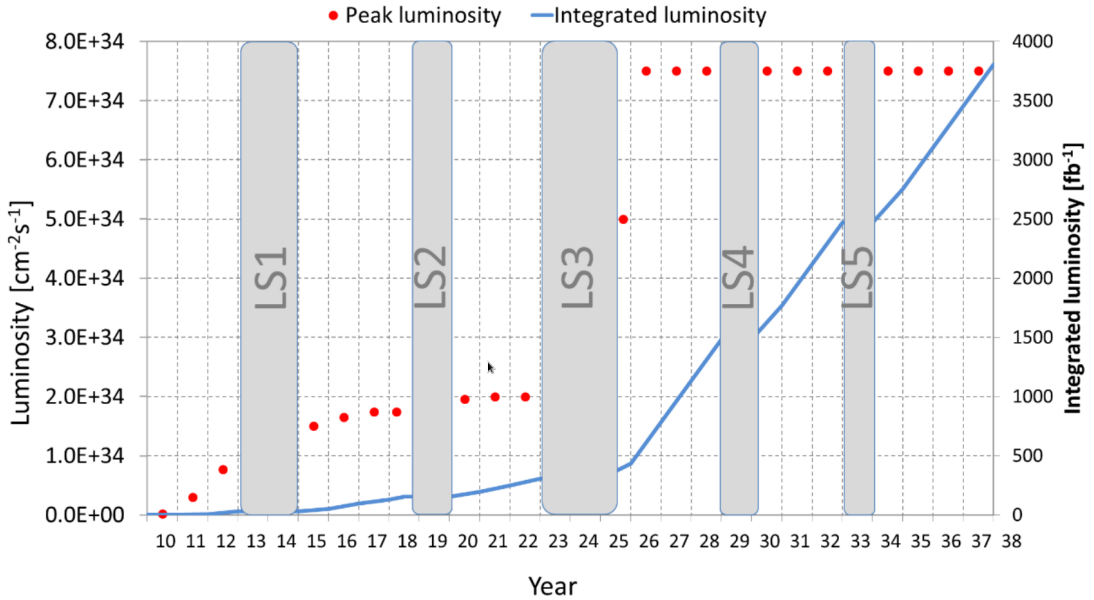


Figure 1.7: Possible peak luminosity evolution with best forecast on the integrated luminosity [22].

a constant value, i.e. “levelled” at  $5 \cdot 10^{34} \text{ cm}^{-2} \text{ s}^{-1}$ . This would make the total integrated luminosity per year of approximately  $250 \text{ fb}^{-1}$  at reach. Luminosity levelling aims at keeping the instantaneous luminosity constant with running time, compensating the proton burn-off with slow modifications in the machine working point at collision.

As it can be seen from its definition (see Eq. 1.1), the instantaneous luminosity can be boosted improving not only the beam parameters, i.e. the number of circulating protons (the product of bunch intensity  $N_b$  times the number of bunches per beam  $n_b$ ) and the normalised emittance  $\epsilon_n$ , but also the working point of the machine, acting on the value of  $\beta^*$  and the crossing scheme. Therefore, the strategy adopted relies on a significant improvement of the machine optics on the one hand, and of the beam characteristics on the other, in particular normalised emittance and bunch intensity. While attaining the former implies modifications to the LHC machine, the latter requires several upgrades of the LHC injection chain. These will be achieved in the framework of the LHC Injectors Upgrade

(LIU) project [24, 25].

A new LHC optics has been recently proposed, based on the novel Achromatic Telescopic Squeezing (ATS) scheme [26]. In this optics, the arcs adjacent to the high-luminosity insertions are used as enhanced matching section and the sextupoles therein correct the chromatic aberrations induced by the final focussing stage more effectively thanks to the larger optics functions thus obtained, with peaks at the correcting sextupoles. As a matter of fact, the new scheme requires the replacement of the IT, at least.

The requirements on the beam quality involve an upgrade of all the accelerators in the LHC injection chain. Relevant machine changes have been already put in place during the LS1 [25]. These modifications involve RF cavities, power supplies (especially those of RF cavities and injection and extraction kickers), new multi-pole magnets, beam instrumentation, and the deployment of a new optics for the SPS. Even though all these upgrades aim at removing bottle-necks to the new beams, the key ingredient for improving beam emittance and bunch population is the installation of the new LINAC4, replacing the existing LINAC2. The new accelerator is meant to generate  $H^-$  ions at 160 MeV, with a current of 40 mA [27]. A stripping foil system is envisaged as injection system into the PSB, after which the regular proton acceleration takes place. Finally, a new bunch splitting scheme has been recently proposed for the PS, the Batch Compression, bunch Merging and Splittings (BCMS), to host a further higher bunch intensity in even smaller normalised emittances [28].

Table 1.5 summarises the main beam parameters at extraction in the SPS for the nominal and ultimate LHC, along with values available in the machine before LS1 and those foreseen with BCMS beams at start-up after LS1. Those for different LIU configurations are presented as well, along with superseded ones, as these have evolved during the time of the present work. The last column

	$n_b$ []	$N_b$ [ $10^{11}$ ]	$\epsilon_n$ [ $\mu\text{m rad}$ ]	$\sigma_{\delta p/p}$ [ $10^{-4}$ ]	$n_b N_b / \epsilon_n$ [ $10^{19} \text{ m rad}$ ]
Nominal LHC	288	1.15	3.5	< 2.8	0.946
Ultimate LHC	288	1.7	3.5	< 2.8	1.399
before LS1	144	1.6	2.0	—	1.152
BCMS after LS1	288	1.3	1.3	—	2.880
LIU Standard	288	2.3	2.1	2	3.154
LIU BCMS	288	2.0	1.3	—	4.431
LIU Superseded					
(SPS Q26, 2011)					
Nominal LIU	288	1.15	1	1.68	3.312
Maximum LIU	288	2.50	2.5	6.80	2.880
(SPS Q20, 2012)					
Nominal LIU	288	1.15	1	1.31	3.312
Maximum LIU	288	2.50	2.5	5.25	2.880

Table 1.5: Main beam parameters at extraction in the SPS. LIU beam parameters are updated to 2013, whereas the superseded ones date to 2011 and 2012.

lists the ratio between the population of the bunch train over the normalised emittance, which gives an indication of the particle density and its capability of locally inducing damage.

## 1.4 Machine Protection

Machine protection is an aspect of accelerator design and operation of growing importance in the last decades. As top energies and intensities are increasing and transverse dimensions are getting smaller, accelerated beams are becoming more and more destructive, while accelerator devices more sophisticated and fragile. Machine protection has to deal with a large variety of fault scenarios triggered by primary beam losses and secondary radiation fields. Hence, solutions and mitigation actions span over a broad spectrum of systems and devices.

### 1.4.1 Machine Protection Needs

In an accelerator environment, different mechanisms can undermine the regular operation of the machine or induce damage to sensitive equipment, depending on the type of device and typical time-scales for the fault or damage to appear. Machine-protection systems usually deal with localised losses occurring in a limited time interval, whereas passive shielding measures protect against radiation fields spread over a larger portion of the machine and spanning over longer time-scales.

Warm and SC magnets can withstand quite different levels of local and sudden energy deposition before a problem begins to appear. Indeed, the fault the most likely to happen to a SC magnet is the quench, whereas warm magnets are sensitive to an abnormal overpressure in the water-cooling channels, leading to a rupture of the cooling pipe. While just few tens of  $\text{mJ cm}^{-3}$  are enough to induce a quench (e.g. see Ref. [29], for recent evaluations concerning a couple of LHC SC magnets), some tens of  $\text{J cm}^{-3}$  are required to trigger an overpressure wave in water capable of breaking the cooling pipes. The largely different energy scales reflect the different processes involved, i.e. a phase transition inducing a fault in SC magnets, and a mechanical breakage leading to a damage in normal conducting magnets.

Patterns of energy deposition in coils are not insensitive to magnet geometry. Since the field lines of normal conducting magnets are shaped by the poles, these sit close to the beam pipe, with the coils being generally further out. On the contrary, the field lines of SC magnets reflect the geometrical arrangement of the coils, and these are necessarily very close to the pipe; thus, they are directly exposed to radiation coming from the inside of the pipe. In addition, poles of normal conducting magnets may offer occasional shielding effects.

Normal and SC magnets can suffer from the more serious issue of damaging the

coil, usually represented by locally melting copper [30]. The maximum allowed energy deposition before this event happens is much higher than the one required by a quench or an overpressure event, being in the order of a few  $\text{kJ cm}^{-3}$ .

Ageing of the coil insulation is another physical process that can limit the performances of both types of devices [31]. The electrical insulation ensures that the current flows only along the conductors and not between individual conductors or between the coil and the ground. Its degradation may lead to current leaks with local heating or unbalanced circulating currents, with distortion of magnetic field lines. Contrary to the previous sources of faults, ageing is a cumulative effect, requiring the coil being irradiated for long times, comparable to life cycles of the accelerator. As a rough indication, few tens of MGy is a typical value of limit integrated dose [32, 33].

Damage to control electronics can also represent a bottle-neck for the operation of the accelerator. Since the electronics is located not immediately close to the beam pipe but far from it, the damage is induced not by the direct impact of the beam, but from streaming radiation generated during regular operation of the machine, due to regular events like the interaction of the beam with the residual gas in the pipe or with cleaning devices or with experimental apparatus (either the beam-beam collisions in the case of a collider, or the target hit in case of fixed-target facility). The electronics may fail in three different ways:

**Single Event Upset (SEU).** A high-energetic hadron (with a kinetic energy typically above 20 MeV) deposits energy in a memory cell through direct ionisation, and flips the stored value. This type of fault is stochastic, and it leads to a sudden misbehaviour of the controlled device;

**damage to the crystalline structure** of the semiconductor. This is a long term type of damage, related to cumulative Displacements per Atom (DPAs);

**damage to the insulator** layer of the device. This is another long term type

of damage, related to the integrated dose received by the electronic device.

### 1.4.2 Machine Protection Systems and Beam–Intercepting Devices

Machine Protection Systems are installed to protect delicate accelerator components from sudden losses, or to keep unavoidable constant losses localised to specific locations of the accelerator, where they have little harm. Crucial for avoiding damage to the machine, they can trigger a beam dump signal in case an abnormal radiation field, due to a localised loss, is detected. As such, they are made up of a system of Beam Loss Monitors (BLMs), a system of interlocks and beam–intercepting devices.

BLMs are monitors distributed all along the beam line. At CERN, they are most frequently ionisation chambers, filled with nitrogen gas. When a loss takes place, beam particles interact with the vacuum chamber and generate secondary particle showers. Being of lower energy, much larger in number and spread over a larger solid angle, these are easily detected by monitors located nearby the pipe. The presence of massive elements like magnets and the position of the monitors change the amount of energy deposited in the active gas region, the intensity of the signal read and consequently the effectiveness of the monitors.

Interlock systems take measures when an abnormal behaviour of an accelerator sub–system is recognised. Operational settings are continuously checked, and if they exceed allowed margins, the beam is automatically dumped. The checks span all over the different devices needed for the regular operation of the accelerator, from optics settings and magnet powering to collimator apertures and signals in BLMs. Accordingly, interlock systems may reach high levels of complexity, depending on the machine they have to protect

Beam–intercepting devices are apparatus installed in strategic locations along

the beam line, aimed at intercepting beam particles. Once they hit the absorbing medium, beam particles start interacting with it through a large variety of processes (see Sec. 1.4.3), which lead to the possible particle loss to the beam and the development of hadronic and electromagnetic (EM) showers. For hadrons above few GeV per nucleon of kinetic energy this last component is responsible for the heat load on the device and its capability to contain the beam energy, whereas nuclear inelastic interactions are the key to beam attenuation and material activation.

Collimators, absorbers, masks, scrapers and dumps are main examples of different types of devices, with specific characteristics and purposes. *Collimators* are meant to remove particles far from the beam core (tails) through direct absorption in the active material or scattering towards downstream *absorbers*. They are featured by massive jaws, parallel to the longitudinal direction of the beam to be cleaned, and their transverse position with respect to the beam core sets the amount of particles to be removed. *Scrapers* are similar devices, but aimed at cleaning closer to the beam core; consequently, the thermomechanical load on the active material is higher, and the jaw length thus decreased. *Masks* are bulky absorbers usually located outside of the vacuum chamber, and meant to protect devices from particle showers started upstream. Hence, they do not necessarily protect against the direct loss of the primary beam, but from spray radiation. Finally, *dumps* are the devices where, during regular operation, the beam is ultimately and safely lost before injecting a new one.

### 1.4.3 Interaction of Radiation with Matter

When a beam particle interacts with the active medium of an intercepting device, a complex series of events takes place, spanning many orders of magnitude in energy. In the case of LHC or SPS beams, the spectrum of events extends from

particle–nucleon interactions at tens or hundreds of GeV in the centre–of–mass reference system down to low–energy nuclear reactions, including absorption reactions of thermal neutrons in the meV energy range. The theoretical framework describing all the involved interactions relies on a century of atomic, nuclear and particle physics (comprehensive summaries can be found in Refs. [34, 35, 36] and in the references quoted therein). The net effects are:

- the *loss* of the particle to the beam, or its *possible survival*, with changed direction and energy. In this last case, the particle continues its path along the beam line following a deviated orbit, and it is definitively lost in a downstream device. Surviving particles determine the pattern of losses in downstream portions of beam line;
- the generation of *secondary particle showers*. While propagating, they induce thermal loads, mechanical stresses and radioactivity in the hit device and in the downstream ones.

## Ionisation

A charged particle travelling through matter can lose energy through collisions against atomic electrons of the traversed medium. If the energy transfer is high enough, electrons are set in motion, and the medium is ionised. The *mean* energy lost per unit path length  $-\mathrm{d}E/\mathrm{d}x$  is called “stopping power”, and it can be expressed by the Bethe–Bloch equation [34]

$$-\frac{\mathrm{d}E}{\mathrm{d}x} = K z^2 \frac{Z}{A} \frac{1}{\beta^2} \left[ \frac{1}{2} \ln \frac{2m_e c^2 \beta^2 \gamma^2 T_{\max}}{I^2} - \beta^2 - \frac{\delta(\beta\gamma)}{2} \right]. \quad (1.3)$$

The expression shows the dependencies onto material properties, such as atomic number  $Z$ , mass number  $A$ , and mean ionisation potential  $I$ , as well as onto the properties of the travelling particle, such as its charge  $z$ , its relativistic reduced

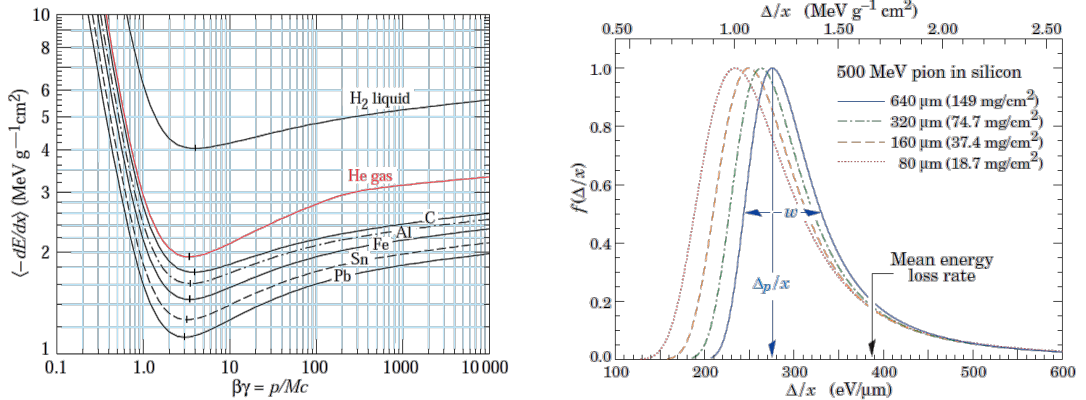


Figure 1.8: Left frame: stopping power in different materials as a function of the relativistic reduced momentum  $\beta\gamma$  [34]. Radiative effects are not taken into account. Right frame: straggling functions in silicon for 500 MeV pions, normalised to unity at the most probable value  $\delta_p/x$  [34].

speed  $\beta$  and energy  $\gamma$ .  $c$  is the speed of light.  $K$  is a constant, obtained from the product of the Avogadro number  $N_A$  by the classical electron radius  $r_e$  and the electron mass  $m_e$  [34]

$$K = 4\pi N_A r_e^2 m_e c^2.$$

$T_{\max}$  is the maximum kinetic energy which can be transferred to a free electron in a single collision, and  $\delta$  represents the density effect, i.e. the polarisation of the material limiting the relativistic expansion in the transverse direction of the electric field of the travelling particle.

Equation 1.3 is the relativistic formulation for particles other than electrons, with neither the corrections at low energies (e.g. shell corrections or Barkas corrections) nor the contribution from radiative effects at high energies. The left frame of Fig. 1.8 shows the stopping power in different materials, as a function of the relativistic reduced momentum.

It should be kept in mind that the stopping power expresses only the *average* energy lost by a particle when going through a material. The electrons put in motion are emitted over a wide energy spectrum, with  $T_{\max}$  being its upper limit. For a particle with mass  $M$  and momentum  $\beta\gamma Mc$  travelling through the medium,

$T_{\max}$  can be expressed as [34]

$$T_{\max} = \frac{2m_e c^2 \beta^2 \gamma^2}{1 + 2\gamma m_e/M + (m_e/M)^2}. \quad (1.4)$$

For protons at 450 GeV/c,  $T_{\max}$  is as high as  $\sim 150$  GeV, many orders of magnitude bigger than typical values of the stopping power integrated over the travelled path (see left frame of Fig. 1.8). Consequently, the energy lost by a single particle can be described by a probability density function, and in particular by the highly-skewed Landau–Vavilov distribution [34] (see the right frame of Fig. 1.8). Rare hard collisions with atomic electrons therefore contribute to significant changes in the energy of a particle surviving short paths in intercepting devices.

## Multiple Coulomb Scattering and Rutherford Scattering

A charged particle traversing a material experiences numerous small-angle deflections due to Coulomb scattering onto atomic nuclei. Since the mass of the atomic nuclei is usually much larger than the one of the travelling particle, the energy transfer is negligible; on the contrary, the direction of the particle is continuously changed by small deflections, the effect of which piles up as the particle travels through the material. The final angular distribution of the particles at the exit of the medium is described by the Molière theory of the Multiple Coulomb Scattering (MCS) [34], with a central Gaussian core and large tails due to single Rutherford scattering interactions at big angles [34]. The Gaussian core of the distribution projected on a plane has a root mean square (rms) width that can be expressed as

$$\theta_0 = \frac{13.6 \text{ MeV}}{\beta c p} z \sqrt{x} \left[ 1 + 0.038 \ln(x) \right], \quad (1.5)$$

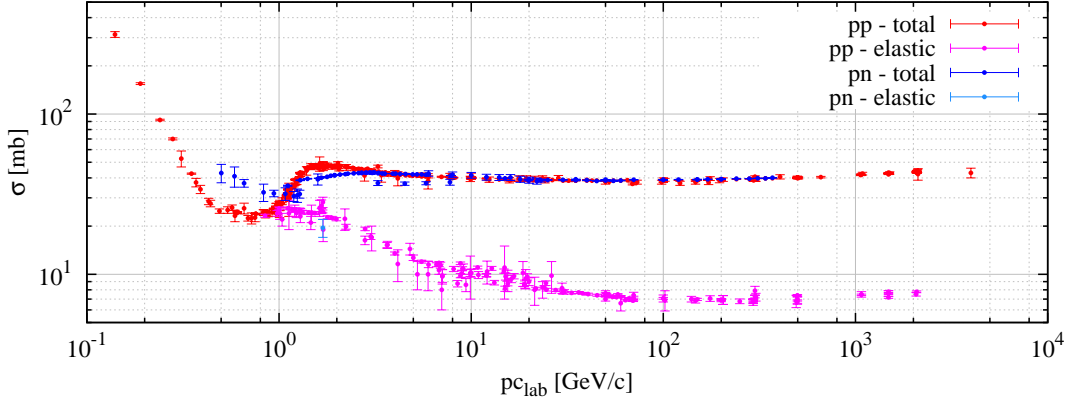


Figure 1.9: Total and elastic cross sections of  $pp$  and  $pn$  reactions [34].

where  $\beta c$ ,  $p$  and  $z$  are the speed, momentum and charge of the travelling particle, and  $x$  is the thickness of the medium, in units of the radiation length (see below).

## Nuclear Scattering

Nuclear elastic and inelastic scattering events determine the performance of beam-intercepting devices, as they are responsible for the largest variations in energy and direction of the primary beam particle (elastic and single diffractive, see later), or for its loss to the beam and for starting secondary particle showers (inelastic).

Figure 1.9 shows measured values of total and elastic cross sections for proton–proton ( $pp$ ) and proton–neutron ( $pn$ ) scattering as a function of the incident proton momentum [34]. The  $pp$  total and elastic cross sections start to differ at the pion production threshold, with the difference being exactly the one of inelastic events. Moreover, while the total  $pp$  cross section stays basically constant above 10 GeV/c, the contributions from elastic and inelastic scatterings change with momentum.

In nuclear *elastic* scattering, the beam particle survives to the event it underwent, and its direction and energy are changed according to the two–body

kinematics. Together with ionisation and MCS, nuclear elastic scattering plays a major role in diluting primary beam particles and reducing their energy when surviving to the impact onto intercepting devices. On the contrary, nuclear *inelastic* scattering is a type of events during which the beam particle is lost to the beam and generate new (secondary) particles. For this reason, nuclear inelastic events are extremely important when designing beam–intercepting devices, as they provide the actual beam attenuation.

A type of inelastic nuclear reaction relevant at SPS and LHC beam energies is the *single diffractive* scattering. This is a quasi–elastic process, where the momentum transfer of the collision implies a high mass excitation state of one of the interacting particles. In particular, a nucleon in the medium gets excited, and the beam particle loses a limited fraction of its energy, such that it can travel along the beam line for several hundreds or thousands of meters before being lost.

The probability that a particle going through a medium survives without undergoing any nuclear interaction decreases exponentially with the travelled path. The parameter characteristic of the attenuation is the “mean free path”, which is the distance required to reduce the number of non–interacting particles by a factor  $1/e$ ; it also corresponds to the mean distance a particle travels on average in the medium before interacting. It can be immediately derived from the corresponding value of cross section as

$$\lambda = \frac{1}{\sigma \rho N_A} \frac{w}{\rho}, \quad (1.6)$$

where  $\sigma$  is the cross section,  $w$  and  $\rho$  the atomic weight and density of the material, respectively, and  $N_A$  the Avogadro number. In particular, the “inelastic interaction length”  $\lambda_I$  is relevant for the design of beam–intercepting devices, as it expresses the average length needed to achieve a certain attenuation of the primary beam, namely a factor of  $e$ , by nuclear inelastic events.

## Secondary Particle Showers

When a proton at SPS or LHC beam energies interacts inelastically with the active medium of an intercepting device, secondary particles are created, starting a complex sequence of events, as in a chain reaction [36]. This secondary particle shower is responsible for a fraction of the initial energy of the particle being deposited in the device where the shower develops, and the activation of the material. The magnitude of these effects depend on the properties of the material and on its geometry and dimensions.

Secondary particle showers have two main components:

**the hadronic shower** The key events which sustain the reaction are hadronic inelastic interactions, where a hadron travelling through the material interacts inelastically with a nucleus, and produces new hadrons at lower energies. The inelastic interaction length  $\lambda_I$  expresses how close to each other the inelastic interactions of the primary particles are on average, thus giving an indication of the extension of the hadron cascade;

**the EM shower** The key events are  $e^-e^+$  pair production by a photon, and photon production by  $e^-$  or  $e^+$  bremsstrahlung. The radiation length  $X_0$  gives the typical scale of the development of EM cascades, as it expresses the length travelled by an electron, positron or photon before being doubled in number and halved in energy, on average. For a pure elemental material,  $X_0$  can be parametrised as [34]

$$X_0 = \frac{716.4 \text{ g cm}^{-2} A}{Z(Z+1) \ln(287/\sqrt{Z})}, \quad (1.7)$$

where  $A$  and  $Z$  are the mass and atomic number of the material. The transverse development of the EM cascade is fairly well described by the

Molière radius  $R_M$  [34]

$$R_M = X_0 \frac{21 \text{ MeV}}{E_c}, \quad (1.8)$$

where  $E_c$  is the critical energy as defined by Rossi, i.e. the energy at which the ionisation loss  $dE/dx$  by an electron is equal to its energy  $E$  divided by the radiation length, i.e.

$$\frac{dE}{dx} = \frac{E}{X_0}.$$

Approximately 99% of the energy carried by the EM cascade is transversely contained in a cylinder with a radius of approximately  $3.5 R_M$ .

Whenever a  $\pi^0$  is created during an hadronic shower, its fast decay into two  $\gamma$  particles starts an EM cascade; thus, EM cascades are always present during the development of an hadronic one. Conversely, an EM cascade could start a hadronic cascade via photonuclear reactions, but this event is much less frequent with respect to the previous one, due to the low values of the concerned cross sections.

Since a hadronic cascade deals with nuclear inelastic events, the nuclei involved remain in a highly excited state, once the cascade is over. Reaction mechanisms like nuclear pre-equilibrium, nucleon evaporation, nucleon coalescence, Fermi break-up and gamma de-excitation are responsible for the final state of the nuclei, with the generation of radioactive species.

While the EM cascade is generally responsible for high levels of energy deposition, the hadronic cascade is responsible for attenuating the primary beam and the radioactivity induced in the device.

Table 1.6 lists atomic number, density, stopping power of protons at the minimum of ionisation, and typical values of inelastic interaction length of protons at 450 GeV/c, radiation length and Molière radius of some materials most commonly

material	Z	$\rho$ [g cm $^{-3}$ ]	$-\frac{dE}{dx}$ [MeV cm $^2$ g $^{-1}$ ]	$-\frac{dE}{dx}$ [MeV cm $^{-1}$ ]	$\lambda_I$ [cm]	$X_0$ [cm]	$R_M$ [cm]
graphite	6	1.83	1.76	3.22	44.6	23.3	5.99
aluminium	13	2.7	1.61	4.35	37.9	8.90	4.38
copper	29	8.96	1.40	12.5	14.6	1.44	1.56
tungsten	74	19.3	1.14	22.0	9.16	0.35	0.92

Table 1.6: Atomic number, density, stopping power of protons at the minimum of ionisation, inelastic interaction length of protons at 450 GeV/c, radiation length and Molière radius of some materials most commonly used in beam–intercepting devices. The inelastic interaction length and the radiation length are taken from FLUKA [37, 38], whereas the minimum ionisation energy have been calculated with the PSTAR code [39]. The Molière radius has been calculated with Eq. 1.8, using the reported radiation lengths.

used in beam–intercepting devices.

#### 1.4.4 Impedance and Wake Fields

A beam of charged particles circulating in an accelerator interacts with the environment, i.e. the vacuum chamber and other equipment around the beam orbit like RF cavities, magnet kickers, beam position monitors, etc... through the EM field lines generated by the beam itself. These must meet boundary conditions imposed by material and shape of the met devices and induce effects back on particles, changing their dynamics and potentially inducing instabilities, thus limiting the intensity reach of the machine.

The coupling between the field lines generated by the beam and their effects on the beam itself through the environment is known as “impedance”. The impedance depends on the material and the geometry of the devices installed along the line seen by the beam. Since beam–intercepting devices, with the exclusion of dumps (as they are meant to stop the beam), are objects among those the closest to the beam; consequently, they are expected to have an impact on the impedance of the whole machine (see for instance Ref. [40] for the LHC

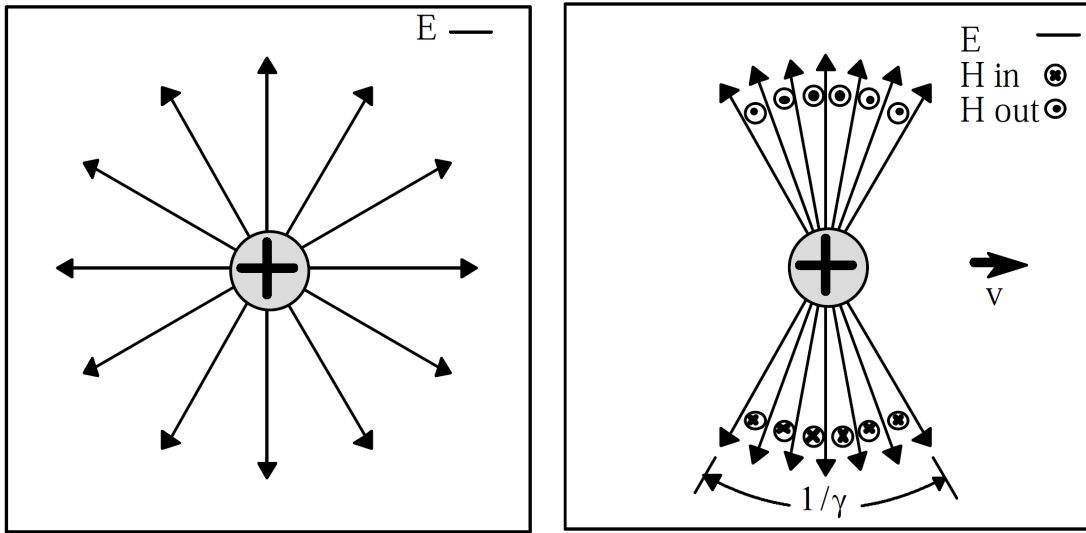


Figure 1.10: Left frame: electric field of a charged particle at rest [43]. Right Frame: EM of an ultrarelativistic charged particle [43].

collimation system - see Sec. 1.4.6), the extent of which depends on their design. A brief introduction to impedance and wake fields (see later) is given in the following, without the aim of giving a complete overview of the subject, for which the reader is addressed to Refs. [5, 41, 42, 43] and to the references quoted therein.

### Field Lines of a Charged Particle

Any charged particle exhibits an EM field. In free space, where no boundary conditions must be met, the field in the reference frame where the particle is at rest is electric and points outwards isotropically (see Fig. 1.10, left frame). In the laboratory frame, where the particle moves, the longitudinal component of the electric field decreases and the azimuthal magnetic field increases as the speed of the particle increases. When the particle becomes ultrarelativistic (i.e. as its speed is extremely close to the one of light or when its kinetic energy is much larger than the rest mass) the electric field gets Lorentz contracted (see Fig. 1.10, right frame).

The same is found in the ideal condition of the charged particle circulating

in an accelerator vacuum chamber which is uniform, axis-symmetric and of a perfectly conducting material. On the contrary, in a real accelerator, any change in the vacuum chamber (either in shape or in material) and the fact that it is made of lossy materials lead the beam to generate wake fields (see below), which have the ability to pull or push particles trailing those originating the fields, modifying their dynamics and inducing perturbations and potential instabilities.

### Wake Fields and Impedance

A particle passing through a metallic structure along the vacuum chamber generates EM field lines which must satisfy the boundary conditions dictated by the structure itself, and a trailing particle at a distance  $\tau$  in time will be subject to their time evolution. An accelerator can be thought as a feedback system where any longitudinal or transverse perturbation appearing in the beam distribution may be amplified (or damped) by the EM forces generated by the perturbation itself [42]. The analysis of this feedback system and the careful design of accelerator components in this respect allow for the mitigation of beam instabilities which may limit the intensity reach of the machine.

The EM fields induced by the beam are referred to as “wake fields”, due to the fact that they are left mainly behind the travelling charge. In the limit case of a charge moving at the speed of light, the fields can only stay behind it because of the causality principle. The interaction between the EM fields generated by the beam and the environment can be described in time domain by means of wake fields, which then act back on charges. Vacuum chamber components can be represented by their frequency-dependent “coupling impedance”, which describes the coupling between the particles exciting wake fields and those subject to them through the components of the vacuum chamber.

Figure 1.11 shows an example of parasitic modes (lowest order) excited by

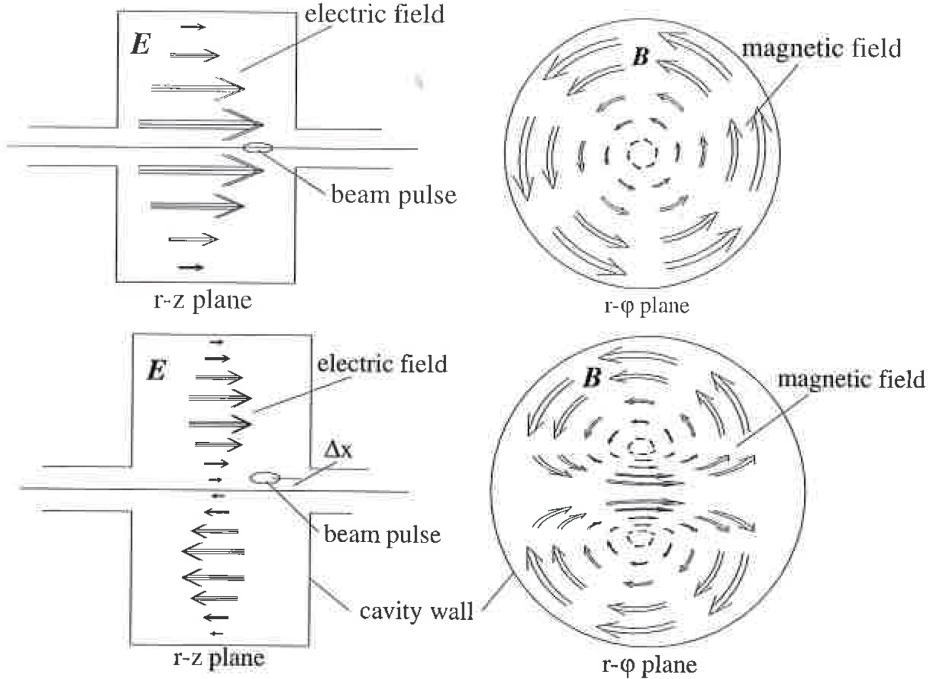


Figure 1.11: Longitudinal (upper frame) and transverse (lower frame) parasitic mode (lowest order) in a pill box cavity [41].

a bunch passing through a structure similar to a pill box cavity. In particular, the upper frame shows the field pattern when the bunch passes on axis; such a field pattern does not cause any transverse deflection of a closely trailing bunch, but only a change in its energy, since the electric field is strictly longitudinal and the transverse magnetic field is zero on the axis. On the contrary, the lower frame shows the field pattern when the exciting bunch passes off axis; such a field pattern causes a transverse deflection of a closely trailing bunch, since the oscillating and asymmetric electric field generates a finite magnetic field on the axis. Any resonating mode of the cavity can be represented by the equivalent  $RLC$  electric circuit shown in the left frame of Fig. 1.12; the qualitative time evolution of the voltage at the capacitor after the heading bunch is passed is shown in the right frame of Fig. 1.12, which affects the dynamics of any trailing bunch at a time distance  $\tau$  from the heading one.

In a more general approach, it is possible to express the effects due to the

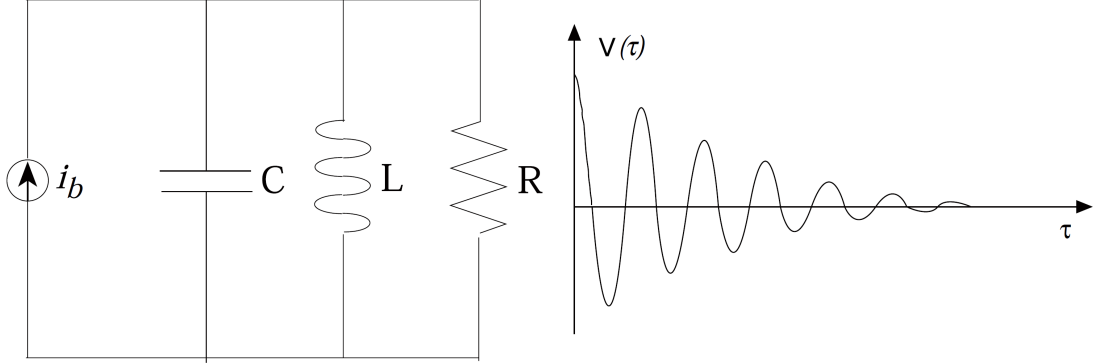


Figure 1.12: Scheme of a parallel RLC circuit equivalent to a pill box cavity (left frame) excited by the passage of a bunch  $i_b(\tau)$  and the qualitative time evolution of the voltage  $V(\tau)$  measured at the capacitor [42].

wake fields generated by a heading charge  $q$  at a longitudinal position  $z$  and transverse offset  $\Delta u = (\Delta x, \Delta y)$  on a trailing one at a distance  $\tau$  in time in terms of the longitudinal (left equation) and transverse (right equation) wake functions, defined as [41, 42]

$$W_{\parallel}(\tau) = \frac{1}{q} \int_L \mathbf{E}_{\parallel}(z, \tau) \cdot dz; \quad W_{\perp}(\tau) = \frac{1}{q\Delta u} \int_L [\mathbf{E} + c\boldsymbol{\beta} \times \mathbf{B}]_{\perp} \cdot dz,$$

where  $\mathbf{E}$  and  $\mathbf{B}$  are the electric and magnetic fields generated by the heading particle, respectively, and the integral is performed over the length of interaction  $L$  (e.g. the length of a component of interest, or the length of the whole accelerator). The two wake functions are measured in V/C and V/C/m, respectively. These functions can be used as Green functions to get the full wake field felt by a trailing particle induced by the whole distribution ahead.

The Fourier transforms of the wake functions are the longitudinal and transverse coupled impedances

$$Z_{\parallel}(\tau) = \int_{-\infty}^{\infty} W_{\parallel}(\tau) e^{-j\omega\tau} d\tau; \quad Z_{\perp}(\tau) = j \int_{-\infty}^{\infty} W_{\perp}(\tau) e^{-j\omega\tau} d\tau,$$

where  $j$  indicates the imaginary unit; its use in the definition of the transverse

impedance indicate that the action of the transverse forces is a mere deflection while the particle energy stays constant. The analysis of the effects induced by the wake fields performed in the frequency domain through the calculation of the coupling impedances is widely used for synchrotrons, given their intrinsic periodicity. Frequency range of interest is the one spanned by the beam, i.e. typically ranging from tens of kHz (determined by the revolution frequency) up to GHz (dictated by the time structure of the bunch).

In general, both impedances are complex numbers

$$Z(\omega) = Z_{\text{Re}}(\omega) + Z_{\text{Im}}(\omega).$$

The resistive (or real) part of the impedance can lead to a betatron tune shift while the reactive (or imaginary) part can damp or drive instabilities. Discontinuities in cross section or material along the vacuum chamber like flanges, kicker magnets with ferrite inserts, beam position monitors, etc... are cause of *broad-band* impedances. Since the involved modes decohere very quickly, these wake fields last for very short times and are in general responsible for single bunch instabilities. Other structures, shaped like resonant cavities, are responsible for *narrow-band* wake fields and impedances. These fields persist for longer times and can act back on subsequent bunches, being thus responsible for multi-bunch instabilities.

## Beam Break–Up

An example of transverse beam instability induced by wake fields is the “beam break–up”, taking place in linear accelerators. It is a single bunch instability, driven by broad–band transverse wake fields generated when high intensity bunches are injected off–axis.

During the development of the instability, the injected bunch becomes bent

first like a banana and later like a snake, with an *apparent* increase in spot size and thus in emittance. The growth takes place until the edge of the aperture is reached, causing the loss of the beam. Even in the case of no loss, this instability is detrimental to the performance of the machine, in particular to the attainable luminosity in case of a linear collider.

The transverse wake fields causing the instability are generated by the head of the bunch; being injected off-axis, it performs free betatron oscillations, driven by the quadrupoles located all along the linear accelerator. The tail of the bunch follows the head and performs betatron oscillations either, but being subject to the wake fields generated by the head, it behaves like a driven oscillator, with the amplitude of the oscillations growing without bound as the bunch travels along the accelerator.

This type of instability cannot be taken under control only with strong focussing or after careful injection and steering. A cure has been proposed by Balakin et al. [44] and it has been successfully implemented into the Stanford Linear Collider. The cure is based on the observation that there is a resonant condition between the betatron oscillations of the head and of the tail. In fact, wake fields are generated in the accelerator following the pattern of the betatron oscillations of the head, which is also followed by the tail. Hence, the resonant condition can be broken if head and tail of the bunch perform betatron oscillations at different frequencies, obtaining a damping effect. This can be attained taking advantage of the chromaticity of the system; in fact, inducing an energy spread correlated to the longitudinal position inside the bunch leads particles in the tail to oscillate with a different frequency than those in the head. This operating mode can be achieved accelerating the bunch behind the crest of the accelerating field, so that the tail gains less energy than the head, with consequent stronger focussing of the tail than of the head.

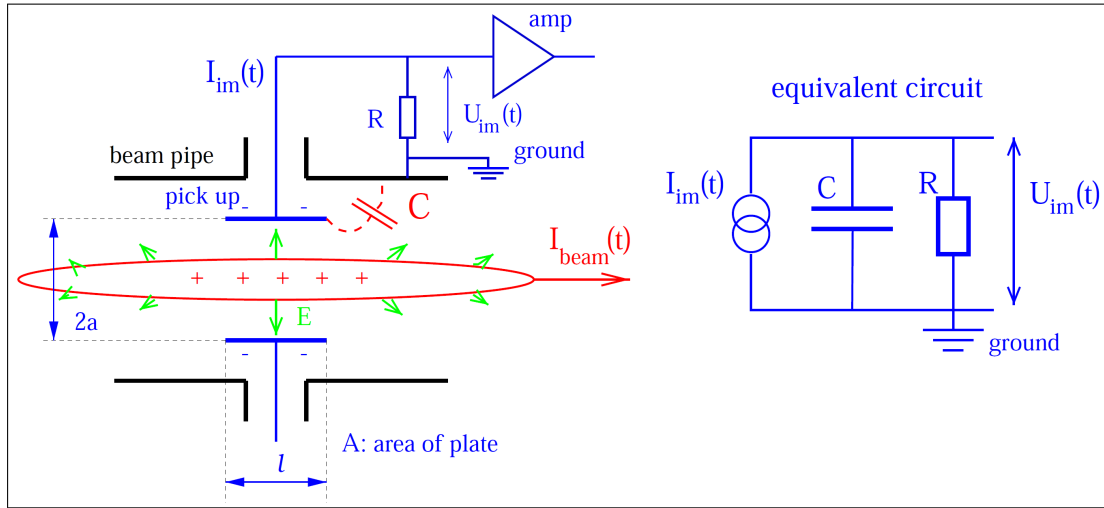


Figure 1.13: Scheme of a pick-up electrode (left frame) and its equivalent circuit (right frame) [45].

### Beam Position Monitors and Stochastic Cooling

Impedance, which can trigger different types of instabilities in case of high intensity beams, can be used to advantage. This is the case of diagnostics devices like Beam Position Monitors (BPMs), for instance. Usually, these devices are pick-ups, made of insulated metal plates where charges induced by the electric field generated by the beam are read. As an example, Fig. 1.13 [45] shows the scheme of a pick-up electrode and its equivalent circuit. The electric field lines  $E$  of the passing beam with intensity  $I_{beam}(t)$  generate an image current  $I_{im}(t)$  in the pick-up plates; the voltage  $U_{im}(t)$  across a resistor connected to the plates is then read and used as input signal. A typical use of BPMs is to provide feedback orbit systems with input approximately the actual beam trajectory. In fact, the beam closed orbit in a real circular accelerator is distorted by errors in magnetic fields or in the alignment of magnets [41]. The readouts from many BPMs distributed all along the circumference can be used to power an equal number of dipole kickers distributed along the ring circumference, to correct the orbit.

Stochastic cooling is another example where impedance can be used to advantage. It is a feedback system aimed at reducing the emittance of the beam in a circular machine, where the signal from a pick-up is fed to a kicker magnet. The pick-up detects small statistical displacements of the beam, due to the fact that the beam is made of a finite number of particles, implying that the phase space is not fully filled with particles, but it exhibits many “holes”. For the same reason, the whole emittance is slightly shifted with respect to the centre of the phase space; this shift is detected and corrected. Thus, the process of stochastic cooling only squeezes the holes out of the volume occupied by the beam particles in phase space, without circumventing Liouville’s theorem.

#### 1.4.5 Design of Beam–Intercepting Devices

Since beam–intercepting devices are located very close to the circulating beam (up to being directly on its orbit) and cope with its direct impact, different needs must be fulfilled at the same time, making their design quite a challenge. A compromise must be found among different needs:

**effectiveness** In order to protect downstream sensitive equipment, the device must effectively absorb the hitting particles. The attenuation requirements are usually set by limits on the heat load the protected elements can stand, and they are achieved choosing a suitable absorbing medium and its length. Space availability might set further constraints to be respected;

**thermomechanical integrity** The medium must stand the stresses induced by the beam impact. Optimum material properties involve high thermal range, to avoid as much as possible loss of absorbance due to liquefaction, evaporation or sublimation; and high mechanical stability, keeping the bulk integrity and avoiding cracking, bubbling or breakage. A *cooling* system may be required, in case the device is expected to perform in steady–state

conditions or with regular loads over a certain period. Moreover, mechanical boundary conditions like good thermal contacts at material interfaces can relax steady-state conditions;

**activation** The device should be designed to minimise the activation after beam impact, in order to limit dose to personnel at intervention and ease the handling of the device. This requirement involves not only the material directly impacted by the beam, but also the rest of the structure;

**impedance** The impedance of the device must be as low as reasonably achievable, especially in case of circular machines, where impedance issues may pile up and trigger beam instabilities;

**machining** The absorbing medium should be available from industry in bulk pieces, for ease of assembling and mechanical stability. This also includes the possibility of a proper surface treatment, to minimise its roughness;

**operational aspects** like precision in positioning and orienting the device should be taken into account;

**costs** The solution should be at an affordable cost.

The hardest challenge in the design of these devices is to ensure enough radiation absorbance in the available space, granting their thermomechanical resistance to the impact and to the generated heat loads. While the former calls for materials with high density and atomic number, featured by high absorption capabilities and thus high levels of heat load, the latter calls for light materials, which show the opposite trend. As far as radiation absorbance is concerned, the most relevant physical properties of the absorbing medium are the inelastic interaction length  $\lambda_I$ , related to the capability of the active medium to attenuate the primary beam, and the radiation length  $X_0$ , expressing the impact of EM showers.

Thermomechanical aspects are dependent on localised values of energy deposition and gradients. In fact, the more concentrated the energy deposition, the higher the heat load and the mechanical stresses. As a consequence, the beam spot size and the bunch population play a dominant role on the pattern of energy deposition. Beam impact conditions are also important. Indeed, qualitatively, while a central impact on the absorbing medium is featured by a low fraction of energy transversely escaping, high compressive stresses and low traction stresses, a superficial impact can be even more dangerous from the stress point of view, even if more energy can transversely escape. Moreover, a change of the beam impact position with time can play a role in lowering or increasing heat deposition values, almost regardless of the original beam dimensions. This can be the case of sweeping systems or movable devices. Quantitatively, simulations are the necessary tool to be used for estimating levels of heat loads in the most severe conditions, and thus drive the design of the device. From this point of view, material properties, device model and assumptions must be carefully verified, for the simulation to give sound results.

When designing beam-intercepting devices, beam-impact conditions are usually already set by machine optics, beam parameters, operational mode and failure scenarios (in case), with little margin of change. As a consequence, a sensible material choice is the key to the proper design of the device. Experience has shown so far that *graphite* is an excellent material whenever energy deposition and mechanical stresses become an issue. In fact, its low density and atomic number keep energy deposition values relatively low; it is featured by good mechanical properties, especially in compression and under vacuum; it has good thermal properties, with heat diffusion playing quite a role in cooldown; finally, its electrical properties have limited impact on the impedance budget.

As bunch intensity increases and beam spot size decreases, mechanical stresses reach very high levels, requiring a careful design of the device and related systems. In extreme cases, the quest for a new, more resistant material can start, or modifications to the beam line should be considered.

#### 1.4.6 An Example: the LHC Collimation System

The energy of the LHC beam in nominal operation would be sufficient to melt 500 kg of copper. Such a high energy must be carefully controlled in a SC environment. In fact, approximately  $10^{-9}$  of the total beam energy can lead a SC magnet to quench. *Beam cleaning* becomes therefore a primary goal of the LHC collimation system [46, 8], which must efficiently intercept the unavoidable particle losses due to the continuous re-population of the beam halo. *Passive machine protection* is another priority, protecting sensitive equipment from losses following a device failure or wrong operation of the machine. A third priority is the *minimisation of collimation-related background to the experiments*, to ensure clean data acquisition. Consequently, a sophisticated collimation system has been designed.

In order to keep the heat load in beam-intercepting devices down to safe levels, a multi-staged approach has been adopted, based on different collimator families. The primary collimators intercept the so-called “primary halo”, i.e. halo particles of the beam, attenuating them via inelastic interactions and scattering the survivors on larger amplitude orbits via Coulomb, elastic and single diffractive scattering. This “secondary halo” is then intercepted by the second family of collimators, distributed downstream of the primary one. Absorbers and tertiary collimators are then used to intercept the “tertiary halo” eventually surviving the secondary collimators.

Figure 1.14 shows a schematics of the multi-stage betatron collimation system

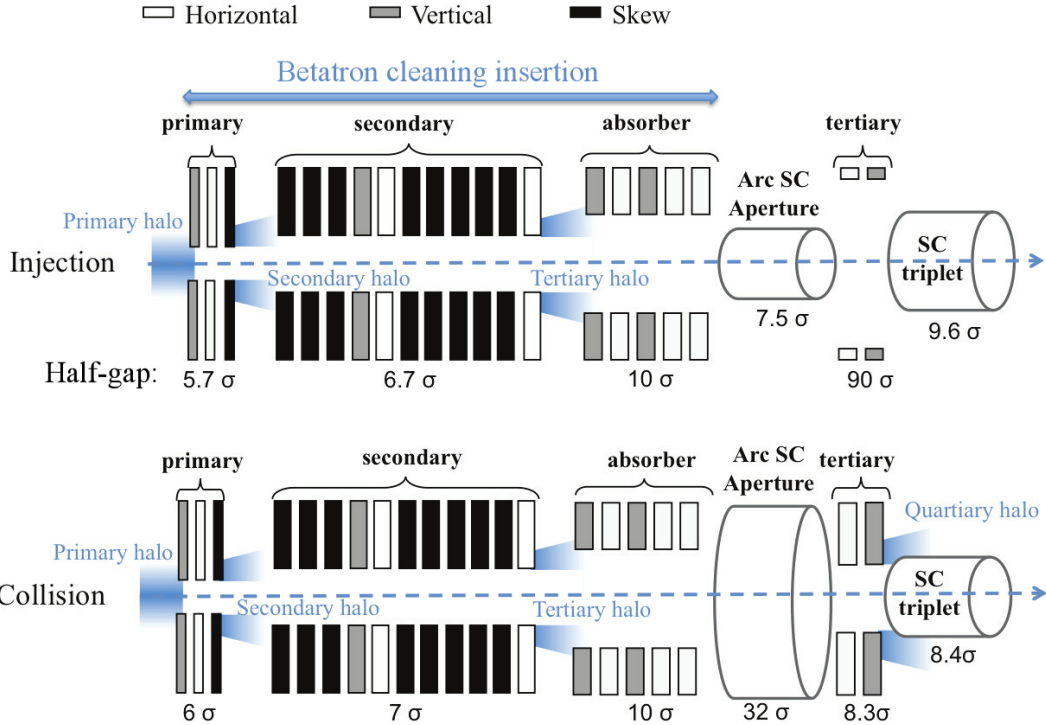


Figure 1.14: Principle of the LHC multi-stage betatron collimation system [47]. Jaw openings are expressed in units of  $\sigma$ , i.e. the betatron contribution to the rms beam size (see Eq. A.11).

of the LHC. Different jaw openings are used according to the collimator location, optics and beam energy. At injection, the LHC aperture is limited by the SC magnets of the arcs, whereas at top energy, during collisions, the ITs are the aperture bottleneck. As a consequence, the collimation system should be able to accommodate changes in the beam shape and machine optics.

Collimators devoted to regular beam cleaning are mainly located in two dedicated insertions of the LHC ring (see Fig. 1.2), i.e. IR3, for momentum cleaning, and IR7, for betatron cleaning. This choice has been taken due to conflicting requirements on the optics for these two stages. An additional set of collimators is installed in the LSSs hosting the detectors, to provide the ITs with local halo cleaning and the DSs with cleaning from collision debris. Additional collimators protect most sensitive equipment in the injection and extraction regions upstream

of IR2/IR8 and in IR6, respectively.

The LHC collimators consist of two movable jaws, centred and aligned with respect to the beam envelope; their transverse position is varied with beam acceleration, in order to follow the change in the beam size. The jaws are lodged in a vacuum tank, and the whole apparatus is mounted on dedicated supports. A fast plug-in system has been designed in order to minimise the time for intervention, as the devices and the environment can become heavily radioactive.

The jaws are made of different materials, depending on the collimator type, and water cooled. In particular, the jaws of primary and secondary collimators are made of graphite for robustness concerns, whereas those of tertiary collimators and absorbers are usually made of metals, for maximising particle absorbance.

## 1.5 Thesis Purpose and Structure

In the context of the LIU project, the protection devices installed along the entire LHC injection chain are under revision, in order to check their effectiveness and mechanical stability with the new, brighter beams required by the HL-LHC and LIU projects (see Tab. 1.5). Among these devices, those used for protection at injection in the LHC are particularly important, since injection takes place in insertion regions of the ring far from the collimation system, and, being this based on a multi-turn cleaning concept, it cannot offer any protection against beams mis-steered by magnet faults in the transfer lines or with over-populated tails during the first turns of the beam in the accelerator after injection.

Among the revised devices, this thesis is focussed on the SPS scraping system, i.e. the collimation system used for halo cleaning before injection in the LHC. This is a “fast” cleaning system, i.e. for most of the SPS cycle it does not interact with the beam but immediately before extraction, when it removes halo particles for approximately few hundreds of ms. Since the device is inserted in the path of the

beam only at a given moment in the accelerator cycle, the relative approach of the beam to the device and the consequent variation of the beam impact conditions with time characterise its cleaning action, resulting in the concentration of the energy deposition in the very first layers of material in contact with the beam. This is the main reason for the high values of energy deposition which expose the device to damage levels in case of accidental interception of the beam core.

In this thesis, I characterise the system presently in use in terms of energy deposition in the absorbing medium, time required for cleaning and losses in the machine. Moreover, in view of the LIU era, a new design has been proposed [48], and it is here characterised. The aim of the thesis is to compare the two systems, to show how the upgraded can take over the existing one. The key point of the upgraded design is the use of a long absorber to clean the beam, with immediate benefit on the energy deposition in the intercepting material, since energy is deposited over a larger volume. Other assets that the new design is expected to have are improved control on the time required for cleaning, reduction of losses induced in the ring and operational flexibility, at the expenses of a more complex design. In addition, since no mechanical component is present, the system is not subject to wear.

The analyses, meant to assess the performance of the two systems and spot critical points, have been performed by means of extensive numerical simulations. These are based on a Monte Carlo code for the description of the interaction of the beam with the intercepting device and the energy deposition it is subject to. Being installed in a ring, multi-turn effects must be taken into account to properly characterise the performance of the scrapers. For this reason, a tracking code for single particle beam dynamics has been coupled to the Monte Carlo code, using both in the same simulations, to take into account the beam dynamics in the accelerator during scraping.

The thesis is structured in four chapters, two introductory ones and two collecting original results. Conclusions are then drawn in Chap. 6.

Chapter 2 introduces the scraping system in both designs, i.e. the existing one, presently installed in the SPS, and the upgraded one, proposed for the LIU era. The chapter gives all the pieces of information necessary to properly put into context the analyses presented in this thesis, including main technical aspects of the SPS scraping system presently installed and foreseen for upgrade, characteristics of the optics at the location of the systems, and most relevant assets/liabilities of the two. Prior to the description of the analysed systems, an overview of the SPS is given, mainly focussed on its lattice structure, optics and magnetic/current cycle. It should be noted that the proposal of upgrade (with the optimisation carried out to converge to the considered design) is not part of this thesis, but has been presented in an original work by Mete et al. [48].

Chapter 3 describes the simulation tools used to carry out the analyses presented in this thesis. In fact, tools simulating the impact of the beam on the intercepting devices like the scrapers and the induced effects play an important role at design level, as far as performance and robustness are concerned, to assure that the desired goals are achieved and the devices can be safely operated. In particular, a brief description of the FLUKA and SIXTRACK [49, 50, 51] codes, used as Monte Carlo for describing the interaction between the beam and the scraper and as tracking code for single particle beam dynamics in the accelerator for taking into account multi-turn effects, respectively, is given. Moreover, their coupling is described either, since this is the actual tool used to carry out the analyses, with a quick overview of the main technical aspects, to which I contributed to a large extent. I also modified the two codes, in order to simulate the change in the beam-device relative distance while scraping, and the modifications are summarised. The chapter is closed by the presentation of additional tools,

i.e. the LineBuilder and the FLUKA Element DataBase [52, 53], used to build the FLUKA geometry used for the benchmark of the FLUKA–SIXTRACK coupling against BLM signals, presented in Chap. 4, and the routine used to sample the beam to be tracked. I largely contributed to the development of all these tools.

Chapter 4 presents the analysis I have performed on the scraping system presently installed in the SPS. The system is characterised in terms of energy deposition in the absorbing medium, time required for cleaning and losses induced in the machine. Previous investigations performed by us in 2010 [54] are briefly reported and used as starting point for original sensitivity studies, aimed at addressing the performance of the device in operational conditions. A large portion of the chapter is then dedicated to the benchmark of simulation results against measurements. In fact, the outcomes of an endurance test of the present system are summarised, showing that the levels of energy deposition predicted by the simulation are compatible to those the system is subject to. The test has been carried out with beam in the SPS, stressing the system with the worst operational conditions foreseen by the simulation. Besides the energy deposition, the benchmark also deals with the time profile of the beam intensity while scraping and the BLM signals in the region of the scraper, recorded during the test and its setup. The comparison of simulation results against the former set of measurements allows one to reconstruct the actual settings of the scraping system during the test, whereas the comparison against the latter set of measurements offers a further opportunity to benchmark the FLUKA–SIXTRACK coupling.

Chapter 5 presents the analysis I have performed on the the scraping system in its upgraded design as proposed for the LIU era. As done for the system presently in use, the characterisation has been carried out in terms of energy deposition in the absorbing medium, time required for cleaning and losses induced in the machine. The chapter is closed by an extensive comparison of the two systems,

based on the most relevant outcomes of the analyses presented in this thesis. It is shown that, with respect to the one presently in use, the upgraded system is characterised by lower values of energy deposition, a higher control on the time required for scraping and lower proton losses induced all along the SPS ring, but locally downstream of the device. In addition to all these advantages, the design of the upgraded system is intrinsically more flexible than the one of the system presently installed. On the other hand, the system presently installed is extremely simple, whereas the upgraded design is more complex, making use of several devices, i.e. magnets and absorbers. In addition, due to its simplicity, short times of intervention and conditioning are expected for the system presently installed, which is not the case for the upgraded system.

This thesis represents the first extensive analysis of performance of the SPS scraping system, both in its configuration presently installed and in its proposed design for possible upgrade. This thesis also represents the first analysis and comparison of collimation systems with varying beam-impact conditions during cleaning, and the results and outcomes here presented can be used as reference for studying similar devices in other machines. Moreover, this thesis represents the first extensive use and benchmarking of the FLUKA-SIXTRACK coupling. This simulation tool has been set up in the most general way, to be used for any accelerator ring and device under study. Moreover, the FLUKA-SIXTRACK coupling is the first simulation tool for halo cleaning studies in circular machines which allows one to properly deal with changing impact conditions on the beam-intercepting device.

# Chapter 2

## The SPS Scraping System and Its Upgrade

The last stage of acceleration before injection in the LHC is the SPS (see Sec. 1.2). It accelerates protons received from the PS at 26 GeV/c up to the LHC injection momentum of 450 GeV/c. Protons are then transferred to the LHC via two dedicated Transfer Lines (TLs) [19]. These are the TI2 and TI8 beam lines (from the French expression “Tunnel d’Injection”). Figure 2.1 shows the schematic layout of the SPS complex, with the PS and the injection channel to the SPS, the extraction to the CERN experimental north area, and the two SPS-to-LHC TLs and the injection points in the LHC. TI2 is dedicated to the injection of the clockwise LHC B1, whereas TI8 is dedicated to the counterclockwise LHC B2.

A very clean and precise injection is required when dealing with nominal LHC beams, and this requirement is even more important when injecting upgraded beams, especially because the intensity gets higher. In fact, the aperture of any accelerator is smallest at injection energy, since the geometrical emittance of the beam (see Sec. A.4), related to its spot size (see Sec. A.2), is maximum at the lowest momentum, and it decreases with momentum. In particular, the aperture of the LHC SC magnets in the arc at 450 GeV/c is  $\approx 7.5 \sigma$  [55] (where

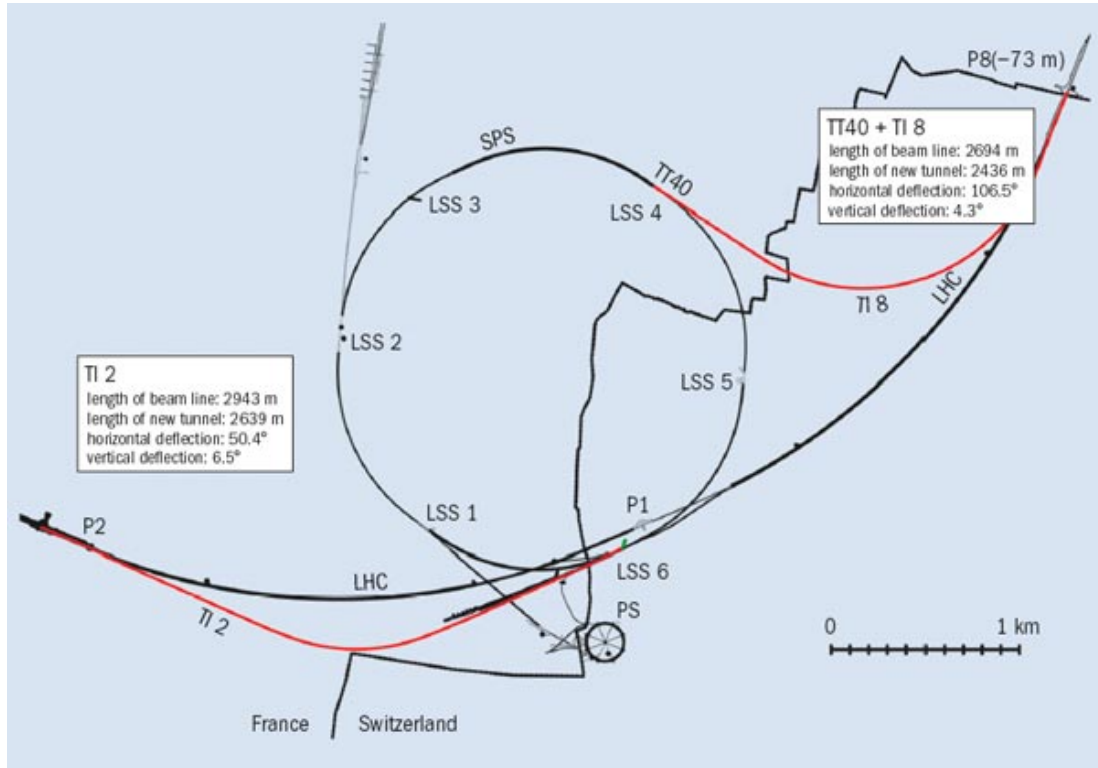


Figure 2.1: Schematic layout of the SPS complex, with the PS and the injection channel to SPS; the extraction to the experimental north area; and the two SPS-to-LHC TLs and the injection points in the LHC.

$\sigma$  indicates the betatron contribution to the rms beam size, see Eq. A.11), for the nominal LHC normalised emittance of  $3.5 \mu\text{m}$  (see Tab. 1.5). Moreover, the full bunch train of a nominal LHC beam in the SPS foresees 288 bunches of  $1.15 \cdot 10^{11}$  protons per bunch (see Tab. 1.5), for a total of  $3.3 \cdot 10^{13}$  protons. This intensity is approximately four orders of magnitude larger than the limit assumed for localised, instantaneous losses before a quench takes place [8], i.e.  $5 \cdot 10^9$  protons (this coincides with the “pilot beam” intensity). Consequently, small fractions of the beam population can induce a quench, even those typically contained in beam tails.

The LHC collimation system (see Sec. 1.4.6) is a multi-turn cleaning system. Consequently, it cannot assure full protection during the first turn of the injected beam. Moreover, it is located in two LSSs of the LHC different from those hosting

the injection points, implying that all the arcs in-between are not protected by the collimation system itself. Therefore, a complex chain of passive systems is presently installed, with the aim of protecting the LHC cold aperture during the process of beam transfer from the SPS to the LHC. These are:

**the SPS scrapers [56, 57]** These devices provide the injection process with regular halo cleaning. Installed in the SPS, they are a multi-turn collimation system for scraping off beam tails, with full phase coverage. Being far from the LHC SC magnets, cleaning can be safely and routinely performed, as proton losses and secondary particle showers induced by the removal of tails cannot induce any quench. Scraping is performed just before extraction, to minimise the risk of tail re-population;

**the collimation system in the SPS-to-LHC TLs [19]** It is aimed at protecting the LHC cold aperture in case of beams mis-steered by the SPS extraction system or by magnets along the TLs. Due to the lack of space, the absorbing devices cannot be long enough to fully dump the impacting beam. Consequently, their aim is to dilute the impacting beam, avoiding damage of the LHC SC coils in case they are hit by the surviving beam;

**the protection devices in the LHC injection regions [8]** They protect the LHC cold aperture against any error in firing the LHC injection kickers.

As it can be seen, these systems are complementary in protecting the LHC cold aperture from any possible loss mechanism during injection (when the LHC collimation system is not effective), and only the synergy among all the three can assure a clean and safe injection. Indeed, during regular injection, the SPS-to-LHC collimation system in the TLs and the protection devices in the LHC injection regions are in the shadow of the SPS scrapers, which perform regular cleaning far from the LHC SC magnets, with no risk of inducing quenches. At the

same time, the SPS-to-LHC collimation system in the TLs and the protection devices in the LHC injection regions come into play in the unlikely event of a magnet fault during beam transfer, against which the SPS scrapers cannot offer any protection.

Among the aforementioned protection devices, this chapter focusses the attention on the SPS scrapers, summarising their design and the main technical aspects, to give an overview of the system and an insight into the main challenges involved. The chapter also represents a reference for the analyses and outcomes of this PhD activity, presented in Chaps. 4 and 5.

The chapter is divided in two main parts, with conclusions drawn in Sec. 2.3. Section 2.1 outlines the layout, the main features and the optics of the SPS. These are relevant to properly put into context the description of the SPS scrapers. In addition, details relevant for the simulation results shown in Chaps. 4 and 5. are given. These involve: the RF settings and the main parameters relevant to the longitudinal beam dynamics; the effects of a permanent magnetic bump, implemented in the LSS1 to ease beam dumping, as oscillations in the closed orbit are relevant for estimating the BLM signal in the LSS1 during scraping; the SPS cycle in case of LHC beams, focussing on the time profile of the beam current and the main sources of losses.

Section 2.2 presents the SPS scraping system. After a brief introduction about the rationale behind regular halo cleaning at injection in the LHC, the section first gives an overview of the system presently installed and currently operationally deployed, which is then characterised in Chap. 4. Afterwards, the section presents the proposed design of upgrade for the LIU era, which is then characterised in Chap. 5. For both systems, technical aspects, assets and liabilities are outlined, and at the end of the section it is shown how the design of the upgraded system represents an improvement with respect to the one of the existing system. It

should be noted that the proposal of upgrade (with the optimisation carried out to converge to the considered design) is not part of this thesis, but has been presented in an original work by Mete et al. [48].

## 2.1 The SPS

The SPS was designed and built in the 1970s [58], and it has undergone several changes, especially in its operational settings. Originally specified as a 300 GeV proton accelerator but actually built for 400 GeV operation, it has been used for several purposes: for fixed-target experiments, as a collider, and as injector to other accelerators. Examples of fixed-target experiments fed by SPS beams are the beam lines in the experimental north area of CERN, and the CERN Neutrinos to Gran Sasso (CNGS) project<sup>1</sup> [59]. In the 1980s, the SPS was used as proton–antiproton collider [2] at the design centre-of-mass energy of 540 GeV. This operational mode allowed the observation of the  $W^\pm$  and  $Z^0$  bosons, leading to the Nobel Prize won by Carlo Rubbia and Simon Van der Meer in 1984. The SPS was also operated as injector to the Large Electron–Positron Collider (LEP), accelerating electrons and positrons up to 20 GeV. Presently, it continues to provide fixed-target experiments in the CERN north area with protons, and it is used as injector to the LHC.

In the following, the SPS is presented. Section 2.1.1 describes the layout and the optics of the machine, in particular the two optics used for accelerating LHC beams: the “Q26” optics, routinely used until 2012, and the “Q20” optics, operationally used nowadays. The main characteristics and differences are pointed out. Section 2.1.2 outlines the RF settings and the main parameters relevant to the longitudinal beam dynamics, taken into account in the analyses presented in

---

<sup>1</sup>The aim of this experiment was the investigation of the neutrino oscillations. It was operational between 2006 and 2012.

Chaps. 4 and 5. The effects of a permanent magnetic bump, implemented in the LSS1 to ease beam dumping, are summarised in Sec. 2.1.3, as oscillations in the closed orbit are relevant for estimating the BLM signal in the LSS1 at scraping. Finally, a short description of the SPS cycle in case of LHC beams is given in Sec. 2.1.4, underlying the main features of the time profile of the beam current and the main sources of losses.

### 2.1.1 The Layout and the Optics

The SPS is a 7 km-long synchrotron, with a 6-fold super-symmetry, i.e. it is structured in six identical arcs and six LSSs. Each LSS is dedicated to one or more specific tasks (see Fig. 2.1):

- LSS1 is devoted to *injection* of the beam from the PS. It also hosts the *dump* system (see Sec. 2.1.3);
- three LSSs are devoted to extraction: LSS2, for the slow extraction towards the north experimental area in Prevessin; LSS4, for the fast extraction of the LHC B2 towards IP8, through TI8, and for the extraction of the beam for the CNGS target area; and LSS6, for the fast extraction of the LHC B1 towards IP2, through TI2, and for the extraction of the beam for the HiRadMat test facility [60, 61];
- LSS3 accommodates the accelerating cavities;
- LSS5 hosts the SPS–UA9 experiment [62], aimed at proving the deployment of crystal channelling as effective method for collimation<sup>2</sup>.

The SPS is made up of 108 regular FODO cells, 16 per arc and 2 per LSS. The design phase advance of the standard cell is approximately 90°, resulting in

---

<sup>2</sup>The investigations are carried out in view of the upgrade of the LHC Luminosity, as possible upgrade of the first stage of the LHC collimation system.

betatron tunes (see Sec. A.1) in the range between 26 and 27. Thanks to this phase advance per cell, suppression of dispersion in the LSSs can be achieved with the missing dipole technique [63]. Betatron tunes have been changed during the years of operation of the accelerator, and they are not the same for all the accelerated beams, depending on the final use. 26.13 and 26.18 are the most updated values of the horizontal and vertical tunes  $Q_x$  and  $Q_y$  for LHC beams in case of the Q26 optics. The upper frame of Fig. 2.2 shows the horizontal and vertical betatron functions  $\beta_x$  and  $\beta_y$ , together with the horizontal dispersion  $D_x$  ( $D_y$  is zero, as the orbit lays on the horizontal plane), for the first sixth of circumference. The minimum in the dispersion function coincides with the centre of the LSS1, i.e. the centre of the QFA.11810 focussing quadrupole magnet. Characteristics of this optics are the minima of the  $\beta$ -functions at  $\sim 20$  m, the maxima at  $\sim 110$  m, and the four big dispersion waves in the arc.

In presence of closely-spaced bunches, highly populated and with small normalised emittances, the SPS performances are limited by many effects: beam loading in the RF system; electron cloud effects; and various single and multi-bunch instabilities. Reference [64] and those quoted therein give a comprehensive overview of all these issues. Without mitigation actions, these effects make it extremely difficult or even impossible to deal with the beam parameters required by the HL-LHC and LIU projects.

While the RF beam loading and the electron clouds can be limited with proper changes in the accelerator hardware, thresholds for single and multi-bunch instabilities depend on the working point of the accelerator. In particular, these thresholds scale with the slip factor  $\eta$ , defined as [41, 65]

$$\eta = \frac{1}{\gamma_t^2} - \frac{1}{\gamma^2}, \quad (2.1)$$

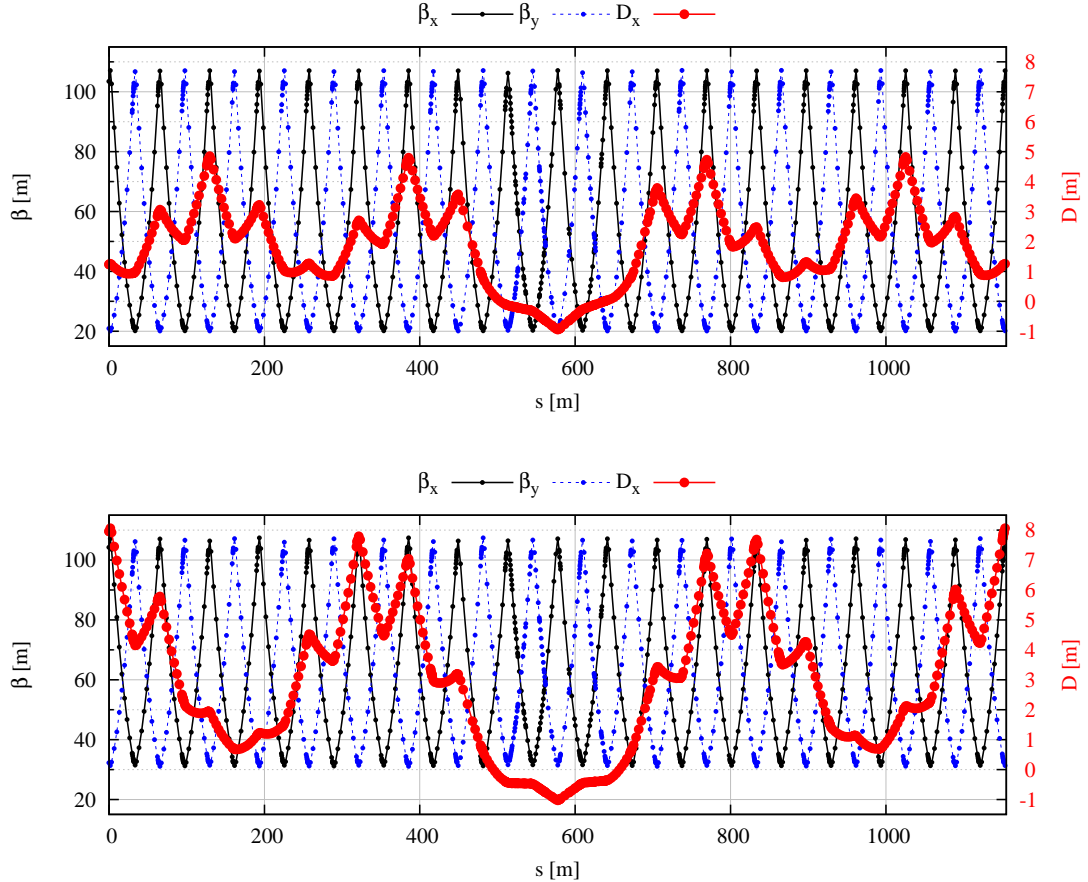


Figure 2.2: Betatron functions and horizontal dispersion of the Q26 optics (upper frame) and of the Q20 optics (lower frame). The shown range of the  $s$  coordinate includes the LSS1, at the centre, and two half arcs on each side.

where  $\gamma$  is the relativistic reduced energy of the beam, and  $\gamma_t$  the *transition energy*. The transition energy is a quantity specific to the machine lattice and the optics used, and it represents the beam energy above which an excess in the energy of a beam particle with respect to the synchronous one translates into a longer revolution time. In general, speed and orbit length are the two factors affecting the revolution time of a particle in a circular accelerator. Moreover, for a particle approaching the speed of light (and thus in relativistic regime), acceleration translates more in a gain in mass rather than in speed; hence, a gain in energy translates more in a longer trajectory rather than in a higher speed or in

a shorter revolution time, and the arrival time at the RF cavity is not dominated by the speed but by the path followed along the ring. Thus, above transition, a beam particle with an energy larger than the one of the synchronous particle follows a path in the accelerator longer than the one followed by the synchronous particle.

The transition energy depends on the dispersion function in bending magnets as

$$\frac{1}{\gamma_t^2} = \frac{1}{C} \oint \frac{D_x(s)}{\rho(s)} ds, \quad (2.2)$$

where  $C$  is the accelerator circumference,  $D_x(s)$  the horizontal dispersion function,  $\rho(s)$  the local radius of curvature, and  $s$  the longitudinal coordinate in the curvilinear reference system (see App. A). For the Q26 optics,  $\gamma_t$  is 22.8. The beam is injected at 26 GeV/c, which is equivalent to  $\gamma = 27.7$ , and hence the SPS is operated always above transition. Since the energy range of the SPS beams cannot be changed, the only way to increase  $\eta$  is to decrease  $\gamma_t$ .

A new optics for SPS has been proposed in 2011 [66], with the aim of reducing  $\gamma_t$  for increasing  $\eta$  and hence the intensity thresholds of bunch instabilities.  $\gamma_t$  is decreased by letting larger dispersion waves in the arcs, reducing the powering of the main quadrupoles. The new optics is thus called the “low- $\gamma_t$ ” or “Q20” optics, and its linear optics functions are shown in the lower frame of Fig. 2.2. It is characterised by larger minima of the optics  $\beta$ -functions while keeping almost the same maxima, resulting in the lower tunes 20.13 and 20.18, for the horizontal and vertical planes, respectively (from which the name of the optics comes from). The larger dispersion waves in the arcs are the main characteristics of this optics, resulting in  $\gamma_t$  equal to 17.8. Three big peaks in the dispersion function are seen instead of the four of the Q26 optics, since the phase advance per arc has been reduced from  $4\pi$  to  $3\pi$  to avoid jeopardising the effect of the DS. This new optics has been extensively tested in machine development sessions [67, 68], and now it

is the operational one for LHC beams since 2012.

### 2.1.2 Parameters of Longitudinal Beam Dynamics

The SPS RF cavities are operated at 200 MHz [19]; taking into account the SPS length of 6911.5038 m<sup>3</sup>, this corresponds to a sequence of 4620 buckets [70] (known as the “harmonic number”  $h$ ), each  $\sim 5$  ns long. In the case of the Q20 optics, the RF cavities are operated at a total voltage of 5.045 MV during the energy ramp [68], and the phase of the synchronous particle is 20.82° [70]. At flat top, i.e. at 450 GeV/c, the voltage is raised at 7 MV [68] and the phase of the synchronous particle is set to 0°.

The momentum acceptance of a stationary bucket is given by the following equation [41, 65]

$$\delta_{\max}^2 = \frac{2 e V_0}{\pi h |\eta_c| c p_0}, \quad (2.3)$$

where the term on the left represents the maximum relative momentum offset (see Eq. A.1) that results in a stable motion in the longitudinal phase space (see Sec. A.1);  $V_0$  is the total RF voltage;  $\eta_c$  is the momentum compaction factor, equal to the inverse of the transition energy squared, i.e.  $\eta_c = 1/\gamma_t^2$ .  $c$  and  $e$  are the speed of light and the electron charge, respectively. Plugging the RF settings at flat top and the momentum compaction factor of the Q20 optics in the equation results in a momentum acceptance of  $\delta_{\max} = 8.32 \cdot 10^{-4}$ , corresponding to a bucket height of  $\Delta E_{\max} = 0.37$  GeV.

The synchrotron frequency, defined for small oscillations in the longitudinal phase space, is given by the following equation [41, 65]

$$\Omega^2 = \frac{h e V_0 c \beta_s}{2 \pi C^2 p_0} |\eta_c \cos \psi_s|, \quad (2.4)$$

---

<sup>3</sup>Taken from the MADX [69] database on **afs**.

parameter	value
RF frequency $f_{\text{RF}}$ [MHz]	200
ring circumference $C_{\text{SPS}}$ [m]	6911.5038
harmonic number $h$ []	4620
revolution period $\tau$ [ $\mu\text{s}$ ]	23.05
total RF voltage $V_0$ [MV]	7 (5.045)
acceleration phase $\psi_s$ [°]	0 (20.82)
transition energy $\gamma_t$ []	17.8
momentum compaction factor $\eta_c$ []	$3.16 \cdot 10^{-3}$
momentum acceptance $\delta_{\text{max}}$ []	$8.32 \cdot 10^{-4}$
energy acceptance (bucket height) $\Delta E_{\text{max}}$ [GeV]	0.37
synchrotron frequency $\Omega$ [Hz]	1620
synchrotron tune $Q_s$ []	$5.95 \cdot 10^{-3}$
synchrotron period $\tau_s$ []	168 turns

Table 2.1: Main parameters for the longitudinal beam dynamics in the SPS for the Q20 optics. Values in parentheses refer to energy ramping.

where, in addition to the variables already used in Eq. 2.3,  $\beta_s$  is the relativistic reduced speed of the synchronous particle,  $\psi_s$  the accelerating phase and  $C$  the circumference of the ring. Plugging the RF settings at flat top, the momentum compaction factor of the Q20 optics, the SPS length and the  $\beta_s$  of protons at 450 GeV/c (i.e. 0.99999782) in the equation results in a synchrotron frequency of 1620 Hz. Taking into account the revolution period of 23.05  $\mu\text{s}$ , the synchrotron frequency corresponds to a synchrotron tune of  $5.95 \cdot 10^{-3}$ , and to 168 revolutions in the accelerator for a synchrotron oscillation.

Table 2.1 summarises all the parameters relevant for longitudinal beam dynamics in the SPS for the Q20 optics.

### 2.1.3 The Permanent Magnetic Bump in LSS1

The SPS beam dump system is located in the LSS1, and it is an internal one, i.e. the beam is not extracted from the machine and steered towards an external dump, but it is kicked and directed onto an absorber block, installed in the ring

quadrupole	displacement [mm]	
	horizontal	vertical
QDA.11710	-4.8	-5
QFA.11810	-2.97	-16.49
QDA.11910	-4.8	-5

Table 2.2: Quadrupole displacements in the SPS LSS1 for generating the permanent orbit bump in LSS1 used for dumping.

but clear of the orbit of the circulating beam. In order to ease beam dumping of high energy protons [71] at 450 GeV/c, a permanent orbit bump has been set up, obtained transversely displacing three quadrupole magnets. Table 2.2 lists the involved quadrupoles, with their horizontal and vertical displacements.

The displacements of the quadrupoles and the induced orbit bump were optimised for the optics and tunes used at the time of their proposal. Since then, the SPS optics have evolved without updating the alignment of these quadrupoles. As a consequence, the magnetic bump is not closed for both the Q26 and the Q20 optics, inducing oscillations in the closed orbit all along the ring. These oscillations are quite important, in particular for the Q20 optics since the phase advance per cell has been significantly changed. Figure 2.3 shows the closed orbits for the two optics including the permanent bump, as computed by MADX with the thick lens description of the accelerator. The upper frames show the SPS closed orbit all along the ring, whereas the lower ones zoom on the bump region in the LSS1. To be noted the large “leakage” (i.e. the presence of oscillations in the beam orbit outside the bump region) in case of Q20, due to lower quadrupole strengths. On the contrary, the small distortions in the optical betatron and dispersion functions, as well as in the nominal tunes and chromaticities, introduced by the orbit bump can be neglected.

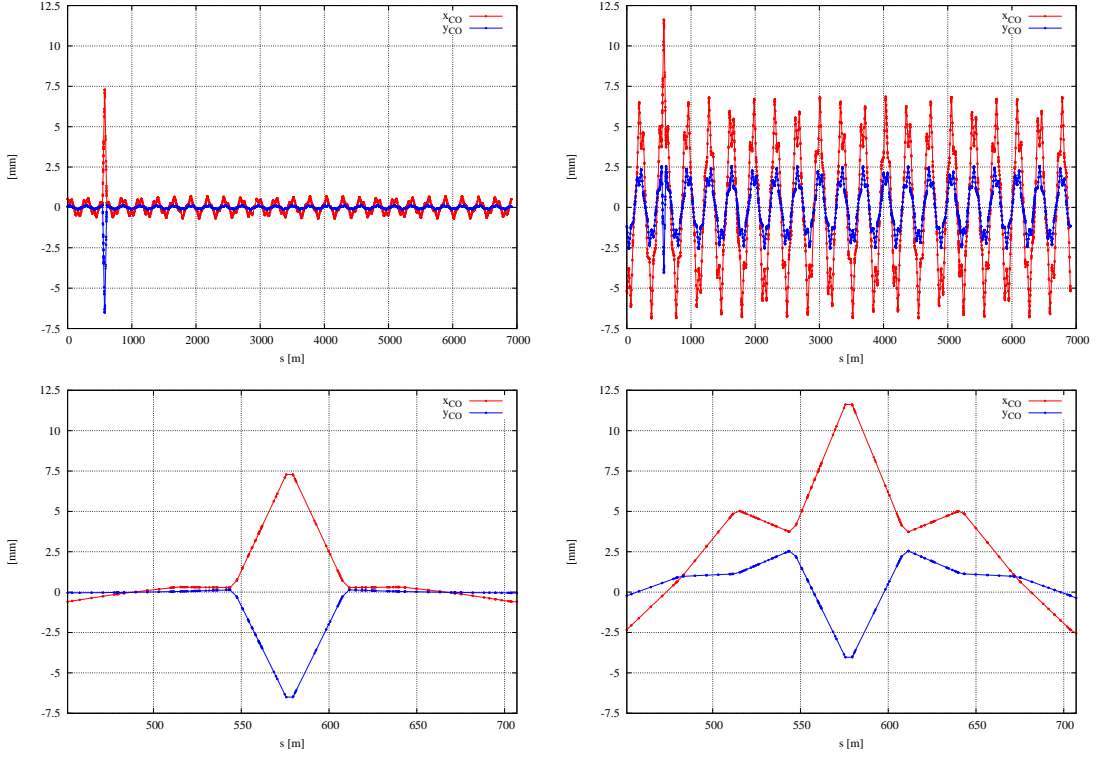


Figure 2.3: Upper frames: SPS closed orbit in case the permanent bump in LSS1 is taken into account in the Q26 optics (left column), and in the Q20 optics (right column). Lower frames: zooms on the LSS1.

### 2.1.4 The SPS Cycle

Figure 2.4 shows an example of the cycle of the LHC beams in the SPS. The timing is a multiple of the basic unit of 1.2 s [19], i.e. the duration of a cycle of the PS, used as injector of the SPS, and the total duration of the cycle is 21.6 s [19], equivalent to 18 PS cycles. After 625 ms from the beginning [70], four PS batches are received, separated by 3.6 s each [19], giving the possibility to the PS to deliver beams to other users, even while filling the SPS. Ramping starts immediately after the last injection, and it is performed with an average rate of  $\approx 80$  GeV/s [70]. At flat top, the extraction bumps are opened, and the kickers fired to extract the beam, selectively from one of the LSSs devoted to extraction towards LHC [71].

The effect of tail scraping is visible in the beam current profile shown in

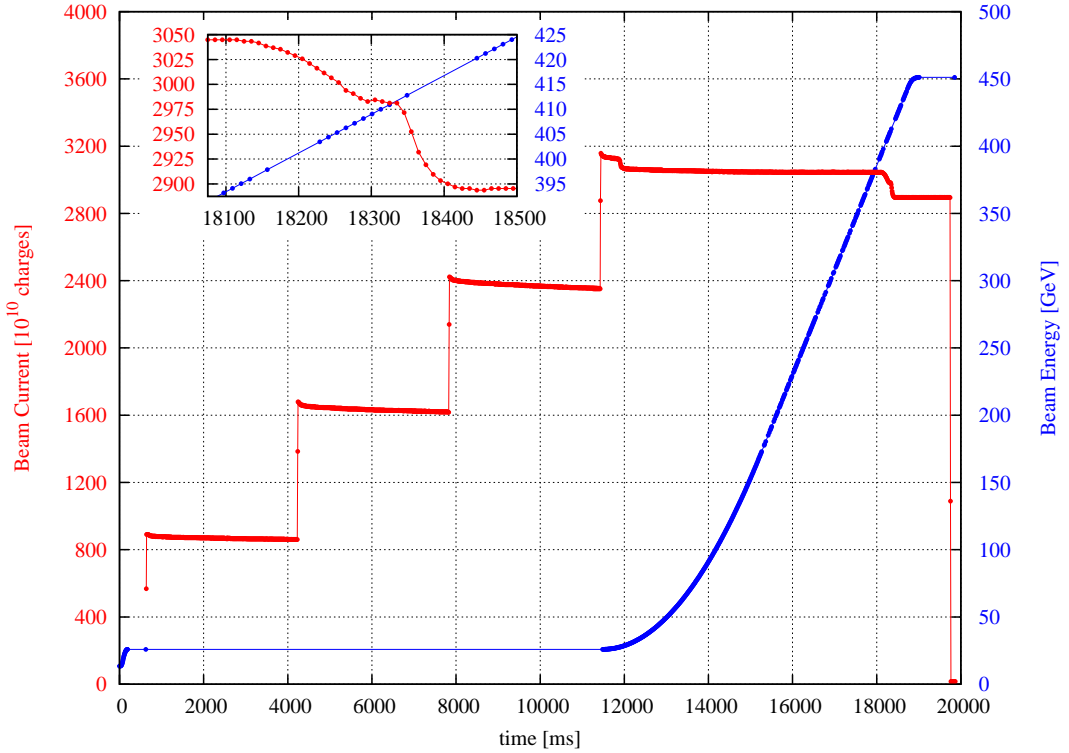


Figure 2.4: Example of SPS cycle when LHC beams are accelerated: measured beam current in machine (red curve, left vertical axis) and energy (blue curve, right vertical axis). It should be noted that the profile of the beam current ends with a beam dump event, and not with a fast extraction. Moreover, ramping magnets down has been omitted. The zoom on the upper-left part of the plot shows the effect of scraping on both the horizontal and the vertical planes. Scraping is performed with the BSHV.11759 scraper, i.e. the spare one (see Sec. 2.2.1).

Fig. 2.4, and it is the tiny decrease towards the end of the ramp. Scraping is performed not exactly at flat top, but at the end of the ramp, in order not to populate the abort gap<sup>4</sup>. The figure shows two small decreases in the beam current, due to successive scraping on both the horizontal and the vertical planes, respectively, as it happens during regular operation.

The beam intensity profile in Fig. 2.4 shows the existence of other small sources

---

<sup>4</sup>The abort gap is a series of consecutive buckets in the longitudinal structure of the beam not filled with bunches. In case of single turn extraction of the beam (or dumping), the kickers responsible for steering the beam are ramped while the abort gap passes through them, so that no beam particle is kicked during ramping and no bunch is sent on an orbit different from the one of the circulating beam or the extraction one.

of losses, present throughout the whole cycle [72]:

- the slow decrease at flat bottom after each injection is due to halo protons being intercepted by the *machine aperture*, in particular the vertical bottleneck represented by the TIDV.11892, i.e. the dump block. It should be kept in mind that the beam has the biggest size at injection, as the geometrical emittance is inversely proportional to the beam momentum;
- fast losses at the four injections (barely visible in the plot) are due to *injection errors*;
- losses are also generated at *RF capturing*, at the beginning of ramping.

## 2.2 The SPS Scraping System

Without adequate protection, quenches in the LHC can be induced during beam injection. In fact [56]:

- *injection oscillations* may lead protons in the tails to touch the beam screen of the SC magnets before they reach the LHC betatron collimation system;
- strongly populated tails intercepted by the *LHC collimators* can induce quenches in the SC magnets of the downstream arc;
- beams extracted from the SPS may touch the *SPS-to-LHC TL collimators*. Some tail protons could reach the LHC and ultimately be lost in SC magnets.

All these scenarios deal with the presence of tails in the injected beam and the possibility for these to be intercepted by aperture restrictions. The consequent development of secondary particle showers is responsible for the energy potentially deposited in the SC coils. The number of intercepted protons is thus crucial for

the energy deposition in the SC coils, and it determines if the quench takes place or not.

Given the highly populated bunches injected in the LHC (see Tab. 1.5), effective tail removal can definitively remove the risk for quenches at injection. This can be achieved by means of a collimation system dedicated to halo cleaning, put in action before injecting beam in the LHC. Halo cleaning implies a decrease in the beam current, and consequently in the luminosity (see Eq. 1.1). Thus, the choice of a proper level of tail removal is relevant for the performance of the LHC as a collider. Extensive studies [56] have shown that tails outside  $3.5\sigma$  can be scraped off with a negligible loss in luminosity, as their contribution to the luminosity would be marginal.

The SPS-to-LHC TLs are equipped with collimators [19], but these are not suitable for regular halo cleaning. Indeed, in case of single-pass systems, many collimators at different phase advances equipped with long jaws are necessary to fulfil the task. The space available in the SPS-to-LHC TLs is not much. Moreover, collimators in the TLs are located relatively close to the LHC SC magnets; thus, scraping would start secondary particle showers, with energy deposition induced in the SC coils and quenches potentially triggered. Consequently, any regular halo cleaning is done more efficiently and safely in the SPS, and without any risk of quench.

The SPS has been thus equipped with scrapers, to regularly remove beam tails and consequently avoid risks of quench at injection in the LHC. These are a fast system, operated only at the end of the SPS cycle not to affect most of the cycle and to minimise tail re-population.

Section 2.2.1 describes the system presently installed and currently operationally deployed, with its main technical aspects, including the mechanical movement of the blades providing cleaning. Moreover, being the scrapers installed on

a circular machine, the basic principles of multi–turn betatron collimation are briefly summarised. Finally, the weaknesses of this system are highlighted.

Section 2.2.2 reviews the upgraded design proposed for the LIU era. The description refers to the most updated configuration, as proposed in an original work by Mete et al. in Ref. [48], and the necessary modifications to the SPS optics are reported as well.

A comparison between the two systems is given at the end, in Sec. 2.2.3, pointing out how the upgraded system can overcome the weaknesses of the existing system.

### 2.2.1 The Existing System

The SPS scrapers [57] are beam–intercepting devices installed in the SPS, aimed at scraping off halo particles before injecting beam in the LHC. They are graphite blades, 1 cm in length, swept through the beam at the desired transverse position. The graphite is of type Steinemann R4550, with a density of  $1.83 \text{ g cm}^{-3}$ . The lower–left frame of Fig. 2.5 shows the technical drawing of the blades. Two blades are installed, one for each plane of cleaning, i.e. horizontal and vertical. The upper–left frame of Fig. 2.5 shows a schematic representation of the mechanical cycle of both blades. It is characterised by a slow and precise movement, to set the blade at the desired scraping position; and a fast movement, with which the blade is swept through the beam. During the injection in the SPS and for most of the ramp, the blades stay in the “parking” position, marked by the yellow dot in the shown schematics. The parking position is a waiting position not far from the one for scraping, but enough far off the beam closed orbit, to avoid any spurious loss. Just before scraping, they are moved to the “target” position, marked by the dark yellow dot in Fig. 2.5, which is the desired position of scraping. Once triggered, the blades are quickly swept through the beam. Finally, they are moved

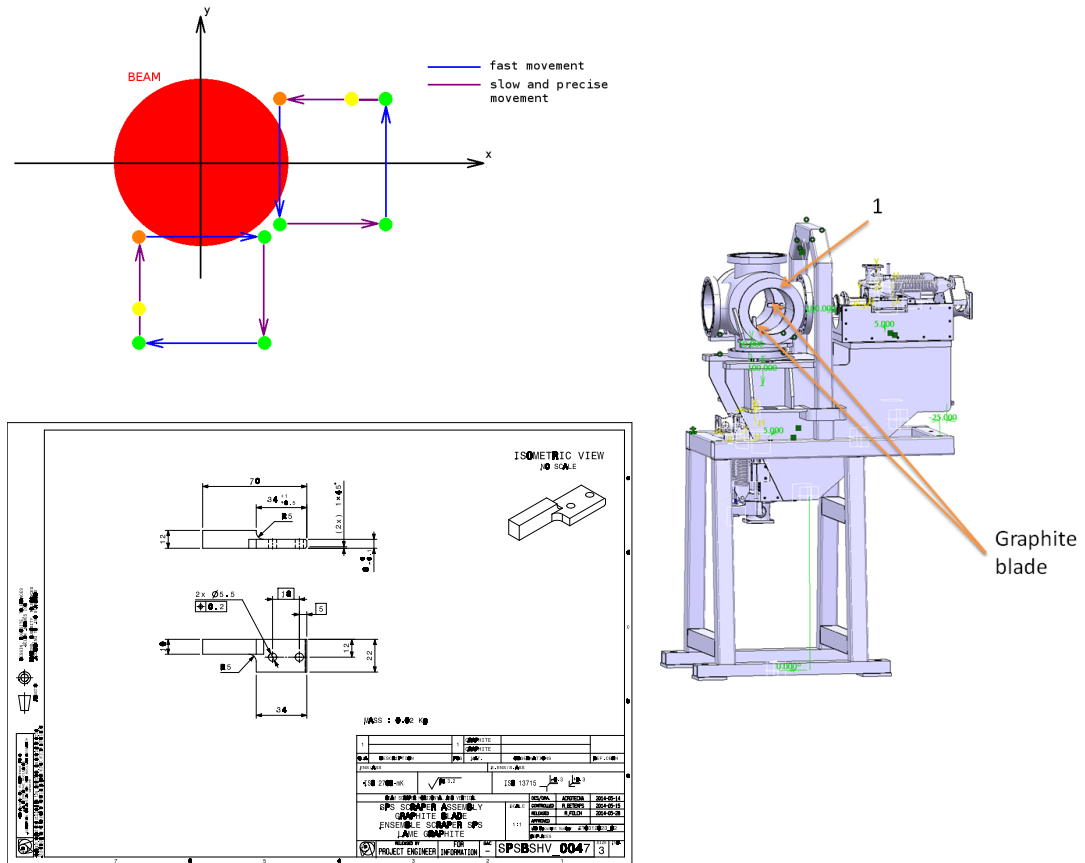


Figure 2.5: Upper-left frame: schematics of the mechanical cycle of both blades of the SPS scrapers. The “parking” position is labelled by the yellow dot, whereas the “target” position is labelled by the dark-yellow dot. Lower-left frame: technical drawing of the scraper blade. Right frame: 3D view of an SPS scraper tank and its mechanics.

back to the parking position, closing the mechanical cycle. Scraping is currently performed at the end of the ramp, in order to lose beam particles scattered by the blades along the ring, and thus not to populate the beam abort gap (see Sec. 2.1.4).

Two blades, one horizontal and one vertical, are installed in one tank, along the beam line, with their own motorisations (see the right frame of Fig. 2.5). The tank is 45 cm in length. The SPS scrapers are presently installed in the LSS1 (see Fig. 2.6). The technical drawing in Fig. 2.7 shows their position in the LSS1, few metres upstream of the TIDH.11795, i.e. the low energy internal beam



Figure 2.6: Installation of the SPS scrapers in the LSS1.

dump. There are two identical sets of scrapers, each with its couple of blades and related mechanics. They are named BSHV.11759 and BSHV.11771. The two sets are installed for redundancy reasons. The BSHV.11771 is used for regular operation, whereas the BSHV.11759 is used as spare. They are installed close to each other in order to have very similar machine optics and thus operational settings.

While the SPS scrapers in the LSS1 are relatively new devices, the original [57] ones are installed in the LSS5, as it can be seen in the technical drawing in Fig. 2.8. They are named BSHV.51659. These devices were used in the Intersecting Storage Rings (ISR), equipped with copper blades. They were moved to the SPS, and the blades changed to graphite ones in 2010, for the sake of robustness of the blades. Since the LSS5 is one of the cleanest regions of the SPS accelerator under

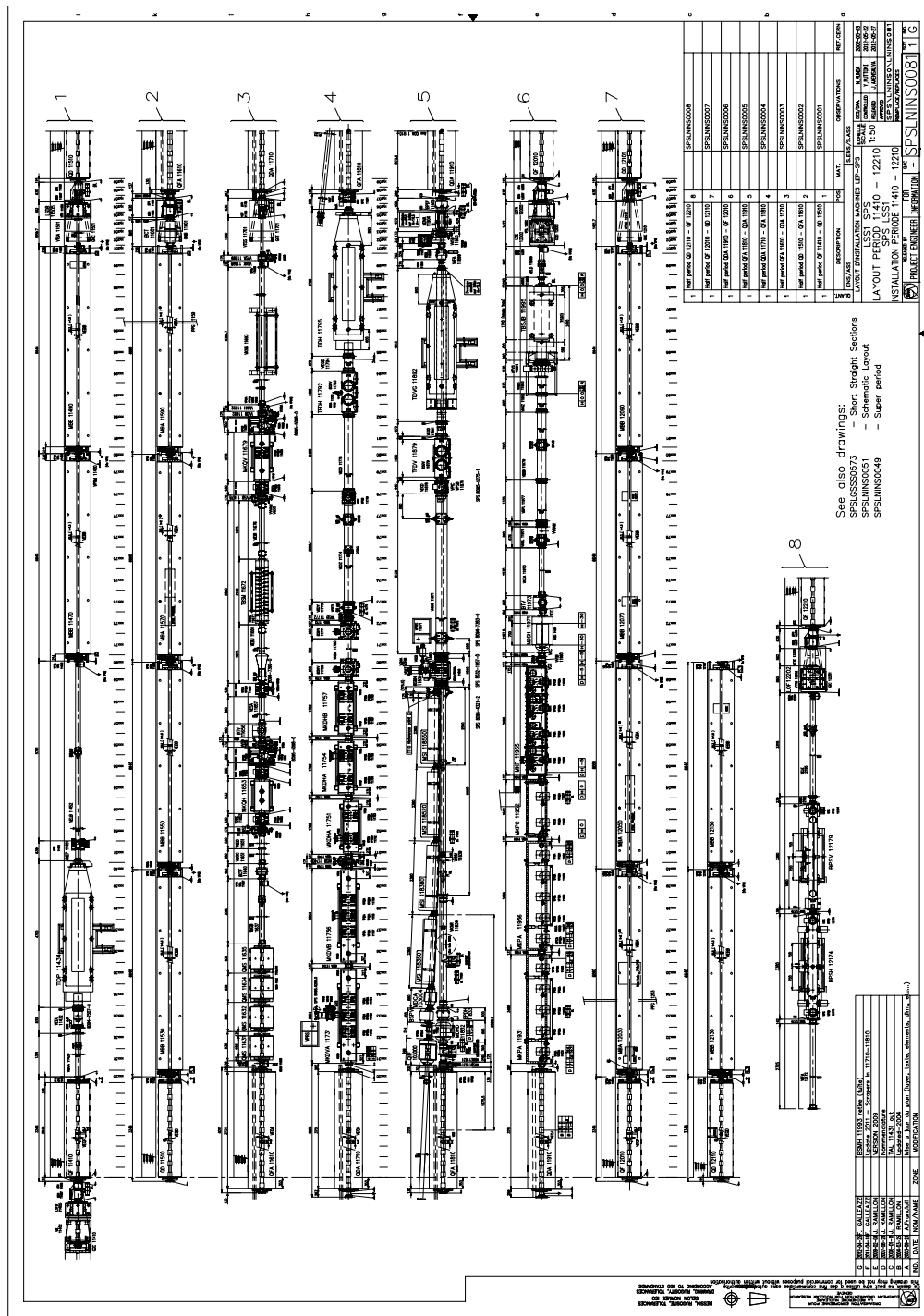


Figure 2.7: Schematics of the SPS LSS1. The scrapers are labelled as BSHV.11759 and BSHV.11771.

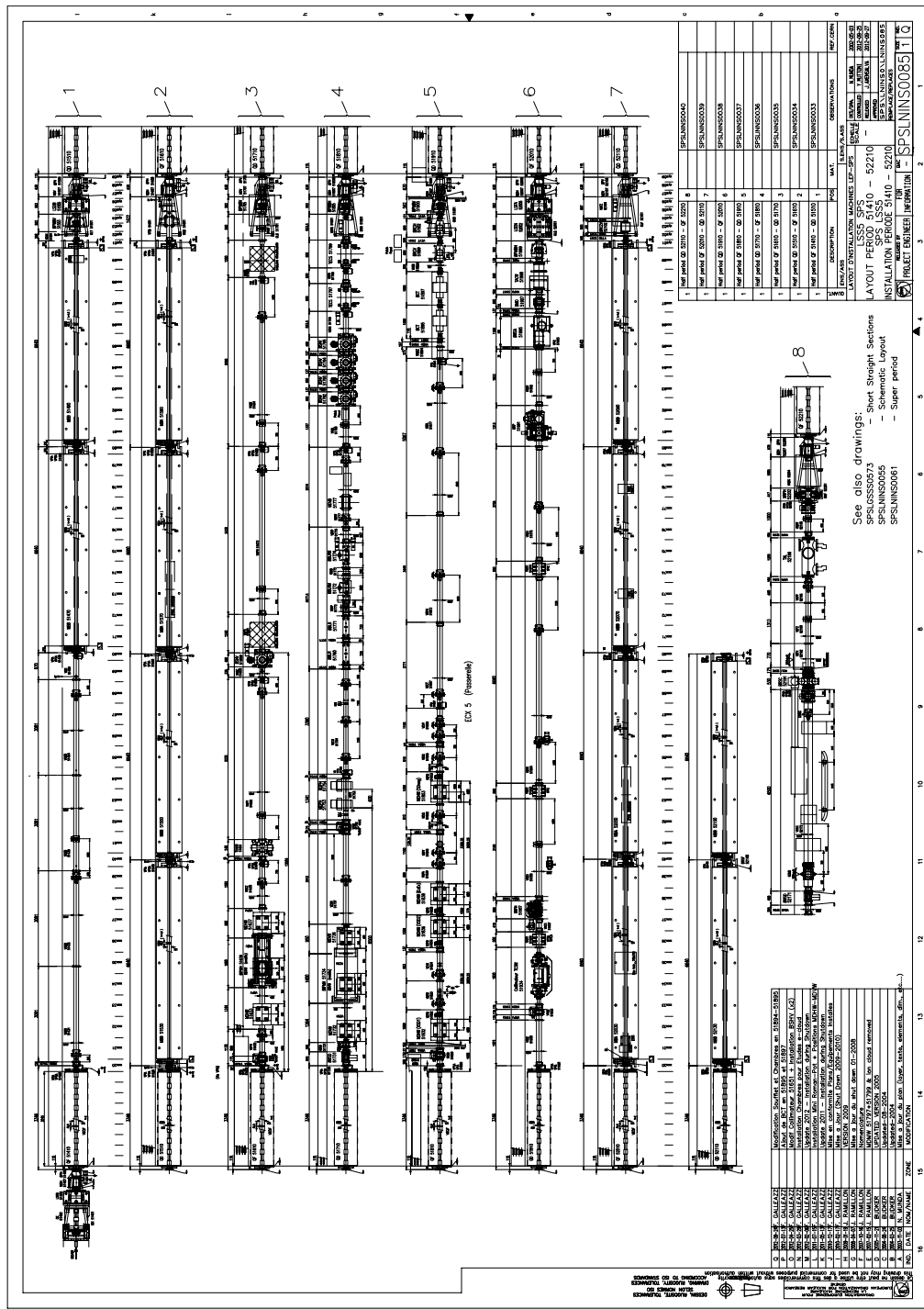


Figure 2.8: Schematics of the SPS LSS5. The scrapers are labelled as BSHV.51659.

		<b>11759</b>	<b>11771</b>	<b>51659</b>
$\beta_x$	[m]	57.6	60.6	61.1
$\alpha_x$	[]	-1.22	-1.27	1.28
$D_x$	[m]	-0.732	-0.755	-0.472
$D'_x$	[]	$-1.85 \cdot 10^{-2}$	$-1.85 \cdot 10^{-2}$	$-1.04 \cdot 10^{-4}$
$\beta_y$	[m]	62.0	59.0	57.6
$\alpha_y$	[]	1.29	1.24	-1.22
$D_y$	[m]	$7.43 \cdot 10^{-3}$	$7.56 \cdot 10^{-3}$	$1.19 \cdot 10^{-3}$
$D'_y$	[]	$-1.15 \cdot 10^{-4}$	$-1.15 \cdot 10^{-4}$	$-1.18 \cdot 10^{-4}$
$x$	[mm]	7.61	7.93	1.71
$x'$	[ $10^{-3}$ ]	0.265	0.265	-0.117
$y$	[mm]	-0.687	-0.954	0.161
$y'$	[ $10^{-3}$ ]	-0.221	-0.221	-0.0295
$\sigma_{x,\beta}$	[ $\mu\text{m}$ ]	490	503	505
$\sigma_{x,s}$	[ $\mu\text{m}$ ]	146	151	9.44
$\sigma_{y,\beta}$	[ $\mu\text{m}$ ]	508	496	490
$\sigma_{y,s}$	[ $\mu\text{m}$ ]	1.49	1.51	0.237

Table 2.3: Optics functions, closed orbit and typical beam dimensions at the three SPS scraper locations, as computed by MADX with the thick lens model of the SPS. Values refer to the Q20 optics, with the permanent magnetic bump in LSS1 switched on. Values are given at the end of the entry in the twiss sequence (45 cm in length). Values of rms beam sizes and divergences have been computed considering a normalised emittance of  $2 \mu\text{m rad}$ , for a proton beam at 450 GeV/c, and with an rms relative momentum offset  $\sigma_\delta = 2 \cdot 10^{-4}$ .

the radiation protection point of view, it was decided to install new scrapers for routine use in the LSS1. In fact, since the LSS1 already hosts the beam dump system, the radioactivity induced by the scrapers is much lower than the one already induced by dumping the beam, leaving the LSS5 clean. Nevertheless, the original devices are still in place and can be operated, but their use is limited to a few exceptional occasions.

Table 2.3 reports the optics functions at the locations of the scrapers for the Q20 optics, in case the permanent magnetic bump in the LSS1 is considered, as computed by MADX with the thick lens model of the SPS. Values are referred to the end of the entry in the twiss sequence. When the bump is off or in case

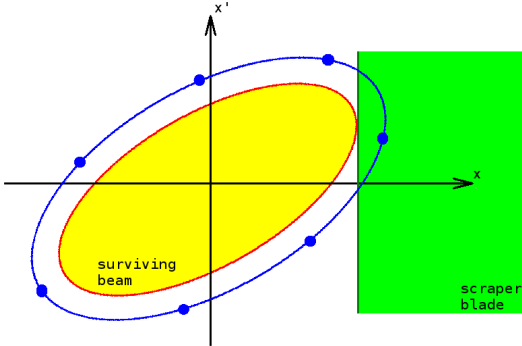


Figure 2.9: Schematics of the betatron cleaning obtained with the scraper blade, as seen in the phase space.

of Q26 optics (for both bump on and off), values are similar, and they have not been reported. The same table also reports the values of the closed orbit, and typical rms beam sizes and divergences computed for a normalised emittance of  $2 \mu\text{m rad}$ , at 450 GeV/c and an rms relative momentum offset of  $\sigma_\delta = 2 \cdot 10^{-4}$ .

Being a collimation system installed on a circular machine, the SPS scrapers are multi-turn cleaning devices. Even though they are single-sided, i.e. the blades are installed and operated on only one side of the beam, they scrape off tails outside the desired normalised betatron amplitude (see Sec. A.1), covering all phases, since beam particles go through the device location turn after turn, always with a different betatron phase. In addition, being installed in a position of the accelerator with a value of dispersion relatively small ( $\approx 10\%$  of the maximum in the arc, in case of Q20 optics), betatron cleaning is mainly performed, removing protons at large betatron amplitudes. Figure 2.9 shows the basic idea behind the multi-turn betatron cleaning performed by the scraper blade, as seen in the phase space (the horizontal one is shown). No dispersion effects are shown. The scraper blade is set at a certain amplitude, and only the protons with a maximum positional excursion lower than the scraper position will survive to cleaning. For instance, the proton moving along the blue ellipse in Fig. 2.9 will be, sooner or later, intercepted by the blade and lost.

Halo particles travelling through the blade undergo all the interactions that a high energy proton at 450 GeV/c undergoes when interacting with matter, mainly: MCS and ionisation, and nuclear elastic and inelastic scattering, including single diffractive events (see Sec. 1.4.3). When swept through the beam, the blades remove the tail protons in two possible ways:

1. through *inelastic interactions*, leading to the actual *loss* of the proton in the blade itself, and the start of particle showers. On average, a proton has to travel in the absorbing medium for a length equal to the inelastic interaction length before undergoing an inelastic scattering event, and this has an impact on the scraping speed (see later);
2. through *all other* aforementioned *interactions*, leading to the survival of the proton in the blade, but with a change in its orbit and/or energy. In case of a change dramatic enough, the proton touches the mechanical aperture somewhere along the machine, most probably in that same turn, and it is lost there, generating a local *loss*.

The main weaknesses of the present system are due to the fact that it is a mechanical device. In particular, the blade is thin, to be quickly swept through the beam. Hence, the length of the active material is short, with relevant consequences on:

**the time required for scraping** Due to the probabilistic nature of all the involved processes and the short length of the blade, protons need to go through the blade many times before undergoing an interaction leading to their loss in the blade, and this implies that a certain amount of time is needed to fully accomplish the scraping action. For instance, the inelastic interaction length of graphite for 450 GeV/c protons is  $\approx 45$  cm (see Tab. 1.6). Given the length of the blade (i.e. 1 cm), this translates into

only  $\approx 2\%$  of the protons undergoing an inelastic interaction per passage, and 45 passages required before a proton undergoes an inelastic event, on average. Given the revolution time of the SPS of  $23.05\ \mu\text{s}$ , this translates into an average time of  $\approx 1\ \text{ms}$  before a proton undergoes an inelastic interaction. A longer absorber would lower the average number of passages required for definitively losing the particle in the intercepting material, and thus the time required for scraping. It should be kept in mind that betatron and longitudinal single particle dynamics determine the transverse position of the proton (see Sec. A.1), always different from turn to turn, leading to many passages where the blade is missed, further increasing the time required for scraping. As an example, the zoom in Fig. 2.4 shows that the actual time operationally required for scraping with the present system is of the order of 150–200 ms (to be compared to the aforementioned value of 1 ms), and this value takes into account the beam dynamics in the accelerator, i.e. betatron and longitudinal motion, and the speed of the blade;

**the energy deposition** All energy deposition events are distributed over the short length of the blade. In addition, due to the sweeping through the beam, the energy deposition is mainly concentrated in the region of the edge immediately facing the beam (see Fig. 2.10, left frame);

**the production of high energy secondary particles** Such a small device provides very limited absorption of high energy secondary particles generated by inelastic events. This implies that almost nothing of the initial energy of the lost proton remains in the blade, but most of it is distributed on the downstream equipment and the tunnel, with consequent possible activation.

It should be kept in mind that a key parameter for the energy deposition in the blade and the time required for scraping is the sweeping speed of the

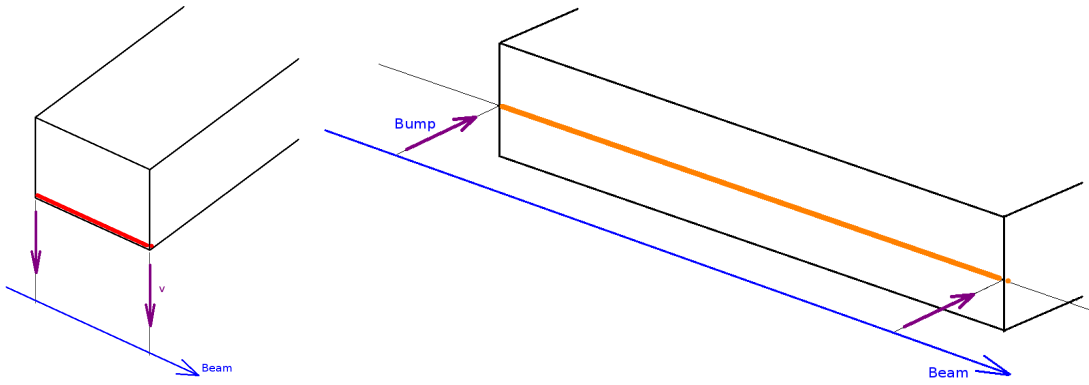


Figure 2.10: Left frame: in the present SPS scraping system, the blade is mechanically swept through the beam, implying increased levels of energy deposition around the edge immediately facing the beam (red region). Right frame: in the upgraded SPS scraping system, the beam is bumped against a fixed absorber block, implying that energy is deposited on the surface used for scraping (red region).

blade. The faster the blade, the larger its displacement per turn, and thus the volume of blade available for performing the scraping. On the other hand, new regions of the phase space are more quickly explored, resulting in intercepting tail protons more rapidly. Being a mechanical device, the higher the desired speed, the more complex is the required mechanics. The nominal speed that the present mechanics allows for is 80 mm/s [73]. Moreover, being a mechanical device, movable components are subject to wear. On the other hand, the present devices are extremely simple, and they fully implement the KISS (Keep It Simple, Stupid!) basic rule of engineering [74]. Short reparation times are expected, mainly related to the exchange of a graphite blade only in case it is seriously damaged.

### 2.2.2 The Upgraded System

In the framework of the LIU activities, a new design of the scraping system, alternative to the existing one, has been proposed and extensively studied [48]. The concept is based on a long, static absorber block made of a light material,

towards which the beam is steered for scraping by means of magnetic bumps. The rationale behind the proposal is:

- to reduce energy deposition values in the medium intercepting beam particles;
- to improve the time required for scraping;
- to decrease losses induced in the ring;
- to have a more flexible system;
- to avoid potential limitations coming from mechanical components, the performances of which may degrade due to wear.

Section 2.2.3 gives an extensive comparison between the designs of the existing system and of the upgraded one, also highlighting how strategic choices in the upgraded design (e.g. the deployment of a long absorber block and the use of a magnetic bump) help in satisfying the rationale. The choice of the location in the SPS ring for the potential installation of the upgraded system and the optimisation of the kicks provided by the bumpers are given in Ref. [48], as they are not part of this PhD activity. In the following, the final layout from Ref. [48] is described.

The upgraded system is made out of two magnetic systems, for independently scraping on the horizontal and the vertical planes. For each plane, the magnetic bump is obtained switching on dedicated dipole magnets, hereafter called “bumpers”, in a four-bumpers scheme, for ensuring full flexibility in setting the position and direction of the beam at the absorber. An absorber per plane is located between the two couples of bumpers, i.e. those opening the bump and those closing it.

Figure 2.11 shows the schematics of the SPS LSS6, with the upgraded system as from the last proposal [48]. The four existing extraction bumpers are used

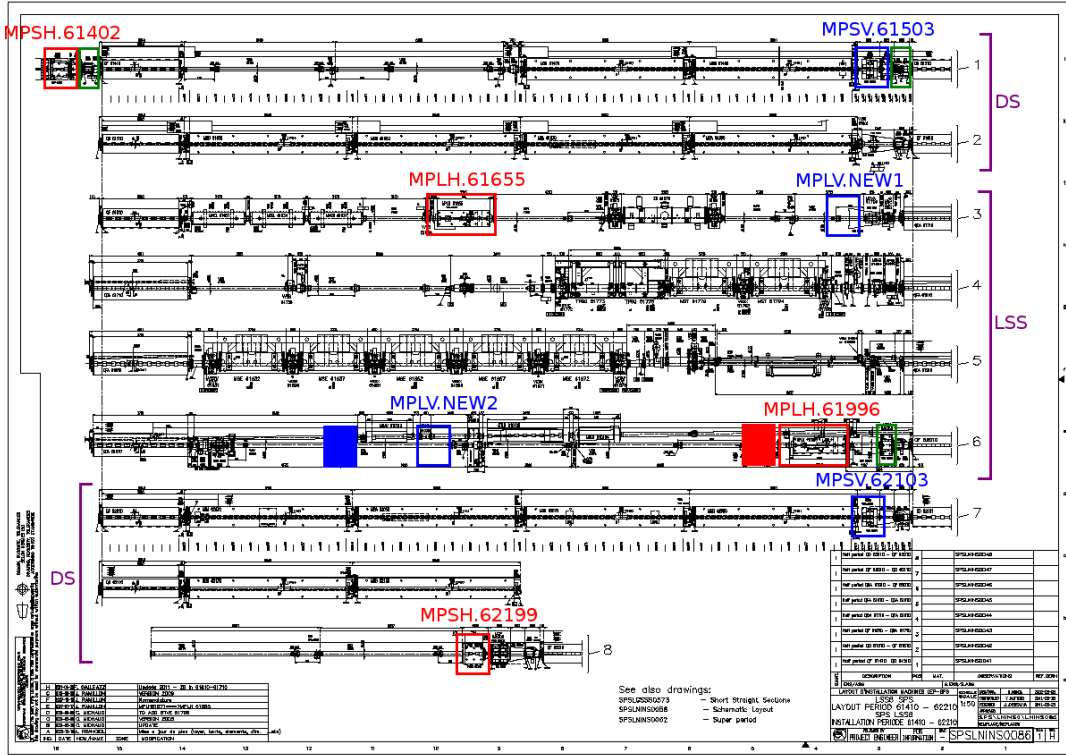


Figure 2.11: Schematics of the SPS LSS6, with the upgraded scraping system, based on magnetic bumps. The system dedicated to the horizontal plane is highlighted in red, whereas the one for the vertical plane is in blue. Empty rectangles indicate the bumper locations, whereas the solid rectangles mark the position of the absorber blocks. Empty green rectangles indicate the position of active sextupoles. The beam goes from–top left to bottom–right.

to horizontally steer the beam against the respective absorber. For the vertical steering, the two existing bumpers can be used, and two new ones are needed, i.e. the MPLVs shown in Fig. 2.11. The magnetic bumps are raised with a speed of  $0.002 \sigma$  per turn, where  $\sigma$  is the rms beam size on the cleaning plane. The absorber blocks are located towards the end of the LSS. These are 1 m in length, and made of graphite at  $1.67 \text{ g cm}^{-3}$ . As a consequence, protons going through them by the whole length have 90 % probability to undergo a nuclear inelastic event, considering a typical value of inelastic interaction length for graphite, i.e. 44.6 cm (see Tab. 1.6).

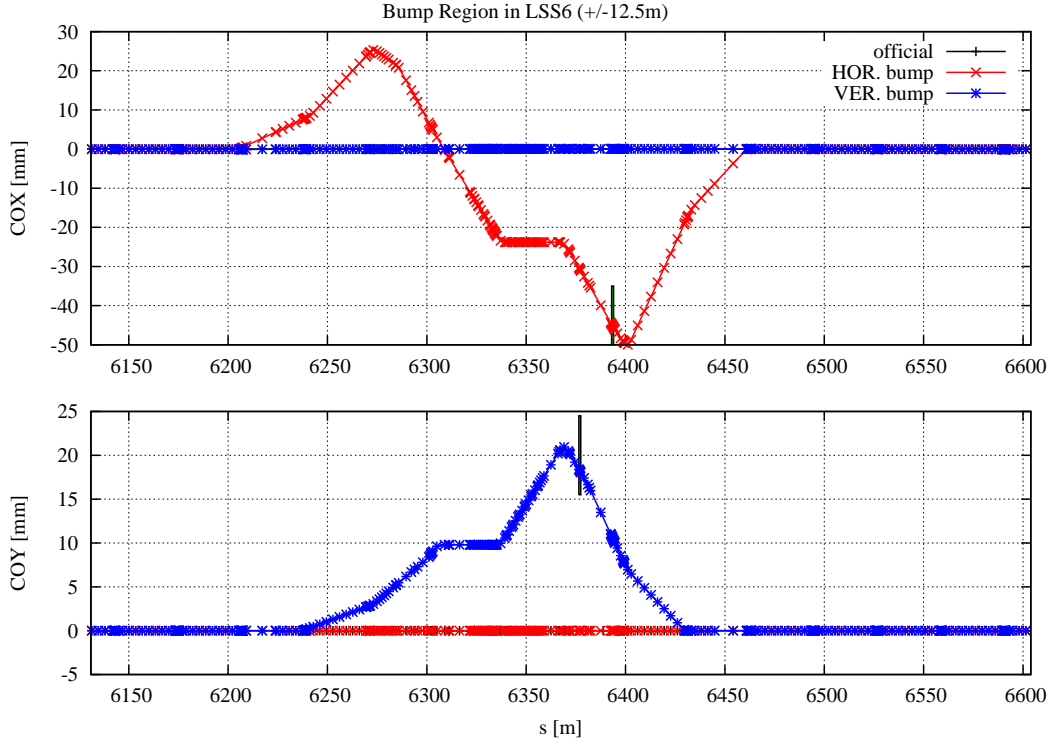


Figure 2.12: Horizontal (upper frame) and vertical (lower frame) closed orbits in the LSS6 and in the two enclosing DSSs for the nominal Q20 optics when the permanent bump in the LSS1 is not considered (black line), and for the same optics when the horizontal (red line) and the vertical (blue line) bumps in the LSS6 are separately switched on at their nominal amplitudes. The location of the absorber relevant to each plane is shown as well.

Figure 2.12 shows the closed orbit on the horizontal (upper frame) and vertical (lower frame) planes as computed by MADX with the thick lens model of the SPS, zoomed on the region of the bumps in LSS6. The figure compares the nominal Q20 optics without orbit bump in the LSS1 (black curve) with the same optics when the bumps are separately switched on to their “nominal” amplitudes (the red curve represents the case with the horizontal bump on, whereas the blue curve represents the case with the vertical bump on), i.e. at full beam scraping, when the beam closed orbit is on the edge of the absorber. It should be noted that there is no leakage outside the bump region, and the beam orbit remains flat in all the rest of the ring.. The figure also shows the position of the absorber relevant to

each plane. The presence of the extraction line in the LSS6 (see Fig. 2.11) poses relevant space constraints on the integration of the system, and have affected the whole design. In particular, it was possible to locate the absorber block for the horizontal scraping system on the inside of the ring, i.e. on the side of the transport path in the SPS tunnel, possibly minimising any reduction of the manoeuvre area, and the one for the vertical scraping system above the ring. It should be noted that the absorbers are located where the closed orbit is not flat, i.e. it is not parallel to the longitudinal axis of the local reference system. This implies that, while ramping the magnets and thus raising the magnetic bump, the closed orbit at the absorbers changes not only in position but also in angle. For the same reason, the blocks are oriented following the natural angle of the bump, i.e. they are tilted to follow the closed orbits shown in Fig. 2.12. Table 2.4 reports the values of the linear optics functions, the closed orbit and beam spot size at the centre of the absorber blocks of the upgraded SPS scrapers, for the nominal magnetic bumps when independently powered. For comparison, values with the regular optics (without considering the permanent magnetic bump in the LSS1) are given. The amplitude of the bump on the cleaning plane expressed in units of beam  $\sigma$  is given as well. Table 2.5 lists the bumpers originating the magnetic bump and their nominal kicks.

Figure 2.11 highlights the presence of three active sextupoles installed in that same portion of accelerator. Two of them are located in the DS upstream of the LSS1 (at the beginning and centre of the DS, respectively), close to the opening bumpers. Consequently, the nominal bumped orbit at their locations does not have large values. On the contrary, the third sextupole is located at the beginning of the downstream DS, at the end of the half cell where the absorbers are located. This implies that the nominal bumped orbits at its location have large values. Figure 2.12 shows that at this sextupole (located upstream of the

parameter	horizontal system		vertical system	
	bumped	not bumped	bumped	not bumped
$\beta_x$ [m]	87.93	83.29	41.91	41.91
$\alpha_x$ []	-1.66	-1.61	-0.898	-0.898
$D_x$ [m]	-0.616	-0.384	-0.420	-0.420
$D'_x$ []	-0.00239	0.00217	0.00218	0.00217
$\beta_y$ [m]	41.2	41.44	82.43	82.43
$\alpha_y$ []	0.878	0.887	1.598	1.598
$D_y$ [m]	0.0	0.0	0.0291	0.0
$D'_y$ []	0.0	0.0	-0.000694	0.0
$x_{\text{CO}}$ [mm]	-45.131	0.0	$5.1135 \cdot 10^{-2}$	0.0
$x'_{\text{CO}}$ [ $10^{-3}$ ]	-0.8745	0.0	$1.0096 \cdot 10^{-3}$	0.0
$y_{\text{CO}}$ [mm]	0.0	0.0	18.227	0.0
$y'_{\text{CO}}$ [ $10^{-3}$ ]	0.0	0.0	-0.38836	0.0
$\sigma_x$ [ $\mu\text{m}$ ]	750.25	689.05	516.74	516.74
$\sigma_y$ [ $\mu\text{m}$ ]	463.21	464.77	655.68	655.51
$\sigma_{x'}$ [ $\mu\text{m}$ ]	14.97	15.04	15.04	15.04
$\sigma_{y'}$ [ $\mu\text{m}$ ]	14.97	14.99	14.99	14.99
$z_{\text{CO}}$ [ $\sigma$ ]	60.155	0.0	27.798	0.0

Table 2.4: Linear optics functions, closed orbit and rms beam spot size and divergence at the centre of the absorber blocks of the upgraded SPS scrapers. Values correspond to the nominal magnetic bumps when independently powered, and have been calculated with MADX, in the case of the Q20 optics and the thick lens description of the SPS accelerator lattice. For comparison, the values with the regular optics (without considering the permanent magnetic bump in the LSS1) are given. The values of  $\sigma$  take into account both the betatron and the dispersion contributions (see Sec. A.2), and have been calculated using the Maximum LIU beam parameters from 2012 (see Tab. 1.5), i.e. a normalised emittance of  $2.5 \mu\text{m}$  and an rms relative momentum offset  $\sigma_\delta$  of  $5.25 \cdot 10^{-4}$ . The amplitude of the bump on the cleaning plane expressed in units of beam  $\sigma$  is given as well ( $z$  stands for either  $x$  or  $y$ ).

bumper	kick [ $10^{-6}$ ]	bumper	kick [ $10^{-6}$ ]
mpsh.61402	263.7	mpsv.61503	93.90
mplh.61655	-583.5	mplv.new001	152.1
mplh.61996	228.0	mplv.new002	-100.2
mpsh.62199	-550.6	mpsv.62103	238.8

Table 2.5: Bumpers originating the magnetic bumps for scraping the beam and nominal kicks.

focussing quadrupole after both absorbers, easily recognisable in the picture by the change in the direction of the closed orbits at  $s = \sim 6400$  m) the closed orbits are  $\approx -50$  mm and  $\approx 7.5$  mm on the horizontal and vertical planes, respectively. This is the reason why the optics functions when the bumps are on are slightly perturbed, particularly affecting the case of the horizontal scraping. Indeed, while in case of the vertical bump the fractional part of the tunes are changed by few tens parts per million, in the case of the horizontal bump they are changed by few percents. The presence of these sextupoles also has an effect on: the rising of the bump and its characteristics, as shown in Fig. 3.1, though a limited one; on the time profile of the beam intensity while scraping, as shown in Fig. 5.8, though not of primary importance; and on the pattern of the energy deposition in the absorber of the vertical scraping system, as shown in Fig. 5.9. More detailed remarks are done when the quoted figures are presented and discussed.

### 2.2.3 Comparison Between the Two Systems

The upgraded SPS scraping system (see Sec. 2.2.2) is based on a design completely different from the one of the existing system (see Sec. 2.2.1). In fact, instead of sweeping a thin blade through the beam, the beam itself is moved towards a long, static absorber block, by means of a magnetic bump. Advantages and disadvantages of the new design over the one of the existing system are related

to the deployment of a long absorber instead of a thin blade, and of the magnetic bump instead of a mechanical movement.

## Advantages

A first relevant advantage of using an absorber block longer than thin blades is the increased probability that a proton, going through it, undergoes an inelastic interaction and it is lost in a single passage. Given the foreseen material and length, i.e. 1 m of graphite at  $1.67 \text{ g cm}^{-3}$  characterised by an inelastic interaction length of 48.7 cm (very close to the value of 44.6 cm, reported in Tab. 1.6 for a slightly denser graphite), an average of  $\approx 10\%$  of the protons going through the absorber *survives* to a single passage through the absorber, to be compared to  $\approx 2\%$  as average fraction of *absorbed* protons going through the blades of the existing system. This advantage has immediate consequences on:

1. the time required for scraping, since basically only one passage is needed to remove a proton from the beam;
2. losses induced in the ring, since protons have a probability to undergo a “deep” nuclear inelastic event at their first passage higher than with the blades.

For the same reason, the upgraded system is expected to be less dependent on multi-turn effects.

Other advantages related to the deployment of an absorber block longer than thin blades are:

1. lower peak energy deposition values. In fact, the absorption of protons is diluted over a larger length, despite the unavoidable development and piling up of EM showers in the block;

2. less energy escaping the absorber in form of secondary particles. Indeed, the volume and mass of the absorber is much larger than those of the blade. This implies that secondary particle showers start to be absorbed in the block itself, increasing levels of energy deposition on one hand, but improving the capability of the device in absorbing the original energy of the impacting proton on the other hand, since less secondary radiation escapes.

Advantages related to the deployment of the magnetic bump are:

1. better control of beam impact conditions and enhanced flexibility. In fact, the use of a four-bumpers scheme allows one to fully control the impact parameters at the absorber, provided that the beam is granted enough clearance in the region of the bump. Contrary to what happens with the existing system, not only the scraping position can be set, but also the impact angle. Moreover, currents in the bumpers can be modulated while scraping, allowing to change the scraping position with time and thus perform a scan of the beam profile in a single cycle. On the contrary, the same scan performed with the existing system requires as many SPS cycles as the number of points of the scan;
2. thanks to the design of the magnetic bumps, the energy deposition in the absorber is not concentrated around one edge, but diluted over a larger volume, the one close to the surface directly impacted by the beam, lowering energy deposition values (see Fig. 2.10, right frame);
3. possible shorter times required for scraping, since the beam could be moved towards the absorber more rapidly than the blade swept through the beam;
4. the deployment of a magnetic system avoids the use of any mechanical component, removing any potential degradation of performance due to wear.

Hence, the system based on a long absorber block and the magnetic bump is expected to be characterised by greater flexibility, precision and resistance to wear than those achieved by a mechanical system, with more relaxed heat loads on the active medium.

### **Disadvantages**

Disadvantages related to the deployment of a long absorber are:

1. a deformation after an overload may result in a loss of proper alignment and surface flatness, with possible loss of performance due to shortening of the length traversed by protons, and consequent increase of local heat loads, leading to possible further damage;
2. in case of damage, the absorber may need to be replaced; in addition to the intervention time, further time should also be taken into account for vacuum treatment and outgassing, since it is a massive object.

Other disadvantages of the upgraded system over the existing one are:

1. the upgraded system is more complex than the existing one, requiring the installation and the maintenance of four bumpers and an absorber block for each plane of scraping; on the contrary, the present system is quite simple and compact;
2. due to the foreseen position of installation of the upgraded system, secondary particle showers are expected to locally load the downstream equipment, and in particular magnets (see Fig. 2.11), with possible complications in terms of magnet lifetime and activation. On the contrary, the existing system profits from the presence of the downstream dump at low energy (see Fig. 2.7), which catches most of the secondary showers. Moreover,

the activation generated in nearby equipment by secondary particle showers escaping the blades would be negligible with respect to the one of the downstream dumps.

Hence, the system based on a long absorber block and the magnetic bump is more complex than the existing one, with possible longer intervention times. Moreover, the existing system is installed close to the dump system, and issues related to energy deposition and induced activation in downstream equipment by secondary particle showers are of limited concern, as they pile up to the existing ones, quite high; on the contrary, this would not be the case for the upgraded system, due to the position where it would be installed.

## 2.3 Conclusions

The last stage of acceleration before injection in the LHC is the SPS. Once extracted, protons are transferred to the LHC by means of the TI2 and TI8 TLs.

A very clean and precise injection is required when dealing with nominal LHC beams, and this requirement is even more stringent in case of LIU beam parameters (see Tab. 1.5). In fact, small fractions of the beam population, in the order of  $5 \cdot 10^9$  protons in case of instantaneous losses, can induce a quench. Moreover, the mechanical aperture of the LHC is minimal at injection. Finally, since it is a multi-turn cleaning system located in two specific portions of the ring different from those where the LHC beams are injected, the LHC collimation system cannot assure full protection during the first turn of the injected beam.

A complex chain of passive systems is thus in place, with the aim of protecting the LHC cold aperture during the process of beam transfer from the SPS to the LHC. Both regular halo cleaning before extraction from the SPS and protection from mis-steering during beam transfer are involved.

Regular halo cleaning is accomplished by the SPS scrapers, immediately before beam extraction. The system presently in operation is made of movable graphite blades swept through the beam to remove tails. They are a multi-turn cleaning system installed in the SPS LSS1.

In the framework of the LIU activities, a new design of the scraping system has been proposed [48], to overcome weaknesses of the existing system. The concept is based on a long, static absorber block made of a light material against which the beam is steered by means of bumpers. Two magnetic systems, both located in the SPS LSS6, are used to independently scrape the beam on the horizontal and vertical planes.

Advantages native to the design of the upgraded system with respect to the present one are: expected lower values of peak energy deposition; less energy escaping from the absorber in the form of secondary particle cascades; better control of beam impact conditions and greater flexibility; a better control on the time required for scraping; lower losses along the ring. In addition, since no mechanical component is present, the system is not subject to wear. On the other hand, the present system is extremely simple and compact; in addition, in case of damage, the replacement of a blade is quite a quick operation. Conversely, for each plane to be collimated, the upgraded system requires four bumpers for steering the beam and the installation of a long absorber block, with consequent problems of misalignment and jaw deformation in case of overheating. Moreover, the upgraded system is more complex than the present one, conversely quite simple and compact.

# Chapter 3

## Simulation Tools

As result of the interaction with an intercepting device for beam halo cleaning (e.g. collimators and scrapers), some beam particles are scattered on orbits leading to their loss in the machine, and others are directly absorbed by the intercepting material, starting secondary particle showers and leading to energy deposition in downstream or nearby equipment. The time necessary to remove the desired amount of beam and the losses generated are requirements of primary importance, dictating the design of the device. Moreover, the energy deposition in the device itself and in the nearby equipment can pose further constraints to its design and operation. Tools simulating the impact of the beam on the intercepting device under study and the induced effects play an important role in the design of the device, as far as performance and robustness are concerned, to assure that the desired goals are achieved and the device can be safely operated.

The present chapter describes the simulation tools used to analyse the SPS scraping system, in both its present installation (described in Sec. 2.2.1 and analysed in Chap. 4) and in the upgraded design (described in Sec. 2.2.2 and analysed in Chap. 5). The key tool is the Monte Carlo code which simulates the interaction of beam particles with the intercepting device and the secondary particle showers

thus started. FLUKA has been chosen, since it is the reference tool for beam–machine interaction studies at CERN. It is routinely used for studies concerning any machine operated and designed at CERN, thanks to the refined physics models implemented in the code and its flexibility in simulating any scenario of interest.

The scraping system, both in its present installation in the SPS and in its upgraded design, is a cleaning system in a circular machine (see Sec. 2.2), and it is subject to multi–turn effects. In order to properly take them into account, FLUKA has been coupled to SIXTRACK, to include the beam dynamics in an accelerator ring in the simulation. In a coupled simulation, the two codes run at the same time, exchanging particles turn by turn. FLUKA takes care of the scattering in the beam–intercepting devices, whereas SIXTRACK takes care of the rest of the accelerator. SIXTRACK is the official simulation tool used at CERN for studies of dynamic aperture and beam cleaning in circular machines, especially targeted to the LHC and its upgrade.

Multi–turn effects are effects on observables of interest due to the fact that beam particles can go through the intercepting device for some turns before undergoing an inelastic event or being lost. Particle coordinates change turn by turn according to the beam dynamics in the ring (see Sec. A.1). In the case of the SPS scraping system, in addition to multi–turn effects, the position of the beam relative to the intercepting device changes during cleaning, i.e. turn by turn. In the case of the system presently installed, this change is due to the movement of the blade performing the cleaning; in the case of the upgraded system, the change is due to the magnetic bump which scrapes the beam against a static absorber block. The change of the relative distance between the beam and the intercepting device turn by turn has consequences on the way beam particles impact the device and exit from it, and on energy deposition results.

The chapter is divided into four main parts, with conclusions drawn in Sec. 3.5. Section 3.1 gives a brief introduction to FLUKA. I added a new functionality, relevant for the analyses presented in this thesis, i.e. the possibility of moving portions of the geometry. This is fundamental for a proper evaluation of the energy deposition in the SPS scrapers and the time required for scraping, shown throughout Chap. 4 and in Sec. 5.1.

Section 3.2 gives a brief introduction to SIXTRACK and to a couple of new features I introduced on purpose, relevant for the analyses presented in this thesis:

- I contributed to debugging the online aperture check native to SIXTRACK, and to its further development. This functionality is fundamental for the analyses presented in Chaps. 4 and 5 about the SPS scrapers, as it allows one to remove beam particles scattered by the scrapers on orbits leading to a loss in the machine; consequently, energy deposition results, time profile of the beam intensity while scraping and losses induced in the ring can be properly estimated;
- I implemented dynamic kicks in SIXTRACK, i.e. the possibility of changing the magnetic settings of selected elements in the accelerator ring. This implementation allows one to properly simulate the rising of the magnetic bump on which the design of the upgraded scraping system is based, and thus to properly estimate energy deposition results, time profile of the beam intensity while scraping and losses induced in the ring (see Chap. 5).

Section 3.3 gives an overview of the coupling between SIXTRACK and FLUKA, to the development of which I substantially contributed. In addition, the results concerning the SPS scraping system presented in Chaps. 4 and 5 represent its first extensive use and benchmark.

Section 3.4 presents some ancillary tools necessary to the preparation of the simulations:

- the Line Builder and the FLUKA Element DataBase are tools presently used at CERN for assembling complex and sophisticated FLUKA geometries of accelerator beam lines. The latter is a collection of FLUKA geometries of accelerator devices, whereas the former is a program for assembling the geometry of the beam line, starting from the optics of the machine and the database of geometries. These tools have been used to prepare the FLUKA simulations for the benchmark against BLM signals (see Sec. 4.3.5). I added to the database almost all the FLUKA geometry models of the devices installed in the SPS LSS1, relevant for the benchmark;
- the routine for sampling the beam to be tracked in a SIXTRACK–FLUKA coupled simulation. In particular, I have extended it, to handle double Gaussian beams, most relevant to the results shown in Chap. 4.

All the code development has been carried out with the most general approach possible, allowing the re-use of all the new functionalities here described to other rings and devices.

## 3.1 FLUKA

In the present section, the FLUKA code is briefly introduced. After the overview of the code given in Sec. 3.1.1, the new feature of moving portions of the FLUKA geometry is presented in Sec. 3.1.2. This is necessary to perform the analyses presented in Chap. 4 and Sec. 5.1, about the scraping system presently installed in the SPS and the preliminary analyses about the upgraded system, respectively. In fact, these analyses rely on simulating the movement of the device performing scraping towards the beam, turn by turn. Finally, Sec. 3.1.3 gives an overview of the PRECISIO settings, i.e. the settings used for the FLUKA simulations presented throughout Chaps. 4 and 5.

### 3.1.1 Overview of the Code

FLUKA [37, 38] is a general purpose Monte Carlo (MC) code for the interaction and transport of particles through matter. The physics implemented in the code covers an extremely wide energy range, extending from cosmic rays in the PeV region (if FLUKA is linked to DPMJET [75]) down to reactions in the keV region (100 eV in the case of photons) and thermal neutrons. Transport in any material is supported, with full particle cascades simulated in great details, including the description of unstable nuclear states, vital for estimations of the induced radioactivity.

FLUKA is maintained at CERN with the aim of including the best possible physics models in terms of completeness and precision, and it is continuously upgraded and benchmarked against experimental data. It is extensively used at CERN, in particular for any MC analysis concerning beam–machine interactions, e.g. estimation of energy deposition in beam–intercepting devices, thermal loads in warm and cryogenic magnets, BLM signals, streaming of radiation in accelerator tunnels, effects of radiation on electronics, induced radioactivity, background to experimental apparati, etc... Source terms of interest that are routinely simulated include: direct impact of the beam on accelerator devices, losses on collimators or on other devices, collision debris, and interaction of the beam with the residual gas in the pipe.

FLUKA allows one to track particles in any geometry arbitrarily complex, and offers extremely flexible options to the user in terms of: variance reduction techniques, meant to optimise the CPU time on regions of phase space relevant for results; scoring, with the possibility to choose plenty of output quantities; tuning of physics settings, especially meant to save CPU time. Tracking in magnetic fields is supported.

FLUKA is conceived in such a way that all the necessary information in input to the code is gathered in only one text file (the `.inp` file), where the user specifies the physics and transport settings, the geometry to be used with the definition of materials, the scoring options, and the settings of possible variance reduction techniques. For most standard problems the user do not need to type a single line of code. Whenever this is unavoidable, a large number of routines is available to the user, as hooks to the main source code for adapting it to the needs of the problem under study.

Flair [76] is a Graphical User Interface (GUI) to FLUKA, which enhances the control of the code and the flexibility in preparing the input file, visualising the geometry, running the simulation and performing the analysis.

### 3.1.2 Moving Portions of Geometry

The possibility of moving portions of geometry during the simulation is fundamental for the analyses shown in Chap. 4 about the existing scraping system, installed in the SPS, and the preliminary analyses about the upgraded system shown in Sec. 5.1. In fact, these analyses rely on simulating the movement of the device scraping the beam, turn by turn. Consequently, I implemented this functionality in FLUKA [77]. For the moment, the respective code is contained only in the SVN repository of the coupling [78] (see later).

The geometry is handled by FLUKA with a combinatorial approach. The building blocks are “bodies”, i.e. surfaces of first or second order that cut the 3D space; the portions of space identified by the bodies are then combined to form “regions” through simple Boolean operations like intersection and union. Since the release 2011.2, it is possible to apply geometry directives that modify the definition of bodies, including transformations of any complexity. The transformations are applied run-time, i.e. during transport.

The implementation of moving portions of geometry relies on changing the definition of the geometrical transformations applied to the concerned bodies. Being the transformations applied run-time during tracking, they can be updated with immediate consequences on particle tracking. In particular, in a FLUKA–SIXTRACK coupled simulation (see Sec. 3.3), position (or orientation) of the concerned bodies are automatically updated when particles are given to FLUKA for a new turn. This implementation also has the advantage that scoring meshes (e.g. for getting energy deposition results) can be associated to geometrical transformations and thus follow the movement of the object.

Bodies, scoring meshes and applied transformations must be already defined in the FLUKA input file. The user specifies in an external text file, processed by FLUKA at initialisation, the transformations to be changed run-time and how. Since translational and rotational speeds are specified, the user also has to declare the timing, i.e. the period of revolution of the beam in the ring. A relevant effort has been put in order to have an implementation as general as possible:

- there are no parameters related to the devices under study hard-coded in the involved subroutines;
- there is no limit in the number of transformations that can be modified;
- any arbitrarily complex movement can be declared, including multiple rotations about any axis.

### 3.1.3 Simulation Settings

FLUKA allows one to assign default values to relevant parameters. Different sets of default values are available to the user, grouped according to assumptions suitable for most common problems (for more information, see the FLUKA manual).

All the original results presented in this thesis produced with FLUKA have

been obtained with PRECISIO settings, which allow for the best accuracy in tracking at the expenses of reasonable CPU time. These settings include:

- transport of electrons, positrons and photons, implying the simulation of electromagnetic cascades. This also includes:
  - Rayleigh scattering and inelastic form factor corrections to Compton scattering and Compton profiles;
  - detailed photoelectric edge treatment and fluorescence photons;
- transport of low energy neutrons (i.e. below 20 MeV) down to thermal energies. This also includes fully analogue absorption;
- particle transport thresholds at 100 keV, except for neutrons, transported down to  $10^{-5}$  eV, and (anti)neutrinos, discarded by default;
- multiple scattering threshold at minimum allowed energy, for both primary and secondary charged particles;
- $\delta$ -ray production, with threshold at 100 keV (i.e. events of energy transfer lower than this threshold are assumed to take place as continuous energy losses);
- restricted ionisation fluctuations, for both hadrons and muons, and photons, electrons and positrons;
- ratio of tabulation of hadron and muon  $dp/dx$  set to 1.04; at the same time, the fraction of the kinetic energy to be lost in a step is set to 0.05, and the number of  $dp/dx$  tabulation points is set to 80;
- electron–positron pair production by heavy particles is activated with full explicit production;

- heavy particle bremsstrahlung with explicit photon production above 300 keV;
- muon photonuclear interactions with explicit generation of secondary particles;
- transport of heavy fragments.

Specific modifications to these defaults are reported in the concerned cases in Chaps. 4 and 5.

## 3.2 SIXTRACK

In the present section, a brief introduction to the SIXTRACK code is given, together with an insight into the online aperture check and the implementation of dynamic kicks, relevant for the results presented in this thesis about the existing scraping system (see Chap. 4) and its upgrade (see Chap. 5). In particular, after an overview of the code presented in Sec. 3.2.1, Sec. 3.2.2 introduces the online aperture check, responsible for determining if any beam particle being tracked touches the mechanical aperture of the machine and is thus lost. This functionality is extremely important, since it allows one to predict the loss position of any beam particle scattered on large amplitudes, allowing one to determine loss maps, and to correctly compute the energy deposition in the intercepting device during tracking, avoiding the re–interaction of lost particles. Section 3.2.3 gives an overview of the implementation of dynamic kicks in SIXTRACK, a brand new functionality I implemented in order to properly describe the rising of the magnetic bump during scraping with the upgraded system, relevant in particular for the estimation of energy deposition in the absorber.

### 3.2.1 Overview of the Code

SIXTRACK [49, 50, 51] is a code for simulating beam dynamics in circular accelerators. It is a single particle tracking code, i.e. each particle is treated independently of the rest of the bunch, hence without taking into account any collective effect. Turn by turn, particles are tracked through the whole accelerator lattice and their coordinates are modified according to the specific dynamics introduced by each element. SIXTRACK can deal with the whole six dimensional phase space (see Sec. A.1), i.e. the particle coordinates being modified during tracking are position and direction on the two planes transverse to the direction, and longitudinal position in the bucket and momentum, in case the longitudinal dynamics is activated.

The original purpose of SIXTRACK is to study the dynamic aperture in circular machines, i.e. to determine at which distance from the beam core the motion of particles starts to be unstable due to non linearities in the lattice structure of the accelerator. For this reason, the code is optimised to track couples of particles with slightly different initial coordinates over a large number of turns, to monitor where their dynamics start to diverge.

SIXTRACK needs two input files: the `fort.2` file, which specifies the machine lattice structure and the settings of the magnetic elements, and the `fort.3`, providing the code with the settings of the simulation. Both are plain text files. The former can be automatically generated by MADX [69], a code for optics design and optimisation largely used at CERN, whereas the latter is manually edited by the user.

### 3.2.2 Online Aperture Check

The online aperture check is a functionality native to SIXTRACK. This functionality is relevant for the results presented in Chaps. 4 and 5, since it is responsible

for determining if any beam particle being tracked touches the mechanical aperture of the machine and is thus lost. Hence, it allows one to predict the loss position of any beam particle scattered on very large amplitudes, allowing one to determine loss maps, and to correctly compute the energy deposition in the intercepting device during tracking, avoiding the re-interaction of lost particles.

I debugged the implementation in the official release of the code [79] and contributed to its further development. The modifications are stable but still in a private version [78] at the time of writing, waiting to be released. The implementation is as general as possible, and it can be applied to any machine simulated by **SIXTRACK**, as no aperture setting belonging to the machine is hard-coded in the source code, but it is declared by the user in the main configuration file of **SIXTRACK**, i.e. the `fort.3` file.

The user can assign an aperture to any non-drift element, including thin lens magnetic elements and markers specifically created. At each occurrence of the assigned element in the lattice structure, the check is performed after the new particle coordinates are computed. In case the particle falls outside of the aperture, it is labelled as lost, it is discarded from tracking, and its coordinates at the loss point are dumped in an output file. This file is then used for building an histogram with the losses along the ring, i.e. the loss map. New aperture types have been added to the native ones [77].

The point of loss is obtained finding the intersection between the particle trajectory and the current aperture type. For simplicity, the actual trajectory of the particle is not taken; on the contrary, the line connecting the updated particle coordinates and those at the previous aperture check is taken as particle trajectory. In case of tracking with a thin lens description of the accelerator lattice and with a sufficiently high density of aperture checks, this approximation can be regarded as satisfactory. Given the different types of aperture handled, the

bisection method is applied, to get the intersection between the particle trajectory and the current aperture type. Other functionalities like handling of offsets and tilts of the aperture types or interpolation over an aperture profile varying with the longitudinal coordinate are supported either [77], but have not been presented here, for the sake of brevity.

### 3.2.3 Dynamic Kicks

In order to properly take into account the rising of the magnetic bump for the upgraded scraping system analysed in Chap. 5, I implemented dynamic kicks [80, 81] in SIXTRACK, i.e. the possibility of changing turn by turn the magnetic setting of selected elements. This functionality has relevant consequences on values of energy deposition in the absorber of the upgraded SPS scraping system, as shown in Chap. 5.

The implementation [77] is based on modulating the kick of selected elements in the lattice structure of the accelerator turn by turn. At the beginning of each turn, the kick is updated and the new value used. The time profile of the kick is input via a plain text file. The user can specify just few relevant points of the profile, as a linear interpolation is performed. This approach gives full flexibility to the user, since any arbitrary profile can be input, and the granularity in its description can be non uniform, i.e. as refined as down to the single turn when rapid changes are to be described or very concise when the profile is smooth. The implementation has been made as general as possible, and it can be applied to any thin lens element in the lattice structure of any accelerator fed into SIXTRACK.

Figure 3.1 compares the closed orbit as simulated by SIXTRACK using dynamic kicks with the expected one, for an arbitrary modulation of the kick of the concerned bumpers (see Tab. 2.5). In particular, the comparison is focussed on the closed orbit on the horizontal plane at the centre of the absorber of the

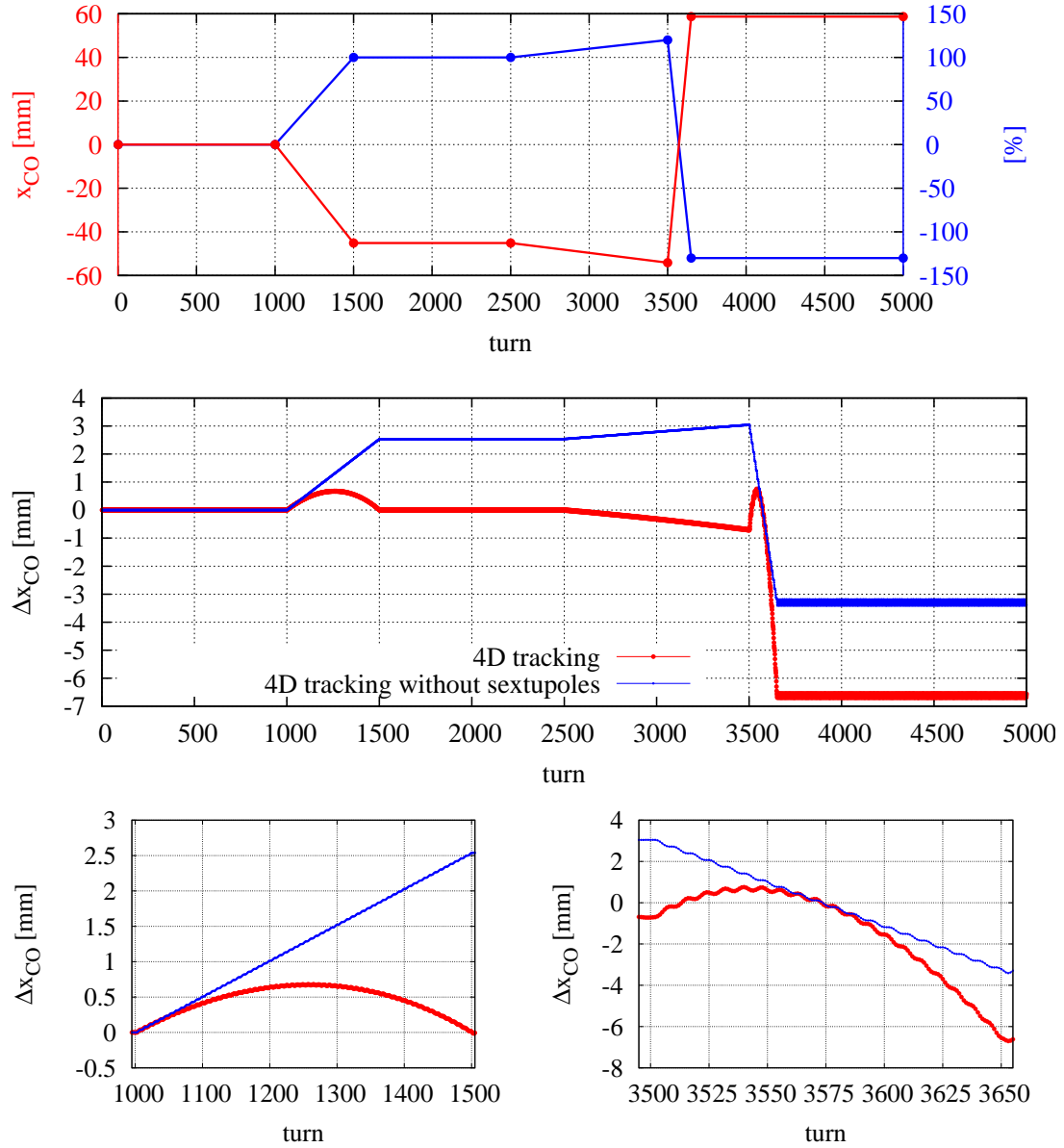


Figure 3.1: Upper frame: evolution of the closed orbit on the horizontal plane at the centre of the absorber of the horizontal upgraded SPS scraping system (red curve - see Tab. 2.4) as expected from an arbitrary modulation of the kick of the concerned bumpers (blue curve - see Tab. 2.5). Middle frame: difference between the horizontal closed orbit as obtained from SIXTRACK simulations with dynamic kicks and the expected one (i.e. the red curve in the upper frame), for two tracking settings. The case with 6D tracking is not shown, as it overlaps with the case of 4D tracking. Simulations have been performed tracking only the synchronous proton of 450 GeV/c. Lower frames: zooms of the curves shown in the middle frame on ranges of turns with a rapid variation of the kicks. Colour coding is the same as the one of the middle plot.

horizontal upgraded SPS scraping system (see Tab. 2.4). The upper frame shows the arbitrary modulation of the kicks fed into all the simulated cases and the expected evolution of the closed orbit, while the middle and the lower frames actually show the comparison (as difference plots). Different tracking settings have been explored, including 6D tracking, but this case is not shown as it overlaps with the case with 4D tracking.

The deviations from the desired closed orbit are not an artifact of the implementation, but are due to the presence of sextupoles in the LSS6, in the region of the magnetic bump (see Fig. 2.11). In fact, they are switched off, the kicks of the bumpers are not sufficient to reach the nominal value of the closed orbit, as the contribution from the sextupoles is missing. On the contrary, when sextupoles are switched on, the nominal value of the closed orbit is regularly reached when the bumpers are powered to their nominal kicks. Moreover, due to the fact that a sextupole introduces a net focussing effect if traversed on one side and a net defocussing effect if traversed on the other side (see Fig. 3.2), sextupoles introduce an asymmetry between positive and negative values of the closed orbit. In fact, when the bumpers are powered to 120 % of the nominal kick, the closed orbit reaches a value slightly larger than the expected one, as visible in Fig. 3.1 (middle frame). Conversely, when the bumpers are powered to  $-130\%$  of the nominal kick, the closed orbit reaches a value clearly lower than the expected one, as visible in the same figure.

Sextupoles are also responsible for another effect, visible in the lower frames of Fig. 3.1, zoomed on two ranges of turns where the kicks of the bumpers are ramped relatively quickly, with a speed of 0.2 % (left frame) and  $-2\%$  (right frame) of the nominal kick per turn. While the bumpers are linearly bumped, the closed orbit grows (or decreases) not linearly, since sextupoles have a non-linear field, and those sextupoles traversed by the beam off-axis contribute non-linearly

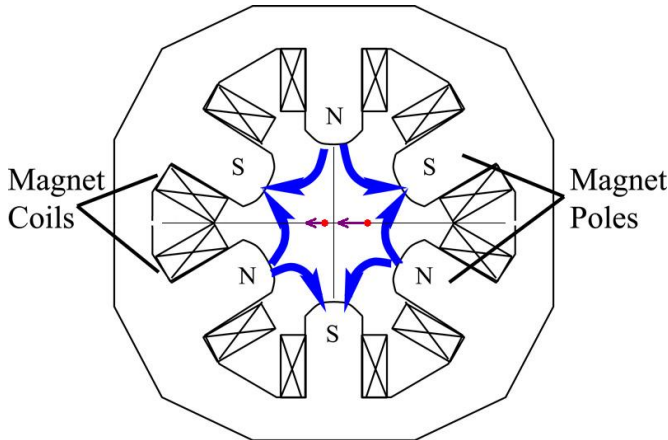


Figure 3.2: A typical cross section of a sextupole magnet. The magnetic configuration of the six poles is shown, together with the sign of the field lines. The two red dots represent two protons passing off-axis the sextupole, directed outwards of the paper. The purple arrows show the direction of the Lorentz force, which is the same no matter on which the side the proton passes, implying a net focussing effect when protons pass on one side, and a net defocussing effect when passing on the other side.

to the change in the closed orbit. When they are switched off, the change in the closed orbit is linear, even though it does not reach the expected values, since the contribution to the closed orbit from the sextupoles is not present. This effect impacts the time evolution of the beam intensity during scraping, as pointed out in Sec. 5.2.

It should be noted that all the aforementioned effects are independent from the type of tracking, i.e. 4D or 6D.

### 3.3 The Coupling Between FLUKA and SIXTRACK

Machine-protection studies are meant to estimate the radiation field in specific locations of an accelerator, and thus evaluate the effects on delicate components or nearby equipment, e.g. energy deposition and thermal load, dose, particle fluence, monitor signal, etc. . . In few cases of circular machines, especially when studies are focussed on cleaning systems, relevant processes may span over several

turns. Consequently, the beam dynamics in the accelerator (i.e. the betatron and longitudinal dynamics, see Sec. A.1) should be taken into account, and possibly embedded in the simulation, in order to properly describe, turn by turn, how beam particles impact the cleaning system (multi-turn effects).

The SPS scraping system, in its present installation and in its upgraded design (see Sec. 2.2), is a cleaning system in a circular accelerator. Given the length of the intercepting device, quantities relevant to its performance, in particular the energy deposition in the device and the time required for cleaning, are subject to multi-turn effects. For this reason, all the analyses presented in Chaps. 4 and 5 have been performed coupling the FLUKA MC code to the SIXTRACK tracking code for single particle beam dynamics.

In a coupled simulation, FLUKA and SIXTRACK run separately at the same time, and exchange particles through a network port while the simulation goes on. The FLUKAIO Application Programming Interface (API) [82] is responsible for providing the coupling with a communication protocol and for managing the flow of information between the two codes. An SVN repository [78] collects all the necessary ingredients for a coupled simulation, i.e. the FLUKAIO API, the modified version of SIXTRACK and the FLUKA user routines suitable for the coupling. Other additional pre- and post-processing tools are available either. Moreover, other tracking codes are collected in the same repository.

The most relevant asset of using FLUKA and SIXTRACK running coupled is the deployment of two codes with a long history of development and benchmarking. In fact, the reliable and refined physics models implemented in one are used for improving the results of the other one, and vice versa. Moreover, the flow of information, managed by the FLUKAIO API, is automatic, with the human intervention limited to the set-up of the simulation. In addition, the use of a network port for exchanging particle data drastically reduces the simulation time

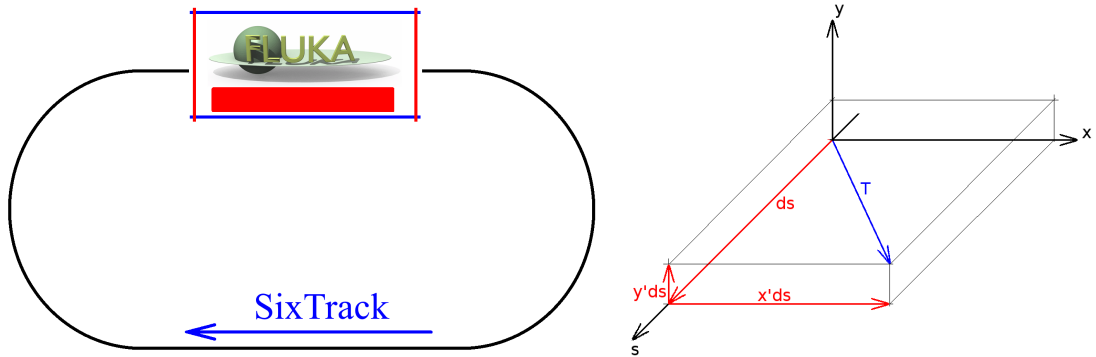


Figure 3.3: Left frame: SIXTRACK takes care of transporting beam particles throughout the accelerator lattice, whereas FLUKA takes over for the interaction of beam particles with intercepting devices. Right frame: schematics of how the direction of a particle is represented in SIXTRACK and in FLUKA.

with respect to writing/reading files, and saves space on disk.

### 3.3.1 Implementation Details

The portion of the accelerator lattice structure given in input to SIXTRACK, where the intercepting device of interest is located, is labelled for transport in FLUKA. Beam particles are transported turn by turn by SIXTRACK throughout the accelerator lattice, and whenever they reach the labelled section, they are transferred to FLUKA, transported in its 3D geometry for simulating the interaction with the accelerator components under study, and given back to SIXTRACK (see left frame of Fig. 3.3). At present, it is possible to label for coupling more than one location in the accelerator lattice structure.

One by one, particles are transferred from one code to the other one. In particular, the following data are transferred:

- ID of the particle and of its parent. The former is an index for the unique identification of the particle. In case secondary particles of the same type as the one of the beam, generated in the interaction with the intercepting device, are given back to SIXTRACK, they are assigned a new index; the

ID of the parent particle becomes thus meaningful, as it stores the ID of the beam particle which underwent the nuclear inelastic event. The double labelling is relevant to single diffractive protons, for instance, as they are treated as regular secondary particles by FLUKA;

- statistical weight. This is relevant for biased simulations in FLUKA. At the time of writing, this quantity is not used;
- $x$  and  $y$  particle coordinates. FLUKA and SIXTRACK use different units of measurement; as a consequence, a simple conversion between mm (used by SIXTRACK) and cm (used by FLUKA) is needed;
- the direction of the particle is represented in the two codes in different ways. In particular, FLUKA makes use of direction cosines, whereas SIXTRACK makes use of the longitudinal derivatives of the particle coordinates (see Sec. A.1) Thus, when transferring particles from SIXTRACK to FLUKA, the following conversion must be done (see right frame of Fig. 3.3):

$$T = \sqrt{1 + x'^2 + y'^2};$$

$$C_x = \frac{x'}{T}; \quad C_y = \frac{y'}{T}; \quad C_z = \frac{1}{T},$$

where  $C_x$ ,  $C_y$  and  $C_z$  indicate the direction cosines. On the way back, the following transformation is applied

$$x' = \frac{C_x}{C_z}; \quad y' = \frac{C_y}{C_z}.$$

It should be kept in mind that  $x'$  and  $y'$  in SIXTRACK are in units of  $10^{-3}$ , and this is automatically taken into account;

- mass number  $A$ , atomic number  $Z$  and mass of the particle  $m$ . The first two variables are relevant when simulating ion beams (still not possible at

the time of writing, but the communication protocol can already handle these pieces of information). A unit conversion on the mass is needed, as in SIXTRACK the mass is expressed in  $\text{MeV}/c^2$ , whereas in FLUKA the mass is expressed in  $\text{GeV}/c^2$ ;

- total energy of the particle. Values are subject to the same unit conversion as the one applied to the mass;
- longitudinal position. In SIXTRACK, this is stored in the lag with respect to the synchronous particle

$$\sigma = s - v_0 t, \quad (3.1)$$

where  $s$  is the length of a given element, i.e. the distance travelled by the synchronous particle at the speed  $v_0$ , and  $t$  is the time taken by the tracked particle to go through that same element along its own path. For each particle, the lag in space used by SIXTRACK is converted into a lag in time, to be used by FLUKA as initial value of the time of flight of the particle to be tracked through the geometry. The conversion comes directly from the definition of the lag (see Eq. 3.1), with  $s = 0$  and  $v_0 = c (p_0 c / E_0)$ , where  $p_0 c$  and  $E_0$  are momentum and total energy of the synchronous particle, and their ratio gives the relativistic reduced speed  $\beta_0$  of the synchronous particle. Units of measurements are mm in SIXTRACK and s in FLUKA, and they are taken into account in the conversion.

When this PhD activity started, it was possible to perform SIXTRACK–FLUKA coupled simulations only with 4D tracking in thick lens, even though most of the FLUKAIO API was ready. Throughout the PhD activity, I strongly participated in the development which made the coupling operational for all possible tracking configurations available in SIXTRACK, i.e. 4D, 6D and 6D with acceleration, with

a description of the accelerator structure either in thick or in thin lenses. While the coupling with thin lens tracking has been extensively used for producing the results shown in Chaps. 4 and 5, following the standard of LHC collimation studies [83], for 4D, 6D and 6D tracking with acceleration, the coupling with thick lens tracking has never been tested with a study case at the time of writing. Moreover, the studies presented in Chaps. 4 and 5 represent the first extensive application of the **SIXTRACK**–**FLUKA** coupling.

Figure 3.4 shows an example of evolution with time of the horizontal position and total energy of a beam proton during scraping at 450 GeV/c in the SPS with the existing system. The same evolution is also shown in the horizontal and longitudinal phase spaces. The data series changes from black to red following two elastic events taking place in two consecutive turns; they change from red to green following an event of Rutherford scattering, with a relevant deflection of the particle, which blows up the single particle emittance (see Sec. A.1); they finally change from green to blue following an ionisation event with relevant energy loss, such that the proton leaves its original bucket and starts debunching, since its momentum offset is out of the SPS RF acceptance (see Sec. 2.1.2).

To date, the **FLUKA**–**SIXTRACK** coupling cannot handle particles different from protons and electrons, the only ones tracked by **SIXTRACK**. Particularly relevant for ions, there is no explicit dependence of the kicks imparted by the active elements along the lattice structure of the accelerator on the charge and mass of the tracked particle. Development is on going at CERN [84] to overcome this limitation, and thus allow detailed collimation studies in case of ion beams. Moreover, unstable particles cannot be tracked either, since no decay process is implemented in **SIXTRACK**.

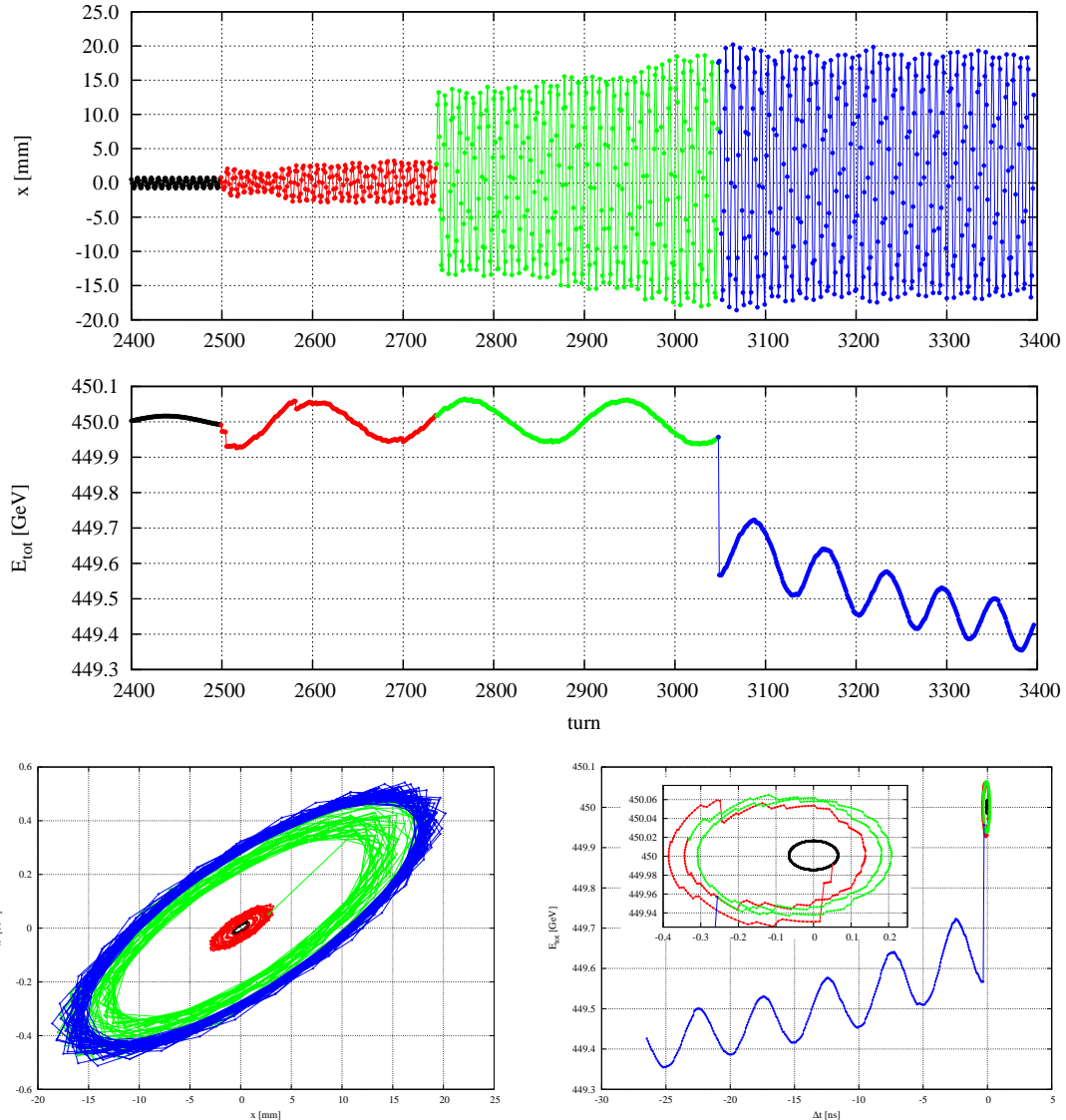


Figure 3.4: Example of evolution of the horizontal position (upper frame) and total energy (middle frame) of a beam proton during scraping in the SPS. The lower frames show the same evolutions as seen in the horizontal phase space (left frame) and in the longitudinal phase space (right frame). In this last plot, a zoom on the dynamics of the beam particle before debunching is also shown. The data series changes from black to red following two elastic events taking place in two consecutive turns; they change from red to green following an event of Rutherford scattering, with a relevant deflection of the particle, which blows up its single particle emittance; they finally change from green to blue following an ionisation event with relevant energy loss, such that the proton leaves its original bucket and starts debunching. Results are obtained when simulating the horizontal blade of the BSHV.11771 scraper, in graphite, swept through the beam at  $0 \sigma$  (see Sec. 4.1), with a speed of 80 mm/s.

## 3.4 Ancillary Tools

In order to perform the simulations required for the analyses presented in this thesis, a couple of ancillary tools are needed, i.e. the Line Builder (LB) and the FLUKA Element DataBase (FEDB), presented in Sec. 3.4.1, and a dedicated routine for sampling the beam to be tracked in a SIXTRACK–FLUKA coupled simulation, presented in Sec. 3.4.2.

The LB and the FEDB are required to assemble the FLUKA geometry used in Sec. 4.3.5 for the evaluation of the BLM signals during scraping. In fact, the LB and the FEDB allow one to easily generate the FLUKA input file whenever an accelerator beam line made of several devices is required, since the geometry is automatically built starting from the machine optics and the geometry model of each family of device to be used. This is a desirable feature, especially when the design of a system to be installed on a beam line can envisage modifications to the beam line itself, or when the orbit is not constant along the beam line, as it happens in the case of the SPS–to–LHC TLs.

The beam sampling routine dedicated to the SIXTRACK–FLUKA coupling has been developed to fully decouple the generation of the beam to be simulated and the actual tracking; indeed, it is a routine external to both FLUKA and SIXTRACK. In this way, when comparing two cases different for any other setting but for the optics, the same exact beam can be used. Moreover, since it is possible to couple FLUKA to other tracking codes, the use of an external generator allows for direct inter–comparisons of different codes, using the same exact beam distributions. This sampling routine has been used for generating the beams simulated in Chaps. 4 and 5.

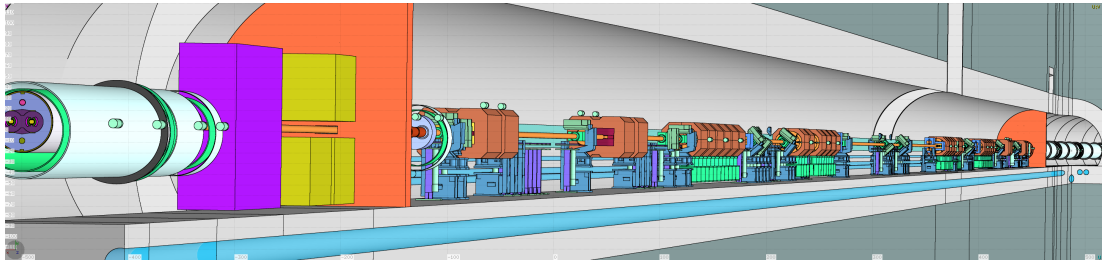


Figure 3.5: A 3D rendering with Flair of the FLUKA geometry of the LHC LSS7, hosting the betatron cleaning system [53].

### 3.4.1 The Line Builder and the FLUKA Element DataBase

The LB and the FEDB [52, 53] are tools used at CERN for the generation of complex and sophisticated FLUKA geometries of accelerator beam lines, especially for LHC and its collimation system (see a 3D rendering with Flair of the FLUKA geometry of the LHC collimation system, for instance). The FEDB is a collection of FLUKA geometries of accelerator devices, e.g. magnets, collimators, etc... The LB is a `python` program I wrote before starting this PhD activity, responsible for the generation of the FLUKA geometry of the beam line to be simulated, starting from the machine optics, the models defined in the FEDB and specific directives from the user. Magnetic fields, scoring detectors for getting simulation results, and other operational settings (e.g. opening of collimators) are automatically synchronised with the machine optics and the beam energy. The beam pipe is automatically built based on directives from the user, and the beam line can be automatically inserted into the geometry of tunnels.

The combination of these two tools has several assets:

- full synchronisation of the final FLUKA input file with the machine optics.

In addition, users are less concerned with the precise positioning of the elements along the beam line, extremely error prone in case of small bend or tilt angles (which might occur in TLs, for instance), and their magnetic settings, automatically assured. Moreover, comparisons between different

optics can be easily set up;

- when preparing the input for the FLUKA simulation, the user modifies many small files, easy to be handled, instead of the large text file containing the entire beam line, automatically generated by the LB just before starting the simulation. This is a method less prone to bugs in the declaration of all the ingredients necessary to the FLUKA simulation. Moreover, follow-ups in the geometry description of elements can be instantaneously propagated;
- enhanced portability of the FLUKA geometry of beam line elements.

Most of the elements coded in the FEDB belong to the LHC. Thus, I implemented the vast majority of the elements required for the benchmark of the FLUKA–SIXTRACK coupling against BLM signals presented in Sec. 4.3.5, namely: the main quadrupoles installed in the LSS1, i.e. QFA and QDA; all the kickers in the LSS1, i.e. MKP, MKPA and MKPC; the orbit correctors MDH and MDV, and the beam position monitors BPH and BPV; the BLMs; the beam–intercepting devices, i.e. TIDVG and TIDH; the LOE octupole. I also prepared a simplified 3D tunnel of the SPS LSS1, since its presence is relevant for the estimation of the BLM signals.

### 3.4.2 Beam Sampling

The beam sampling routine is a routine available in the SVN repository of the coupling [78], and it is responsible for sampling the beam to be tracked. The sampled beam is matched to the optics functions at the specific element of choice in the accelerator lattice structure. Since the repository contains other single particle tracking codes for beam dynamics, the beam sampling is performed by an external generator; in this way, inter–comparisons of codes or of cases can be performed starting from the same exact beam distribution. The coordinates of

the sampled particles are dumped in a text file, which is loaded by the tracking code at the beginning of the simulation.

All the necessary input is provided to the routine via a configuration file. The user is given quite some flexibility in the choice of the beam to be sampled [77], as different types of distributions are available, and can be used at the same time on different planes. Moreover, cutting algorithms for sampling only the tails or the core of the beam are at the user disposal. Offsets can be added to particle coordinates, to take into account possible bumps in the closed orbit.

The sampling algorithm is based on the fact that, according to linear accelerator physics [41, 65], the betatron and the synchrotron contributions to the coordinates of beam particles are independent from each other, and they can be summed together (see Eqs. A.2 and A.3). Moreover, sampling starts from normalised distributions, and then the normalised coordinates (see Sec. A.3) are transformed into particle coordinates (only betatron contribution) using the inverse of the Floquet's transformations (see Eqs. A.14 and A.15), i.e.

$$z_\beta = \xi \sqrt{\epsilon \beta};$$

$$z'_\beta = (\xi' - \xi \alpha) \sqrt{\frac{\epsilon}{\beta}},$$

where  $z_\beta$  and  $z'_\beta$  are the real particle coordinates,  $\xi$  and  $\xi'$  the normalised ones,  $\beta$  and  $\alpha$  the Twiss parameters (see Sec. A.1), and  $\epsilon$  the geometrical emittance (see Sec. A.4).

Concerning the contribution to particle coordinates from synchrotron motion, the relative momentum offset  $\delta$  (see Eq. A.1) is first sampled, and then the momentum of the particle is given by

$$p = (1 + \delta \sigma_\delta) p_0,$$

where  $\sigma_\delta$  is the rms value of the normalised momentum offsets (see Sec. A.2). As already mentioned, the contribution from synchrotron motion to the particle coordinates is added to the betatron contribution, following Eqs. A.8 and A.9.

When sampling independently on the three phase spaces, i.e. horizontal, vertical and longitudinal, particle coordinates are sampled in couples, i.e.  $x$  and  $x'$ ,  $y$  and  $y'$ ,  $pc$  and  $\sigma$ . Thus, the sampling is inherently bi-dimensional. In the case of the longitudinal plane, the 2D sampling (not presented here) is valid only in case of longitudinal emittances much smaller than the bucket area, as the implementation is valid only for small amplitude oscillations in the longitudinal phase space. Otherwise, as done for the cases studied in Chaps. 4 and 5, the value of the lag with respect to the synchronous particle (see Eq. 3.1, for instance) must be set to 0, and sampling is performed on the longitudinal plane only in momentum.

Throughout the PhD activity, I contributed to the development of this routine. In the following, one of the original contributions is reported, i.e. the sampling of double Gaussian distributions, as the beam in the SPS has been operationally found to be distributed accordingly (see Fig. 4.37).

## Sampling Double Gaussian Distributions

The beam at flat top in the SPS can be described by a double Gaussian distribution (see Sec. D.2.1) on both transverse planes. This has been proven by beam scans obtained with the SPS scrapers, as those in Fig. 4.37, which show that the amount of beam scraped  $I_S(R)$  as a function of the blade position  $R \sigma_\beta$  (where  $\sigma_\beta$  is the rms beam size, restricted to the betatron contribution only, see Sec. A.2) can be expressed as (see Eqs. D.3 and D.14)

$$I_S(R) = I_1 \exp \left[ -\frac{R^2}{2f_1^2} \right] + (1 - I_1) \exp \left[ -\frac{R^2}{2f_2^2} \right]. \quad (3.2)$$

This expression is the linear combination of two 2D Gaussian distributions, each different from the normal distribution by the magnification factors  $f_1$  and  $f_2$  of the standard deviations (otherwise unitary), and the presence of the weight  $I_1$  applied to the first Gaussian, and its complement to 1, applied to the second Gaussian. The normalised betatron amplitude (see Eq. A.16) of particles in the beam is distributed accordingly (see Eq. D.13), corresponding to a probability density function (pdf) in horizontal position  $x$  (for instance) as

$$\text{pdf}_\beta(x) = \frac{I_1}{2\pi(f_1\sigma_\beta)^2} \exp\left[-\frac{x^2}{2(f_1\sigma_\beta)^2}\right] + \frac{(1-I_1)}{2\pi(f_2\sigma_\beta)^2} \exp\left[-\frac{x^2}{2(f_2\sigma_\beta)^2}\right]. \quad (3.3)$$

In order to perform the sampling according to Eq. 3.2, the Box–Muller algorithm [85] is used to get a couple of coordinates distributed according to a 2D normalised Gaussian distribution. Afterwards, the sampled normalised coordinates are multiplied by  $f_1$  for an average of  $I_1$  times and by  $f_2$  for all the other times, to get to the actual double Gaussian distribution.

The Box–Muller method [85] allows one to map a couple of random numbers  $u_1$  and  $u_2$ , sampled independently from a uniform distribution over [0:1), into a couple of random numbers  $\xi$  and  $\xi'$ , distributed according to a 2D Gaussian distribution centred in the origin of the 2D space with variance 1 as

$$\begin{aligned} \xi &= \sqrt{-2 \ln u_1} \cos(2\pi u_2); \\ \xi' &= \sqrt{-2 \ln u_1} \sin(2\pi u_2). \end{aligned}$$

As it can be seen, the sampled numbers can be regarded as polar coordinates sampled according to a 2D Gaussian distribution.  $u_1$  is used to sample the module of the couple of polar coordinates, whereas  $u_2$  is used to sample the angular phase.  $\xi$  and  $\xi'$  are thus taken as the normalised betatron coordinates, and the corresponding normalised betatron amplitude  $n$  is given by Eq. A.16.

In case the desired range of values of the normalised betatron amplitude is restricted to tails outside  $n_{\min}$ , i.e.  $n \in [n_{\min} : \infty)$ , the sampling is slightly modified as follows:

- values larger than  $n_{\min}$  are obtained modifying the expression of the amplitude sampled by the Box–Muller method from  $\sqrt{-2 \ln u_1}$  to  $\sqrt{-2 \ln u_1 + n_{\min}^2}$ .

This is due to the fact that, in order to sample  $n \in [n_{\min} : \infty)$ , the uniform random number must be sampled in the range  $[0 : e^{-\frac{n_{\min}^2}{2}}]$ ;

- the discrimination in the use of the first or the second Gaussian is based not only on  $I_1$ , but also on the integrals of each Gaussian component on the sampling interval, i.e.  $[n_{\min} : \infty)$ . The new discriminator  $J$  is thus obtained with the following steps

$$\begin{aligned} J_1 &= I_1 \int_{n_{\min}}^{\infty} \frac{n}{f_1^2} \exp \left[ -\frac{n^2}{2f_1^2} \right] dn = I_1 \exp \left[ -\frac{n_{\min}^2}{2f_1^2} \right]; \\ J_2 &= (1 - I_1) \int_{n_{\min}}^{\infty} \frac{n}{f_2^2} \exp \left[ -\frac{n^2}{2f_2^2} \right] dn = (1 - I_1) \exp \left[ -\frac{n_{\min}^2}{2f_2^2} \right]; \\ J &= \frac{J_1}{J_1 + J_2}. \end{aligned}$$

The biased sampling here summarised has been used for the results shown in Sec. 4.3.4, whenever regular scraping has been simulated, and thus the sampling of the beam to be tracked is focussed only on the beam tails, to save CPU time.

## 3.5 Conclusions

In this chapter, the simulation tools used for the analyses presented in Chaps. 4 and 5 have been briefly introduced. Relevant modifications to existing codes made by me have been reported either.

The tool mainly used is the coupling between FLUKA and SIXTRACK. FLUKA

is the MC code for simulating the interaction of the beam with the intercepting devices under study, whereas **SIXTRACK** is the tracking code for describing the beam dynamics in the SPS. In fact, the scraping system, both in its existing installation in the SPS and in its upgraded design, is a cleaning system in a circular machine, and it is subject to multi-turn effects. In order to properly take them into account, **FLUKA** and **SIXTRACK** have been coupled, to include the appropriate beam dynamics in the simulation.

In the context of this PhD activity, I have modified both **FLUKA** and **SIXTRACK** to add functionalities relevant to the studies presented in the next chapters. In particular:

- the possibility of moving portions of the **FLUKA** geometry. This is fundamental for a proper evaluation of the energy deposition in the SPS scrapers and the time required for scraping, shown throughout Chaps. 4 and in Sec. 5.1;
- I substantially contributed to the debugging of the online aperture check native to **SIXTRACK**, and to its further development. This feature is fundamental for the analyses presented in Chaps. 4 and 5, as it allows one to remove beam particles scattered by the intercepting devices on orbits leading to a loss in the machine; consequently, energy deposition results, time profile of the beam intensity while scraping and losses induced in the ring can be properly estimated;
- I implemented dynamic kicks in **SIXTRACK**, i.e. the possibility of changing the magnetic settings of selected elements in the accelerator ring. This implementation allows one to properly simulate the rising of the magnetic bump on which the design of the upgraded scraping system is based, and thus properly estimate energy deposition results, time profile of the beam intensity while scraping and losses induced in the ring.

I also contributed to the development of the coupling between **SIXTRACK** and **FLUKA**, and the results presented in Chaps. 4 and 5 represent its first extensive use and benchmark.

The LB and the FEDB, tools widely used at CERN for defining complex and sophisticated **FLUKA** geometries of accelerator beam lines, have been used to generate the **FLUKA** geometry used for the benchmark of the **SIXTRACK**–**FLUKA** coupling against measured BLM signals (see Sec. 4.3.5).

I have extended the routine for sampling the beam to be tracked in a **SIXTRACK**–**FLUKA** coupled simulation. Most relevant to the results shown in Chap. 4, the sampling of double Gaussian beams have been added, as the beam in the SPS has been operationally found to be distributed accordingly.

All the code development has been carried out with the most general approach possible, allowing the re-use of all the new features here described to other rings and devices. Indeed, all the modified codes are available in the **SVN** repository of the coupling [78].

# Chapter 4

## Characterisation of the Existing SPS Scraping System

A clean beam injection is fundamental for the LHC operation, otherwise the quench of SC magnets may occur immediately at injection, preventing the regular operation of the LHC, even before beam acceleration. The SPS scrapers are the devices designed at halo cleaning during beam injection into the LHC (see Sec. 2.2). The existing system (see Sec. 2.2.1) is a multi-turn cleaning system, ensuring full phase-space coverage, consisting of two graphite blades, one per plane of cleaning, swept through the beam to remove tails.

The present chapter characterises the performance of the existing system, to highlight its assets and liabilities. The outcomes will then be used in the next chapter to compare the existing system to the one proposed for upgrade, to show how the new design can improve endurance and performance. The new system (see Sec. 2.2.2) has been proposed in view of the upgrade of the LHC luminosity (see Sec. 1.3); by design, it has a series of assets over the existing one (Sec. 2.2.3), addressed with this comparison.

The characterisation of the existing system is carried out in terms of:

1. energy deposition in the active material responsible for tail removal. This is relevant for the estimation of the induced thermal loads and stresses;
2. time evolution of the beam intensity during scraping. This is used to assess the typical time-scales required to accomplish scraping;
3. pattern of losses induced in the ring. This is used to identify locations with high losses, leading to possible ageing of the insulation in magnet coils or material activation.

The analyses are performed by means of numerical simulations, combining **SIXTRACK**, a code for particle tracking in accelerator lattices (see Sec. 3.2), with **FLUKA**, a Monte Carlo code (see Sec. 3.1). The former is used to simulate the dynamics of the beam in the SPS, whereas the latter is used to simulate the interaction of the beam with the scraper blades. The combination of the two (see Sec. 3.3) is necessary, as the analysed device is a multi-turn cleaning system, implying that any estimation related to cleaning must take into account the dynamics of the beam in the accelerator. Moreover, the distance between the beam closed orbit and the blade changes with time during scraping, due to the blade sweeping. This must be taken into account in the simulation, since it affects the estimation of the energy deposition in the blade and the time evolution of the beam intensity during scraping. For this reason, the possibility of moving portions of geometry has been implemented in **FLUKA** (see Sec. 3.1.2) and used in the simulations.

Interest in the existing scraping system is related not only to its characterisation in view of the comparison with the upgraded design, but also to the benchmark of the **FLUKA**–**SIXTRACK** coupling. An endurance test of the scraper blades has been carried out, to verify the levels of energy deposition predicted by the simulation. Moreover, this test, and its setup, also provided the opportunity to compare the time profile of the beam intensity during scraping and the

proton losses predicted by the simulation against measurements from the SPS monitors. The results presented in this chapter are the first benchmark of the FLUKA–SIXTRACK coupling against measurements.

The chapter is divided in three main parts. Section 4.1 gives an overview of past estimations [54] about the original scrapers installed in the SPS LSS5. I performed those studies in 2010 (i.e. before starting this PhD), to support the exchange of the blades from the original ones in copper to the new ones in graphite (see Sec. 2.2.1). In fact, those studies show that, even though copper achieves cleaning faster than graphite, graphite blades are preferable over the copper ones, since they are more robust.

Section 4.2 updates and completes the picture given in the preceding section with new results. Starting from 2011, the operational scrapers are those installed in the SPS LSS1, and the Q20 optics became operational in 2012 (see Sec. 2.1.1). The main outcomes of the previous section are confirmed, and further cases presented, showing the effects on the observables of interest when more realistic machine settings are considered in the simulations, such as the presence of the permanent magnetic bump in the SPS LSS1 (see Sec. 2.1.3), and the fact that scraping is performed at the end of the ramp (see Sec. 2.1.4). A sensitivity analysis on the tilting of the blade is given at the end. Contrary to the preceding one, this section deals entirely with original contributions for this thesis.

Section 4.3 presents the results of the “burst test”, the aforementioned endurance test of the scraper blades. During the test, the blades were put under stress associated with the worst conditions predicted by the simulation. Afterwards, the blades were analysed using a Scanning Electron Microscope (SEM). A change in the material porosity was found, confirming the high levels of energy deposition predicted by the simulation. The endurance test and its setup also gave the opportunity to compare the time profile of the beam intensity during

scraping and the proton losses predicted by the simulation against measurements from the SPS monitors. It should be noted that, while the burst test was proposed and carried out by colleagues responsible for the operation of the SPS and the microstructural analyses of the blades were carried out by colleagues expert in material structural analysis, my original contribution for this thesis includes: the full analysis of the monitor readouts; the running and analysis of the simulations required for the benchmark; the comparisons between simulation results and measured data; the realistic reconstruction of the beam distribution in machine, the actual operational settings of the blades, the amount of scraped beam and levels of energy deposition in the blades during the burst test. Section 4.4 draws conclusions.

Results given in the present chapter always refer to either a proton in the beam or a train of Nominal LHC bunches, i.e.  $1.15 \cdot 10^{11}$  protons per bunch and 288 bunches (see Tab. 1.5). Error bars in results from FLUKA, when visible, refer only the statistical error. Finally, evaluations of energy deposition and temperature increase are performed using adiabatic assumptions, i.e. without simulating heat diffusion during the scraping process. As reasonably expected, this assumption gives slightly overestimated results, which can be regarded as conservative.

## 4.1 Overview of Past Investigations

In 2010, I performed a set of simulation studies [54] supporting the exchange of the blades of the original scrapers, i.e. the BSHV.51659 (this is their optics name in the lattice structure of the accelerator, see Fig. 2.8), from copper to graphite (see Sec. 2.2.1). The aim of the study was to prove that graphite is preferable as blade material, since it is more robust than copper, and thus more suitable for regular operation, especially in view of the high beam currents of the Nominal

and Ultimate LHC beams (see Tab. 1.5). The outcome of these studies forms the basis of the deployment of graphite blades in the scrapers installed in the LSS1, regularly used during injection since 2011 (see Sec. 2.2.1).

The main plots and results from the studies from 2010 are reported here, and are intended as a starting point for the original studies presented in the rest of the chapter. In particular, the advantages in using graphite over copper as blade material are stressed, as far as robustness is concerned. Moreover, results show the dependence of the energy deposition on the scraping position, proving that scraping with the edge of the blade at the centre of the beam distribution (hereafter referred to as “full beam scraping” or “ $0 \sigma$  scraping”) is the setting which maximises the load on the blades. For this reason, it was decided to perform the “burst test” (i.e. the test for verifying the endurance of the blades, see Sec. 4.3) with this setting, in order to maximise the stresses on the blades.

In these studies, a copper blade, 3 cm in length, is compared to a shorter one, 1 cm in length, made of graphite. Given the length of the blades and the radiation lengths of the materials (i.e. 1.44 cm and 23.3 cm for copper and graphite, respectively, see Tab. 1.6), the copper blade is expected to be subject to the development of the EM cascade much more than the graphite one. Expected peak energy deposition values are thus higher in copper than in graphite. This is still true even though the density of scattering events is higher in graphite than in copper. The higher density of scattering events is due to the shorter length of the blade, meaning that more passages are needed through the graphite blade than a copper blade to attenuate beam particles because of the inelastic scattering, thus piling up the contribution from ionisation per turn.

### 4.1.1 Simulation Settings

The simulations in 2010 were performed by coupling FLUKA to ICO SIM [86, 87] and not to SIXTRACK, as done for the analyses presented in the rest of the thesis. ICO SIM performs single particle tracking through accelerator lattice structures described by thick lenses, and, at the time of the simulations, it could perform only 4D particle tracking, i.e. with no longitudinal motion. The potential impact of this limitation has not been evaluated for the analysed cases, either at the time of the studies or in the present chapter. Nevertheless, Sec. 5.2 shows the effect of 6D tracking in SIXTRACK over the 4D one, in the case of the upgraded scraping system. The effects are lower peak energy deposition values, since transverse positions of protons at impact on the absorber are diluted, and slightly faster scraping, since orbit ellipses in phase space are brought on the side of the absorber by the longitudinal motion (see Sec. A.3). The same effects can be expected for the blades of the existing system. Transverse dynamics could be simulated up to sextupoles, taking into account chromatic effects as well. The aperture check, for detecting losses and determining loss locations, is performed online during tracking, at the beginning and end of each element in the lattice structure. In case a beam particle falls outside of a given aperture, a linear interpolation is performed, to improve the estimation of the loss location, even when this happens to be inside a magnetic element. Protons of any energy above the FLUKA transport threshold are given back to ICO SIM to be further tracked in the accelerator lattice.

The thick lens model of the SPS lattice structure was used, loading the Q26 optics (see Sec. 2.1.1), as this was the one used for accelerating LHC beams at the time of the studies. The aperture model of the machine is taken from the MADX database on `afs`, likewise for the lattice structure and optics. The modelled scrapers are the original ones installed in the SPS LSS5.

plane	type	$\epsilon_N$ [ $\mu\text{m}$ ]	$\sigma_\delta$ []
hor	Gaussian 2D	3.5	-
ver	Gaussian 2D	3.5	-
lon	Gaussian 1D	-	$10^{-3}$

Table 4.1: Parameters describing the beam sampled and tracked: plane (first column), distribution type (second column), normalised emittance (third column), rms relative momentum offset (fourth column).

The FLUKA geometry consists only of the scraper blade, 1.2 cm wide in both transverse directions, whereas the length was set according to the blade material. Both copper and graphite blades, 3 cm and 1 cm in length respectively, were considered. The main physical properties of these two materials and the quantities most relevant to radiation–matter interactions are listed in Tab. 1.6. The nominal speed of the blade considered in these studies was 20 cm/s, with a couple of cases with graphite blades moving at 3 cm/s. PRECISIO settings were used (see Sec. 3.1.3), with their default transport thresholds, except for photons, where the threshold was lowered to 10 keV. Single Coulomb scattering was switched on near boundary crossings, to better describe the exit angle of beam particles which do not undergo any nuclear interaction in the blade. A Cartesian mesh covering the whole scraper blade was used for the estimation of the energy deposition in the blade, with a bin size of 100  $\mu\text{m}$  on both the horizontal and vertical transverse dimensions, and 1 mm on the longitudinal one.

The tracked beam was given a Gaussian distribution on both transverse planes, matched to the machine linear optics and with a normalised emittance of 3.5  $\mu\text{m}$ . The sampling routine native to ICO SIM was used. The effects from the momentum spread of the beam were addressed as well, considering a Gaussian distribution of momenta with an rms relative momentum offset  $\sigma_\delta = 0.001$  (see Sec. A.2). All the simulations have been performed for an average beam momentum of 450 GeV/c. Three scraping positions were simulated, namely 0  $\sigma$ ,

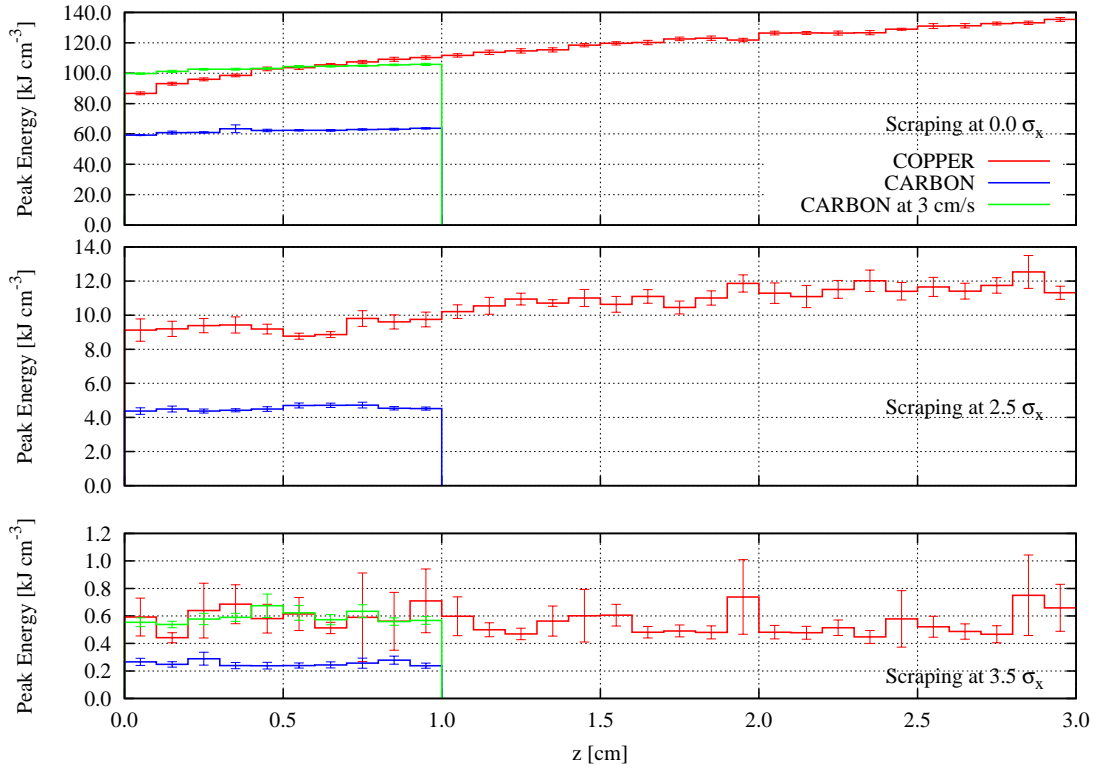


Figure 4.1: Peak energy deposition in the SPS scraper blades when scraping at  $0\sigma$  (upper frame),  $2.5\sigma$  (middle frame) and  $3.5\sigma$  (lower frame), as from the studies performed in 2010 [54]. The curves for copper and graphite are shown. The speed of the blades is 20 cm/s, unless explicitly indicated. Results are obtained simulating the horizontal blade of the BSHV.51659 scraper, and are scaled to a total beam intensity of  $3.312\ 10^{13}$  protons.

$2.5\sigma$  and  $3.5\sigma$ , where  $\sigma$  is the betatron contribution to the rms beam size (see Sec. A.2). The scraping positions refer to the distance between the edge of the blade and the centre of the beam core. Results are always normalised to a train of 288 bunches of the Nominal LHC beam, i.e. with  $1.15\ 10^{11}$  protons (see Tab. 1.5), for a total intensity of  $3.312\ 10^{13}$  protons, unless explicitly stated. Table 4.1 summarises the parameters of the beam distribution sampled and tracked.

### 4.1.2 Results

Figure 4.1 shows the longitudinal pattern of the peak energy deposition in the SPS scraper blades, comparing copper and graphite as blade materials. Different

material	limit [kJ cm <sup>-3</sup> ]
graphite	12.8
copper	5.8

Table 4.2: Ultimate limits of local energy deposition in graphite and copper considered in the present work (see App. B for their calculation). The values reported here represent the heat necessary to locally reach the sublimation temperature at atmospheric pressure in graphite, and to locally melt copper, and they are meant just for reference.

scraping positions and speeds are shown. In general, the peak energy deposition in graphite is lower than in copper for the same blade speed, no matter the scraping position, with an overall gain on the maximum value between 2 and 3. This is mainly due to the fact that copper has a density and an atomic number greater than graphite. Moreover, the copper blade is longer than the graphite one; consequently, the pattern of energy deposition reflects the development of secondary particle showers. In fact, the longitudinal pattern of the peak energy deposition in copper shows an increasing trend (even though not too steep), which is typical of the first stages of development of secondary particle showers, especially the EM component. Indeed, if the peak energy deposition was mainly determined by ionisation of beam particles, a decreasing trend would be visible, reflecting the attenuation of the beam particles by inelastic scattering.

No matter the scraping position, values of peak energy deposition in graphite increase when lowering the speed to 3 cm/s, and values of energy deposition similar to those found in the copper blades swept at the original speed are found. Indeed, as the speed of the blade decreases, a smaller volume of the blade sees new beam turn after turn, resulting in a higher concentration of scattering events. The scaling with the speed is sub-linear.

The absolute values shown in Fig. 4.1 should be compared to ultimate limits

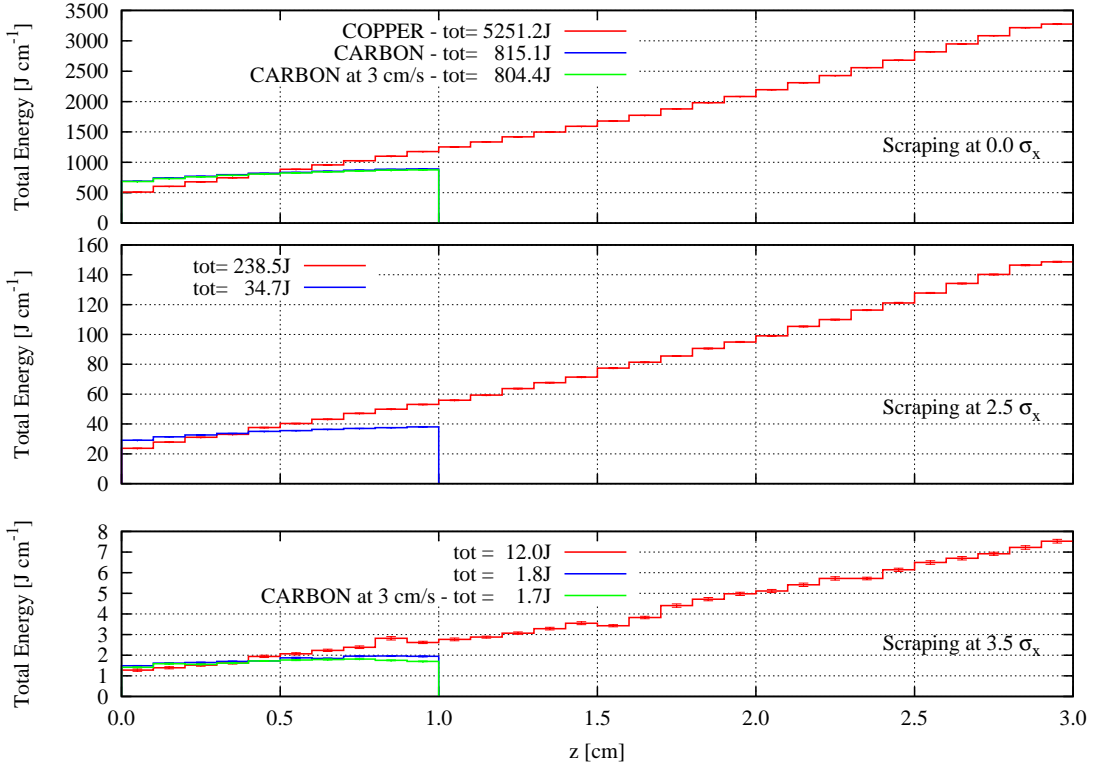


Figure 4.2: Total energy deposition in the SPS scraper blades when scraping at  $0\sigma$  (upper frame),  $2.5\sigma$  (middle frame) and  $3.5\sigma$  (lower frame), as from the studies performed in 2010 [54]. The curves for copper and graphite are shown. The speed of the blades is 20 cm/s, unless explicitly indicated. Results are obtained simulating the horizontal blade of the BSHV.51659 scraper, and are scaled to a total beam intensity of  $3.312 \cdot 10^{13}$  protons.

of energy deposition. These are listed in Tab. 4.2 (see App. B for their calculation), and they represent the heat necessary to start sublimating graphite and locally melt copper. Comparing the values shown in Fig. 4.1, which are obtained considering the full intensity of Nominal LHC beams in SPS, against the ultimate limits, it can be seen that both copper and carbon can stand the heat loads induced when scraping at  $3.5\sigma$ , whereas already at  $2.5\sigma$  peak values of energy deposition in copper are above the limits while values in graphite are still acceptable. In case of full beam scraping, i.e. at  $0\sigma$ , neither material can stand the heat loads, as peak values of energy deposition are above the limits.

Figure 4.2 shows the longitudinal pattern of the total energy deposition in

the SPS scraper blades, for the cases already shown. These profiles have been obtained integrating over the two transverse directions the values from the same mesh as the one used for estimating the peak energy deposition, whereas the values reported in the key of the plot have been obtained integrating also over the longitudinal dimension.

The pattern of copper shows a clear increasing trend, typical of the development of secondary particle showers in the medium, as already mentioned for the longitudinal pattern of the peak energy deposition. On the contrary, the trend for graphite remains almost flat. There is almost no difference in the values for graphite when changing the blade speed.

It should be noted that the total energy deposition in the blade is not paramount for the assessment of its robustness, even though it is important for a complete characterisation of the device. In fact, thermomechanical stresses, related to the integrity of the device, induced by the energy deposition are in general more sensitive to peak values and gradients rather than to the total amount of energy absorbed.

Figure 4.3 shows the scaling of the maximum and total energy deposition in the blade with the scraping position. While the points represent the results from the simulations, the solid lines show a possible scaling of  $0 \sigma$  values, based on the number of scraped protons. The total number of protons  $I_S(R)$  scraped off by the blade when set at  $R \sigma$  from the beam centre is given by the integral of the beam distribution over normalised betatron amplitudes (see Sec. A.3) larger than  $R$ , as given by Eqs. D.2 (the synchrotron part has been omitted) and D.3. In case of a Gaussian distribution,  $I_S(R)$  is (see Eq. D.10)

$$I_S(R) = \exp \left[ -\frac{R^2}{2} \right]. \quad (4.1)$$

The maximum value of energy deposition in the blade does not scale with the

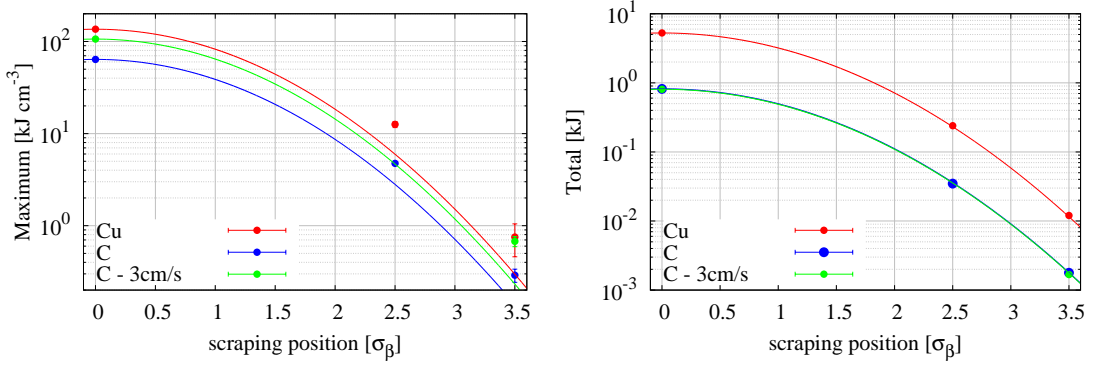


Figure 4.3: Scaling of the maximum (left frame) and of the total (right frame) energy deposition in the blade of the SPS scrapers with the scraping position, as from the studies performed in 2010 [54]. The points represent the results from the simulations, whereas the solid lines represent the scaling of  $0\sigma$  values as from Eq. 4.1, for the shown combinations of material and speed (colouring has the same meaning as for the points). The curves for copper and graphite are shown. The speed of the blades is 20 cm/s, unless explicitly indicated. Points are obtained simulating the horizontal blade of the BSHV.51659 scraper, and values are scaled to a total beam intensity of  $3.312 \cdot 10^{13}$  protons.

dependence expressed by Eq. 4.1, with the points at  $2.5\sigma$  and  $3.5\sigma$  sitting clearly above the respective curves. This can be understood considering the fact that the value of maximum energy deposition depends not only on the number of beam particles impacting on the devices, but also on their spatial distribution, including the one on the non-cleaned plane. On the contrary, the values of total energy deposition follow this scaling law.

Figure 4.4 shows the evolution of the beam intensity as a function of turn number when scraping at  $3.5\sigma$ , for the copper and the graphite blades. As expected, the amount of beam finally surviving scraping in all the three cases is compatible within the statistical error (indicated at the end of each curve) with the theoretical prediction from Eq. 4.1. The copper blade is faster than the graphite one in fully accomplishing scraping, requiring  $\sim 500$  turns, whereas for the graphite one almost the double of the turns is needed, i.e.  $\sim 1000$ . Taking into account the revolution time in the SPS, i.e.  $23.05\ \mu\text{s}$  (see Sec. 2.1.2), these correspond to  $\sim 11.5\ \text{ms}$  and  $\sim 23\ \text{ms}$ , respectively. Contrary to expectations,

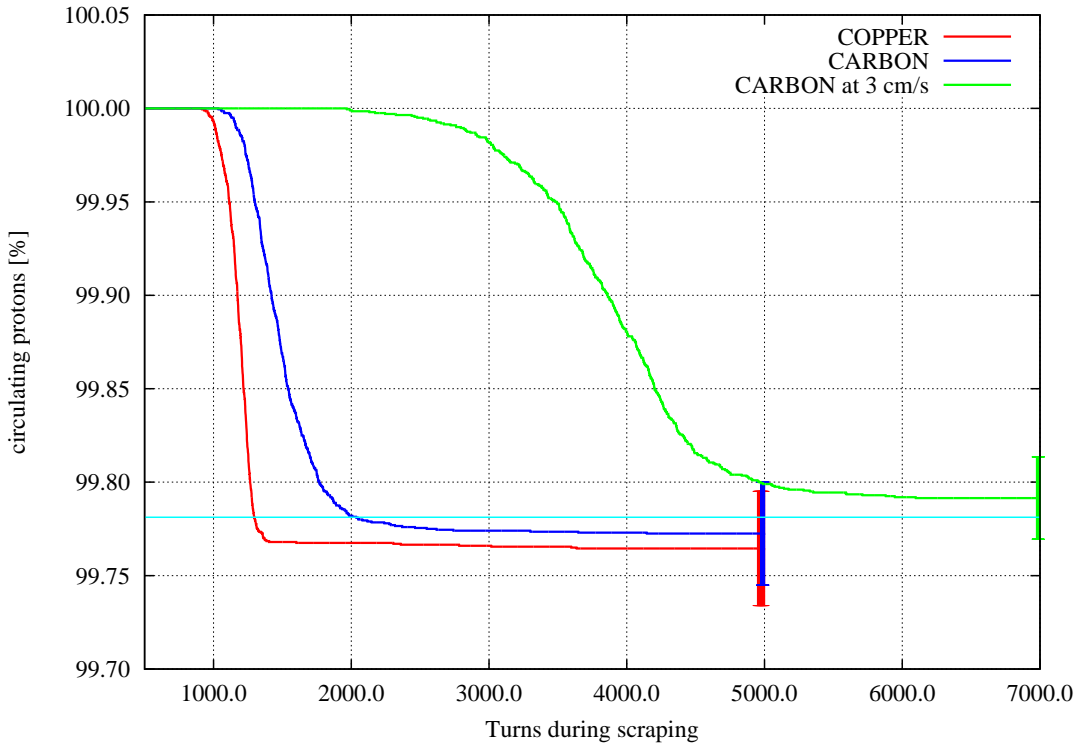


Figure 4.4: Evolution of the beam intensity as a function of turn number when scraping at  $3.5 \sigma$ , as from the studies performed in 2010 [54]. The curves for copper and graphite are shown. The cyan line marks the expected final value (see Eq. 4.1). The speed of the blades is 20 cm/s, unless explicitly indicated. Results are obtained simulating the horizontal blade of the BSHV.51659 scraper.

these values do not scale with  $l/\lambda_I$ , where  $l$  is the length of the blade and  $\lambda_I$  is the inelastic interaction length of the beam particles (i.e. protons) at the beam energy (i.e. 450 GeV) in the considered material. Moreover, the graphite blade at the reduced speed of 3 cm/s requires  $\sim 3000$  turns or  $\sim 75$  ms, i.e. three times longer than the one at the nominal speed, even though the ratio between the speeds is  $\sim 7$ .

While the qualitative outcomes on the time required for scraping as a function of blade characteristics (i.e. material and length) and speed are intuitive, this is not the case for the quantitative dependencies. This is due to the fact that for most of the duration of scraping, there is an interplay between the number of

beam particles in phase space at reach of the moving blade turn by turn, which depends on the distribution of the beam and the speed of the blade, and the attenuation capabilities of the blade, which depend not only on material and length, but also on the beam dynamics, responsible for the passages where the blade is missed. This is not the case once the blade is at the centre of the beam in the moving plane, for example, as shown in Sec. 4.2 and in Fig. 4.10, when all particles are at reach of the blade and the attenuation depends only on the blade characteristics. On the other hand, if the blade had an infinite absorbance, the time required for scraping would only depend on the beam distribution and the speed of the blade, with an unavoidable dilution effect due to beam dynamics. This is a desirable feature of the scraping system, as it allows one to fully control the time required for scraping acting on the speed of the system, as it happens in the case of the upgraded design (see Sec. 5.1).

Figure 4.5 shows the loss pattern in the SPS when scraping at  $0 \sigma$ , for the copper and the graphite blades. From the overview of the whole machine it can be seen that most of the losses take place just downstream of the BSHV.51619 scraper, as expected, at the “momentum scraper” TIDP.11434, i.e. a bulky absorber located in a region of the SPS LSS1 with high dispersion (see Fig. 2.7), and at the TPST.21759, an intercepting device protecting the extraction septa in the LSS2 (see Sec. 2.1.1). Qualitatively, the patterns from copper and graphite are similar. The zoom on the first 150 m downstream of the scraper given in the lower frames shows that in the case of copper more protons are lost immediately downstream of the scraper, whereas the losses from the graphite blades are more intense further downstream, where the DS is located. This is due to the multiplicity of the secondary protons emitted, their energy and angular distributions. Indeed, in the case of the longer and denser copper blade, an average of  $\sim 1.53$  protons are emitted and lost in the mechanical aperture of the SPS

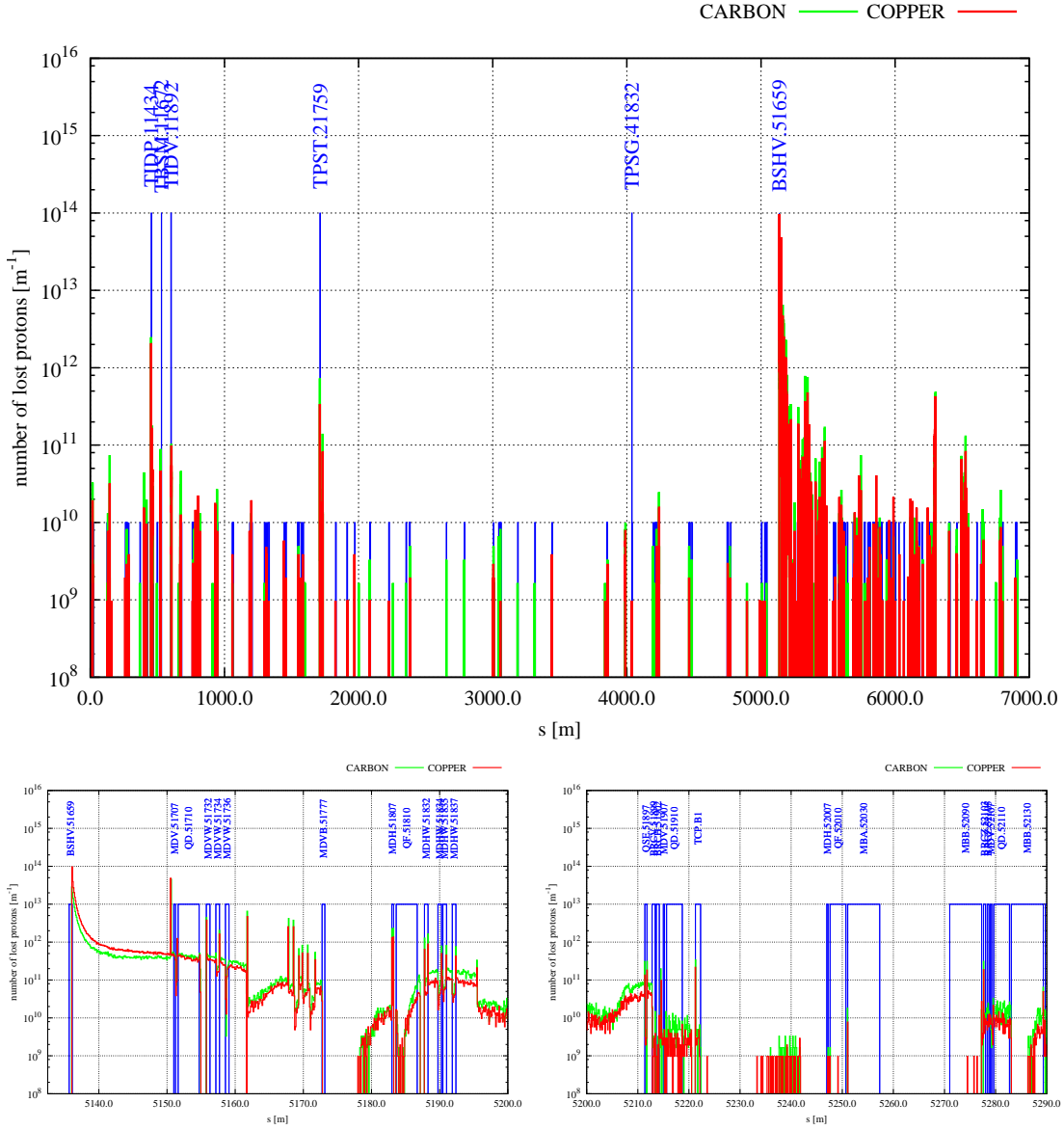


Figure 4.5: Loss pattern in the SPS when scraping at  $0 \sigma$ , as from the studies performed in 2010 [54]. The upper frame gives the overview of the whole SPS ring, whereas the two lower frames zoom on the region downstream of the scrapers. The curves for copper and graphite are shown. The speed of the blades is 20 cm/s. Results are obtained simulating the horizontal blade of the BSHV.51659 scraper, and are scaled to a total beam intensity of  $3.312 \cdot 10^{13}$  protons.

per scraped proton; out of this, an average of  $4.7 \cdot 10^{-3}$  protons are lost in the DS immediately downstream of the scraper and  $8.2 \cdot 10^{-2}$  are lost in the rest of the machine. In the case of the graphite blade, an average of  $\sim 1.1$  protons are emitted and lost in the mechanical aperture of the SPS per scraped proton; out of this, an average of  $9.1 \cdot 10^{-3}$  are lost in the DS immediately downstream of the scraper and  $8 \cdot 10^{-2}$  are lost in the rest of the machine<sup>1</sup>. As it can be seen, most of the protons are lost immediately downstream of the scraper, especially in the case of the longer and denser copper blade, which produces more secondary protons than the graphite one, and of lower energy and with larger angles on average. The losses in the DS immediately downstream of the scrapers are double for the graphite blade than for the copper one, whereas in the rest of the accelerator the losses are comparable. Similar numbers are found for the other scraping positions.

### 4.1.3 Conclusions

The investigations performed in 2010 have proved that graphite blades of 1 cm in length are subject to lower values of peak energy deposition than copper blades of 3 cm in length, with an overall gain of a factor between 2 and 3. The atomic number and density of graphite are the key to this result, as they lower values of energy deposition induced by all the interactions that a beam particle undergoes while going through the blade. In addition, the shortening of the blade further prevents the development of the secondary particle showers, and in particular the EM part. The speed of the blade plays an important role in determining the maximum value of energy deposition, even though the dependence is sub-linear. Values of maximum energy deposition in the blade do not linearly scale with the amount of beam scraped, whereas this is the case for the total energy

---

<sup>1</sup>For these estimations, the LSS is considered to extend between the middle of the two quadrupoles enclosing it, i.e. the QF.51610 and the QF.52010, whereas the DS downstream of the scraper is considered to extend between the middle of the QF.52010 and the middle of the QF.52210 (see Fig. 2.8), which closes the DS and marks the beginning of the following arc.

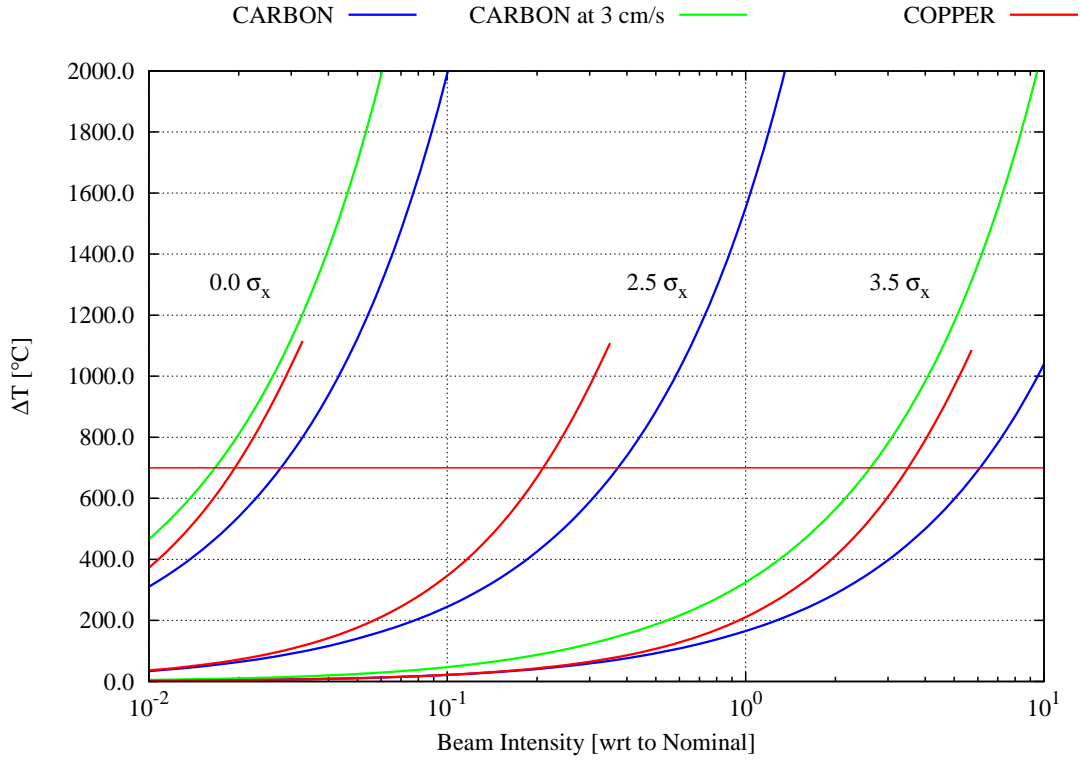


Figure 4.6: Temperature rise from room temperature in the SPS scraper blades as a function of beam intensity when scraping at  $0\ \sigma$ ,  $2.5\ \sigma$  and  $3.5\ \sigma$ , as from Ref. [54]. The curves for copper and graphite are shown. The speed of the blades is 20 cm/s, unless explicitly indicated. Results are obtained simulating the horizontal blade of the BSHV.51659 scraper. The horizontal red line marks the temperature rise to reach the maximum service temperature that can be accepted for copper from the engineering point of view, whereas the maximum value on the  $y$ -axis shows the one for graphite.

deposition in the blade – but this second observable is not particularly relevant for the assessment of the robustness of the blades.

As a summary of the considerations about energy deposition, Fig. 4.6 shows the temperature rise from room temperature in the SPS scraper blades as a function of beam intensity for all the cases presented in this overview. The lower values of energy density in graphite coupled to its higher maximum service temperature support choosing graphite as blade material, allowing beam currents in the SPS higher than those allowed by blades in copper for any scraping position. Nevertheless, full beam scraping (i.e. at  $0\ \sigma$ ) at full beam intensity (Nominal

LHC beams) remains prohibitive even for graphite as far as the robustness of the scraper blade is concerned. This last case is an accident scenario rather than an operational one, as in case of beam injection into the LHC only the tails are scraped off, and, in case the scrapers are used as a tool to characterise the profile of the circulating beam, diagnostics are not usually performed at full beam intensity.

The main drawback of the deployment of graphite blades is the longer time required to fully accomplish scraping, increased by a factor of  $\sim 2$  with respect to copper. It should be noted that, given the length of the blade and the value of the inelastic interaction length of protons at 450 GeV/c in graphite (see Tab. 1.6), the time required to fully accomplish scraping does not scale linearly with the speed of the blade. This implies that a possible effort to increase the speed of the blade would not appreciably reduce the time required to fully accomplish scraping.

No significant differences are found between copper and graphite in terms of losses around the SPS ring. The use of copper blades results in a larger number of secondary protons lost immediately downstream of the scrapers, i.e. an average of  $\sim 1.53$  and  $\sim 1.1$  protons is emitted and lost in the mechanical aperture of the SPS per scraped proton for copper and graphite, respectively, but the losses around the ring do not change either qualitatively in shape or as total per scraped proton, amounting to  $8.5\text{--}9\ 10^{-2}$ .

## 4.2 Analysis of the Existing System

In this section, some of the results from previous investigations (see Sec. 4.1) are updated and extended with new calculations, and brand new ones are presented, to complete the characterisation of the scraper blades. As for past results, the characterisation of the scraper blades is performed in terms of energy deposition in the blade itself, time evolution of the beam intensity during scraping, and

pattern of losses around the SPS ring.

Updates with respect to past investigations involve both the operational settings of the SPS and the simulation tools:

- the scrapers investigated are the operational ones installed in the SPS LSS1 in 2011 (see Sec. 2.2.1), i.e. the BSHV.11771. Here I do not investigate those installed in the SPS LSS5, i.e. BSHV.51659, and the BSHV.11759, which are immediately upstream of BSHV.11771. The latter is used as spare and for the burst test of the blades (see Sec. 4.3);
- the SPS optics was changed in 2012, with Q26 being replaced by Q20 (see Sec. 2.1.1);
- the simulations are performed coupling FLUKA to SIXTRACK (see Sec. 3.3) and no longer to ICO SIM.

All the new results presented in this section are aimed at addressing effects on relevant observables due to operational aspects unexplored by previous studies:

- the comparison between graphite and copper is updated and extended, with an insight into the main events that protons going through the scraper blades undergo and typical ranges of energy loss. Moreover, losses around the ring are classified on the basis of the last event the lost protons underwent while going through the blade;
- a permanent magnetic bump is present in the SPS LSS1 (see Sec. 2.1.3), obtained by displacing three consecutive quadrupoles. Important oscillations are induced in the SPS closed orbit, up to more than 5 mm on the horizontal plane, for which the mechanical aperture of the machine is reduced all around the ring with respect to the situation of a perfectly closed bump. Effects are addressed as follows;

- scraping is performed towards the end of the energy ramp (see Sec. 2.1.4), to avoid populating the abort gap. All the simulations presented in this thesis have been performed at top energy, and thus a case simulating scraping during the ramp is presented, to address differences;
- the effects due to tilting of the blade are presented. These are relevant for the time required to fully accomplish scraping and in view of the benchmark of the simulation results, presented in Sec. 4.3.

In the following, the general simulation settings common to all the cases presented in the section are reported first. Then, all the aforementioned aspects are investigated separately. Local modifications of the simulation settings are explicitly stated before results are reported. Finally, conclusions are drawn. It should be noted that all the material presented in this section is original contribution to this thesis.

### 4.2.1 Simulation Settings

All the simulations presented in this section and in the following one about the benchmark of the simulation tool have been performed coupling FLUKA to SIXTRACK (see Sec. 3.3). All the cases have been carried out in 6D tracking, i.e. activating the longitudinal dynamics of the beam at flat top, using the corresponding RF settings (see Sec. 2.1.2). This allows one to have more realistic results, as scraping takes place typically over a number of turns comparable to the synchrotron period (expressed in number of turns, see Tab. 2.1). The case of scraping during the energy ramp has been run changing the RF settings from those at flat top to those used during ramp (see Sec. 2.1.2). As with ICO-SIM, the aperture check is performed online during tracking, but only at the end of each element in the lattice structure. In case a beam particle falls outside of a given aperture, a linear interpolation is performed, to improve the estimation of the loss location.

Protons of any energy above the FLUKA transport threshold are given back to SIXTRACK, as happens in the coupling with ICO SIM.

The thin lens model of the SPS lattice structure is given as input to SIXTRACK, loading the SPS Q20 optics (used in operation for accelerating LHC beams since 2012). The permanent magnetic bump is always considered, unless explicitly stated. The optics file has been obtained with MADX, slicing the thick lens model of the SPS lattice structure with the `teapot` algorithm [88]. This algorithm slices a given thick element in  $n$  thin lenses, optimising the lengths of drift spaces at the extremes and in-between, in order to improve the convergence of the compound matrix towards the matrix of the thick lens element. Three slices for each magnetic element have been chosen. After slicing, the optics is re-matched, to ensure that the proper tune and chromaticity are deployed. Furthermore, since the main bending magnets of the SPS are rectangular whereas the thin lens tracking in SIXTRACK expects thin lenses of sector dipoles, the focussing effect locally missing has been restored inserting dipole edge lenses at locations corresponding to the entrance and exit faces of each dipole in its thick lens description<sup>2</sup>. As for the coupling of FLUKA to ICO SIM, the aperture model of the machine is taken from the MADX database on `afs`, likewise for the lattice structure and optics. Aperture markers at locations corresponding to the entrance and exit faces of the main quadrupoles and dipoles in their thick lens description have been inserted on purpose, to ensure the best match between the aperture model in thin and thick lens settings, especially at transitions. The simulated scrapers are those installed in the SPS LSS1, either the operational ones, i.e. the BSHV.11771, or the spare ones, i.e. the BSHV.11759.

The FLUKA geometry mainly consists of the scrapers, i.e. the BSHV.11759

---

<sup>2</sup>Dipole edges are automatically inserted by MADX in the description of the lattice structure when the optics is converted from thick to thin lenses only if triggered on purpose, i.e. in case the flag `MAKEDIPEDGE` in the `MAKETHIN` command is set to `true`. In this case, the kicks of the dipole edges are automatically calculated by MADX.

and the BSHV.11771, each equipped with two blades, with realistic shape, dimensions and material density, as described in the mechanical drawing shown in Fig. 2.5. Their mechanical sweep through the beam is simulated changing the geometrical transformations applied to each moving blade turn by turn (see Sec. 3.1.2). In order to improve the description of the aperture profile of the SPS and take into account possible re-interactions of protons already scattered by the scraper blades against other beam-intercepting devices installed in the ring, small segments of the SPS LSS5 and LSS6 are modelled as well, for a total of three insertions to be handled by the coupling. In particular, the portion in the LSS5 comprises (in sequence, as seen by the beam, see Fig. 2.8): a beam intercepting device, the TCXHW.51651, i.e. a small collimator with two jaws, 10 cm in length, made of a tungsten alloy; the original SPS scrapers, with their graphite blades, equipped with a shielding wall downstream of them. The portion of the LSS6 comprises the TPSG.61773 and the TPSG.61776, two beam-intercepting devices protecting the extraction septa in the LSS6. Apart from the comparison between graphite and copper presented in Sec. 4.2.2, the material of the blade is always graphite, as stated in the technical drawing. In general, the horizontal blade is always simulated, with the nominal speed of  $80 \text{ mm s}^{-1}$  [73]. **PRECISIO** settings are used (see Sec. 3.1.3), with single Coulomb scattering switched on near boundaries between materials, to better describe the exit angle of beam particles which do not undergo any nuclear interaction in the blade, requesting 5 consecutive interactions. Four Cartesian meshes covering the whole blade or just a transverse portion of it have been used to estimate levels of energy deposition, with differing transverse bin dimensions, with  $10 \mu\text{m}$  being the smallest one, but with the same longitudinal binning, i.e. 0.5 mm. In order to use such fine meshes, the transport thresholds have been lowered from the default values foreseen by the **PRECISIO** settings to  $10^{-5} \text{ GeV}$  for all particles but neutrons (kept at  $10^{-5} \text{ eV}$ ) and photons

(lowered to 1 keV). In order not to be penalised in terms of CPU time by the development of EM cascades, extensive use of Leading Particle Biasing (LPB) has been applied on the beam-intercepting devices in the LSS5 and the LSS6 explicitly modelled in **FLUKA**, as the interest is not on the energy deposition these devices are subject to.

The tracked beam has been given a bell-shape distribution on both transverse planes and in momentum, matched to the machine linear optics. The beam distributions, normalised emittance and rms relative momentum offset are given case by case. The sampling routine available in the coupling repository has been used to generate the beam distribution to be tracked (see Sec. 3.4.2). All the simulations have been performed at top energy, i.e. 450 GeV/c, except the case checking effects by energy ramping, presented in Sec. 4.2.4. The scenario predominantly simulated is scraping at 0  $\sigma$ , as this is the most demanding one in terms of energy deposition (see Sec. 4.1), but also the fastest one in achieving acceptable statistics. Energy deposition values are given per proton in the beam and are also normalised to a train of 288 bunches of the Nominal LHC beam, i.e. with  $1.15 \cdot 10^{11}$  protons per bunch, for a total intensity of  $3.312 \cdot 10^{13}$  protons. All other observables are referred to a beam proton. All cases presented in this section have been run with approximately a million protons in the tracked beam.

### 4.2.2 Material of the Blade

The updated comparison between copper and graphite as blade materials has been performed simulating full beam scraping with the horizontal blade of the BSHV.11771. Contrary to the past estimations reported in Sec. 4.1, the blade is 1 cm in length in both cases. In general, results for the copper blade are always shown by red curves, whereas those for graphite are shown by green curves.

plane	type	$\epsilon_N$ [ $\mu\text{m}$ ]	$\sigma_\delta$ []
hor	Gaussian 2D	1	-
ver	Gaussian 2D	1	-
lon	Gaussian 1D	-	$10^{-4}$

Table 4.3: Parameters describing the beam sampled and tracked: plane (first column), distribution type (second column), normalised emittance (third column), and rms relative momentum offset (fourth column).

### Simulation Settings

The machine optics considered for the studies is Q20, with no magnetic bump. The input to SIXTRACK has modified settings with respect to those presented in Sec. 4.2.1. In fact, when slicing the accelerator structure, each bending magnet has been sliced in 5 lenses instead of 3. Moreover, in this version of the optics, dipole edge lenses have not been added. It will be shown later (see Sec. 4.2.3) that, for the number of revolutions typically simulated (i.e. few thousands), the presence of these lenses has no visible effects on results, also because the optics is re-matched by MADX after slicing, before creating the files in input to SIXTRACK. Finally, aperture markers at locations corresponding to the entrance and exit faces of the quadrupoles and dipoles in their thick lens description have not been inserted.

The tracked beam is given a Gaussian distribution on both transverse planes, with  $1 \mu\text{m}$  normalised emittance, and a Gaussian momentum spread, with  $\sigma_\delta = 10^{-4}$ . These values of normalised emittance are smaller than any value presently considered for LHC operation (see Tab. 1.5); hence, energy deposition values presented in this section are overestimated. Nevertheless, values of normalised emittance for the LIU BCMS scheme are quite close to those presently considered in the simulations, and thus energy deposition results can be regarded as slightly conservative for BCMS beams. Table 4.3 summarises the parameters of the beam

distribution sampled and tracked.

The FLUKA geometry of the couple of cases presented here comprises only the operational scrapers, without the spare ones located upstream and without the additional objects in the LSS5 and the LSS6, since they were not yet modelled at the time of the simulations. Thus, the coupling between SIXTRACK and FLUKA involves only one insertion, i.e. that of the operational scrapers.

## Results

Figure 4.7 shows the pattern of energy deposition in the scraper blade for the two considered materials. As expected, copper is subject to values of energy deposition much higher than those found in graphite. With respect to the past estimations shown in Fig. 4.1, new peak values are a factor of 5 and 3 higher for copper and graphite, respectively. Many factors contribute to this increase: the speed of the blade, lowered from the value of 20 cm/s considered in the past investigations to the nominal value of 80 mm/s (see Sec. 2.2.1); the normalised emittance of the beam, decreased from  $3.5 \mu\text{m}$  (Nominal LHC beams, see Tab. 1.5) to  $1 \mu\text{m}$  (very close to the value for LIU BCMS beams, see Tab. 1.5); the granularity of the mesh for the present simulations ( $10 \mu\text{m} \times 10 \mu\text{m} \times 0.5 \text{ mm}$ , hor  $\times$  ver  $\times$  lon), much more refined than the one used in the past ( $100 \mu\text{m} \times 100 \mu\text{m} \times 1 \text{ mm}$ , hor  $\times$  ver  $\times$  lon). Comparing the values of peak energy deposition with the limits given in Tab. 4.2, this scraping position remains prohibitive in case of full beam intensity, even in the case of the new optics and new location of the scrapers. For both blades, the horizontal scan, i.e. the profile of energy deposition on the cleaning plane, along which the blade does not move, shows a Full Width at Half Maximum (FWHM) between  $850 \mu\text{m}$  and  $1.1 \text{ mm}$ , compatible with the same value calculated from the optics for the given normalised emittance and momentum spread, i.e.  $860 \mu\text{m}$  (see Tab. 2.3). The vertical scan, i.e. the profile

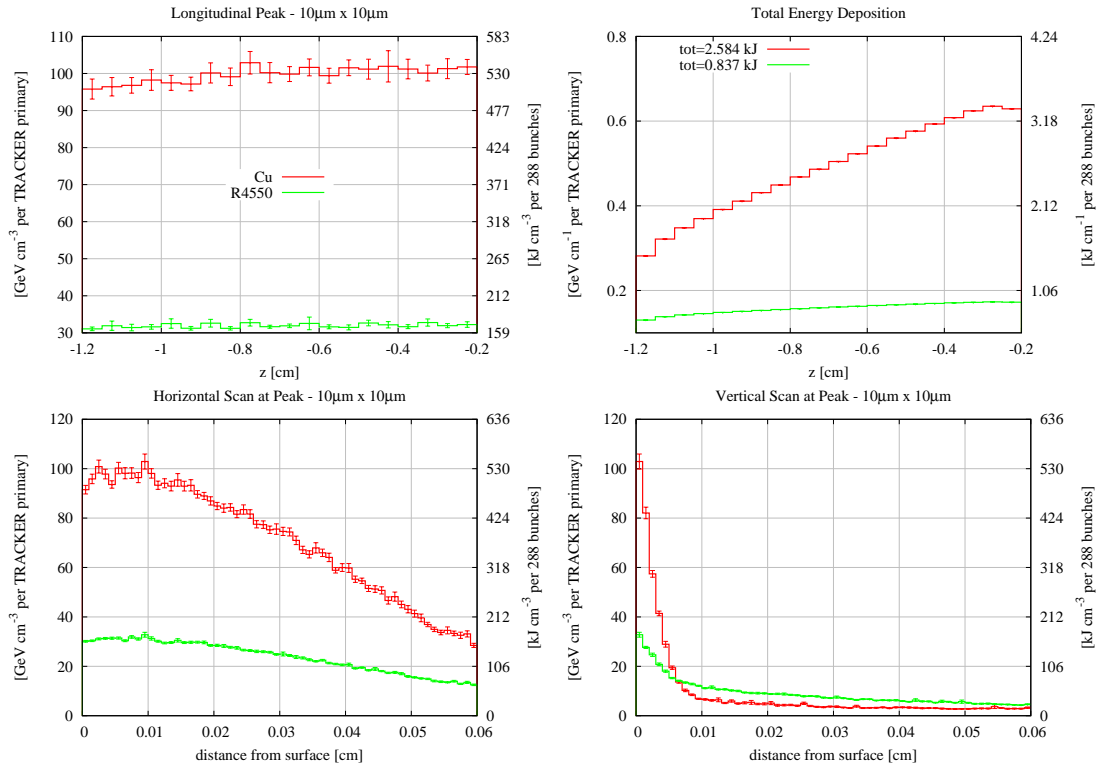


Figure 4.7: Energy deposition in the blades of the SPS scrapers when scraping at  $0 \sigma$ , in the case of copper (red curve) and graphite (green curve) blades. The upper-left frame shows the longitudinal pattern of the peak energy deposition, whereas the upper-right frame shows the longitudinal pattern of the total energy deposition. The lower frames show the horizontal (left frame) and vertical (right frame) scans of the energy deposition map at the maximum (see longitudinal pattern of the peak). The speed of the blade is 80 mm/s. Results are obtained simulating the horizontal blade of the BSHV.11771 scraper, and are scaled on the right vertical axes to a total beam intensity of  $3.312 \cdot 10^{13}$  protons.

of energy deposition on the non-cleaning plane, along which the blade moves, shows a moderately steep gradient, justifying such a detailed mesh. As can be seen, the pattern of the energy deposition retains a memory of the dimensions of the beam distribution on the collimation plane, whereas along the direction of the movement of the blade the energy deposition is extremely localised and collapsed in the very first tens of  $\mu\text{m}$  of material directly facing the beam. The longitudinal pattern of the total energy deposition confirms the findings from past investigations, i.e. the increasing trend in the energy deposition, especially

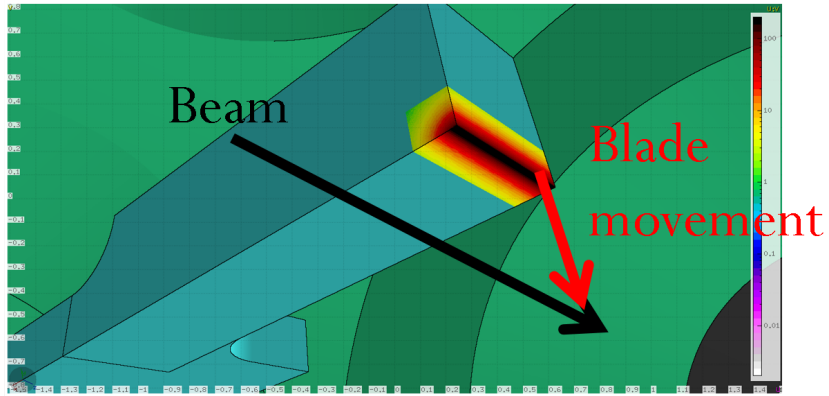


Figure 4.8: Energy deposition in the horizontal blade of the BSHV.11771 as from simulations, layered over a 3D rendering of the same blade obtained with Flair. View from the bottom.

for copper, typical of the first stages of development of secondary particle showers. The integrated value for copper, shown in the key of the plot, is a factor of 2 lower than the value obtained in the past – it should be kept in mind that the length in the present studies is shorter than the one considered in the past, i.e. 1 cm instead of 3 cm. Values for graphite are very similar, as expected.

Figure 4.8 shows a 3D visualisation of the energy deposition map superimposed on the geometry of the blade. As can be seen, the energy deposition is highly concentrated along the edge which performs the scraping, with a broad distribution on the plane of cleaning and steep gradients on the axis of movement.

The two materials have been characterised also in terms of main events undergone by any proton going through the blade and energy losses typically involved, no matter if the interacting proton is then immediately lost in the machine or scattered on a new stable orbit. The estimation has been carried out recording the type of event undergone by any proton going through the blade and the energy thus lost, computed as difference between the energy at the entrance of the FLUKA geometry and at its exit.

Figure 4.9 shows the results of this analysis for the graphite and the copper

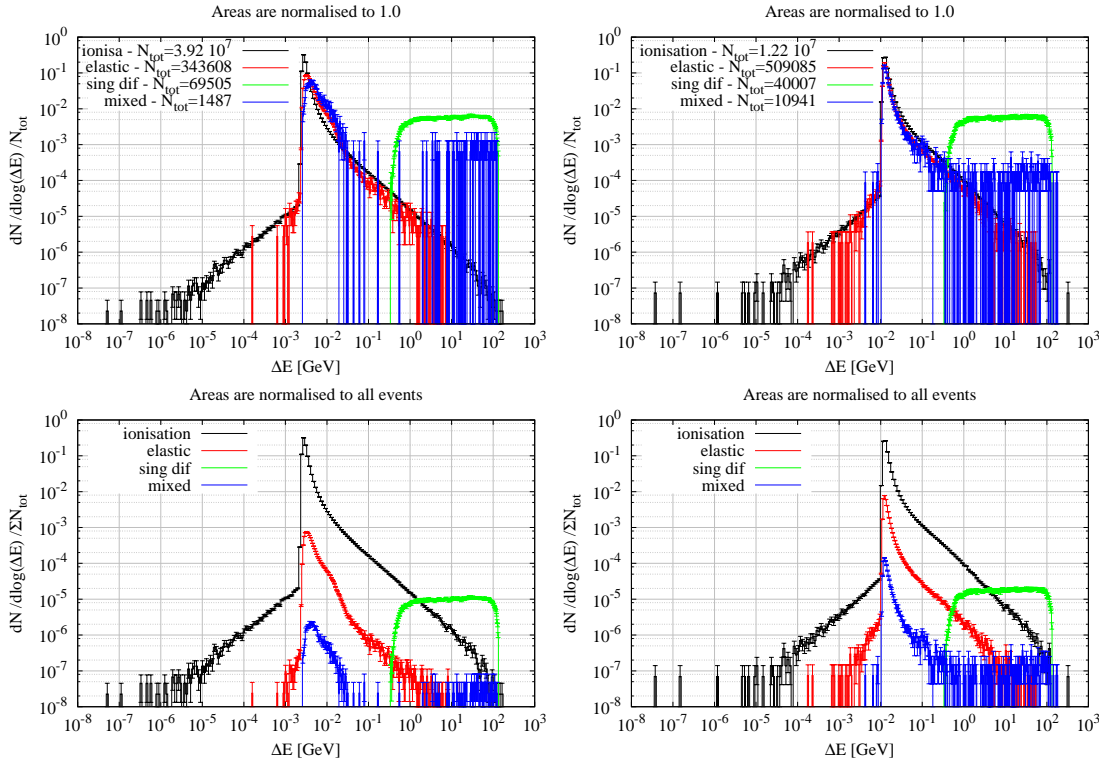


Figure 4.9: Distribution of the energy loss in the blades of the SPS scrapers per single proton passage when scraping at  $0\sigma$ , according to the most relevant event undergone by the traversing proton surviving the interaction (“deep” inelastic interactions are thus excluded). Results for graphite are shown in the left column, whereas those for copper are shown in the right column. In the upper frames, all the distributions are singularly normalised to 1, whereas in the lower frames all the distributions are normalised to the total number of passages. Results are obtained simulating the horizontal blade of the BSHV.11771 scraper.

blades. The distributions in black represent single proton passages with only MCS and ionisation; those in red and in green represent single proton passages affected by only one nuclear elastic and one single diffractive event on top of ionisation and MCS, respectively; those in blue collect all other events.

As it can be seen, ionisation and MCS are the events happening with the highest frequency. They are peaked at a value extremely close to the mean predicted by the Bethe–Bloch formula (see Eq. 1.3), but span the entire range of energy shown. The lowest values, starting from a few hundred eV, are due to protons going through only a small portion of the blade, almost missing it,

whereas the highest values, up to a hundred GeV, are due to hard knock-on interactions with electrons in the medium (see Sec. 1.4.3). Single diffractive events are responsible for energy losses between fractions of a GeV up to a hundred GeV, as well as most of the events with more than ten GeV of energy loss, as visible in the lower frames of the figure. The distributions of elastic events are very similar to those from ionisation, showing that the contribution to the energy loss by this type of event is very limited. In particular, in the case of graphite, the peak of the distribution is at a slightly higher energy than the one for pure ionisation, and the bump around 10 MeV gives an idea of the energy loss induced by this event; on the contrary, in the case of copper, the mean energy loss by ionisation is already comparable with the typical energy loss due to the nuclear elastic scattering, and the two distributions are extremely similar. Due to the short length of the blade, mixed events are rare, and they reflect the distribution of ionisation, elastic and single diffractive events. It should be noted that the curve for mixed events is much more populated in the case of copper than in the case of graphite, due to the higher density of the material.

Figure 4.10 shows the evolution of the beam intensity and of the rate of intercepted protons for the two materials considered in the simulation. Though the copper blade is faster than the graphite one in fully achieving cleaning, the time scales do not differ with past simulations, since the copper blade is as long as the graphite one, i.e. 1 cm. Once the blade reaches the centre of the beam on the axis of movement, the beam intensity decreases exponentially. This implies that, starting from that moment, the time for cleaning is not dominated by the speed of the blade or by the type of distribution any more (as happens in the beginning), but only by the characteristics of the material of the blade, its length, the frequency of the betatron motion and the aperture profile of the machine. In particular, since the optics, machine aperture profile and length of the blade are

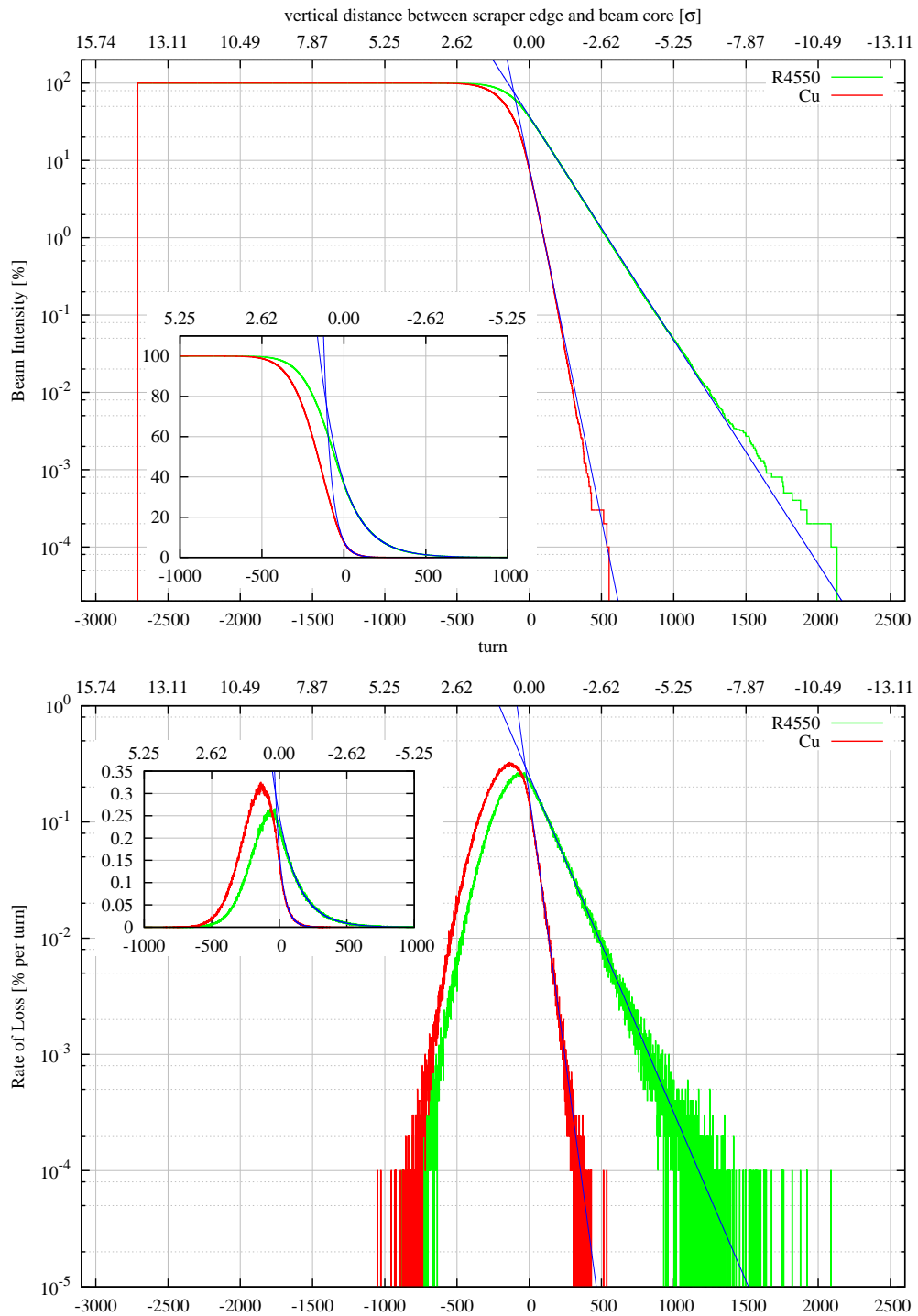


Figure 4.10: Evolution of the beam intensity (upper frame) and rate of intercepted protons (lower frame) when scraping at  $0 \sigma$  with a copper and a graphite blade. The zooms are focussed on the moment when the scraper blade actually intercepts the beam. Results are obtained simulating the horizontal blade of the BSHV.11771 scraper.

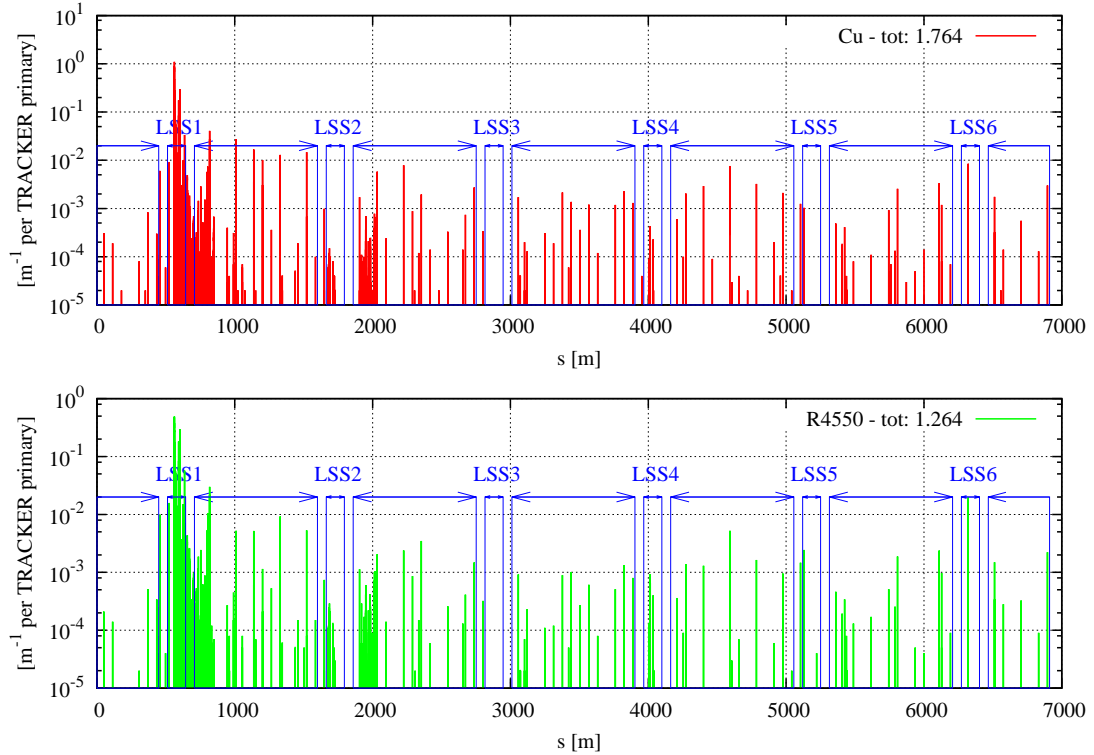


Figure 4.11: Pattern of proton losses around the SPS ring when scraping at  $0\sigma$  with a copper (upper frame) and a graphite (lower frame) blade. The total reports the average number of protons lost per beam proton. Results are obtained simulating the horizontal blade of the BSHV.11771 scraper.

the same in the two cases, the difference in the exponential attenuation is simply due to the inelastic interaction length of the two materials. Indeed, the decay time obtained from the curves which are fit to the data is 150 and 47.7 for graphite and copper, respectively, and they scale almost perfectly with the inelastic interaction lengths of the two materials (see Tab. 1.6), with the discrepancy being due to all other events that lead to proton losses in the ring.

Figure 4.11 shows the pattern of proton losses around the SPS ring, for copper and graphite. There are no major differences between the two patterns. The totals in the key of the plot report the average number of protons lost per scraped proton. In the case of the copper blade, an average of 1.76 protons are emitted and lost in the mechanical aperture of the SPS per scraped proton; out of this,

an average of  $3.8 \cdot 10^{-2}$  protons are lost in the DS immediately downstream of the scraper and an average of  $4.8 \cdot 10^{-2}$  protons are lost in the rest of the machine. In the case of the graphite blade, an average of 1.26 protons are emitted and lost in the mechanical aperture of the SPS per scraped proton; out of this, an average of  $4.2 \cdot 10^{-2}$  protons are lost in the DS immediately downstream of the scraper and an average of  $4.0 \cdot 10^{-2}$  protons are lost in the rest of the machine. It should be noted that only protons with an energy greater than 100 GeV can reach the DS, whereas only those with an energy greater than 435 GeV can survive the DS and be lost in the rest of the machine<sup>3</sup>.

With respect to past estimations, the average number of protons lost per intercepted proton is greater by  $\sim 15\%$  for both materials. This might possibly be due to the implementation of the whole stainless steel tank, extending also downstream of the blades and thus producing further secondary protons. It should be noted that the losses in the DS immediately downstream of the scrapers are very close to those in the rest of the machine for both materials, whereas in the past there was a factor of almost 10 between the two, with no evident reason. Nevertheless, the total losses outside the the LSS where the simulated scraper is installed is consistent.

Figure 4.12 shows the pattern of proton losses around the SPS ring, grouped according to the last event the lost proton underwent in the scraper blade. As expected, inelastic and single diffractive scattering events dominate in the LSS1 and in the DS immediately downstream, whereas most of the losses around the ring are due to MCS and elastic events, with an occasional contribution from single diffractive scattering.

---

<sup>3</sup>For these estimates, the LSS is considered to extend between the middle of the two quadrupoles enclosing it, i.e. the QFA.11610 and the QF.12010, whereas the DS downstream of the scraper is considered to extend between the middle of the QF.12010 and the middle of the QF.12210 (see Fig. 2.7), which closes the DS and marks the beginning of the following arc.

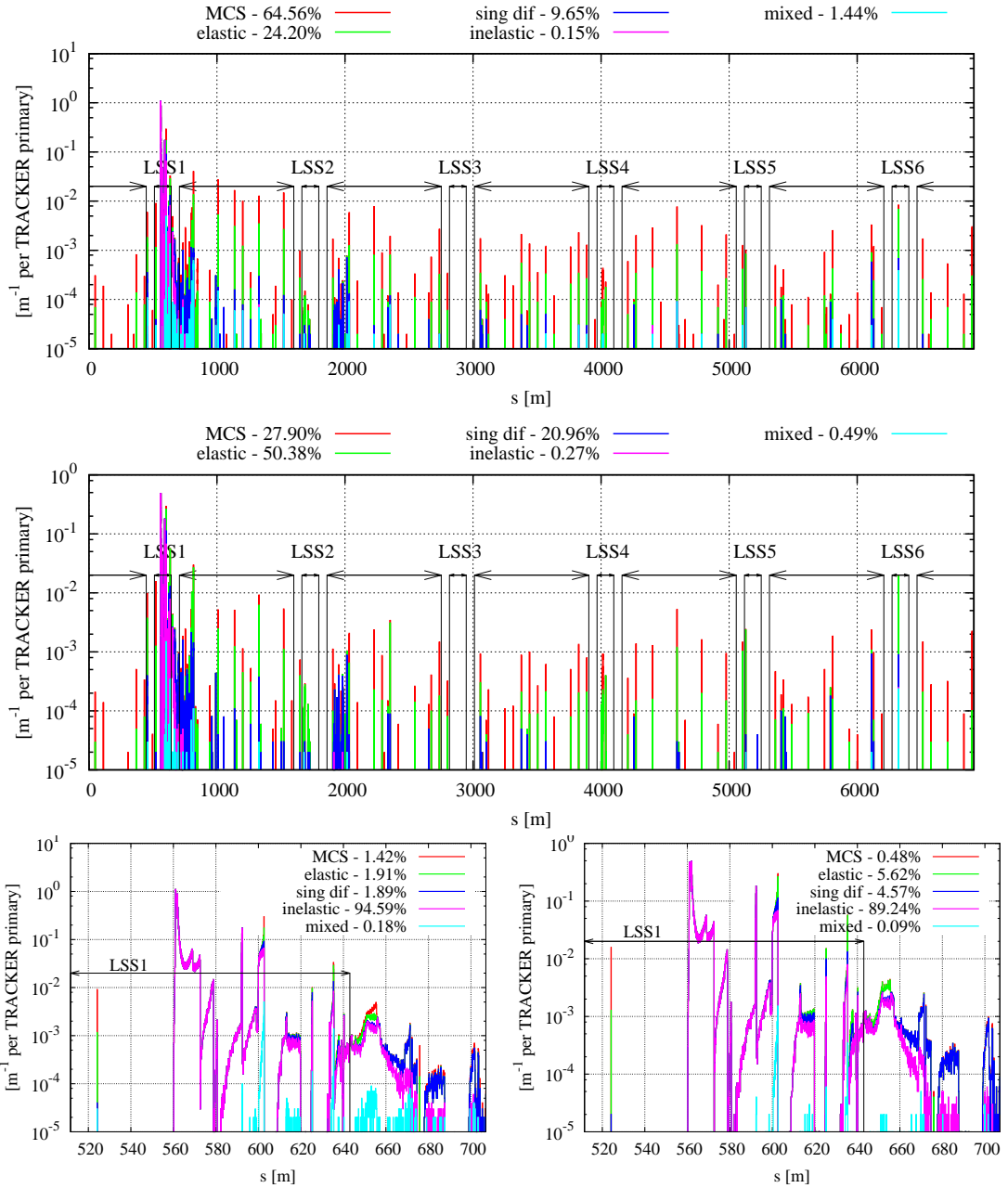


Figure 4.12: Pattern of proton losses around the SPS ring when scraping at  $0 \sigma$ , grouped according to the last event the lost proton underwent in the scraper blade, for copper (upper frame) and graphite (middle frame). It should be noted that MCS and ionisation follow any discrete event. For each event, the percentage refers to the protons lost everywhere in the SPS ring but in the LSS1 and in the downstream DS. The lower frames show the zoom on the LSS1 and the downstream DS, with the curves for copper on the left and those for graphite on the right. For each event, the percentage refers to the protons lost in the shown range of the longitudinal  $s$ -coordinate. Histograms are added on top of each other, starting from the one of the mixed events up to one of the MCS events. Results are obtained simulating the horizontal blade of the BSHV.11771.

### 4.2.3 Permanent Bump in the LSS1

A permanent magnetic bump is present in the SPS LSS1 (see Sec. 2.1.3), to ease the dump of proton beams at flat top. The bump is obtained by transversely displacing three consecutive quadrupoles in the same LSS.

The effect of the bump on the beam closed orbit is quite important, as it induces oscillations up to 5 mm on the horizontal plane, with a possible decrease of the available aperture in the machine. Moreover, the presence of the bump has also some consequences on the estimation of the BLM signal for the benchmark of the simulation tools (see Sec. 4.3.5). Consequently, the present section characterises the effects induced by the magnetic bump. The characterisation is done considering the case of full beam scraping with the horizontal blade of the BSHV.11759 scraper, in case the permanent magnetic bump in the LSS1 is active or not. Contrary to what was done in the previous section, the analysed scraper is no longer the operational one, but the spare one (see Sec. 2.2.1), chosen in view of the burst test (see Sec. 4.3). As for the operational scraper, its blades are made of graphite.

### Simulation Settings

The simulations have been run with the same settings as those presented in Sec. 4.2.1. The tracked beam is given a double Gaussian distribution (see Sec. 3.4.2 and Sec. D.2.1) on both transverse planes, to address the effects due to over-populated tails, more than what a single Gaussian distribution describes. In fact, it has been operationally proven (see Fig. 4.37, for instance) that beams at flat top in the SPS can be described by such a pdf. The distributions on both the transverse planes have the same settings, i.e. the inner Gaussian has a weight  $I_1 = 0.54$  and a standard deviation  $\sigma_1 = 0.6 \sigma_\beta$ , whereas the outer Gaussian has a weight

plane	type	$I_1$	$f_1$	$f_2$	$\epsilon_N$ [ $\mu\text{m}$ ]	$\sigma_\delta$
hor	double Gaussian 2D	0.54	0.6	1.27	2	-
ver	double Gaussian 2D	0.54	0.6	1.27	2.3	-
lon	Gaussian 1D	-			-	$2 \cdot 10^{-4}$

Table 4.4: Parameters describing the beam sampled and tracked: plane (first column), distribution type (second column), normalised emittance (sixth column), standard deviation of relative momentum offset (seventh column). Values in columns three through five are the parameters [89] of the double Gaussian distribution (see Sec. 3.4.2 and Sec. D.2.1).

$I_2 = 1 - I_1$  and a standard deviation  $\sigma_2 = 1.27 \sigma_\beta$  [89].  $\sigma_\beta$  is the betatron contribution to the rms beam size (see Eq. A.11).  $2 \mu\text{m}$  and  $2.3 \mu\text{m}$  are the normalised emittances on the horizontal and vertical planes, respectively. The beam is given a Gaussian momentum spread, with  $\sigma_p = 0.09 \text{ GeV}/c$ , corresponding to an rms relative momentum offset  $\sigma_\delta = 2 \cdot 10^{-4}$ , cut at  $4.15 \sigma_p$ , to avoid sampling protons out of the RF acceptance of the stable bucket (see Sec. 2.1.2). These values of normalised emittance are bigger than those considered in the previous section, and thus closer to those presently considered for LHC operation (see Tab. 1.5). Actually, since the inner Gaussian has a standard deviation 60 % of the optical one and the normalised emittance is double the one used in the previous section (see Tab. 4.3), the standard deviation of the inner Gaussian is  $\sim 85 \%$  of the one used in the previous section. Table 4.4 summarises the parameters of the beam distribution sampled and tracked.

Results presented in this section are obtained by tracking a beam different from the one used in the previous section; in particular, the normalised emittances are double those previously assumed, and the transverse distributions have enriched tails. Moreover, the spare scraper is simulated and not the operational one, as previously done. The description of the SPS lattice structure previously used is different from the one used for the present results and those to come in

the following sections, especially for the absence of aperture markers at locations corresponding to the entrance and exit faces of the main quadrupoles and dipoles in their thick lens description. Finally, the FLUKA geometry used for the simulations presented in the previous section consists only of the operational scrapers, with no other insertion involved in the coupling, whereas the geometry of the simulations presented here comprises not only the spare and operational scrapers in sequence as installed in the SPS, but also the additional beam-intercepting devices in the SPS LSS5 and LSS6, as described in Sec. 4.2.1. For all these reasons, in addition to the new results presented in this section, the case of the graphite blade from the previous section is re-presented, to address the effects of all the aforementioned aspects. As a consequence, all the plots here reported will always show three curves, with the same colour coding: the black one refers to the results for the graphite blade from the previous section; the red one refers to new results without considering the magnetic bump; and the green one refers to new results considering the magnetic bump.

## Results

Figure 4.13 compares the evolution of the beam intensity and of the rate of intercepted protons for the three cases considered. As for the results presented in the previous section (black curve), the new results (red and green curves) show the exponential attenuation of the beam intensity versus revolutions in the accelerator as soon as the blade reaches the centre of the beam along the axis of movement. The difference in the slopes between the two curves with the new results is due to the presence of the bump, which slightly reduces the mechanical aperture of the SPS and prevents some protons which have already interacted with the blade from coming back to the scraper and interacting again. This will also have an effect on energy deposition values (see below). The different slope

between the new results without magnetic bump (red curve) and the results from the previous section (black curve) shows the effect of the different description of the accelerator structure, in particular the combination of the absence of aperture markers at locations corresponding to the entrance and exit faces of the main quadrupoles and dipoles in their thick lens description, and the presence of the beam-intercepting devices in the SPS LSS5 and LSS6 explicitly modelled in the FLUKA geometry. The effect of the beam distribution is clearly visible in the zoom of the beam intensity, and in particular in the region before the exponential attenuation (starting when the edge of the blade reaches the centre of the beam). As expected for the two new cases (red and green curves), featuring a broader beam distribution, this first phase of scraping has a longer duration than that of the narrower distribution (black curve), by approximately a factor of 2. This is in agreement with the use of a different distribution on the vertical plane and, taking into account the magnification factor of the outer Gaussian and the emittance, i.e. 1.27 and  $2.3 \mu\text{m}$ , respectively, a scaling factor of  $1.27\sqrt{2.3} = 1.93$  is found (see Tabs. 4.3 and 4.4 for the beam distributions in case of the black and coloured curves, respectively). Indeed, a broader beam distribution implies that beam particles start to be intercepted at a larger distance along the axis of movement from the centre of the beam. Once at the centre of the beam the exponential attenuation is almost the same, as the blade characteristics have not changed. It should be kept in mind that all the results shown here have been obtained with the same blade in different locations in the accelerator (i.e. at either the operational scraper or at the spare one), and moved with the same nominal speed of 80 mm/s.

Figure 4.14 shows the pattern of energy deposition in the blade of the SPS scrapers for the considered cases. In general, energy deposition values are higher for the narrower beam (black curve) than for the broader beam (red and green

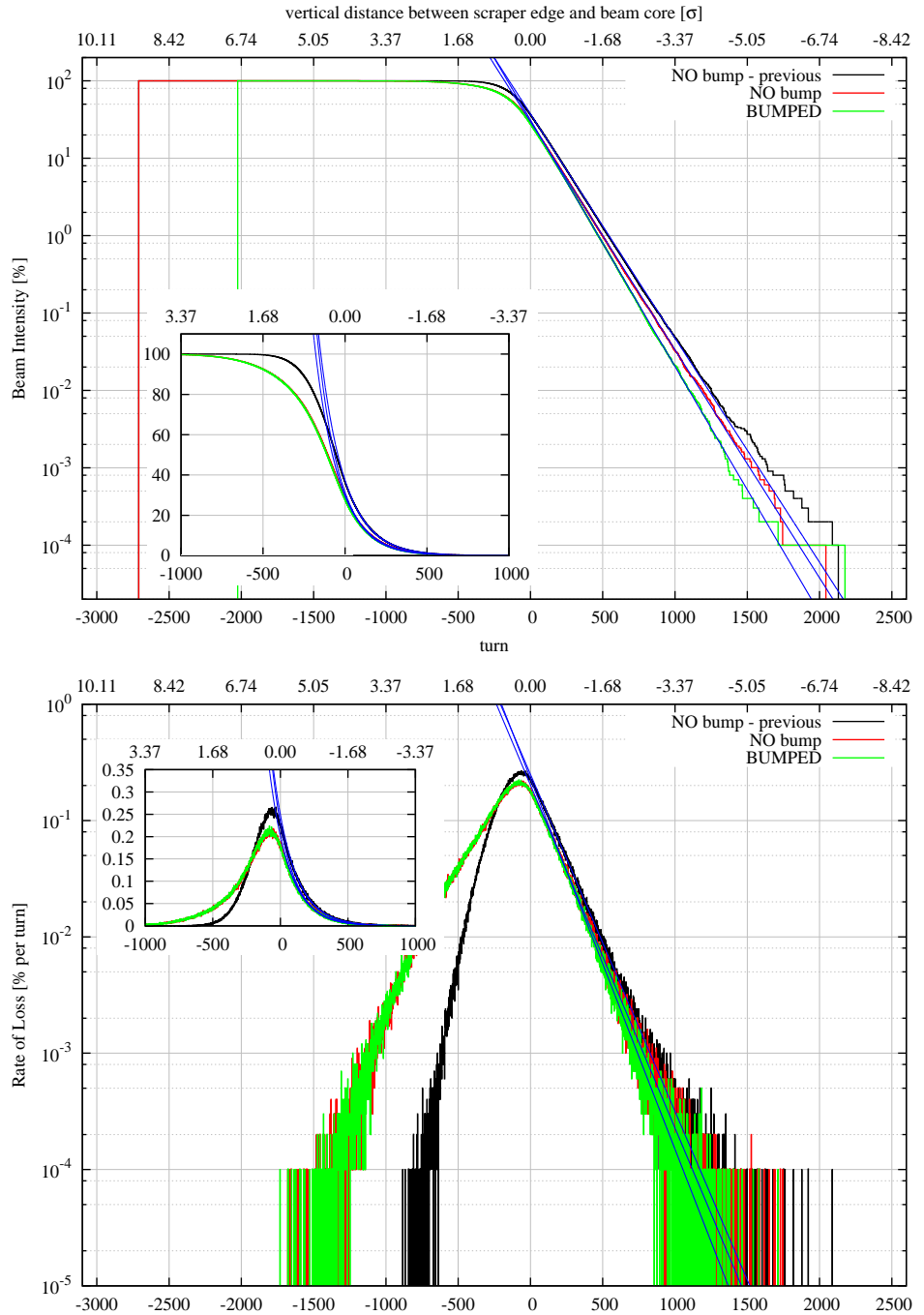


Figure 4.13: Evolution of the beam intensity (upper frame) and the rate of intercepted protons (lower frame) when scraping at  $0 \sigma$ , in the case the permanent magnetic bump in the LSS1 is considered or not in the machine optics. The zooms are focussed on the moment when the scraper blade actually intercepts the beam. Results are obtained simulating the horizontal blade of the BSHV.11759 scraper but for the black curve, obtained simulating the horizontal blade of the BSHV.11771.

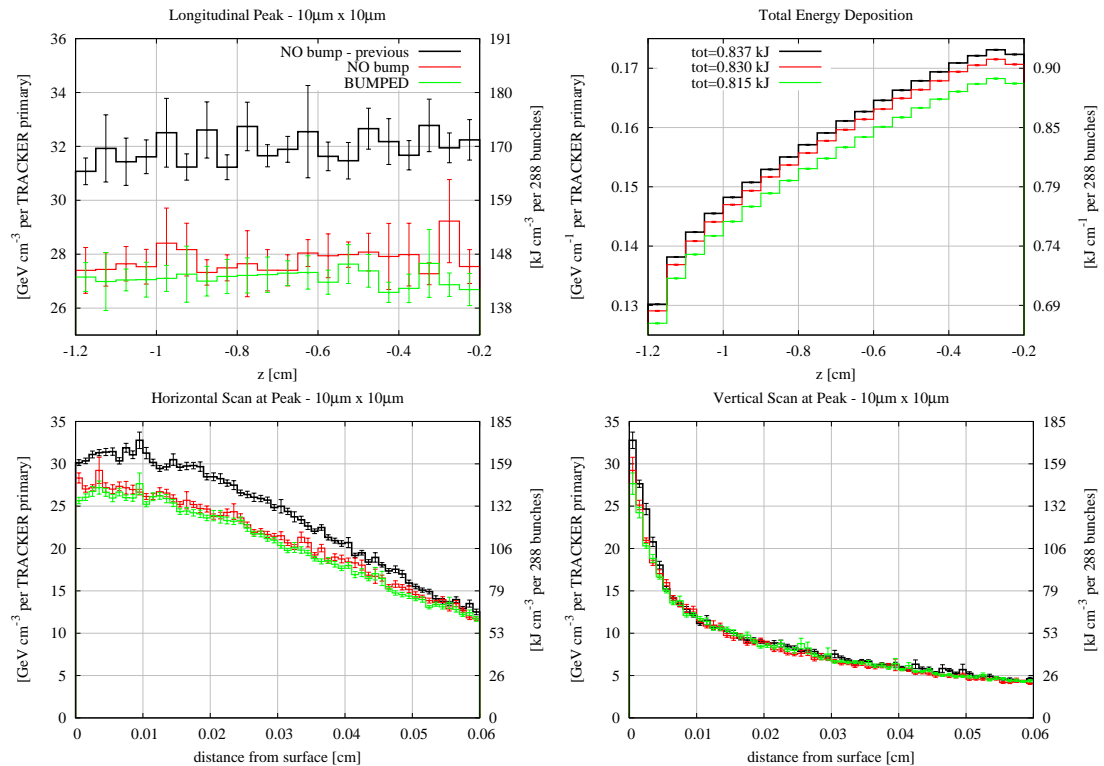


Figure 4.14: Energy deposition in the blades of the SPS scrapers when scraping at  $0 \sigma$ , in the case the permanent magnetic bump in the LSS1 is considered or not in the machine optics. The upper-left frame shows the longitudinal pattern of the peak energy deposition, whereas the upper-right frame shows the longitudinal pattern of the total energy deposition. The lower frames show the horizontal (left frame) and vertical (right frame) scan of the energy deposition at the maximum (see longitudinal pattern of the peak). The speed of the blades is 80 mm/s. Results are obtained simulating the horizontal blade of the BSHV.11759 scraper but for the black curve, obtained simulating the horizontal blade of the BSHV.11771, and are scaled on the right vertical axes to a total beam intensity of  $3.312 \cdot 10^{13}$  protons.

curves), but the scaling does not reflect at all the scaling of the normalised emittances (see Tabs. 4.3 and 4.4 for the beam distributions in case of the black and coloured curves, respectively). As expected, the difference in the beam distribution primarily affects local values rather than total values. Moreover, the presence of the magnetic bump slightly decreases values of energy deposition, for the same reason as the one behind the faster exponential attenuation of the beam intensity, i.e. less protons come back to the scraper blade to interact again.

The horizontal scan shows a FWHM for the new cases (red and green curves) of  $\sim 1$  mm, similar to the one from the previous calculations, in spite of the much larger normalised emittance (see Tabs. 4.3 and 4.4 for the beam distributions in case of the black and coloured curves, respectively). It should be noted that the inner Gaussian has a standard deviation  $\sim 85\%$  the one of the narrow beam, but it describes only 54 % of the beam population; the rest is described by a broader Gaussian distribution. The vertical scan of the new cases shows the same steep gradient previously found. As already observed for the previous cases, the pattern of the energy deposition seems to retain a memory of the original characteristics of the beam distribution on the cleaning plane, whereas along the direction of movement of the blade the energy deposition is extremely localised and collapses in the very first tens of  $\mu\text{m}$  of material directly facing the beam. The longitudinal pattern of the total energy deposition confirms the findings from past investigations, i.e. an increasing trend typical of the development of secondary particle showers in the medium, even if mild. The integrated values are very close to each other, i.e. 0.830 kJ and 0.815 kJ for the new cases (red and green curves, respectively) and 0.837 kJ for the previous calculation with graphite, in case of a train of 288 Nominal LHC bunches (see Tab. 1.5).

Figure 4.15 shows the pattern of proton losses around the SPS ring, in case the permanent magnetic bump in the LSS1 is considered or not in the machine

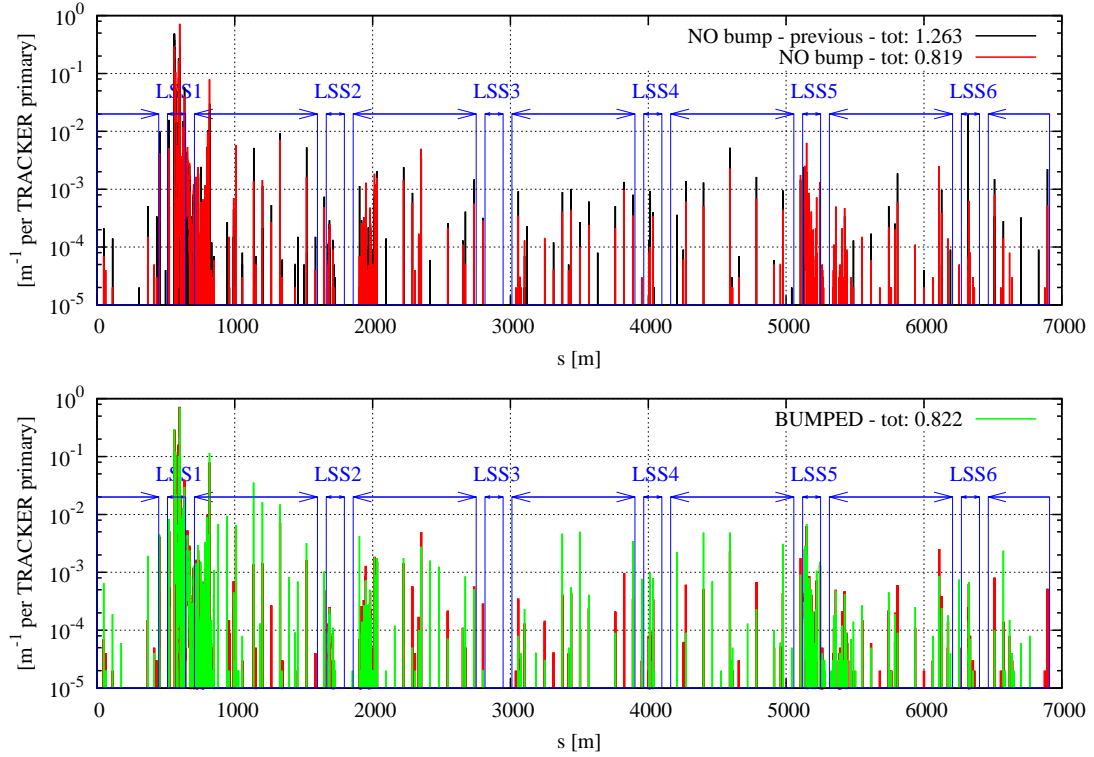


Figure 4.15: Pattern of proton losses around the SPS ring when scraping at  $0 \sigma$ , in the case the permanent magnetic bump in the LSS1 is considered or not in the machine optics. The upper frame shows the comparison between the results from the previous section and new ones without the magnetic bump, whereas the lower frame shows the comparison between new results, in case the magnetic bump is considered or not. The total reports the average number of protons lost per beam proton. Results are obtained simulating the horizontal blade of the BSHV.11759 scraper but for the black curve, obtained simulating the horizontal blade of the BSHV.11771.

optics. There are no major differences in the patterns of the new results with respect to those from the previous section, apart from the losses in the LSS5, as the aperture model in that region has been improved. I also modelled explicitly beam-intercepting devices installed in this location with FLUKA. The totals in the key of the plot report the average number of protons lost per beam proton. In the case of the results from the previous section, an average of 1.26 protons are emitted and lost in the mechanical aperture of the SPS per scraped proton; out of this, an average of  $4.2 \cdot 10^{-2}$  protons are lost in the DS immediately downstream of

the scraper and an average of  $4.0 \cdot 10^{-2}$  protons are lost in the rest of the machine. In the case of the new results, an average of 0.819 and 0.822 protons are emitted and lost in the mechanical aperture of the SPS per scraped proton, in the case where magnetic bump is not considered and when it is considered, respectively; out of these, an average of  $3.7 \cdot 10^{-2}$  and  $2.9 \cdot 10^{-2}$  protons are lost in the DS immediately downstream of the scraper in the case where the magnetic bump is not considered and when it is considered, respectively, and an average of  $3.3 \cdot 10^{-2}$  and  $5.2 \cdot 10^{-2}$  protons are lost in the rest of the machine in the case the magnetic bump is not considered and when it is considered, respectively.

With respect to the results from the previous section, the average number of protons lost per intercepted proton is smaller. This might possibly be due to the fact that the spare scraper has been simulated, which is installed upstream of the operational one (see Fig. 2.7), implying that most of the secondary protons, which are emitted at low-energy and large angle, do not reach the end of the FLUKA geometry, hence they are not sent back to SIXTRACK for continued tracking and eventual loss in the mechanical aperture of the machine. Losses in the DS downstream of the scraper are lower than those previously found, pointing to an increase in the losses immediately downstream of the scrapers. On the other hand, due to the presence of the beam-intercepting devices explicitly modelled in the FLUKA geometry, losses in the rest of the accelerator cannot be immediately compared with previous results.

From the new results, it can be concluded that the presence of the bump leads to a very mild increase in the losses in the machine aperture, as shown by the average number of lost protons per intercepted proton, i.e. from 0.819 to 0.822. The same bump seems to slightly reduce the losses occurring in the DS immediately downstream of the scrapers, as they decrease from  $3.7 \cdot 10^{-2}$  to  $2.9 \cdot 10^{-2}$  protons per intercepted proton. Finally, losses around the rest of the

accelerator grow from  $3.3 \cdot 10^{-2}$  to  $5.2 \cdot 10^{-2}$  protons per intercepted proton, as they are affected by the presence of other beam-intercepting devices, more loaded in the case where the bump is considered, due to the oscillations in the beam closed orbit.

#### 4.2.4 Energy Ramping

Scraping is performed at the end of the energy ramp during the SPS cycle, in order to not populate the abort gap (see Sec. 2.1.4). In fact, if scraping was performed at flat top, protons interacting with the blade might lose enough energy to leave their original bucket and start drifting in longitudinal phase space (see Fig. 3.4, for instance), reaching the empty buckets of the abort gap. On the contrary, during the ramp, the shape of the separatrices [41, 65] would lead the proton to be lost in the mechanical aperture of the accelerator.

#### Simulation Settings

To address the effect of the energy ramp, a new simulation has been run, to be compared with the one with the bump presented in the previous section – in particular, see Tab. 4.4 for the parameters of the beam distribution sampled and tracked. The differences between the two simulations lie just in the settings in input to SIXTRACK concerning the energy ramping, and the average momentum at which the tracked beam has been sampled, i.e. 393 GeV/c. This value of beam momentum has been chosen in order to properly synchronise scraping with energy ramping. The rest of the simulation settings are the same as those reported in Sec. 4.2.1. All the plots here show two curves, with the same colour coding: green refers to the results with the magnetic bump in from the previous section; red refers to new results presented in this section, obtained tracking the beam during the energy ramp and with the bump in.

## Results

Figure 4.16 compares the evolution of the beam intensity and the rate of intercepted protons when scraping at flat top and during the energy ramp. As for the case at flat top, the beam intensity during ramping shows the exponential attenuation with revolutions in the accelerator as soon as the blade reaches the centre of the beam along the axis of movement. The slight difference in the slopes between the two curves is mainly due to two effects related to tracking at lower energies: on one hand, scattering events result in larger emission angles, due to the lower energy carried by the impacting proton; on the other, larger geometrical emittances mean proton orbits feature larger transverse and angular excursions, resulting in longer paths in the scraper blade, and consequently a slight increase in effectiveness of the blade when scattering protons. The larger geometrical emittance, a consequence of the lower beam momentum (see Sec. A.4), is also responsible for the slightly longer time required to fully accomplish scraping, as visible in the zoom of the beam intensity. In fact, due to the larger beam spot size, the protons most peripheral to the beam distribution get intercepted by the blade slightly earlier than at flat top.

To check the synchronisation between the movement of the scraper blade and the energy ramping, Fig. 4.17 shows the evolution of the beam intensity and of the beam energy during the ramp as a function of time, comparing data from the simulation with data from a real case taken as reference. The beam current measurements were taken with a Beam Current Transformer (BCT, see Sec. 4.3.2). If the appropriate time shift is applied to simulation results, the curves of the energy ramp can be made to coincide, as shown in the figure. Applying the same time shift to the evolution of the beam intensity from the simulation, the agreement with the BCT measurement is quite good, with the discrepancies related more to a tilt of the blade (see Sec. 4.2.5) rather than to an error in the

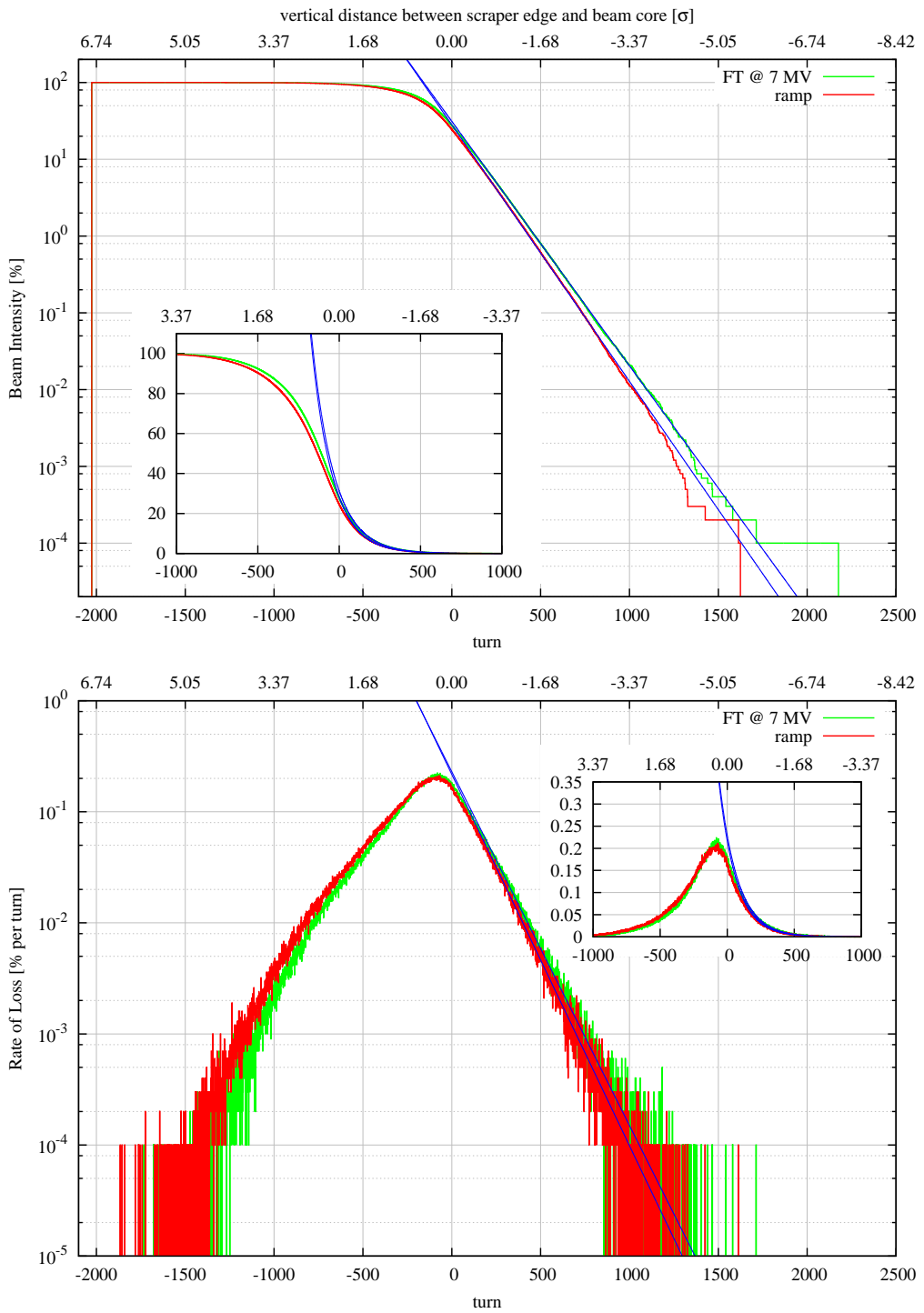


Figure 4.16: Evolution of the beam intensity (upper frame) and rate of intercepted protons (lower frame) when scraping at  $0 \sigma$  at flat top (green curve) and during the energy ramp (red curve). The zooms are focussed on the moment when the scraper blade actually intercepts the beam. Results are obtained simulating the horizontal blade of the BSHV.11759 scraper, moving at 80 mm/s.

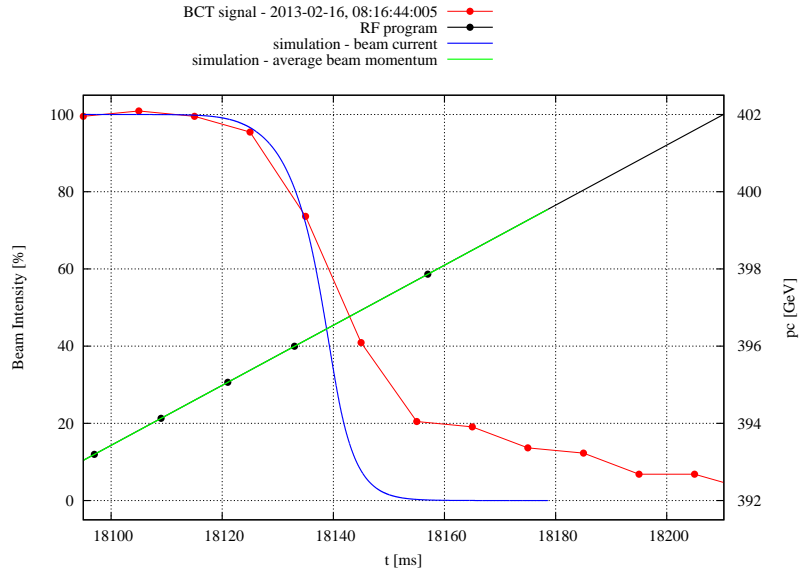


Figure 4.17: Comparison of the time evolution of beam intensity and energy ramping between simulations and data from the SPS at the moment of scraping. The red curve shows the beam current measured by a BCT monitor during full beam scraping at low intensity (i.e. at  $\sim 10^{12}$  protons in the beam) with the horizontal blade of the BSHV.11759, cleaned of the background and normalised to the intensity before scraping, and the black curve shows the RF program of the SPS for LHC beams. The blue curve shows the beam intensity for the same scraper blade and position as predicted by the simulation. The green curve shows the energy of the beam during ramping as from the simulation.

synchronisation between energy ramping and blade movement. Consequently, the synchronisation can be regarded as acceptable.

Figure 4.18 compares the patterns of energy deposition in the blade of the SPS scrapers when scraping at  $0 \sigma$  at flat top and during the energy ramp. As expected, values at flat top are higher than during the ramp. In particular, maximum values (i.e.  $\sim 27 \text{ kJ cm}^{-3}$  and  $\sim 23 \text{ kJ cm}^{-3}$  for a train of 288 LHC Nominal bunches, for the case at top energy and during the ramp, respectively) seem to scale in an almost perfectly linear way with the beam energy (i.e. 450 GeV at flat top and 393 GeV as starting energy for the simulation), even though this turns out to be more by chance rather than a direct effect of the different beam energy. In fact, a linear dependence of the beam spot size on the beam momentum

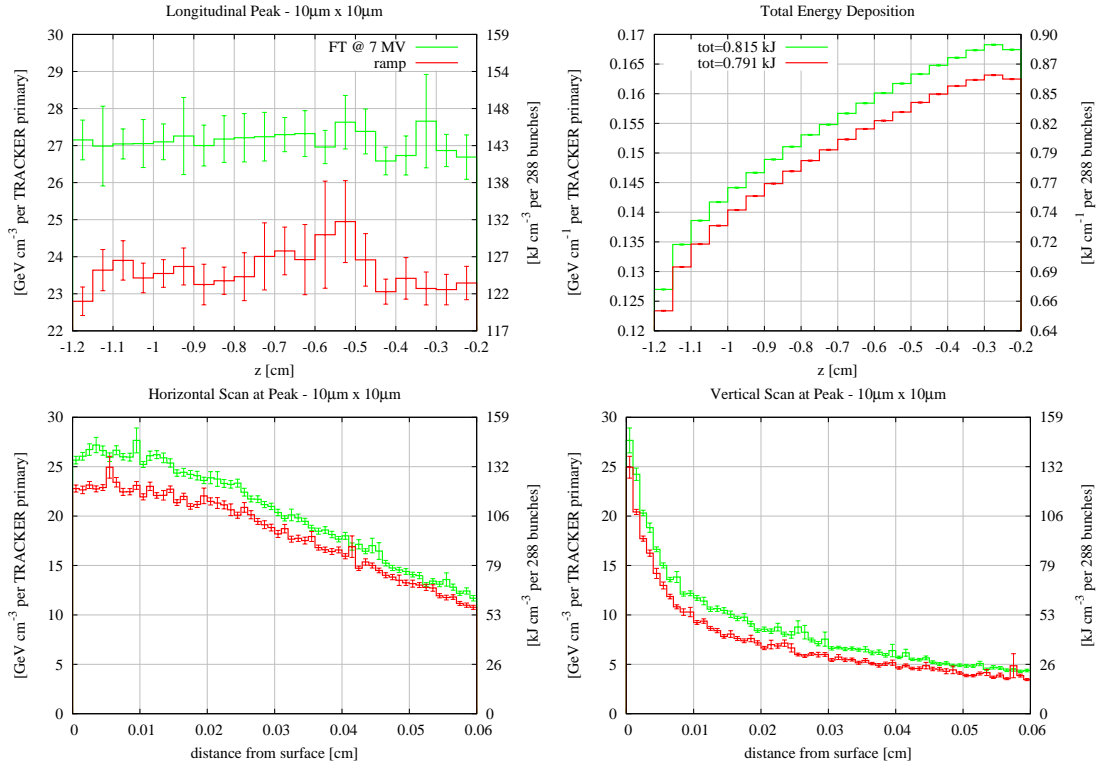


Figure 4.18: Energy deposition in the blades of the SPS scrapers when scraping at  $0 \sigma$  at flat top (green curve) and during the energy ramp (red curve). The upper-left frame shows the longitudinal pattern of the peak energy deposition, whereas the upper-right frame shows the longitudinal pattern of the total energy deposition. The lower frames show the horizontal (left frame) and vertical scan (right frame) of the energy deposition at the maximum (see longitudinal pattern of the peak). The speed of the blades is 80 mm/s. Results are obtained simulating the horizontal blade of the BSHV.11759 scraper, and are scaled on the right vertical axes to a total beam intensity of  $3.312 \cdot 10^{13}$  protons.

can be found through the geometrical emittance, since it affects the beam  $\sigma$  of both planes through a square root operation (see Sec. A.2) and is inversely proportional to the beam momentum (see Sec. A.4). As already seen, and as is visible in the scans shown in the lower frames of Fig. 4.18, the energy deposition map retains a memory of the initial beam distribution only on the cleaning plane, whereas no trace of memory is found on the axis of movement. Finally, no event undergone by protons in the medium gives rise to energy deposition values which scale linearly with the beam momentum. As a confirmation, the scaling of the

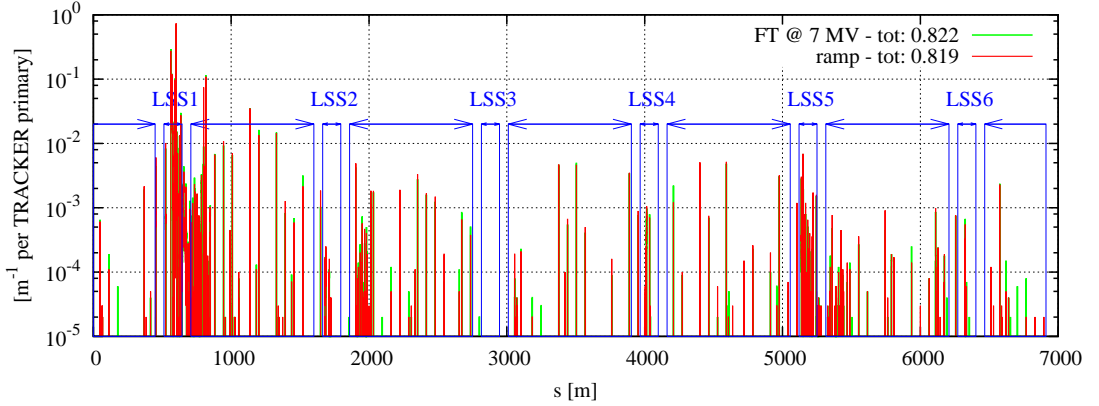


Figure 4.19: Pattern of proton losses around the SPS ring when scraping at  $0 \sigma$  at flat top (green curve) and during the energy ramp (red curve). The total reports the average number of protons lost per beam proton. Results are obtained simulating the horizontal blade of the BSHV.11759 scraper.

total values of energy deposition do not follow at all the linear scaling with the beam energy.

Figure 4.19 compares the patterns of proton losses around the SPS ring when scraping at  $0 \sigma$  at flat top and during the energy ramp. There are no major differences between the two patterns. The totals in the key of the plot report the average number of protons lost per beam proton. In the case of the simulation at flat top, an average of 0.822 protons are emitted and lost in the mechanical aperture of the SPS per scraped proton; out of this, an average of  $2.9 \cdot 10^{-2}$  protons are lost in the DS immediately downstream of the scraper and an average of  $5.2 \cdot 10^{-2}$  protons are lost in the rest of the machine. In the case of the energy ramp, an average of 0.819 protons are emitted and lost in the mechanical aperture of the SPS per scraped proton; out of this, an average of  $2.6 \cdot 10^{-2}$  protons are lost in the DS immediately downstream of the scraper, and an average of  $6 \cdot 10^{-2}$  protons are lost in the rest of the machine. The lower beam energy is clearly responsible for the decrease in the average number of secondary protons produced in nuclear reactions, and thus in the total losses. As seen when checking the effect of the magnetic bump, the decrease in the losses in the DS immediately downstream

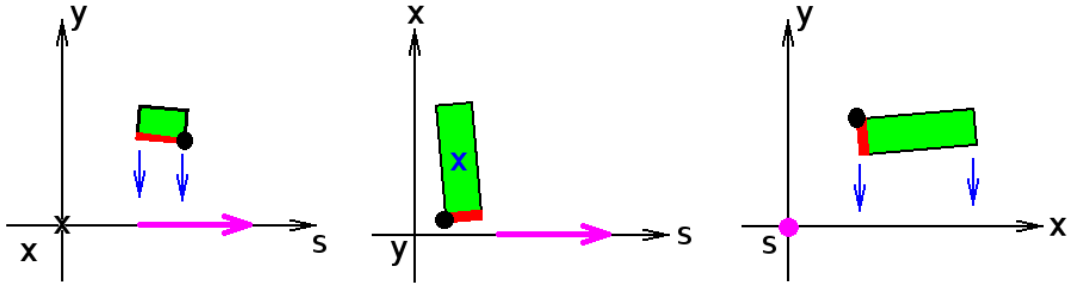


Figure 4.20: Schematics of the tilting of the scraper blade by a positive angle for the present systematic studies: tilting about the horizontal  $x$ -axis (left frame), the vertical  $y$ -axis (middle frame), and the longitudinal  $s$ -axis (right frame). The magenta arrows mark the direction of the beam, whereas the blue ones mark the movement of the blade. The black point marks the innermost tip of the blade, used as reference for setting the scraping position of the blade, and the red band the portion of the blade most loaded with energy deposition values.

of the scraper reflects the presence of more losses in the LSS where the scraper is installed, whereas the increase in the losses around the ring is the effect of an increased rate of interactions in the beam-intercepting devices in the LSS5 and the LSS6 as explicitly modelled in the FLUKA geometry.

#### 4.2.5 Blade Tilting

Given their small dimensions, the blades of the scrapers can be regarded as always aligned, and studies about the effects of a possible misalignment have never been carried out. This section presents a systematic study about the effects of a tilt angle accidentally applied to the blades, due to errors in assembling the mechanics or precision of alignment. Indeed, it will be seen that a tilt angle about the longitudinal axis (i.e. parallel to the  $s$ -coordinate of the local curvilinear reference system, see Fig. A.1) can explain the shape of the beam intensity measured by the BCT used for benchmarking the simulation tools (see Sec. 4.3.4).

## Simulation Settings

A tilt angle of  $3^\circ$  about each axis has been simulated, i.e. about the horizontal  $x$ , vertical  $y$  and longitudinal  $s$  axes, with both positive and negative sign. Figure 4.20 schematically shows how the horizontal scraper blade impacts the circulating beam in the case of a positive angle about each of the three axes. Since all the simulated cases deal with  $0 \sigma$  scraping, the blade is set with the innermost tip available for scraping in correspondence to the centre of the beam. The value of  $3^\circ$  as tilt angle has been chosen not only because its effects turn out to be compatible with signals measured by the BCT (see Sec. 4.3.4), but also because it is quite large with respect to values that can be reasonably expected by mechanical considerations [90], thus maximising consequence on observables of interest. Six new cases are here presented and compared to the case of a perfectly aligned blade. The simulation settings are exactly the same as those used for addressing the effect of the magnetic bump in the SPS LSS1 presented in Sec. 4.2.3, and this one is taken as reference case with a blade perfectly aligned – refer to Tab. 4.4 for the parameters of the beam distribution sampled and tracked.

## Results

Figure 4.21 shows the pattern of energy deposition in the blade of the SPS scrapers when scraping at  $0 \sigma$  with a tilt angle. In general, energy deposition values are comparable to those for a blade perfectly aligned. In particular, the longitudinal patterns of the peak and total energy deposition can be immediately understood keeping in mind the orientation of the blade in each simulated case (see Fig. 4.20). For instance, the tilt by a positive angle about the vertical  $y$  axis concentrates the fluence of protons towards the upstream edge of the blade (see the middle frame in the schematics shown in Fig. 4.20), as it is seen in the patterns of the peak and total energy deposition (see dark green curves in Fig. 4.21). The longitudinal

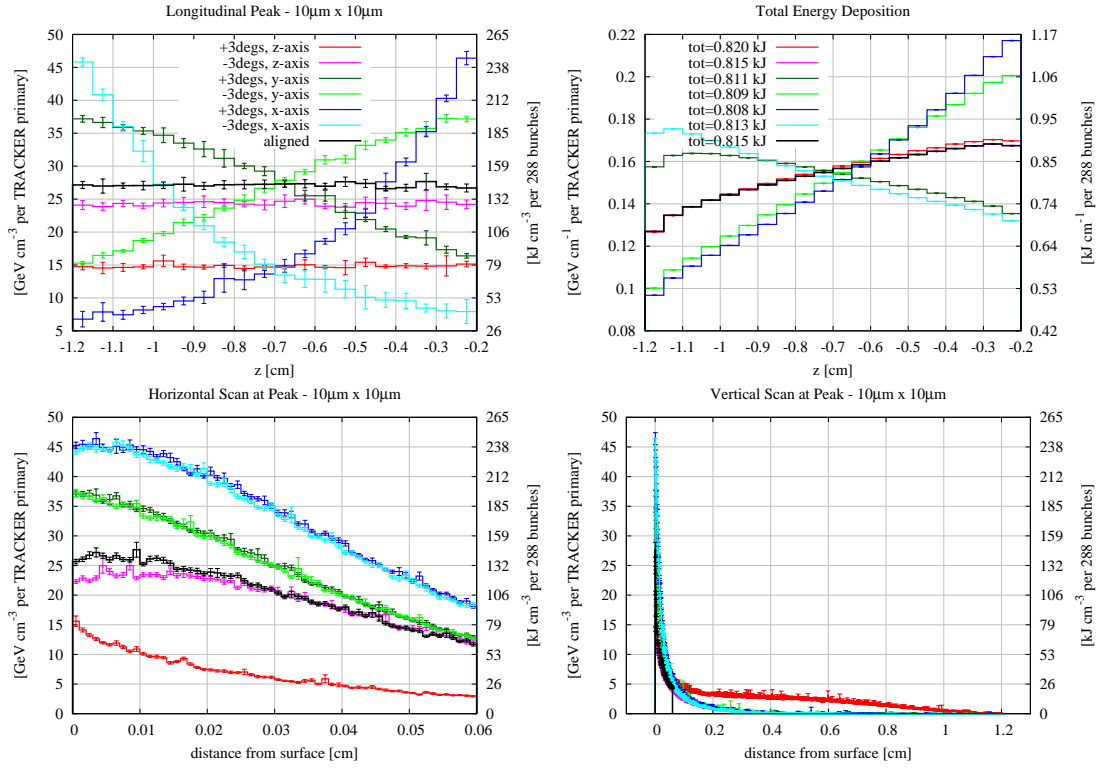


Figure 4.21: Energy deposition in the blades of the SPS scrapers when scraping at  $0 \sigma$  with a tilt angle. The same angle on the three main axes and with opposite sign is shown together with the curves for the blade perfectly aligned. The upper-left frame shows the longitudinal pattern of the peak energy deposition, whereas the upper-right frame shows the longitudinal pattern of the total energy deposition. The lower frames show the horizontal (left frame) and vertical (right frame) scan of the energy deposition at the maximum (see longitudinal pattern of the peak). The speed of the blade is 80 mm/s. Results are obtained simulating the horizontal blade of the BSHV.11759 scraper, and are scaled on the right vertical axes to a total beam intensity of  $3.312 \cdot 10^{13}$  protons.

pattern of the peak energy deposition sees an intensification of values towards the upstream or the downstream face of the blade as can be reasonably expected according to the tilt angle, but for tilting about the longitudinal axis, for which lower values are found no matter the sign of the angle. This is due to the fact that the lower edge of the blade, which actually performs the scraping, sees only a fraction of the beam (see below). The horizontal and vertical scans show that no matter the tilting of the blade, energy deposition values remain concentrated around the lower edge, which actually sees the beam, and the energy deposition

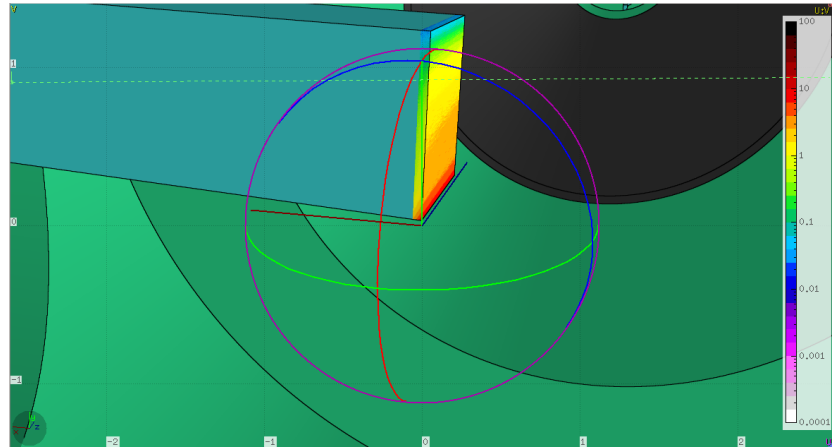


Figure 4.22: The energy deposition in the scraper blade tilted by  $3^\circ$  about the longitudinal axis is concentrated along the lower edge, which directly faces the beam while scraping, even though the core of the beam is then scraped by the face on the inside of the vacuum chamber. Energy deposition in the horizontal blade of the BSHV.11759 as from simulations, layered over a 3D rendering obtained with Flair of the same blade, in graphite. View from upstream. The beam follows the blue axis. When scraping, the blade is swept through the beam from top to bottom. To be noted the tilt angle of the blade about the longitudinal axis with respect to the local reference system.

along the cleaning plane retains a memory of the beam distribution, as already seen.

Figure 4.22 shows a 3D visualisation of the energy deposition map superimposed to the geometry of the blade for the case of a positive tilt angle about the longitudinal axis. The energy deposition is concentrated around the lower edge of the blade, which first sees the beam and intercepts most of it, even though the core of the beam, with the highest concentration of protons, is actually scraped by the innermost face of the blade, on the inside of the vacuum chamber (see next paragraph).

Figure 4.23 shows the evolution of the beam intensity when scraping at  $0 \sigma$  with and without a tilt angle about each axis. All the cases, but one, follow very closely the pattern of the blade when perfectly aligned. The case that differs from all the others is the one with the positive tilt angle about the longitudinal axis.

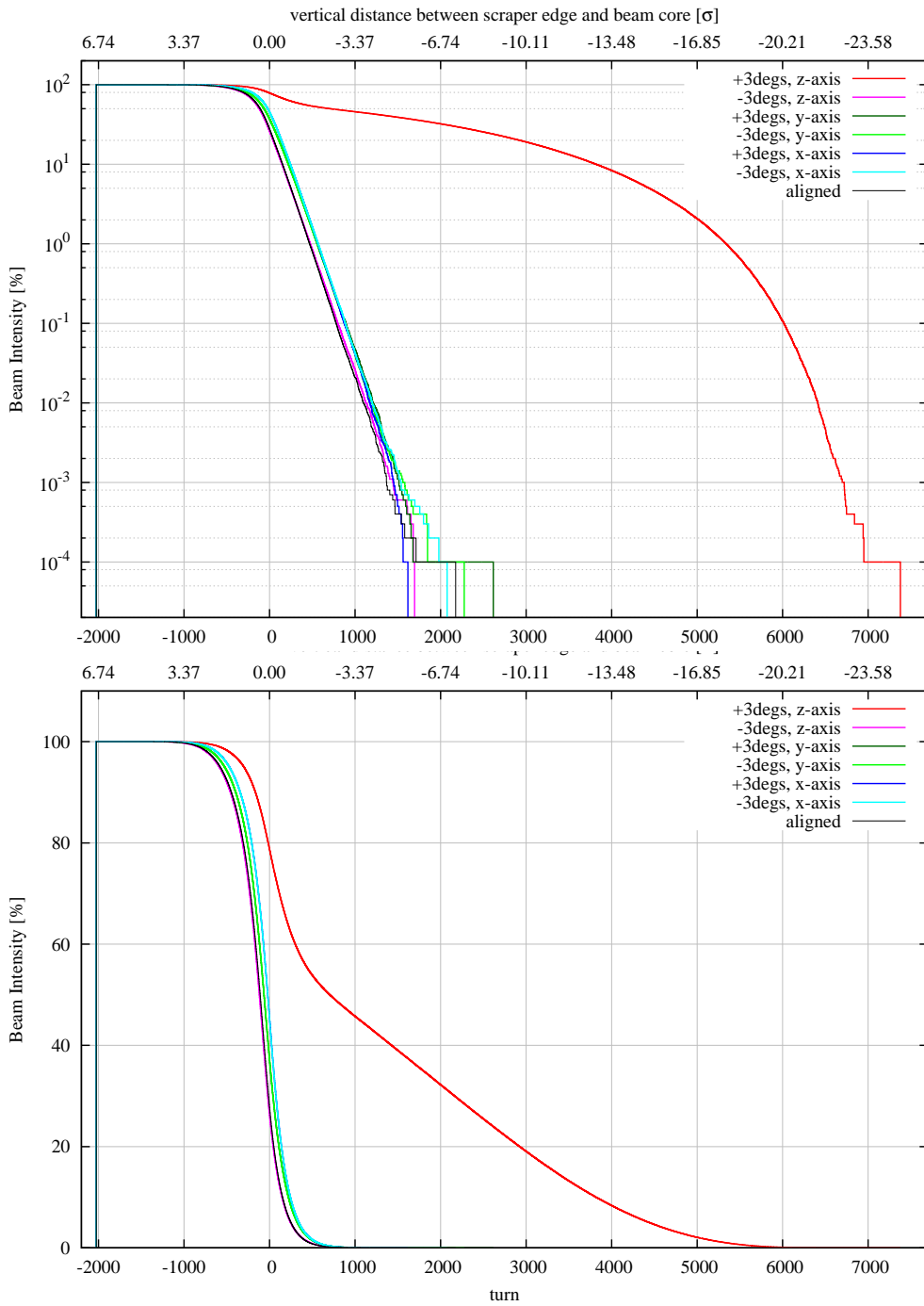


Figure 4.23: Evolution of the beam intensity when scraping at  $0 \sigma$ , in logarithmic (upper frame) and in linear scale, with and without a tilt angle. The curves for the same tilt angle on the three main axes and with opposite sign are shown together with the curves for the blade perfectly aligned. The speed of the blade is 80 mm/s. Results are obtained simulating the horizontal blade of the BSHV.11759 scraper.

This pattern can be explained keeping in mind the schematics shown in Fig. 4.24. Indeed, once the lower edge of the blade (marked by the red point in Fig. 4.24) has reached the core of the beam along the direction of movement (i.e. the vertical axis), the blade has still not reached the centre of the beam on the cleaning plane (i.e. the horizontal one), since it is the innermost tip of the blade (marked by the magenta point in the figure) which has been located in correspondence of the centre of the beam on the cleaning plane. Thus, the innermost face of the blade (marked by the orange line in the figure) has still to scrape off the protons of the core of the beam on the cleaning plane until the innermost tip reaches the centre of the beam on the axis of movement. In particular, the profile as shown in the plot with the logarithmic scale in Fig. 4.23 indicates that the regime of exponential attenuation is never reached until the very end of scraping; the profile as shown in the plot with the linear scale highlights some features peculiar to this blade tilting, with a profile at the beginning slower than the one of all the other cases, and an extremely long tail, which is responsible for most of the time required for scraping. A knee marks the separation between the two regimes. Both are dominated by the speed of the blade, implying that the lower the speed, the longer both regimes are, with the knee staying at the same height. The position of the knee depends on the angle, and for a smaller angle it is found at a lower intensity and closer in time to the pattern of the blade perfectly aligned. As it can be understood looking at Fig. 4.24, the change of regime marked by the knee coincides with the innermost face of the blade taking over the scraping of protons.

Figures 4.25, 4.26 and 4.27 show the pattern of proton losses around the SPS ring in case of a tilt about the longitudinal  $s$ -axis, about the vertical  $y$ -axis, and about the horizontal  $x$ -axis, respectively, compared to the case of the blade perfectly aligned. There are no major differences among the patterns as well as

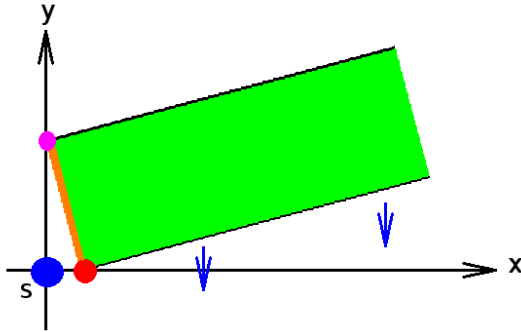


Figure 4.24: Schematics of the tilting of the scraper blade by a positive angle about the longitudinal  $s$ -axis. The blade is moved from top to bottom, as shown by the blue arrows. The beam comes out of the page, centred where indicated by the blue point. The red point marks the lower edge of the blade, the magenta point marks its innermost tip, and the orange line marks the innermost face.

in the totals, reported in the key of the plots.

#### 4.2.6 Conclusions

The characterisation of the scraper blades has been updated and extended with respect to past investigations. The updates involve operational settings, e.g. machine optics and location of the scrapers in the ring, and the simulation tools, e.g. the use of **SIXTRACK** as tracking code, an improved thin lens description of the SPS lattice, a detailed model of the aperture profile in the machine, and the explicit implementation in the **FLUKA** geometry of other beam-intercepting devices installed in other portions of the SPS ring, to better describe losses in the ring due to re-interactions of protons in these devices. Reference values for the existing system, are given with beam at top energy, i.e. at 450 GeV/c, with the SPS Q20 optics and the permanent magnetic bump in the LSS1 not taken in consideration, for a graphite blade perfectly aligned and moving at the nominal speed of 80 mm/s. For this case, a relatively narrow Gaussian beam with of 1  $\mu\text{m}$  normalised emittance and  $\sigma_\delta = 10^{-4}$  is considered.

As a consequence of the movement of the blade, values of energy deposition

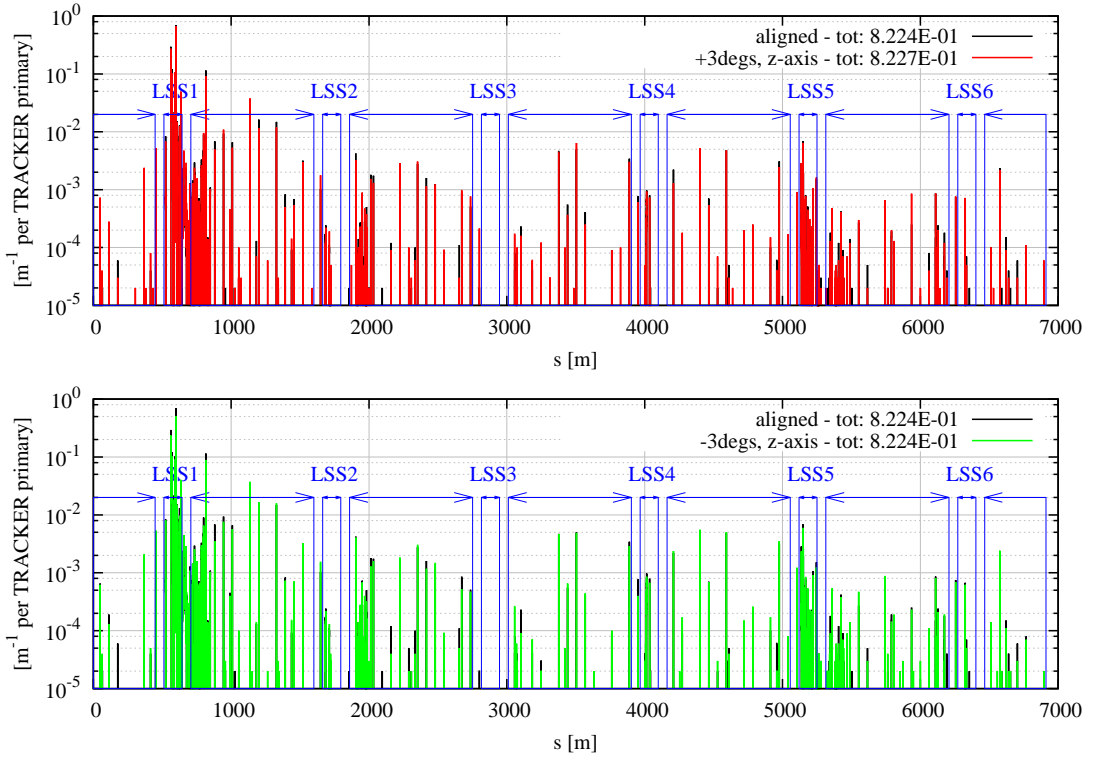


Figure 4.25: Pattern of proton losses around the SPS ring when scraping at  $0\sigma$  with a blade tilted about the longitudinal  $s$ -axis. The curves for a positive (upper frame) and a negative (lower frame) tilt angle of  $3^\circ$  are compared to the one for the blade perfectly aligned. The total reports the average number of protons lost per beam proton. Results are obtained simulating the horizontal blade of the BSHV.11759 scraper.

are concentrated around the edge of the blade which directly faces the beam. On the plane of cleaning, the energy deposition map seems to retain some memory of the dimensions of the tracked beam, resulting in a mild dependence of the maximum energy deposition on the beam spot size. The graphite blades of the scrapers are subject to values of energy deposition up to  $30\text{--}35\text{ GeV cm}^{-3}$  per proton, corresponding to  $160\text{--}185\text{ kJ cm}^{-3}$ , in the case of full beam scraping, i.e. at  $0\sigma$ , and at full beam intensity, i.e. per train of 288 bunches of Nominal LHC beam. These values are too far above the limit for graphite reported in Tab. 4.2, taken as the heat necessary to locally sublimate graphite at atmospheric pressure, making this scenario extremely challenging as far as the robustness of

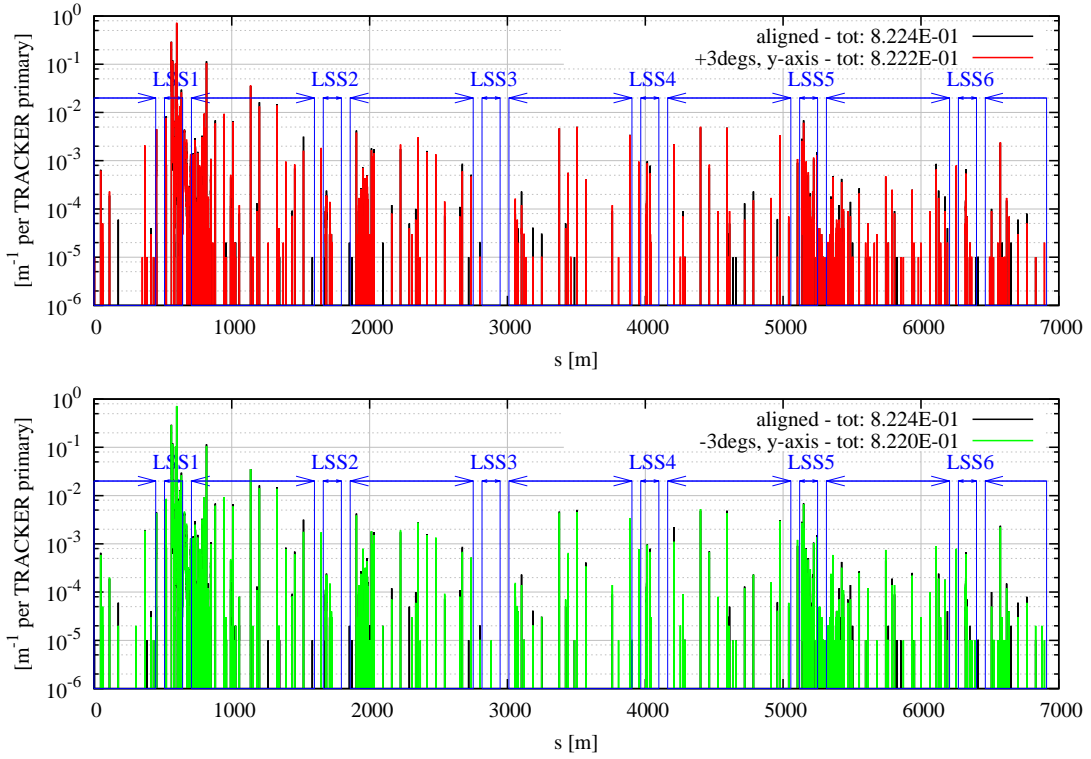


Figure 4.26: Pattern of proton losses around the SPS ring when scraping at  $0\sigma$  with a blade tilted about the vertical  $y$ -axis. The curves for a positive (upper frame) and a negative (lower frame) tilt angle of  $3^\circ$  are compared to the one for the blade perfectly aligned. The total reports the average number of protons lost per beam proton. Results are obtained simulating the horizontal blade of the BSHV.11759 scraper.

the scraper blade is concerned. Nevertheless, this is more an accident scenario rather than an operational one, as in case of beam injection into the LHC only the tails are scraped off, and, in case the scrapers are used as a tool to characterise the transverse distribution of the circulating beam, diagnostics are not usually performed at full beam intensity. Total values are in the range 0.8–0.9 kJ for the same train of bunches.

The characterisation of the scraper blades has also been performed in terms of main scattering events undergone by the intercepted protons. Ionisation and MCS are the events that scraped protons undergo most frequently. They span many orders of magnitude in terms of energy loss per single proton passage,

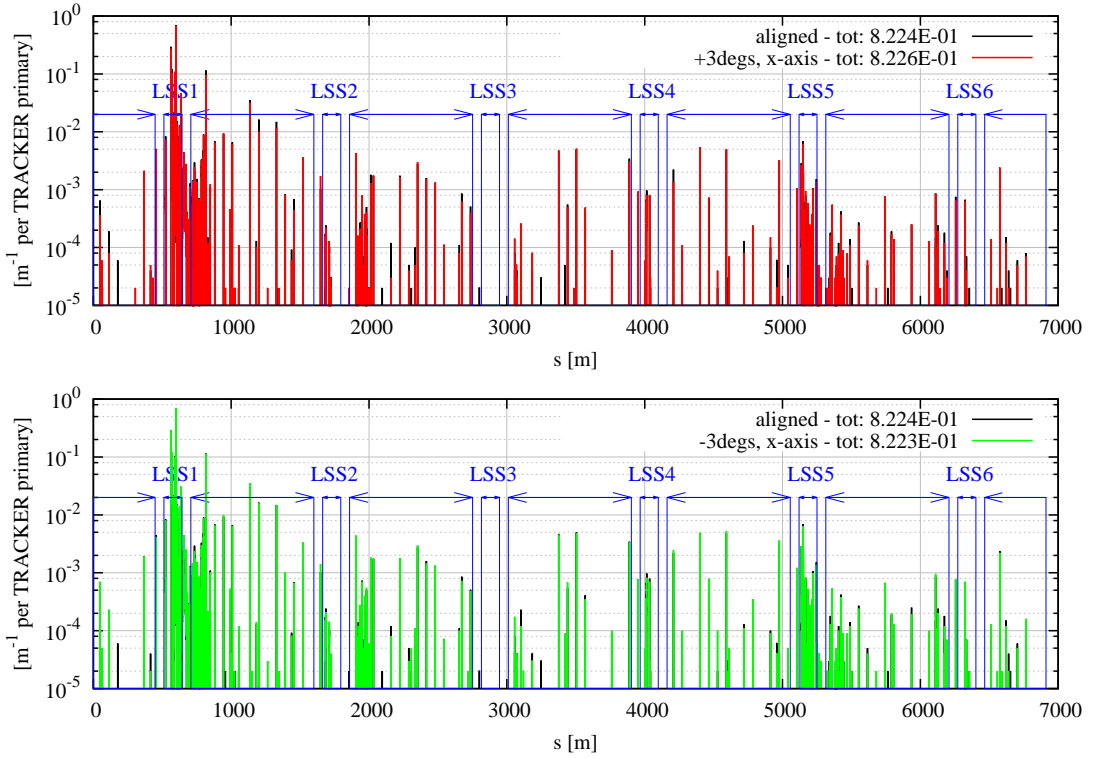


Figure 4.27: Pattern of proton losses around the SPS ring when scraping at  $0 \sigma$  with a blade tilted about the horizontal  $x$ -axis. The curves for a positive (upper frame) and a negative (lower frame) tilt angle of  $3^\circ$  are compared to the one for the blade perfectly aligned. The total reports the average number of protons lost per beam proton. Results are obtained simulating the horizontal blade of the BSHV.11759 scraper.

from a few hundred eV up to a hundred GeV. Elastic scattering results in a very limited energy loss. Single diffractive events are responsible for most of the events involving an energy loss of some tens of GeV.

The beam intensity decreases with time during scraping. In particular, the profile at the beginning is dominated by the beam distribution and the speed of the blade, whereas once the blade has reached the centre of the beam along the axis of movement a regime with an exponential attenuation is found, depending only on the characteristics of the blade (e.g. density and inelastic interaction length of the material, and length of the blade), the betatron tune and the aperture profile inside the machine.

Secondary protons are emitted as a consequence of nuclear inelastic interactions in the blade. An average of 0.8–0.85 secondary protons are emitted and lost in the ring per intercepted proton; out of this, an average of  $4\text{--}5\ 10^{-2}$  protons per intercepted proton are lost in the DS immediately downstream of the scraper, and a similar amount are lost in the rest of the machine excluding the LSS where the scraper is installed. Protons lost in the DS have an energy larger than 100 GeV, whereas those lost in the rest of the ring have an energy larger than 435 GeV. Locally, at the scraper, proton losses are mostly due to “deep” inelastic and single diffractive scattering, whereas in the rest of the machine losses are mainly due to elastic scattering and MCS, and occasionally by single diffractive scattering. The DS immediately downstream of the scrapers represents a transition region, where losses due to elastic scattering and MCS start to surpass losses due to “deep” inelastic and single diffractive scattering.

Effects induced by operational aspects previously unexplored in literature have been addressed as well, temporarily changing some simulation parameters with respect to the aforementioned ones. In particular, the sampled beam follows a more realistic description, characterised by double Gaussian distributions with tails more populated than in the case of a simple Gaussian, larger normalised emittances ( $\sim 2\ \mu\text{m}$ ) and larger values of  $\sigma_\delta$  ( $2\ 10^{-4}$ ).

**Magnetic bump in the LSS1** A permanent magnetic bump is present in the LSS1 to ease dumping of high energy protons. In the case of the Q20 optics it induces important oscillations in the closed orbit. Simulation results show that the presence of the bump has an impact on the observables used to characterise the scraper blades, though limited. Its main effect is to decrease the mechanical aperture of the machine, with a consequent increase of losses around the ring, although of less than 0.5 %. This small increase in the losses is confirmed by slightly lower energy deposition values in the

blade and a slightly faster exponential attenuation of the beam intensity with respect to what happens when the bump is not considered. Difference in values can be regarded as substantially negligible for practical considerations. The main reason for these modifications is to be found in scattered protons not able to get back to the scraper blade any more, since the closed orbit modified by the presence of the bump leads them to touch the mechanical aperture of the machine earlier than what happens without the bump;

**Energy ramping** Scraping is operationally performed at the end of the energy ramp, to avoid populating the abort gap. All the effects seen on relevant observables are mainly related to the lower energy at which scraping is performed rather than to the fact of operating the scrapers during the ramp. In particular, the larger spot size, consequence of the larger geometrical emittance, is responsible for the slightly longer time required for scraping (the beam is larger, thus the blade starts to scrape protons slightly in advance with respect to what happens at top energy), for the lower values of energy deposition (beam protons have a broader distribution), and for slightly lower losses in the ring (less secondary protons are produced, and on average of lower energy, less likely to reach the DS and the rest of the ring; moreover, they are more likely to interact with beam-intercepting devices located elsewhere in the accelerator). Variations can be neglected for practical considerations, but for the maximum energy deposition there is a shift from  $27 \text{ GeV cm}^{-3}$  per proton to  $23 \text{ GeV cm}^{-3}$  per proton, i.e. a variation of  $\sim 15\%$ ;

**Blade tilting** Even though the scraper blades are small objects and can thus be always considered as aligned, a systematic study of the effects induced by tilting of the blade has been carried out. In general, for the considered

values of tilt angles, larger than what can be reasonably expected by mechanical considerations [90] but in agreement with what was reconstructed from measurements (see later the benchmark against BCT readouts), thus maximising effects, the net effect is an intensification of energy deposition values up to a factor of 2 on a corner of the blade according to the tilt angle. The profiles of the beam intensity with time and of the losses around the ring basically do not change. The only exceptional case is represented by a positive angle blade tilt about the longitudinal axis, as this changes quite substantially the impact conditions of the beam onto the blade. Consequences are a decrease in the peak energy deposition values by a factor of 2 for the considered angle, and more importantly a much longer time required for scraping, in the order of a factor of 6 with respect to the case of a perfectly aligned blade.

The effects induced by a different speed of the blade have not been reported here, as they have not been studied in a systematic way. Nevertheless, the expected behaviour is an increase in the scraping time (as shown also by some cases dedicated to the benchmark of simulation results against measurements, reported in Sec. 4.3.4) and in peak energy deposition values for a lower speed, whereas no relevant changes are expected on the loss pattern. These effects are expected not to depend linearly on the speed of the blade (see also Sec. 4.1, where effects due to a different speed of the blade have been shown for one value).

## 4.3 The Burst Test and the Benchmark of the Simulation Tools

All the results from simulations presented in this chapter prove the presence of extremely high values of energy deposition in the scraper blades in case of scraping

at  $0 \sigma$  (i.e. with the innermost face of the blade in correspondence to the centre of the beam) at full beam intensity (see Fig. 4.6 or Sec. 4.2.6), with values far above the limits for graphite reported in Tab. 4.2. This is more an accident scenario rather than an operational one, as in case of beam injection into the LHC only the tails are scraped off, and, in case the scrapers are used as a tool to characterise the profile of the circulating beam, diagnostics are not usually performed at full beam intensity.

A test was carried out to verify with beam how realistic are such high values of energy deposition, as well as the actual endurance of the blades. The expression “burst test” comes from the extremely high levels of energy deposition foreseen by the simulation. The basis of the idea is to test the blades with the worst conditions possible as far as local energy deposition is concerned, and then find traces of damage with a microscopic analysis, to benchmark the predictions by the simulation. Hence, the test foresaw to scrape the SPS beam at full intensity at  $0 \sigma$  with both the horizontal and the vertical blades, and then to analyse the blades, to find traces of material damage.

While collecting information to reconstruct the conditions of the beam and the scrapers during the test, it was realised that signals from the BCT, which records the beam intensity during the SPS cycle as a function of time, and the readouts from the BLMs located along the ring, which record the signal from secondary particle showers started by beam protons intercepted by the scraper blade or by the mechanical aperture, could be used to benchmark the simulation tools. The former measurements contain information about the beam distribution and the operational settings of the scraper blade, like speed and possible tilt angle; these are relevant for the estimation of actual levels of energy deposition in the blade inducing damage. Moreover, they can confirm that multi-turn effects, extremely important for a short beam-intercepting device like the scrapers, are

correctly treated by the coupling. The latter set of measurements can confirm that scattering events are properly handled. It should be noted that while a set of BCT measurements is made of many acquisitions in time over a single SPS cycle (see Figs. 2.4 or C.1, for instance), BLM readouts are integrated over the whole SPS cycle, giving a resolution in space according to the location of each monitor, but not in time. BCT readouts have been retrieved from the computers in the CERN control room, whereas BLM readouts have been retrieved from the main logging system of CERN, i.e. Timber [91].

In the following, a brief introduction to the set up of the test is given and the main outcomes are presented, including the images from the Scanning Electron Microscope (SEM) which detected damage to the blades [92]. A brief description of the monitors which record the beam current intensity and beam losses (through detection of secondary particle showers) used for the benchmark of simulation results is added afterwards. The measured BCT and BLM signals are analysed and the benchmark of the simulation tools is presented. Finally, conclusions are drawn regarding the tests and the lessons learnt are recorded.

The test shows that high levels of energy deposition are reached in the blades when performing full beam scraping at full beam intensities, confirming expectations from simulations; values are so high that sublimation is locally induced in the blade. Moreover, the benchmark proves the maturity of the simulation tool.

While the burst test was proposed and performed by colleagues responsible for the operation of the SPS and the microstructural analyses of the blades were carried out by CERN colleagues expert in material structural analysis, the full analysis of BCT and BLM signals; the performance and analysis of the simulations required for the benchmark, including the effort of development of the FLUKA geometry for the quantitative benchmark against BLM signals (see later); the comparisons between simulation results and measured data; and the estimations

of the beam distribution in machine, the actual operational settings of the blades, the amount of scraped beam and actual levels of energy deposition in the blades during the burst test; are all original contributions for this thesis.

### 4.3.1 Set–Up of the Burst Test

The burst test of the scraper blades was carried out at the end of the SPS activity in February 2013, just before the beginning of the LS1, more precisely between 7:00 AM and 9:00 AM (Geneva local time) on Saturday 16<sup>th</sup> February 2013 [93]. The test was carried out using the blades of the spare scrapers, i.e. the BSHV.11759, since they had been rarely used during the LHC Run 1, and thus recognising possible signs of damage would be easier than with the operational ones. The test was performed with the Q20 optics.

A set of preliminary measurements were performed with a Wire Scanner (WS) to characterise the distribution of the beam available in machine and its emittance. A WS is a device which sweeps a thin carbon wire through the beam; the scattering taking place in the wire generates secondary particle showers which are recorded by a scintillator located downstream of the scanner. Correlating the signal in the scintillator to the position of the wire during its movement, the profile of the beam can be measured [94]. Figure 4.28 [93] shows the scans performed before the test. The comparison between the data and the Gaussian fit shows that the beam has a bell–shape distribution on both planes, with highly populated tails, more than for a simple Gaussian distribution. The legend of the figure shows the main settings of the WS, including beam energy at which the scans have been performed and the normalised emittance estimated from the Gaussian fit to the core of the distribution, reported in Tab. 4.5 (second column).

Prior to the burst test of each blade, a set of SPS cycles were loaded with low intensity beams of  $\sim 10^{12}$  protons, in order to scan the beam with each blade and

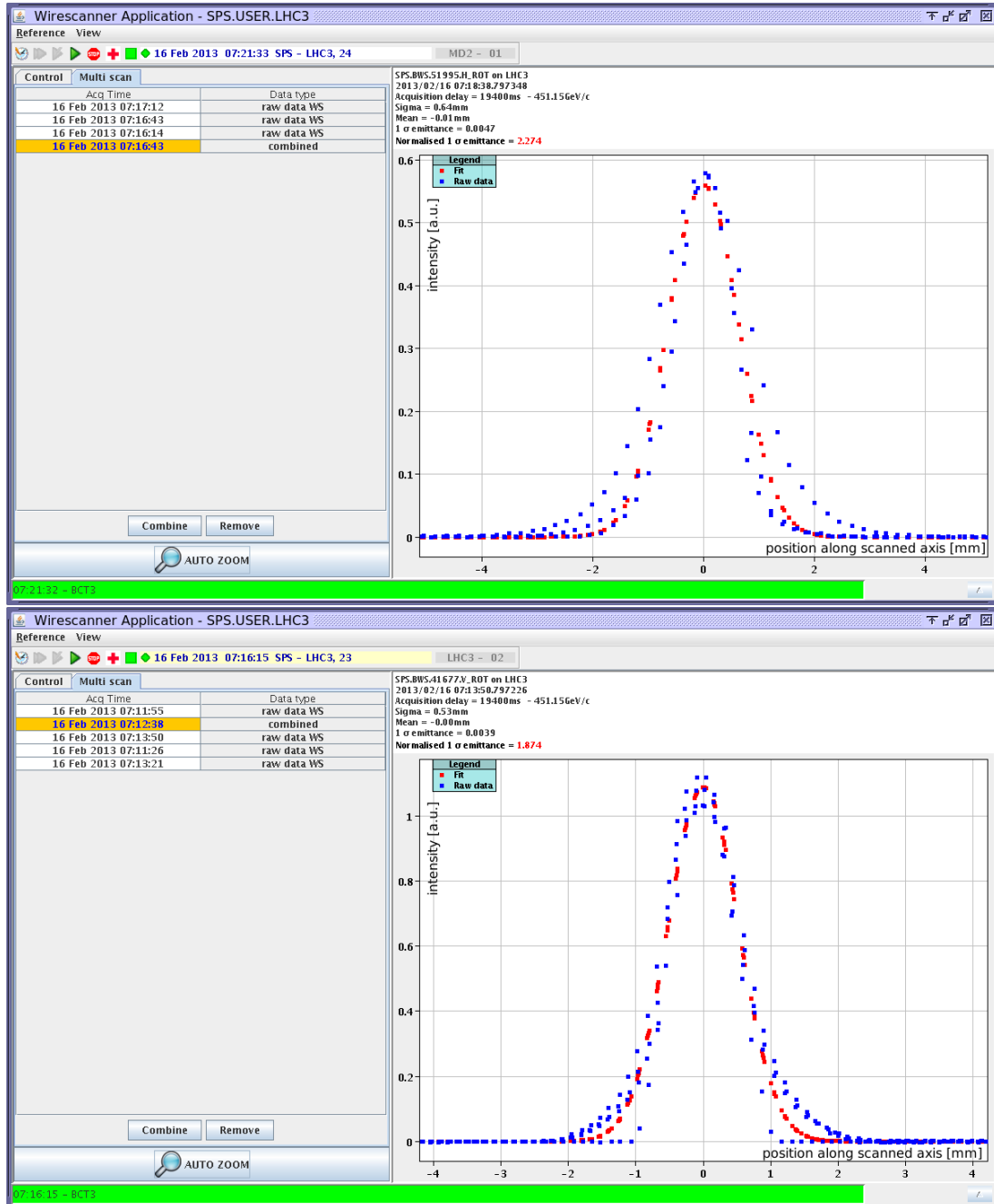


Figure 4.28: WS measurements [93] showing the spatial distribution of the beam on the horizontal (upper frame) and on the vertical (lower frame) planes. For each frame, multiple scans (blue points) are superimposed, and a Gaussian fit (red points) performed.

plane	$\epsilon_N$ [ $\mu\text{m}$ ]	$z_{\text{test}}$ [mm]	$z_{\text{regular}}$ [mm]
H	2.274	-11	-13.2
V	1.874	5.7	3.5

Table 4.5: Settings of the burst test: normalised emittance as from the fit to WS measurements (2<sup>nd</sup> column); position of the blade during the test (3<sup>rd</sup> column), corresponding to the centre of the beam; position of the blade during regular scraping (4<sup>th</sup> column), to check the performance of the blades before and after the test.

thus identify the correct settings, in mm, corresponding to the centre of the beam. Several transverse positions were set, and for each of them the reduction in the beam intensity recorded. The position which produced a reduction of 100 % was taken as the one marking the centre of the beam; see Tab. 4.5 (third column). The low intensity was necessary to avoid damaging the blades prior to the main experiment. The full collection of measurements is reported in App. C.

Immediately before and after the burst test of each blade, a few SPS cycles were filled with full intensity beams of  $\sim 3 \cdot 10^{13}$  protons, to detect any change in the blade performance during regular scraping, i.e. when removing a few percent of the beam intensity. Table 4.5 reports the settings in mm (fourth column) corresponding to the regular scraping of tails, off by 2.2 mm with respect to the settings of the burst test. These measurements are also collected in App. C.

### 4.3.2 SPS Monitors

Monitor readouts are used to reconstruct the actual conditions of scraping during the burst test and for benchmarking the simulation tool. The measurements reported here come mainly from the BCT installed in the SPS, and the BLM distributed around the ring, including the LSS1, where the scrapers being tested are installed.

The Beam Current Transformer (BCT) is a device which measures the beam

intensity, using the working principle of a transformer. The BCT is made of a metallic torus, with a wire wound around it. The beam passes along the axis of the torus, and the magnetic field lines generated by the bunched beam get trapped in the torus and induce a current in the wire, which is read. The SPS BCT is located in the LSS3, where the RF cavities are installed (see Sec. 2.1.1), in cell 18. As the hardware is based on a DC transformer, the analogue bandwidth has an upper limit, i.e.  $\sim 50$  Hz at  $-3$  dB [95]. This implies that the signal given by the SPS BCT cannot faithfully reproduce fast variations of the beam current; for instance, a beam dump event is not seen as an abrupt drop down from the signal with circulating beam to 0 (or to the noise level), but few additional middle points are displayed (see Fig. 4.30, for instance). An Analog-to-Digital Converter (ADC) system digitises the signal every 10 ms, for a total of 1924 acquisitions and 19.24 s. When reading high beam currents (as in the case of proton beams, shown in all the measurements presented here), the calibration factor is  $1.59 \cdot 10^{10}$  charges per bit<sup>4</sup>. The calibration factor is also used as Least Significant Bit (LSB), for the estimation of the quantisation error.

The BCT measurements are saved on the local computers in the control room, and not in Timber. Moreover, timing is not the same as the one of the SPS cycle; there is a delay of 625 ms, identical to the time between the start of the SPS cycle and the first injection in the SPS (see Sec. 2.1.4). Table 4.6 summarises the main parameters of the BCT signals.

The SPS Beam Loss Monitors (BLMs) are nitrogen-filled ionisation chambers [96]. They have a cylindrical shape, with the region of active gas 19 cm in length. 30 parallel plates separated by a distance of 5.75 mm and with a diameter of 9.2 cm are used to collect the secondary charges. The gas volume is  $\sim 1$  l, containing over-pressured nitrogen at 1.1 bar, for a density of  $1.29 \text{ g dm}^{-3}$ .

---

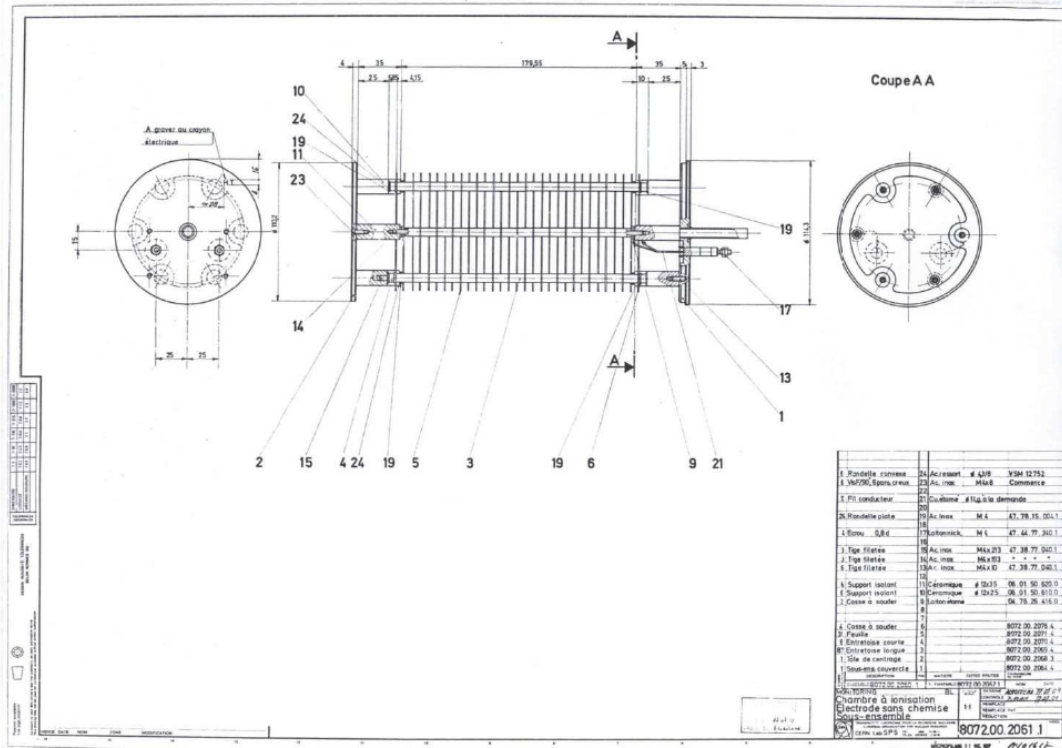
<sup>4</sup>It should be noted that this value is actually given by parsing many BCT readouts and looking for the smallest change in the signal, in absolute value.

parameter	value
sampling rate	100 Hz (10 ms)
total number of acquisitions	1924
total duration of signal	19240 s
delay wrt SPS timing	625 ms
calibration factor	$1.59 \cdot 10^{10}$
analogue bandwidth	-3 dB @ 50 Hz

Table 4.6: Main parameters of the BCT signals used for the benchmark of the simulation tools against measurements.

Figure 4.29 shows the main technical drawing of the SPS BLMs.

A total of 268 BLMs are distributed all around the SPS ring. In particular, a BLM is regularly assigned to each half-cell of the accelerator, in the same longitudinal position along the cell and with a constant transverse offset with respect to the machine axis; additional BLMs are installed in the LSSs, and their positions depend on the devices installed there. Unfortunately, there is no database stating the precise locations of these monitors. Thus, their positions along the ring have been deduced from the technical drawings of the SPS [97], and the lattice structure of the accelerator [98]. In some cases, the drawings showing zooms on specific cells of the SPS LSSs are not consistent either on the longitudinal or on the transverse (i.e. how far off the machine axis) position of the BLMs. In these situations, priority is given to the detailed drawings. Transversely, the related uncertainty can be similar to the BLM dimensions, whereas longitudinally the related uncertainty can be even larger than the BLM dimensions. While longitudinally off-positioning BLMs even by a meter can be neglected when analysing patterns around the whole ring (7 km in length), the uncertainty on the positions becomes relevant when coming to the quantitative benchmark against BLM readouts. Results from the simulations are extremely sensitive to the details of the FLUKA geometry (see later), as these monitors are sensitive to the development of secondary particle showers. The burst test



location	Calib. Fact. [Gy]	Max [Gy]	location	Calib. Fact. [Gy]	Max [Gy]
Sextant 1	$1.140 \cdot 10^{-4}$	0.2335	LSS1	$1.27 \cdot 10^{-3}$	2.6010
Sextant 2	$1.140 \cdot 10^{-4}$	0.2335	LSS2	$5.28 \cdot 10^{-4}$	1.0813
Sextant 3	$1.104 \cdot 10^{-4}$	0.2261	-	-	-
Sextant 4	$1.100 \cdot 10^{-4}$	0.2253	LSS4	$1.14 \cdot 10^{-4}$	0.2335
Sextant 5	$1.140 \cdot 10^{-4}$	0.2335	LSS5	$1.27 \cdot 10^{-3}$	2.6010
Sextant 6	$1.100 \cdot 10^{-4}$	0.2253	LSS6	$5.28 \cdot 10^{-4}$	1.0813

Table 4.7: Calibration factors of the SPS BLMs and maximum signal they can read given the 11-bit ADC system, grouped according to their positions along the ring. The BLMs regularly distributed along the ring are grouped in Sextants, i.e. a segment of accelerator which includes an LSS and half of the arcs upstream and downstream of it, listed on the left, whereas the additional ones installed in the LSSs are listed on the right. There are no BLMs in LSS3.

each BLM is affected by all the processes leading to a local loss, superimposing the contribution from different events to the signal (see Sec. 2.1.4). This will have an impact on the choice of the BLM measurements and their handling.

### 4.3.3 Outcomes of the Test

The test was conducted by scraping the whole beam at full intensity, i.e. with  $\sim 3 \cdot 10^{13}$  protons. While performing the analysis of monitor readouts to reconstruct what actually happened during the test, it was realised that the beam was prematurely dumped. Indeed, while scraping the whole beam at full intensity, secondary particle showers were so intense that the BLM which was closest to the test scraper triggered a beam dump, interrupting the test. This happened during the testing of both blades.

Figure 4.30 shows the BCT signals recorded during the burst test of each blade. Both signals are characterised by a sharp decrease in the beam intensity at the moment of scraping; the zoom shows how difficult it is to disentangle the abrupt change expected because of the beam dump from the pattern due to scraping. On one hand, this is due to the fact that the upper limit to the DC

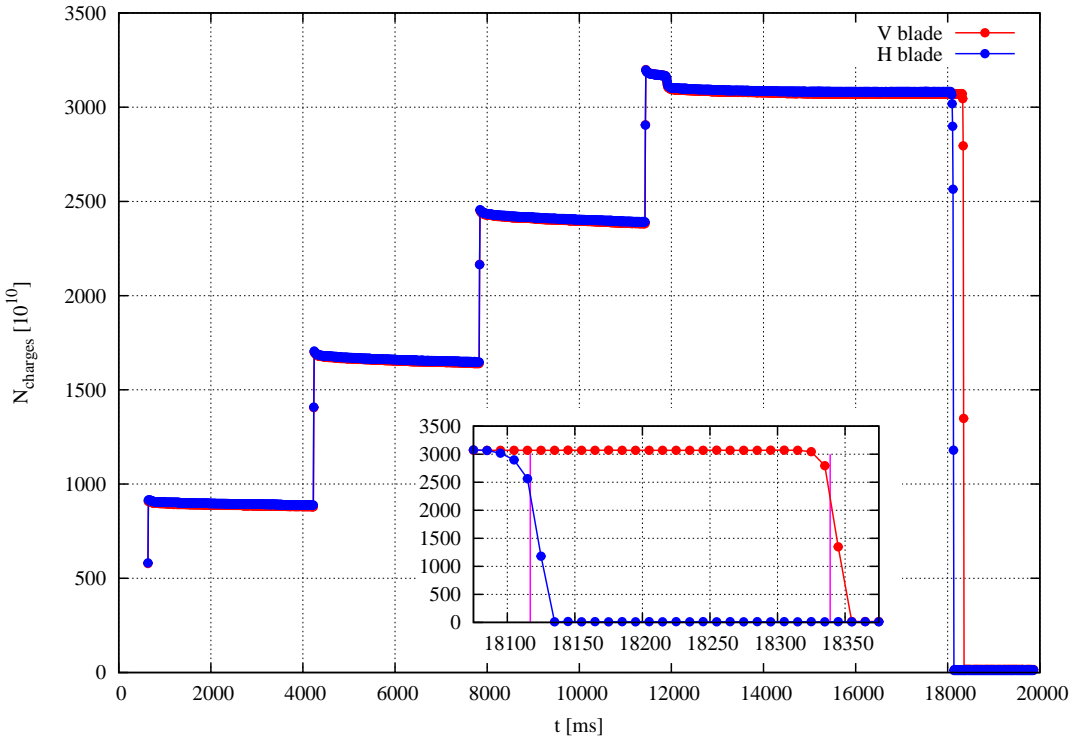


Figure 4.30: BCT signals during the burst test of the horizontal (blue curve) and the vertical (red curve) blades. The zoom focusses on the actual moment of scraping. The vertical lines in magenta mark the triggering of the beam dump, as retrieved from the Timber logging system. The timing shown in the plot is the one of the SPS cycle, not the one of the BCT monitor. When visible, error bars refer to the LSB.

analogue bandwidth ( $-3$  dB at  $50$  Hz, see Tab. 4.6) does not allow the BCT to properly follow fast changes in the beam current, like the case of a beam dump (i.e. from circulating beam intensity to 0 or to noise level), since the involved frequencies exceed the BCT analogue bandwidth (see Sec. 4.3.2); on the other hand, the time resolution of the BCT signal, i.e.  $10$  ms (see Tab. 4.6) is quite coarse with respect to the revolution time of the beam in the SPS, i.e.  $23.05\ \mu\text{s}$  (see Sec. 2.1.2), and in particular to the timing of the dump trigger. It should be kept in mind that the beam dump takes place in one single turn, once the dumping kickers get synchronised with the abort gap, which happens in few SPS turns. Given the revolution time of the beam in the SPS, the delay between the

dump trigger and the actual dump is extremely small with respect to the time resolution of the BCT signal, and can be regarded as negligible. The time stamps of the dump signal during the test were retrieved from Timber, i.e. 18117 ms and 18339 ms for the horizontal and vertical blade, respectively. These are shown in Fig. 4.30 by the magenta vertical lines.

Even though the beam was prematurely dumped during the burst test, vacuum spikes were observed in the MKD dump kickers immediately upstream of the scrapers under test (see the schematics layout of the SPS LSS1 shown in Fig. 2.7). The vacuum spikes, covering some orders of magnitude in a very short time, indicate that some damage was induced in the blades, with consequent sudden emission of atoms or clusters of atoms responsible for the abrupt degradation of the vacuum quality. Figure 4.31 shows the time profile of the vacuum in the MKD dump kickers during the period of the test. Two spikes can be clearly identified, in conjunction with the test of the blades.

Figure 4.32 shows the pattern of the BLM signals during the test. The zoom in the region of the BSHV.11759 and downstream of it allows one to focus on the LSS1. The first BLM, located at  $\sim 560$  m, is immediately downstream of the scrapers, and its values are extremely close to the limit given in Tab. 4.7, indicating some possible saturation taking place. Being the BLM with the highest readout and the closest to the scrapers, it is almost sure that on both occasions it was responsible for triggering the dump signal. The two BLMs at  $\sim 580$  m and  $\sim 610$  m belong to those regularly distributed in the half-cells; their readout is also very close to the limit reported in Tab. 4.7. The three LSS BLMs in-between seem to be saturating as well, with an almost flat pattern.

The BLM signals retrieved in Timber are integrated over the whole SPS cycle, and thus collect contributions from other sources of losses taking place at other moments during the cycle (see Sec. 2.1.4). For comparison, a BLM pattern

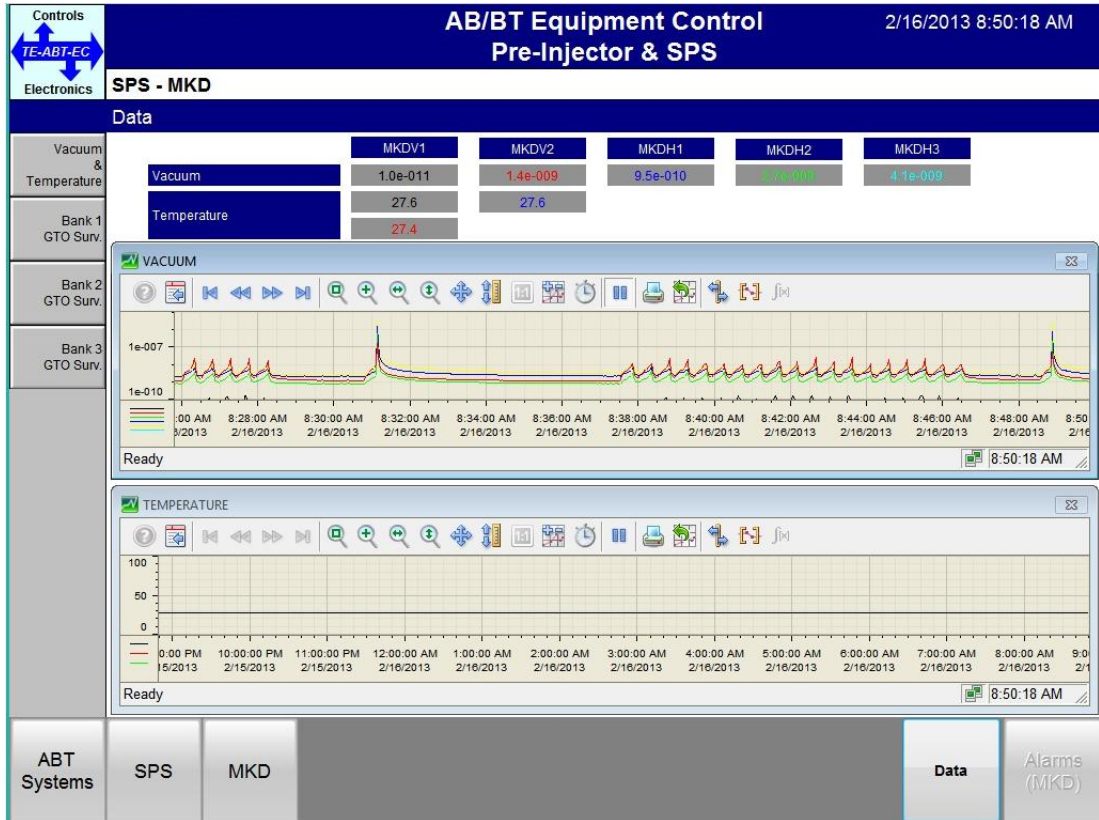


Figure 4.31: Time profile of the vacuum in the MKD dump kickers [93] immediately upstream of the BSHV.11759, the blades of which have been tested. The vacuum spike at  $\sim$ 08:31 AM is due to the burst test of the vertical blade, whereas the one at  $\sim$ 08:49 AM is due to the burst test of the horizontal blade. All other small spikes are due to checks of the performance of the blades with regular scraping before and after the burst test.

obtained at full beam intensity but with no scraping is shown as well in the same figure. Its pattern in the zoom reflects the event of a beam dump, being the main beam dump located at  $\sim$  600m. The shift between the BLM pattern from the test and that with no scraping shows how important the direct contribution from scraping is over that of the dump.

Figure 4.33 shows the normalised and averaged BCT signals when performing regular scraping before and after the burst test of the blades. Normalisation and averaging was performed as reported in App. C. Operationally, it seems that there is a loss of performance of the blades following the burst test, even if the

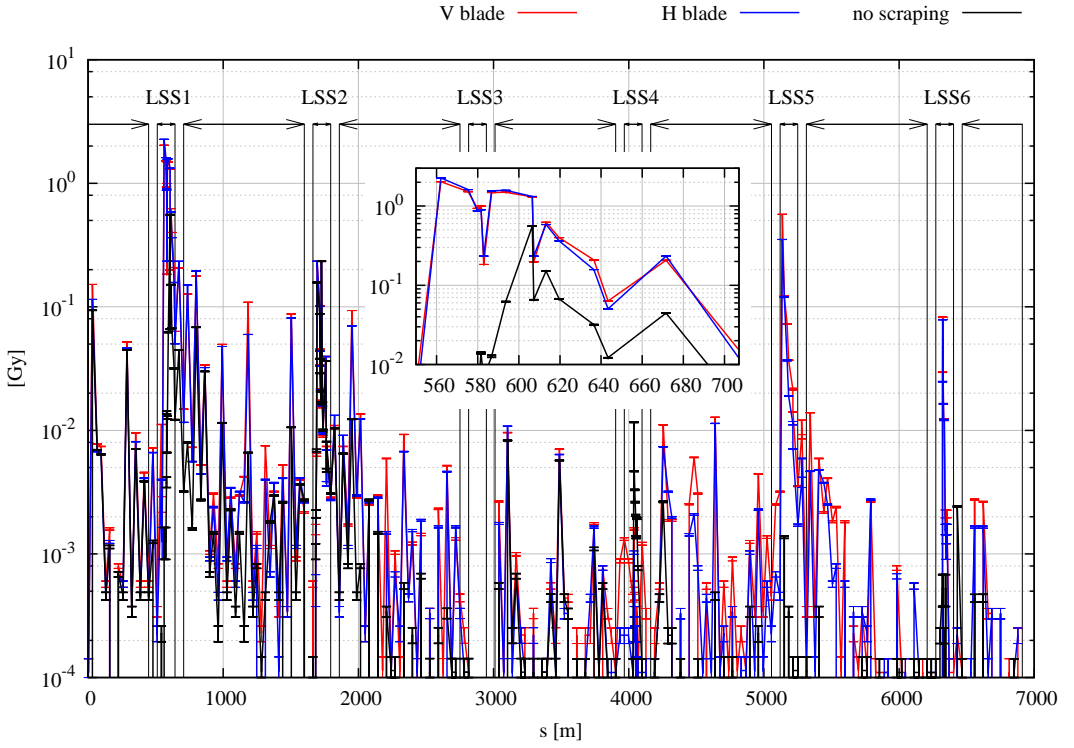


Figure 4.32: BLM readouts along the SPS ring recorded during the burst test of the horizontal (blue curve) and of the vertical (red curve) blades. For comparison, a pattern recorded with beam at full intensity (08:38:57.735 AM, Geneva local time) but no scraping is shown as well (black curve). The zoom focusses on the LSS1 downstream of the BSHV.11759 scrapers under test, located at  $s = \sim 560$  m. When visible, error bars refer to the LSB.

test was prematurely interrupted due to the sudden beam dump.

After the test, the blades were unmounted for analysis. The upper frame of Fig. 4.34 shows a picture of the vertical blade of the tested scraper on removal [99]. Signs of a change of crystallographic state in graphite are visible along the edge in foreground, which is the one that scraped the beam (see the upper-left frame in Fig. 2.5 for the schematics of the movement of the blades). This fact is in agreement with the concentration of the energy deposition around the edge actually facing the beam, shown by the simulations (e.g. see Fig. 4.8). The overall shape of the blade was untouched. The lower frame shows an image from the SEM of the same blade, in the region of the chamfer [92]. A change

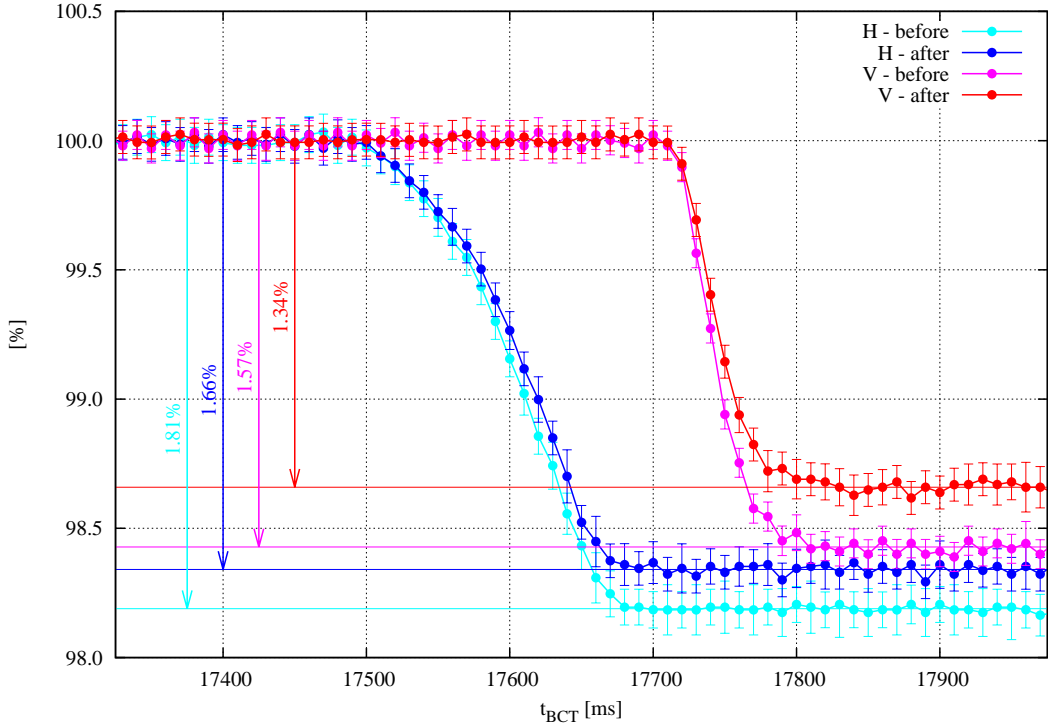


Figure 4.33: Normalised and averaged BCT signals when performing regular scraping before (light colours) and after (dark colours) the burst test of the horizontal (blueish curves) and vertical (reddish curves) blades. Normalisation and averaging of BCT signals has been performed as reported in App. C. Error bars refer to the maximum between the dispersion of the sets of data used to compute the averages and the error propagation. The timing shown in the plot is the one of the BCT monitor, not the one of the SPS cycle.

in the material porosity can be immediately seen, moving from the edge of the blade (on the left) towards the inside (on the right). The change in porosity can be due to sublimation taking place locally and resulting in outgassing. A more quantitative analysis [92] allowed the identification of the three zones numbered in the picture: region 1 has a porosity of  $\sim 31\%$ , region 2  $\sim 10\%$  and region 3  $9\%$ . Similar values have been found for the horizontal blade. Table 4.8 summarises the estimated values of porosity for the two blades, in the most affected area (i.e. along the edge directly facing the beam) and nearby. The estimation of the porosity has been performed with a visual technique, based on the difference

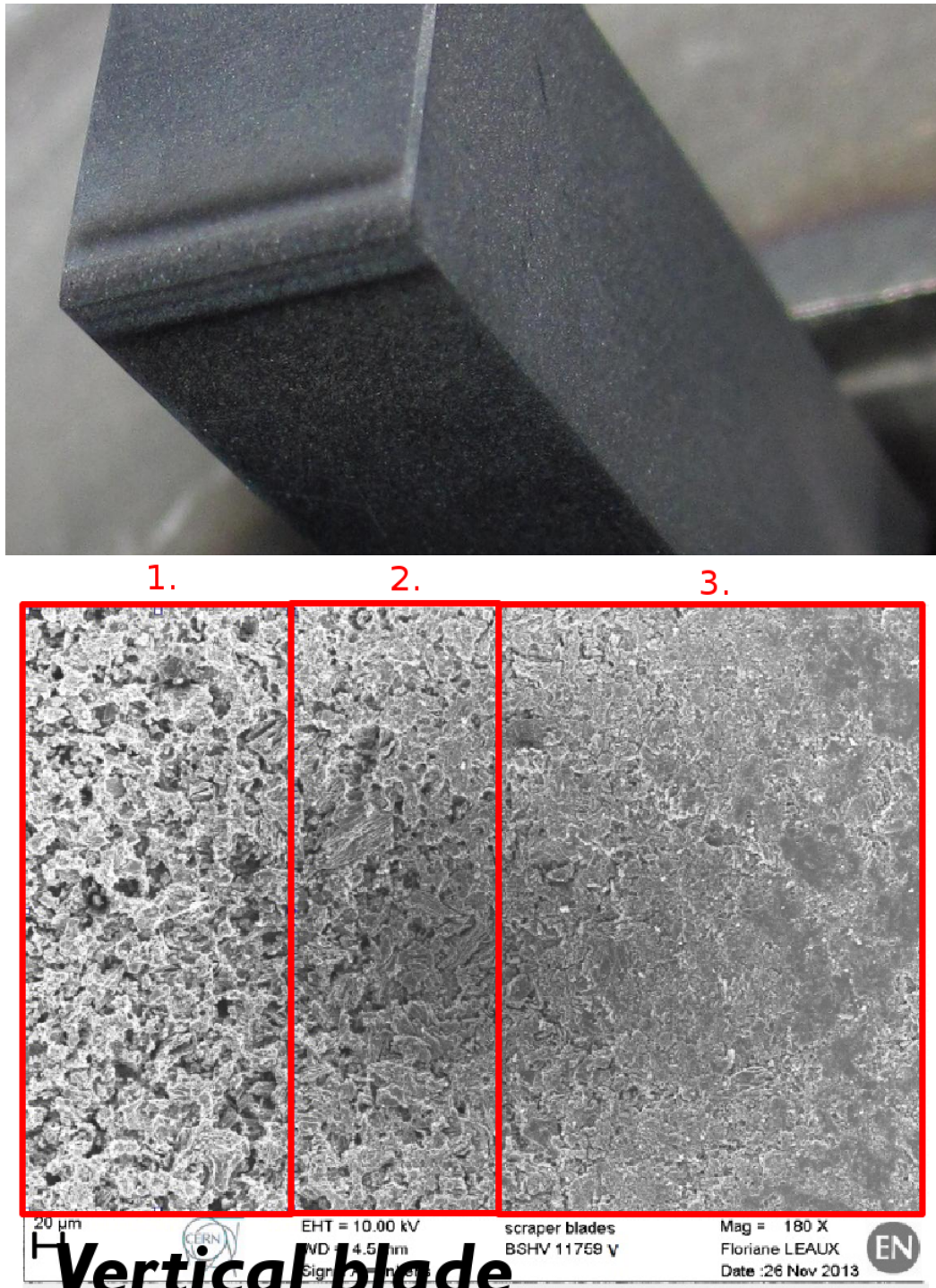


Figure 4.34: Upper frame: vertical blade of the BSHV.11759 scraper after the burst test, as when dismounted [99] for the microscopic analysis. Lower frame: SEM visualisation of the same blade [92], zoomed on the region around the chamfer affected by the burst. Three zones with different levels of porosity have been identified and numbered in decreasing order.

blade	porosity	
	[%]	[%]
H blade	28	9
V blade	31	9

Table 4.8: Estimated porosity of the BSHV.11759 scraper blades after the burst test [92]. The second column reports the values in the most affected area, i.e. around the edge directly facing the beam, whereas the third one reports the values nearby.

in contrast visible in the picture between the bulk material (light colour) and the porous one (dark colour) [92].

Porosity can be defined as the ratio between the volume taken by vacuum over a unit volume of specimen, i.e.

$$\phi = \frac{V_V}{V_V + V_M},$$

where  $\phi$  is the porosity,  $V_V$  and  $V_M$  are the volumes occupied by vacuum and by the material of the specimen. The porosity can be used to express the average density of the specimen in the damaged region  $\rho$ , starting from the original density of the material  $\rho_M$

$$\rho = \rho_V \phi + \rho_M (1 - \phi) = \rho_M (1 - \phi), \quad (4.2)$$

where  $\rho_V$  is the density of vacuum, obviously set to 0 and thus disappearing in the last passage of the equation. As can be seen, given a certain degree of porosity, the average density of the specimen scales accordingly. This implies that a value of porosity of 30 % in the damaged region translates to a density 70 % of the original one. In particular, a decrease in the density translates to an increase of the inelastic interaction length, which equates to a possible degradation of the performance of the blade.

The best way to estimate the amount of beam scraped before dumping the beam would be through the BCT signal. As already mentioned while commenting Fig. 4.30, the upper limit to the DC analogue bandwidth and the sampling rate of the ADC do not allow the clear identification of a sharp drop down of the signal due to dumping. So, even if the time of the trigger of the dump is known, a sensible estimation of the amount of beam scraped is not straightforward, since there is no reliable indication of the beam current at dumping. In an attempt to overcome this, Fig. 4.35 compares the normalised BCT signals during the burst test of both blades to the normalised and averaged BCT signals obtained with the same scraper settings with low intensity beams (i.e.  $\sim 10^{12}$  protons), which are not affected by the dump event, showing what should have been seen during the test if the dump was not triggered<sup>6</sup>. Normalisation and averaging of BCT signals have been performed as reported in App. C.

In the case of the *horizontal* blade, the curves at high and low intensity almost coincide in the region before the dump trigger, confirming the stability and reproducibility of LHC beams in the SPS, and is extremely encouraging about the reliability of the present analysis. After the dump trigger, the two curves are quite distinct, a fact that allows the use of the curve at low intensity for a sensible estimation of the amount of beam scraped before the dump. From the figure, it can be estimated that approximately 20 % of the beam was scraped during the burst test before dumping, corresponding to  $\sim 6.1 \cdot 10^{12}$  protons.

The curves at low and high intensity of the *vertical* blade are in good agreement as well. The reason why there is not a big difference in the pattern of the two curves after the dump trigger, as happens for the horizontal blade, lies in the tilt of the blade, as will be seen in Sec. 4.3.4. From the figure, it can be estimated that approximately 30 % of the beam was scraped during the burst test before dumping, corresponding to  $\sim 9.2 \cdot 10^{12}$  protons.

---

<sup>6</sup>This comparison is historically the way how the dump of the beam was actually realised.

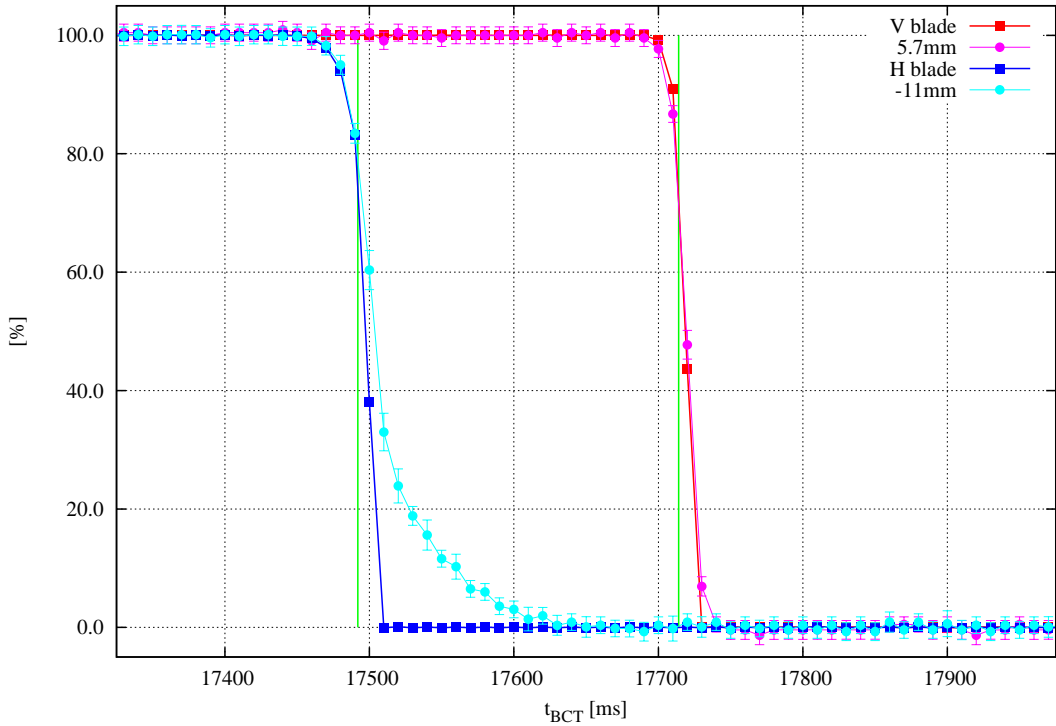


Figure 4.35: Normalised BCT signals during the burst test of the horizontal (blue curve) and the vertical (red curve) blades compared to the normalised and averaged BCT signals obtained with the same scraper settings with low intensity beams (i.e.  $\sim 10^{12}$  protons) for the horizontal (light blue) and the vertical (magenta) blades. The green vertical bars mark the timing of the dump. The shown range in time is focussed on scraping. Normalisation and averaging of BCT signals have been performed as reported in App. C. Error bars of the normalised and averaged data refer to the maximum between the dispersion of the sets of data used to compute the averages and the error propagation, whereas error bars on the normalised data at the burst test refer to the LSB, when visible.

Thanks to the additional sets of BCT measurements at low intensity, it was possible to estimate the amount of beam scraped before the dump, and thus the number of primary protons that caused the damage observed with the SEM. Another estimation, based on BLM readouts, is given in Sec. 4.3.5. Nevertheless, at this stage, two questions still remain open:

1. which levels of energy deposition were reached in the blade? This question is relevant to address the validity of the energy deposition results from the

simulation and give reasons for the sublimation of material observed;

2. is the change in the performance of the blades seen in Fig. 4.33 a direct effect of the damage induced in the blades or is it due to a change in the distribution or emittance of the beam, or in the relative position between the beam and the blade?

Both these open questions need results from further simulations, and will be answered in the next section.

#### 4.3.4 Benchmark Against BCT Signals

The benchmark presented in this section shows the quantitative comparison between the evolution of the beam intensity as a function of time (i.e. number of revolutions in the accelerator) predicted by the simulation and the BCT signals obtained with beam. Since the beam was prematurely dumped during the burst test, BCT signals from other SPS cycles with low intensity beams collected in the same morning of the test are used (see later).

This benchmark allows one to infer the energy deposition values in the blade that occurred during the burst test which caused the observed damage. Indeed, knowing the characteristics of the beam in machine and reproducing them in the simulation, the settings of the blade, i.e. speed and tilt angle, can be varied in the simulation until the time evolution of the beam intensity matches the time profile from the measurements. The map of energy deposition at  $0\sigma$  scraping with the settings matching the BCT measurements can be used to estimate the actual energy deposition in the blade during the burst test, taking into account the intensity of the beam during the test and the estimated amount actually scraped.

In order to have a more reliable estimation of the blade settings, the benchmark is performed for each blade in different scraping positions, using BCT signals

at low intensity recorded the same morning as the test (see later).

As already seen in the simulation studies presented in Sec. 4.2.5 and as will be clarified later with the benchmark, the time evolution of the beam current is sensitive to speed and tilt angle of the blade, and to the beam distribution. As a consequence, the use of a given beam distribution in the simulation affects the reconstructed settings of the blade and thus values of energy deposition. In order to be as accurate as possible, the beam distribution is derived from the amount of beam scraped for different scraping positions measured in different SPS cycles collected the same morning as the test (see later).

The present benchmark is also relevant to the development of the coupling between FLUKA and SIXTRACK as a simulation tool for the production of reliable results. In fact, due to their short length, SPS scrapers are cleaning devices that are extremely sensitive to multi-turn effects, and important deviations of simulation results from measured BCT signals may reveal subtle artifacts in the code.

## BCT Signals

The BCT signals used for the present benchmark are taken from the SPS cycles dedicated to the identification of the centre of the beam at the scraper. Beam scans were performed with each blade of the BSVH.11759 scrapers, recording the amount of beam scraped as a function of the blade transverse position. Since the aim was to identify the centre of the beam at the scraper, the scan is accurate in the vicinity of 100 % beam scraping, and less refined for other scraping positions. To avoid premature beam dump or blade damage while scraping large fractions of the beam, these cycles were filled with low intensity beams, i.e.  $\sim 10^{12}$  protons per cycle. In order to compensate for possible cycle-by-cycle variations of the characteristics and position of the beam, scraping at each position was performed

more than once in consecutive SPS cycles. Similarly, due to the extreme sensitivity of BCT signals to beam and scraping conditions, and the presence of an important signal jitter at 50 Hz, all the readouts have been normalised to the beam intensity immediately before scraping and averaged together, according to the blade position, to give a more stable signal. The procedure and the list of all the processed signals is given in App. C. Figure 4.36 shows the normalised and averaged BCT signals obtained during the beam scans prior to the actual burst test.

## Beam Distribution

For the quality of the benchmark, it is fundamental that the beam tracked in simulations reproduces adequately the beam in the machine at the time of the test. Indeed, the beam distribution, as well as the speed and tilt of the blade, affect the pattern of the beam intensity during scraping and values of energy deposition. Therefore, a description of the simulated beam representative of the one actually in machine is important to properly reconstruct the speed and tilt angle of the blade and to finally estimate energy deposition levels in the blade during the test. During Run 1, several scans obtained with the operational scrapers BSHV.11771 were performed. An example is given in Fig. 4.37 [100]. As is visible in the figure and proved with other scans [89] during SPS operation throughout 2012 and 2013, the beam in the SPS at the moment of scraping (i.e. during the ramp and very close to flat top, see Sec. 2.1.4) has over-populated tails with respect to a Gaussian distribution, with a pattern well fitted by a double Gaussian distribution (see Secs. 3.4.2 and D.2.1).

From the averaged and normalised BTC signals shown in Fig. 4.36, the amount of scraped protons has been recorded as a function of the blade position, creating the beam scans shown in Fig. 4.38, to characterise the beam in machine during

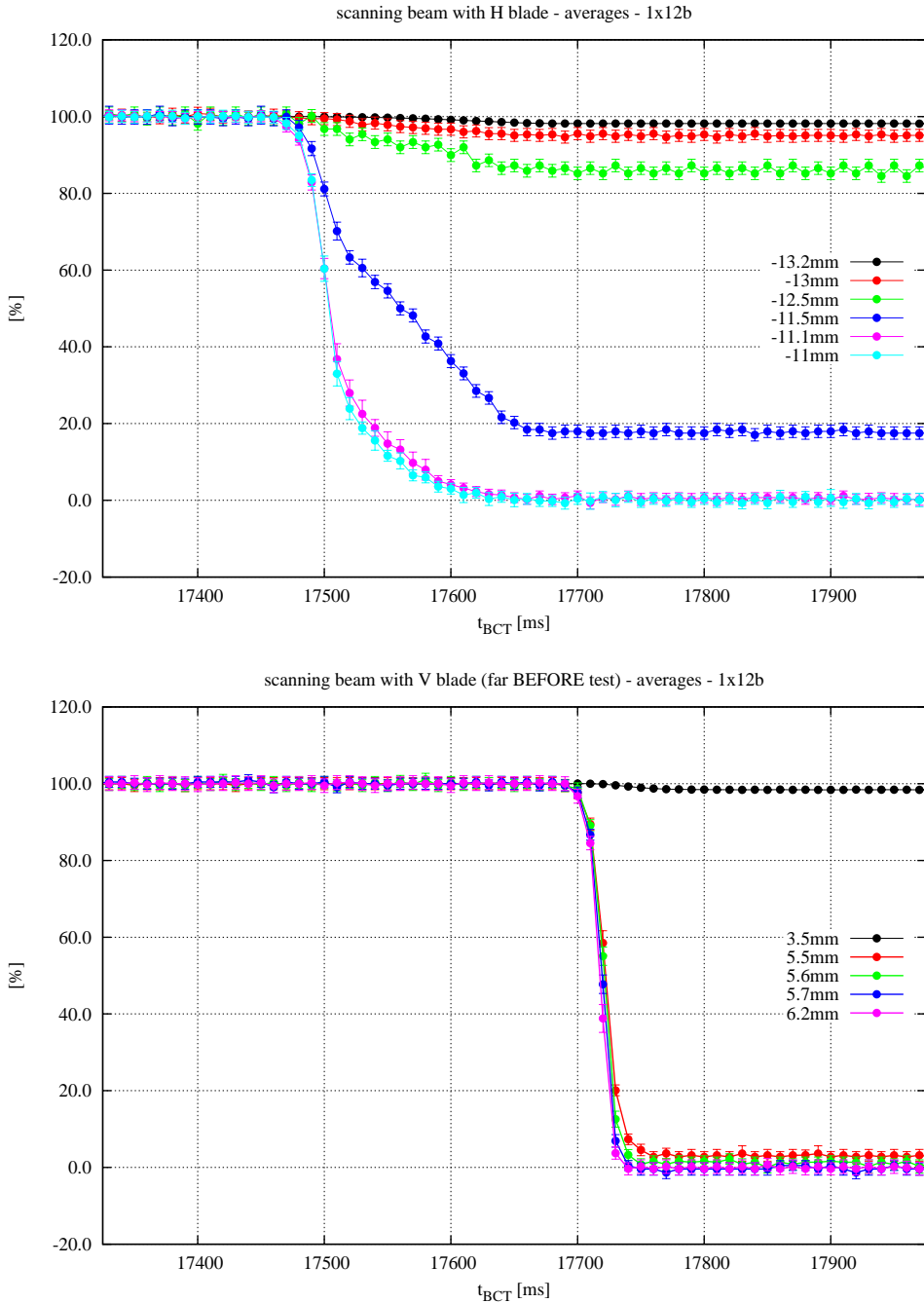


Figure 4.36: Normalised and averaged BCT signals at low beam intensity, obtained when identifying the centre of the beam, prior to the burst test of each blade of the BSHV.11759 scrapers. Upper frame: signals obtained with the horizontal blade. Lower frame: signals obtained with the vertical blade. Normalisation and averaging of BCT signals have been performed as reported in App. C. Error bars refer to the maximum between the dispersion of the sets of data used to compute the averages and the error propagation.

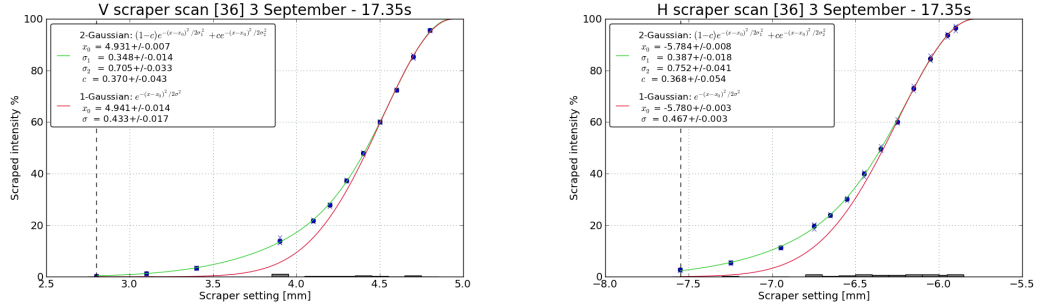


Figure 4.37: Beam scans performed with the BSHV.11771 operational scraper [100]. Left frame: horizontal plane. Right frame: vertical plane. The scans have been performed on the 3<sup>rd</sup> September 2012, with trains of 36 bunches per SPS cycle. Each data point is an average over at least three consecutive cycles.

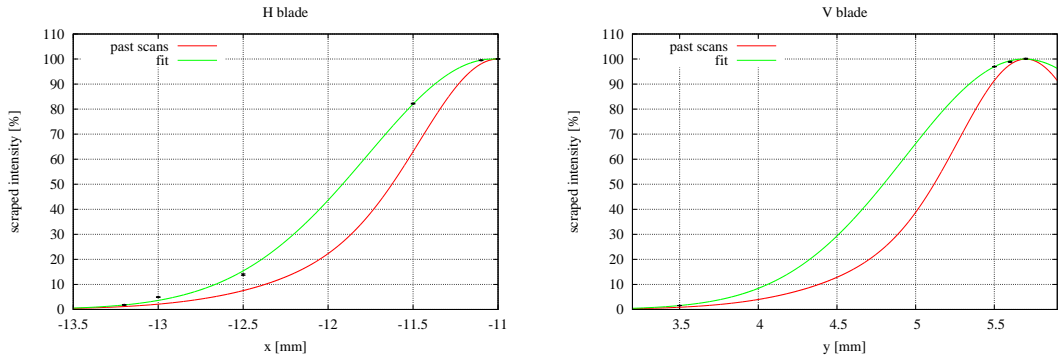


Figure 4.38: Beam scan obtained with the BCT measurements as given in Fig. 4.36. Left frame: horizontal plane. Right frame: vertical plane. The red curves represent the prediction obtained with double Gaussian distributions as from Fig. 4.37, scaled to the emittances available in machine (see Tab. 4.5). The green curves are the fits of a double Gaussian distribution through the data.

the test. Neither are the number of scraping positions as abundant as for the scans shown in Fig. 4.37 nor are they equally spaced. Indeed, they are primarily meant to determine the position of the centre of the beam and not to characterise the beam itself. Nevertheless, as the faithful description of the beam in machine is extremely important for the correct estimation of the settings during the test (i.e. speed and tilting of each blade) and the energy deposition, these scans have been used to characterise the beam in machine, and thus the population to be sampled and used in the simulations. The green curves in Fig. 4.38 are fitted to

	$I_1$ []	$\sigma_1$ [mm]	$\sigma_2$ [mm]	$x_0$ [mm]
fit-H	$0.0626 \pm 0.731$	$0.518 \pm 1.79$	$0.772 \pm 0.0832$	$-11.03 \pm 0.109$
meas-H optics	0.632	0.431	0.837	-11
		0.520		
fit-V	0.565	0.760	0.760	5.69
meas-V optics	0.63	0.398	0.805	5.7
		0.495		

Table 4.9: Comparison between the parameters of the fitting curves for a double Gaussian distribution (see Secs. 3.4.2 and D.2.1) from the scan of the beam in machine at the test, shown in Fig. 4.38, and those from a previous scan [100], shown in Fig. 4.37. While for the horizontal plane the absolute error on the fitting parameters is reported, for the vertical plane the error is 0, as the number of fitting parameters is equal to the number of data points, and it has thus not been reported. Values of  $\sigma$  (only betatron contribution) from optics (i.e. SPS Q20, when the permanent bump in the LSS1 is considered, at the centre of the BSHV.11759 scrapers) and normalised emittances available in machine (see Tab. 4.5) at 450 GeV/c are shown for comparison.

the data, using the expression of a double Gaussian distribution (see Eq. 3.2). The results from the fits are reported in Tab. 4.9. The red curves are the beam distributions foreseen using the fitting curves from the scans in Fig. 4.37, scaled to the emittances measured just before the test and the positions of the centre of the beam given in Tab. 4.5. The scaling was performed calculating the ratio between each  $\sigma$  of the double Gaussian fits in Fig. 4.37 to the  $\sigma$  of the single Gaussian fit in the same figure (taken as reference, to cancel out the dependence on the emittance actually in machine at the time of the scan), and then multiplying the ratios by the  $\sigma$  from linear optics at 450 GeV/c, with the quoted normalised emittances. Table 4.9 also summarises the parameters of the red curves. From the scans, the beam in machine seems to be broader than expected, and with a distribution closer to a single Gaussian than to a double Gaussian.

The description of the SPS lattice structure used for the simulations does not start at the SPS scrapers, but in the middle of the arc between the LSS6 and the

LSS1 (see Figs. 2.1 and 2.2); more precisely, it starts at the entrance face of the QF.10010. To start the simulation, the beam has to be sampled using the linear optics functions at this element. At the same time, the sampling must be such that the simulated beam has a distribution at the scraper as close as possible to the one seen in reality. Consequently, the beam distribution from the scan of Fig. 4.38 has to be “scaled” to match the optics functions at the beginning of the lattice structure. In addition, the scaling must take into account the contribution from dispersion to the beam distribution, since the horizontal dispersion at the scraper is non-negligible, being  $-0.732$  m (see Tab. 2.3), i.e.  $\sim 10\%$  of the maximum value found in the arc (see Fig. 2.2).

The scaling of the beam distribution involves only the values of  $\sigma$  used by each double Gaussian distribution, as the relative intensity is not affected by the optics. In addition, the beam distribution is sampled centred on the closed orbit as from linear optics, with the centre measured at the scraper used only to adjust the scraping position of the blade in the simulation. The scaling of the values of  $\sigma$  is performed on the basis of its definition

$$\sigma_j^2 = (f_j \sigma_\beta)^2 + \sigma_s^2 = f_j^2 \frac{\beta \epsilon_N}{\beta_r \gamma_r} + (\sigma_\delta D)^2, \quad (4.3)$$

where  $\sigma$ ,  $\sigma_\beta$  and  $\sigma_s$  are the rms beam sizes as given by the fit, and as given by the betatron contribution and the one from synchrotron motion from linear optics, respectively (see Sec. A.2). The subscript  $j$  refers to both the inner and the outer Gaussian distributions used in the expression of the double Gaussian, and  $f$  is the magnification factor which states how much the betatron component of the inner or outer Gaussian is enlarged (see Secs. 3.4.2 and D.2.1).  $\epsilon_N$  is the normalised emittance, which scales by the relativistic reduced momentum  $\beta_r \gamma_r$  (see Sec. A.4).

Unfortunately, no information about the actual characteristics of the beam

plane	$I_1$	$f_1$	$f_2$	$\epsilon$ [ $\mu\text{m}$ ]	$\sigma_\delta$ [ $10^{-4}$ ]
H	0.0626	0.94078	1.4101	2.5	1
V	0.5646	1.33031	1.33032	2.5	1

Table 4.10: Parameters used to sample the beam for the benchmark against the BCT readouts. The betatron sampling is performed according to a double Gaussian distribution (see Sec. 3.4.2), whereas the momentum sampling is performed with a simple Gaussian. The beam is given an average momentum of 450 GeV/c.

on the longitudinal plane during the test was recorded. Thus, the sampled beam is arbitrarily given a Gaussian distribution in momentum, with an rms relative momentum offset  $\sigma_\delta = 10^{-4}$ . The assumed distribution in momentum is the only one with a bell shape available for sampling at the time of the simulations, and thus it is the best distribution that can be assumed in order to reasonably profit from the longitudinal motion; the value of  $\sigma_\delta$  is smaller than any value reported in Tab. 1.5 and this is done to limit dispersive effects on the number of scraped protons in presence of a tilt angle of the blade, without losing significance of results (see later on). With the given value of  $\sigma_\delta$  and assuming a normalised emittance of  $2.5 \mu\text{m}$ , close to the measured value (see Tab. 4.5), Tab. 4.10 summarises the parameters of the double Gaussian distributions used for sampling the beam to be tracked in simulations. As can be seen from the table and from Fig. 4.38, the beam distribution sampled has an almost pure Gaussian distribution, especially on the vertical plane, in clear contradiction with the double Gaussian distribution measured in the SPS in the past [100], see Fig. 4.37. Moreover, the values of  $\sigma$  are definitively larger than those expected by the linear optics, using the optics functions at the scraper and the measured normalised emittance (see Tab. 4.9). Nevertheless, for the sake of the benchmark, it is more sensible to use the beam distribution as given by the scans before performing the test (shown in Fig. 4.38) instead of arbitrarily taking nominal distributions based on past results, but not measured on the day of the test.

It could be remarked that the simple Gaussian distribution operationally seen by the scrapers might reveal a relevant contribution from dispersion, assuming a very broad distribution of the beam in momentum. It should be noted that given the values of  $\sigma_\beta$  (i.e. the betatron contribution to the beam size) and  $\sigma_s$  (i.e. the contribution from synchrotron motion to the beam size) calculated at the BSHV.11759 scrapers and reported in Tab. 2.3, a factor of  $\sim 6$  should be applied to the present value of  $\sigma_\delta$  for  $\sigma_s$  to be close to  $\sigma_\beta$ , for the horizontal plane. This would imply that only a fraction of the beam population, distributed in momentum according to a Gaussian, would fit in the bucket area (see Sec. 2.1.2), and in particular only the amount contained in  $\sim 1.4 \sigma$ , corresponding to  $\sim 84 \%$ . For the distribution to be dominated by dispersive effects, a further increase in  $\sigma_\delta$  would be needed, ruling out this hypothesis as un-realistic. Furthermore, this argument cannot hold for the vertical plane, where a similar beam distribution is found, but where the dispersion is a factor 100 smaller than the one on the horizontal plane (see Tab. 2.3).

It should be noted that, while for the cases of full beam scraping and for intermediate scraping positions presented in the following (see Fig. 4.39), the whole transverse phase space has been sampled, for regular scraping (i.e. at  $3\text{--}4 \sigma$ ) the sampling on the cleaning plane has been focussed on the tails (see Sec. 3.4.2), starting from a normalised betatron amplitude half a  $\sigma$  smaller than the blade position all the way up, to catch dispersive effects when visible. The cut in the beam sampling has been done to optimise the CPU time and track a beam the main portion of which would interact with the blade, without missing significant regions of phase space. Simulation results in case of regular scraping have been thus corrected, taking into account the fraction of beam actually sampled.

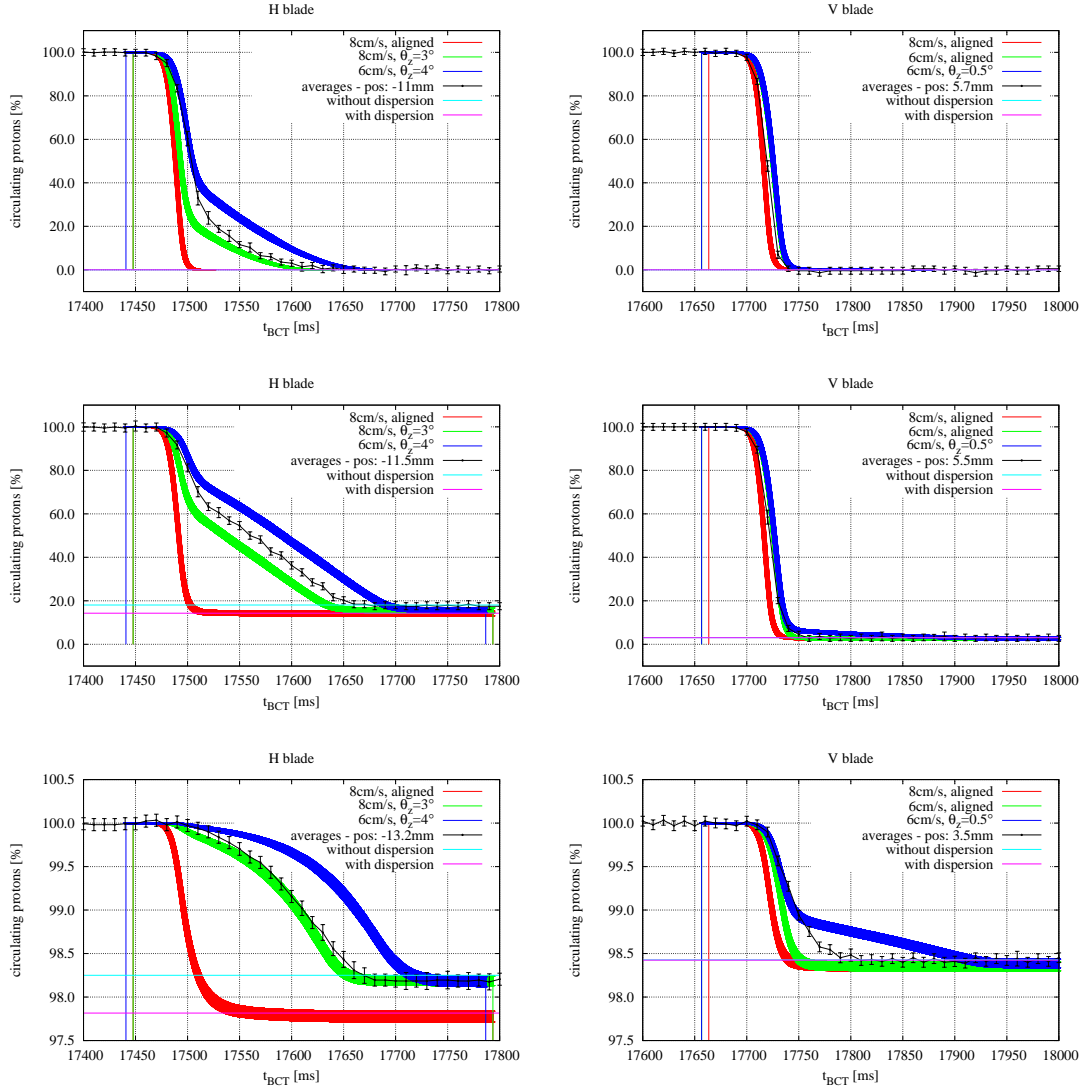


Figure 4.39: Comparison of the time evolution of the beam intensity during scraping as predicted by the simulation and as from normalised and averaged BCT signals. Results for the horizontal blade are shown on the left, whereas those for the vertical one are shown on the right. For each blade, three scraping positions are shown: full beam scraping (i.e. at  $0 \sigma$ , top frames), regular scraping (i.e. with the blades off the beam centre by  $\sim 2.2$  mm, bottom frames) and scraping at an intermediate position. Three combinations of blade speed and tilt are shown. The magenta and light blue lines show the expected beam intensity after scraping in case dispersion effects are and are not taken into account, respectively (see App. D). Normalisation and averaging of BCT signals have been performed as reported in App. C. Error bars of the measurements refer to the maximum between the dispersion of the sets of data used to compute the averages and the error propagation. The errors on the simulation results refer to the statistical error only. The timing shown in the plot is the one of the BCT monitor, not the one of the SPS cycle.

## Comparison Against BCT Readouts

Figure 4.39 compares the time evolution of the beam population during scraping as predicted by the simulation and as from normalised and averaged BCT signals (normalisation and averaging of BCT signals have been performed as reported in App. C). Results for both blades are shown for different scraping positions. Given the centre of the beam as from the fits shown in Fig. 4.38 and reported in Tab. 4.9, the scraping position set in each simulation has been obtained as difference between the position of the respective measurement and the centre found by the fit. This implies for example that, in case of full beam scraping, the innermost edge of the blade (see Fig. 4.24) is not exactly coincident with the centre of the beam, but a bit further in. Different values of speed and tilt angles have been explored, in order to identify a reasonable range of values. Only positive tilt angles about the longitudinal axis have been considered, since, as visible in Fig. 4.23, it is the only setting able to explain a pattern of the beam intensity very similar to the one of the horizontal blade at full beam scraping.

The comparison between the red and the green curves for the horizontal blade (left frames of Fig. 4.39) shows the effect of a tilt angle of the blade about the longitudinal axis. The presence of the angle qualitatively explains the important deviations of the measured BCT signals from the simulated case of a blade perfectly aligned, for all the three scraping positions. On the other hand, while an angle of  $3^\circ$  seems to be not too far from the real one, the simulated case with the blade at the nominal speed seems to be too fast to catch the measured pattern. The blue curves are shown as upper limit to the measured patterns, as they are featured by a speed implying too long times to fully achieve scraping, and an angle pushing the knee between the two scraping regimes (see Sec. 4.2.5) too far up. As a consequence, it can be concluded that, with the given beam distribution, the horizontal blade seems to move at a speed between 60 mm/s and 80 mm/s, and

to be featured by a tilt angle between  $3^\circ$  and  $4^\circ$ . In the case of full beam scraping the whole beam is scraped, no matter the value of the tilt angle; on the contrary, the other scraping positions show a difference in the amount of surviving beam due to the tilt angle, as some protons do not see the whole blade but only its innermost tip (see Fig. 4.24), and the betatron and longitudinal motions lead to too few passages through the blade, resulting in their survival (see below). The sensitivity on the value of the angle seems to be limited over the spanned range.

Contrary to the case of the horizontal blade, the comparison between the red and the green curves for the vertical blade (right frames) shows the effect of a change in the speed of the blade, which is to dilute the time scale of scraping especially at the beginning of the profile, where the speed of the blade and the beam distribution rule the pattern (see Sec. 4.2.5). Since the BCT patterns for the vertical blade are qualitatively different from those of the horizontal one, the case of the blade with a small tilt angle was run as well more for the sake of completeness rather than for the need to explain a feature of the measured patterns. This set of results is shown by the blue curves. The case of regular scraping shows that this value of angle is far too big, as the curve with simulation results deviates too much from the measured one, especially towards the end of scraping. On the other hand, the green curve does not catch the tail in the measured pattern either. It is suspected that, in addition to a very small angle, much lower than the one shown, the vertical blade's speed is even smaller than 60 mm/s, and probably with a value of density smaller than the nominal one. Almost no dependence on the amount of scraped beam is found on the tilt angle.

Table 4.11 summarises the ranges of values of speed and tilt angles of the BSHV.11759 scraper blades as from the benchmark of simulation results against the BCT measurements shown in Fig. 4.39.

blade	speed [mm/s]	tilt angle [°]
H	60–80	3–4
V	$\leq 60$	< 0.5

Table 4.11: Speed and tilt angle of the tested scraper blades as reconstructed from the benchmark of simulation results against the BCT measurements shown in Fig. 4.39. Values have been obtained tracking in the simulations a beam sampled according to the fits shown in Fig. 4.38, the parameters of which are reported in Tabs. 4.9 and 4.10.

The range of angles identified for the horizontal blade is larger than values expected from considerations on the design of the mechanics [90], even when adding up the contributions from all possible sources of tilt, in the most pessimistic and unrealistic assumptions. On the other hand, it is possible that the whole mechanics has been mounted not properly aligned [101]. On the contrary, the vertical blade seems to be aligned, as the only angle considered in the simulation, way smaller than those explored for the horizontal blade, turns out to be too big. The difference between the inferred tilt angles of the two blades might look acceptable taking into account the fact that the scraper blades are mounted on relatively long mechanical arms in stainless steel, tied to the blade on one end and to the mechanics generating the movement on the other end. In particular, the arm of the horizontal blade is kept horizontally and it is moved vertically, whereas the arm of the vertical blade is kept vertically and it is moved horizontally (see Fig. 2.5). Thus, gravity is expected to have a different impact on wear of joints under vibrations induced by continuous cycling. Nevertheless, it should be kept in mind that the tested scrapers are the spare ones, rarely used over the whole Run 1.

The range of speeds identified for the horizontal blade is closer to the nominal speed of the blades of 80 mm/s than the ranges identified for the horizontal blade.

It should be kept in mind that the inferred values of speed and tilt angle

depend on the assumed beam distribution, especially for the horizontal blade, which is also affected by dispersive effects, i.e. effects due to synchrotron motion visible in the transverse dynamics of beam particles. Given all the uncertainties and unknowns on the beam distribution assumed for the simulations, these values should be taken not literally.

The magenta and light blue lines in Fig. 4.39 show the prediction of the amount of scraped beam in case dispersive effects are considered or not, respectively. In fact, a beam proton sees the scraper blade if its maximum transverse position on the cleaning plane  $z$  is larger than or equal to (limit condition) the scraping position  $z_R$  (see Sec. D.1). Taking the limit condition represented by the equality and explicitly expressing the betatron and synchrotron contribution to the maximum transverse position of a particle in terms of normalised betatron and momentum amplitude  $n_\beta$  and  $n_\delta$  of the particle,  $\beta$  function, geometrical emittance  $\epsilon$ , dispersion function  $D$  and rms relative momentum offset  $\sigma_\delta$ , a simple mathematical expression between  $n_\beta$  and  $n_\delta$  can be found, i.e.

$$n_\delta = \frac{\sqrt{\beta\epsilon}}{D\sigma_\delta}(R - n_\beta), \quad (4.4)$$

where  $R$  is the position of the blade expressed in units of  $\sigma_\beta = \sqrt{\beta\epsilon}$ . This expression shows that for any given value of normalised betatron amplitude there exists a value of normalised momentum amplitude such that, taking into account the longitudinal motion of the beam, the particle sees the blade of the scraper, even if the normalised betatron amplitude of the particle is smaller than the settings of the blade. This means that the longitudinal motion leads to remove particles that in absence of dispersion would survive, i.e. even among those with a normalised betatron amplitude smaller than the settings of the blade. This dispersive effect depends on the linear coefficient in the above expression, equal to the ratio between  $\sigma_\beta$  and  $\sigma_s$ . For the values of emittance and  $\sigma_\delta$  considered in

the present studies, this dispersive effect is visible when the dispersion function is not negligible, as it happens at the SPS scrapers (see Tab. 2.3).

The predictions shown by the magenta and light blue lines in Fig. 4.39 are obtained analytically, based on the characteristics of the beam distributions and the optics functions at the scraper, and they are thus not derived from simulation. In particular, they are obtained integrating the beam distribution on the plane of cleaning and in momentum through the following integral (see Sec. D.1)

$$\int_0^R \text{pdf}_\beta(n_\beta) dn_\beta \int_0^{n_{\delta,\max}} \text{pdf}_\delta(n_\delta) dn_\delta, \quad (4.5)$$

that expresses the amount of beam which does not see the blade. The two pdfs are the pdfs of the beam population in the normalised betatron transverse and longitudinal phase spaces, respectively; the other variables have the same meaning as in Eq. 4.4. The difference in the two estimations (given by the magenta and light blue lines in Fig. 4.39) is given by the upper extreme of integration on the dispersive part  $n_{\delta,\max}$ . In fact, when no dispersion effects are taken into account, scraping is supposed to be independent of the distribution in momentum; thus, the two pdfs can be integrated independently, and in particular the upper limit on the momentum part is  $n_{\delta,\max} = \infty$ . On the contrary, when dispersive effects are taken into account, Eq. 4.4 sets a dependence on the extremes of integration between the two pdfs, and in particular it is the upper one on the momentum part. Thus, the integration in momentum must be performed first, and then the integration on the betatron part. For calculations on simple distributions and the numbers shown in Fig. 4.39, see App. D.

To better illustrate the aforementioned dispersion effect on the number of scraped protons, Fig. 4.40 shows the density of scraped protons in the  $n_\beta - n_\delta$  space for some cases of regular scraping shown in the lower frames of Fig. 4.39, as predicted by the simulations. The frames on the left refer to the case of aligned

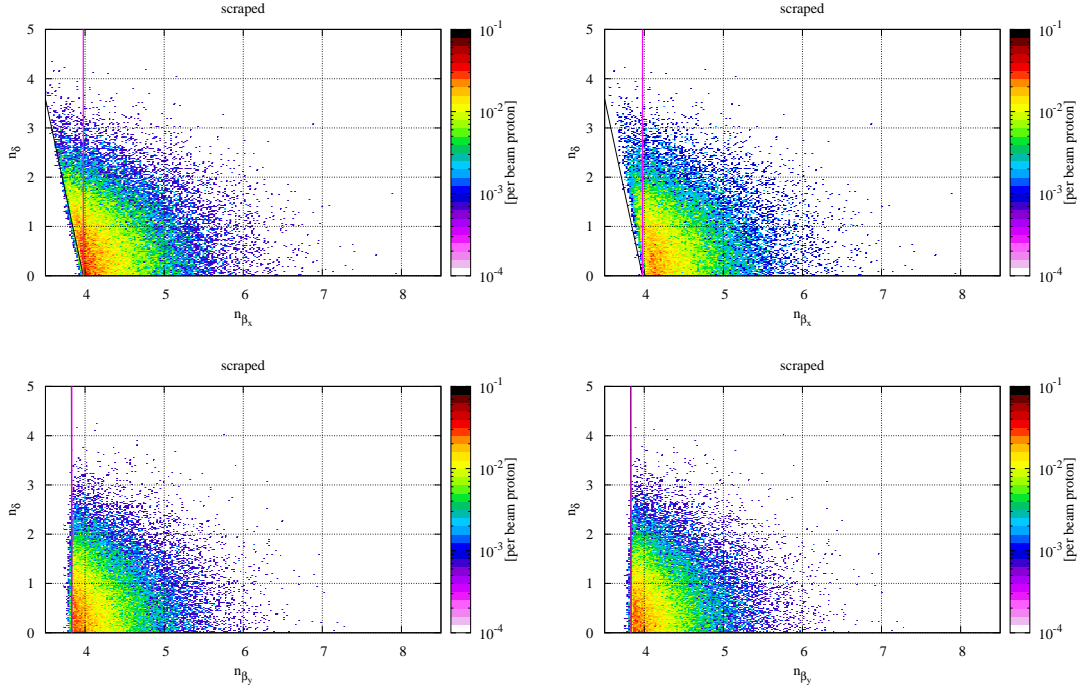


Figure 4.40: Density of scraped protons in the  $n_\beta - n_\delta$  space in case of the regular scraping shown in the lower frames of Fig. 4.39 as predicted by the simulations. In the upper frames, results refer to the horizontal blade moving at 80 mm/s, when aligned (left frame) and when tilted by  $3^\circ$  about the  $z$ -axis (right frame). In the lower frames, results refer to the vertical blade moving at 60 mm/s, when aligned (left frame) and when tilted by  $0.5^\circ$  about the  $z$ -axis (right frame).

blades; in particular, the upper one refers to the horizontal blade, whereas the lower frame refers to the vertical blade. The magenta line marks the position of the scraper blade. In case no dispersion effect is considered, the blade should scrape only those protons on the right of the magenta line, i.e. the protons with a normalised betatron amplitude larger than the setting of the blade, performing a pure betatron cleaning; conversely, in case dispersion effects are taken into account, the blade scrapes off all the protons above the black line, which represents the condition expressed by Eq. 4.4. The difference in the amount of scraped protons is exactly represented by all those protons lying above the black line and on the left of the magenta one, which are scraped only because of dispersive effects. While for the horizontal plane it is non-zero, for the vertical plane this

difference cannot be even appreciated in the figure, since the dispersion on the vertical plane is extremely small (two orders of magnitude smaller than the one on the horizontal plane, see Tab. 2.3), and indeed the magenta and the black lines essentially coincide. Thus, while on the vertical plane the scraper blades perform pure betatron cleaning, on the horizontal plane they perform combined betatron and momentum cleaning. The same figure also shows the case of tilted blades, on the right frames. The case of the horizontal blade shows a depletion in every part of the space, not only in the region of protons scraped only because of dispersion effects (i.e. those above the black line and on the left of the magenta one), but also in the region of pure betatron cleaning. The same remarks apply to the vertical blade, even though the tilt angle is way smaller than the one applied to the horizontal blade, and dispersive effects are absent.

It should be noted that the predictions of the amount of scraped beam in case dispersive effects are *not considered* shown in Fig. 4.39 for the horizontal blade match the *BCT signals* after scraping. This is consistent with the derivation of the parameters for sampling the beam, as the fitting curve takes into account only the betatron part of the beam distribution, with dispersion being given a limited impact (small  $\sigma_\delta$ ) and affecting only the values of  $\sigma_1$  and  $\sigma_2$ , without explicit corrections on measurements (for dispersive effects). Similarly, the predictions in case dispersive effects *are taken into account* match the *simulation curve for the aligned blade*, as the aligned blade scrapes off all the circulating protons with a normalised betatron amplitude larger than the position of the blade and the protons intercepted because of dispersive effects. This is also the reason why the amount of beam surviving scraping in the case of the aligned blade does not match the measurement from the BCT. On the contrary, the same predictions for the vertical blades coincide, as dispersive effects are extremely limited; consequently, the BCT signals and the results for the aligned blade match. The fact that

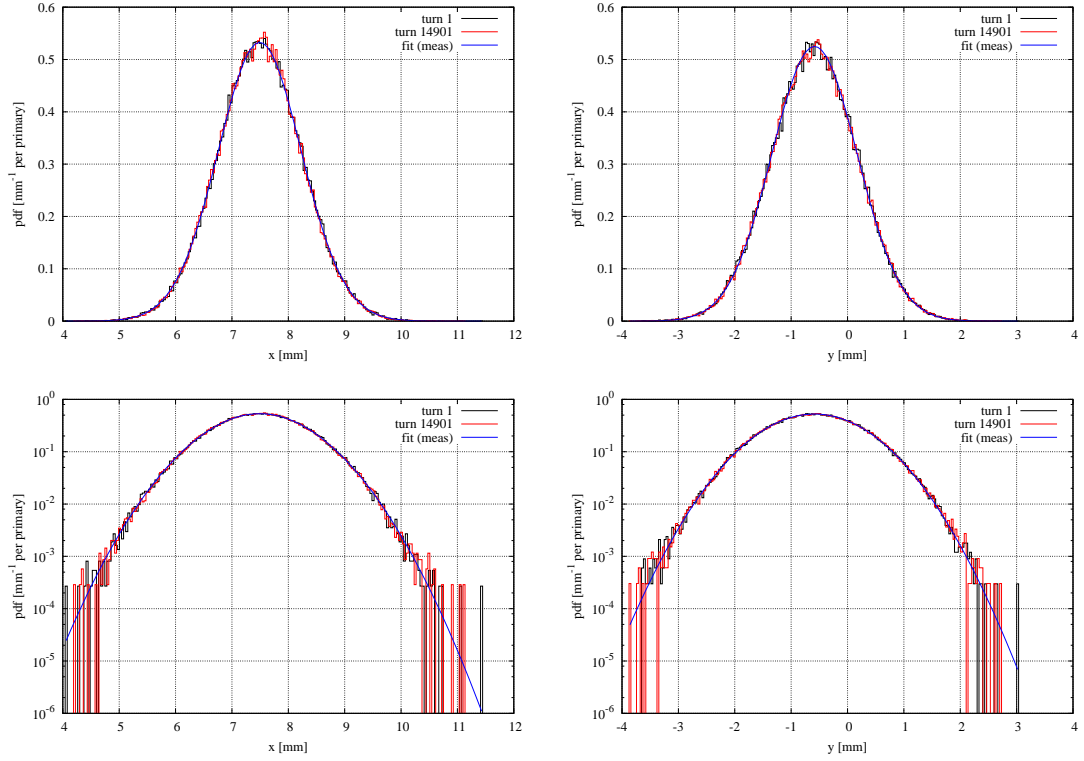


Figure 4.41: Beam distribution on the horizontal (left frames) and on the vertical (right frames) planes as at the beginning and towards the end of a FLUKA–SIXTRACK coupled simulation, at the entrance of the BSHV.11759 scraper tank. Results are given in both linear (upper frames) and logarithmic (lower frames) scale, to appreciate differences in the central part of the distribution and in the tails, respectively. The shown blue curves are the fit through the BCT data shown in Fig. 4.38, the parameters of which are reported in Tabs. 4.9 and 4.10.

the results from simulation with a tilt angle match the BCT measurements is unexpected.

The fact that the amount of beam surviving scraping predicted analytically in case dispersive effects are taken into account matches the one from the simulation with the aligned blade is an additional proof that the coupling between FLUKA and SIXTRACK has been done properly, and in particular the continuous exchange of particles and the numerous transformations of reference frame and dimensions do not perturb tracking over the considered range of revolutions in the accelerator. As an example, Fig. 4.41 shows the beam distribution at the begin-

blade	intensity		mesh [ $\mu\text{m}$ ]	max	
	[%]	[ $10^{12}$ ]		[ $\text{GeV cm}^{-3}$ per $\text{p}^+$ ]	[ $\text{kJ cm}^{-3}$ ]
H	20	6.1	50 x 50	14–16	14–16
			10 x 10	20–25	20–24
V	30	9.2	50 x 50	13–16	19–24
			10 x 10	18–25	27–37

Table 4.12: Summary of amount of beam scraped as estimated via the BCT signals and energy deposition expected in the blade during the burst test. The given intervals on energy deposition consider all the cases of scraping at  $0\sigma$  shown in Fig. 4.39, for different combinations of tilt angle and speed. Simulation results are based on the beam distribution as reconstructed by the fits shown in Fig. 4.38 and the derived parameters reported in Tabs. 4.9 and 4.10. The quoted meshes have a longitudinal stepping of  $500\ \mu\text{m}$ .

ning and towards the end of the simulation, at the entrance of the BSHV.11759 scraper tank, in case scraping is not performed, to test the stability of the sampled beam while using the FLUKA–SIXTRACK coupling. The distribution does not appreciably change over almost 15000 turns, and does not drift away from the desired beam distribution, given by the fit through the BCT data shown in Fig. 4.38, the parameters of which are reported in Tabs. 4.9 and 4.10.

Table 4.12 summarises the energy deposition values estimated with the simulations at full beam scraping shown in Fig. 4.39. The values from two meshes are reported for comparison. Those for the more refined mesh cover a wider range due to statistics. Nevertheless, all the meshes report a value clearly above the sublimation heat for graphite (see Tab. 4.2), confirming that the blades were locally set in sublimation, generating the vacuum spikes recorded during the test.

In the attempt to spot the apparent change in the blade performance seen in Fig. 4.33 due to the damage induced with the burst test, Fig. 4.42 shows the effect of a change in the porosity of the blade of the BSHV.11759 scraper on the profile of the beam intensity, in case of regular scraping. In particular, one of the cases with a tilt angle among those shown in the lower frames of Fig. 4.39 has

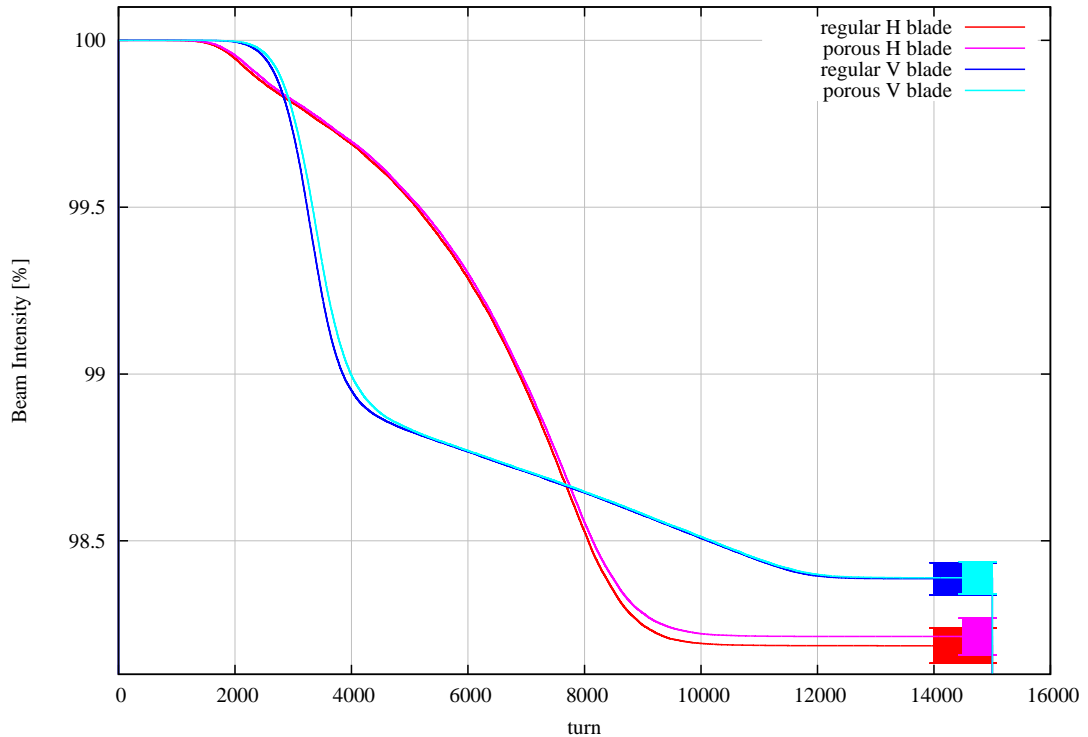


Figure 4.42: Effect of a change in the porosity of the blade of the BSHV.11759 scraper on the profile of the beam intensity in case of regular scraping. A case of regular scraping with the horizontal (reddish curves) and the vertical (blueish curves) blades with regular graphite from those shown in Fig. 4.39 are compared to the same ones but with a porous graphite. In particular, the case of the horizontal blade moving at 80 mm/s and with a tilt angle of 3°, and the case of the vertical blade moving at 60 mm/s and with a tilt angle of 0.5° are shown. The porous blades are featured by a 30 % porosity in the most affected area, i.e. around the edge directly facing the beam, and a 10 % porosity in the rest of the blade, average values very close to the estimations done after the test (see Tab. 4.8). Error bars refer to the statistical error only, and they are shown only at the end of the pattern, where they are maximum, for the sake of clarity.

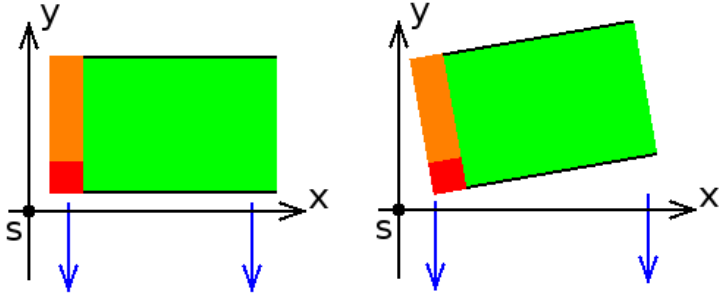


Figure 4.43: Schematics of a damaged blade, aligned (left frame) and with a tilt angle about the longitudinal  $s$ -axis (right frame). The schematics shows only the case of the horizontal blade, moving as indicated by the blue arrows, as the vertical one is conceptually identical, but for the axes and the direction of movement. The beam comes out of the paper, along the longitudinal axis. The green part of the blade represents the un-damaged part, i.e. with its original density, whereas the orange and red parts indicate increasing levels of damage, i.e. porosity.

been chosen for each blade. The porous blades foresee a 30 % porosity in the most affected area, i.e. around the edge directly facing the beam, for a thickness of approximately  $750 \mu\text{m}$ , and a 10 % porosity in the rest of the blade, average values very close to the estimations done after the test (see Tab. 4.8). Given the original density of the blade of  $1.83 \text{ g cm}^{-3}$  (see Sec. 2.2.1), these two values correspond to densities of  $1.281 \text{ g cm}^{-3}$  and  $1.647 \text{ g cm}^{-3}$ , respectively (see Eq. 4.2). The change in porosity in the area of the edge facing the beam is responsible for the delay accumulated by the curves with the porous blades over the regular ones at the beginning of the pattern, whereas the delay visible passed the knee (see Sec. 4.2.5) is due to the lower density in the rest of the blade, as this second part of the pattern is due to scraping by the innermost face of the blade (see Fig. 4.24). Moreover, the change in the intensity surviving scraping is extremely small for the horizontal blade, featured by a relatively large tilt angle (and also by important dispersive effects), and it is almost invisible for the vertical blade, featured by a small tilt angle (and not affected by dispersive effects). In the assumptions that a perfectly aligned blade interacts with the beam for times longer than what strictly

needed to fully accomplish scraping, no loss of performance should be expected in case of damage. Referring to Fig. 4.43, even though the performance of the part seriously damaged is worse than when it is not damaged, the orange part, affected by a medium level of damage, is still effective, since it is seen for a large number of turns by all the protons to be scraped. The effect of damage is simply longer times to achieve scraping. On the contrary, a tilted blade which is damaged is characterised as well by the aforementioned longer times for scraping, but most of all it experiences a loss of performance, since the protons the innermost in the distribution see the part of blade with medium levels of damage only for few passages, and have higher chances to survive with respect to the same blade un-damaged. As a consequence, despite the very generous assumption of a 10 % porosity over the whole blade, the change in the blade porosity coupled to possible tilt angles is far from explaining the change in performance of the blade shown in Fig. 4.33. Consequently, this might be induced by a systematic change in the characteristics of the beam distribution or in the relative distance between the centre of the beam and the blade position, typically induced by a drift of the orbit. For instance, a change of  $0.1 \mu\text{m}$  in the normalised emittance or a drift of the orbit of  $\sim 20/50 \mu\text{m}$  on the H/V plane can explain the variations seen in Fig. 4.33.

### 4.3.5 Benchmark Against BLM Signals

The benchmark presented in this section shows the comparison of simulation results against BLM measurements obtained with beam during the test. While for the benchmark against BCT readouts results with different scraping positions are given, the current benchmark deals only with the case of full beam scraping, i.e.  $0 \sigma$ , with both blades.

Since BLM signals are integrated over the whole SPS cycle, local sources of

losses may influence the readout of monitors (examples of losses taking place in the SPS during cycles with LHC beams are given in Ref. [72]). Hence, the scenario of full beam scraping has been chosen since it maximises the contribution to BLM readouts from scraping. Similarly, it is also the scenario that optimises the CPU time of the simulation, since all the beam protons tracked are intercepted by the blade and contribute to results. All the other scenarios would imply some delicate algebra on BLM signals for subtracting the contribution from other sources and isolating the contribution from scraping, without adding any relevant detail to the picture. Indeed, given the complexity of secondary particle cascades and the fact that monitors are located relatively far from the scraper blades, with massive elements along the path of secondary particles, the actual beam distribution and impact conditions have limited effects on BLM readouts, leaving very little memory of the primary impact on the SPS scraper blades.

The first part of this section is dedicated to a *qualitative comparison* between the BLM signals along the whole SPS ring and the losses predicted by the simulation. This comparison can only be qualitative, since the result of the simulation is a loss map, i.e. a map showing the average number of protons lost along the ring, whereas the BLM signal is due to secondary particle cascades initiated by the lost proton at the impact on the machine aperture. The focus is then moved to the LSS1, where the tested BSHV.11759 scrapers are located, for a *quantitative comparison* between the BLM readouts and energy deposition values in BLMs from the simulation. This comparison can be quantitative as it relies on the simulation of the entire particle cascades taking place during scraping, and thus reaching the BLMs, including the mechanisms of energy deposition in the BLMs themselves.

The qualitative comparison is done using the BLM measurements directly from the burst test of the blades, as this case maximises the number of scraped

protons, giving the highest and cleanest signals due to scraping all along the ring. Some BLMs locally in the LSS1 saturated, and the one the closest to the blades triggered the premature beam dump. Consequently, if readouts from BLMs in the LSS1 during the burst test are not fully trustworthy for a quantitative comparison, the readouts from the BLMs located in the rest of the ring are not in saturation, and they can thus be used. As already mentioned, this comparison can only be qualitative, since the result of the simulation is a loss map, i.e. a map showing the average number of protons lost along the ring, whereas the BLM signal is due to particle cascades initiated by the lost proton at the impact on the machine aperture. Thus, only trends can be compared, at most. For this comparison, the loss map obtained from the case of  $0 \sigma$  scraping when the permanent magnetic bump in the LSS1 is considered shown in Fig 4.15 is used, with no need of performing new simulations.

The actual benchmark is then given by the quantitative comparison between the measurements from BLMs located in the LSS1 and the signals predicted by the simulation. An important effort has been put in the development of the FLUKA geometry of the LSS1 downstream of the BSHV.11759 scrapers, in order to take into account all details possibly affecting the development of secondary particle showers, and thus results. Not only a model of the monitors has been added to the geometry, but also all the elements along the portion of beam line chosen for the benchmark, including magnetic elements and their magnetic fields. Indeed, since BLMs are sensitive to secondary particle cascades, what matters the most for a proper estimation of the BLM signals is the description of the objects involved in the development of the showers and those nearby the monitors. Since many of the BLMs in the LSS1 were saturating during the test, BLM readouts obtained with low beam intensities are used. In particular, among those recorded while looking for the centre of the beam at the scraper location before the actual

test, those with the same blade settings as those of the burst test are used, i.e. at full beam scraping. These readouts are shown to be affected only by scraping, and to scale pretty linearly with the number of scraped protons.

The present benchmark is relevant mainly to the development of the coupling between FLUKA and SIXTRACK as simulation tool for the production of reliable results rather than to the reconstruction of the actual conditions of beam scraping during the test, as BLM signals are primarily ruled by factors other than the impact conditions. The challenge for the SIXTRACK–FLUKA coupling is represented by the fact that a portion of  $\sim 80$  m of the LSS1 including magnetic elements has been modelled in the FLUKA geometry, and correspondingly skipped by SIXTRACK, with possible effects on the long term stability of the beam tracked. Indeed, while in SIXTRACK the tracking is based on a symplectic integration of the equations of motion of charged particles in magnetic fields, the tracking in magnetic fields is handled in FLUKA dividing the path of a particle in steps, computing at each step the Lorentz force and thus kicking the particle accordingly.

In the following, the qualitative comparison between the loss map shown in Fig. 4.15, obtained for full beam scraping with the horizontal blade of the BSHV.11759 scraper in case the permanent magnetic bump in the LSS1 is considered, and the BLM readouts along the SPS ring, obtained during the burst test of the blades, is first presented. Afterwards, the focus is moved on the quantitative comparison between the BLM readouts in the LSS1, obtained for full beam scraping at low beam intensity, and the values of energy deposition in the BLMs as predicted by the simulation. In-between the two, an overview on the BLM signals used for the quantitative comparison and a brief description of the extended FLUKA geometry of the LSS1 are given. In particular, it will be shown that, being the SPS BLMs ionisation chambers, readouts scale linearly with the

number of lost protons provided that the readout is far from saturation, even though BLMs are relatively old devices. This is an important verification which opens to a further estimation of the amount of beam scraped during the burst test before dumping is given, in addition to the one already found with BCT signals.

### Qualitative Comparison Against BLM Signals Along the Ring

Figure 4.44 shows the qualitative comparison between a beam loss map from simulations and the readouts from all the BLMs along the SPS during the burst test of the horizontal blade of the BSHV.11759 scrapers. The readouts obtained during the test of the vertical blade have been omitted, as they are very similar to those for the horizontal one (see Fig. 4.32). For comparison, the BLM signals obtained in case of full beam scraping with that same horizontal blade at low intensity are shown as well. Even though the beam intensity is lower by a factor 24 with respect to the test, this additional case gives a more essential overview of those loss locations in the SPS really affected by scraping. The BLM readouts have been cleaned of the signal from other sources, subtracting from the original values the measurements without scraping (e.g. see the curves at full intensity shown in Fig. 4.32). As a consequence, the shown BLM patterns should represent the net effect due to scraping. The shown loss map is the one computed for the horizontal blade (in graphite) of the BSHV.11759 at  $0 \sigma$  scraping, moving at 80 mm/s, when the permanent magnetic bump in the LSS1 is taken in consideration, shown in Fig. 4.15. Given the similarity between the patterns of the BLM measurements for the two blades, results from simulations are shown only for the case of the horizontal blade.

The loss map exhibits the main features of the BLM patterns, i.e. selected LSSs are most loaded and arcs are affected by moderate losses. In particular,

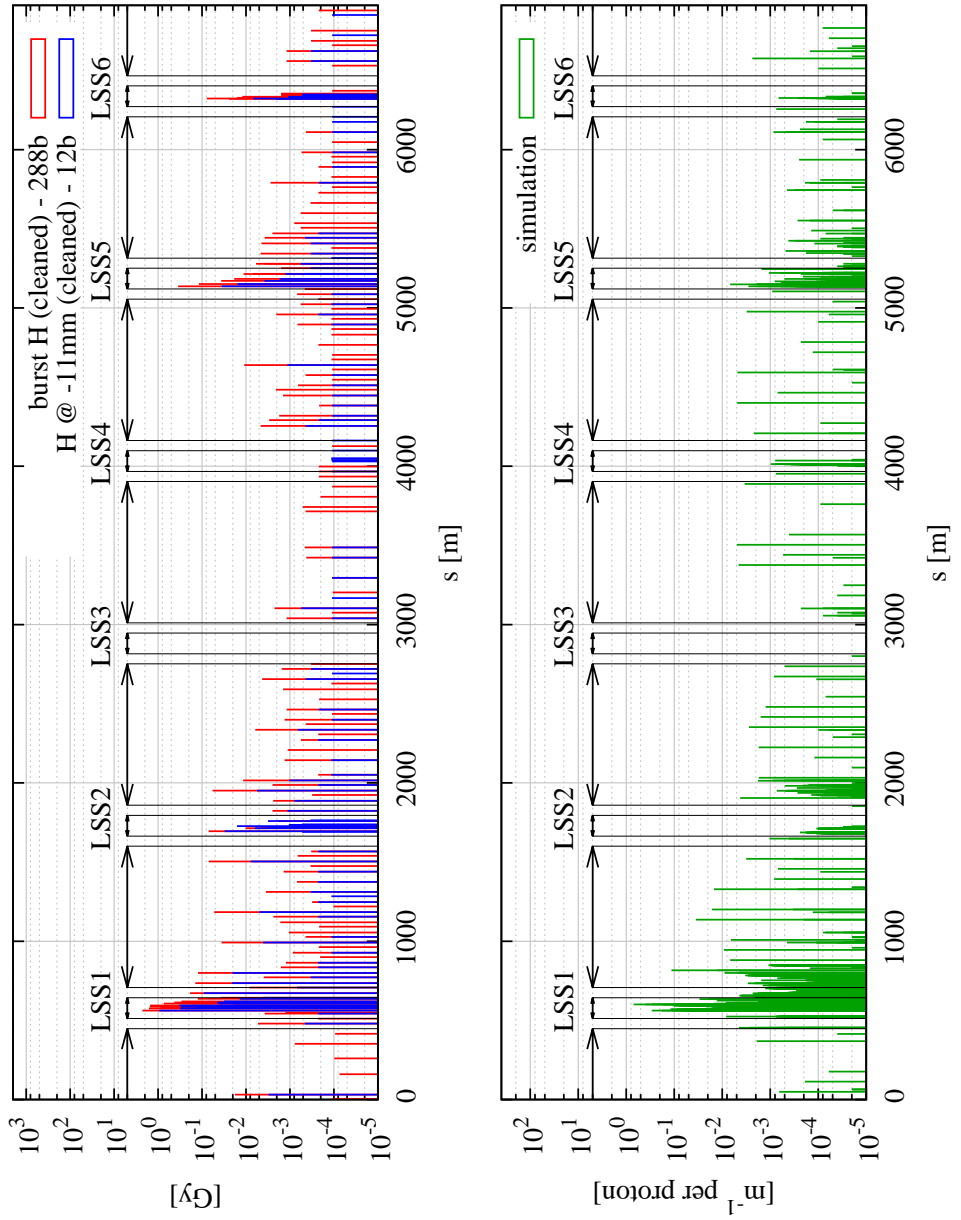


Figure 4.44: Qualitative comparison between the readouts from all the BLMs along the SPS during the burst test of the horizontal blade of the BSHV.11759 scrapers (upper frame, red curve) and a beam loss map from simulations (lower frame, green curve). For comparison, the BLM readouts at low intensity with the same settings, i.e. at full beam scraping, is shown as well (upper frame, blue curve). The BLM readouts have been cleaned of the signal from other sources, subtracting from the original values the measurements without scraping (e.g. see the curves at full intensity shown in Fig. 4.32). The shown loss map is the one computed for the horizontal blade (made of graphite) of the BSHV.11759 at  $0\sigma$  scraping, moving at 80 mm/s, when the permanent magnetic bump in the LSS1 is taken in consideration, shown in Fig. 4.15. No error bar is shown for the sake of clarity.

the LSS1 and the LSS5 are the most populated ones with losses. The former is where the scrapers, i.e. the source of lost protons, are located. Losses in the LSS5 are reproduced thanks to the explicit modelling in the FLUKA geometry of beam-intercepting devices there installed (see Sec. 4.2.1), even though the half-gap of the jaws of the TCXHW.51651 has been artificially reduced to get sufficiently high losses. The mechanical aperture of the SPS in the LSS5 is quite wide, and the reason for so high BLM signals is not known. The losses in the LSS6 as well are present thanks to the explicit modelling in the FLUKA geometry of beam-intercepting devices installed in that LSS; the aperture profile in that LSS may be improved, even though the readouts from the local BLMs are more than an order of magnitude lower than the maximum, i.e. in the LSS1. Losses in the LSS2 and the LSS4 are moderate, as the readout of the BLMs there installed is. The LSS3 is completely empty<sup>7</sup>.

Losses in the arcs reproduce fairly well the BLM pattern, with a kind of “U” shape visible between the LSS1 and the LSS5. The beginning of the arcs between the LSS1 and the LSS2, between the LSS2 and the LSS3, and between the LSS5 and the LSS6 see a local intensification of losses, as it also happens for the BLM signals. Local loss spikes in the arc take place nearby a spike in the BLM pattern, even though with a large variety in the relative ratio between the BLM readout and the intensity of the predicted loss.

As already mentioned, even though the agreement between simulation results and measurements can be regarded as satisfactory, the current comparison can be only qualitative, since the simulation results describe a pattern of losses along the ring, whereas the monitor signals are due to secondary particle showers initiated by the lost protons. On the contrary, the quantitative comparison focussed on the LSS1 presented in the following will show more robust outcomes. Before the

---

<sup>7</sup>It should be kept in mind that no BLMs are installed in the LSS3 (see Tab. 4.7), but the ones for the regular FODO cells.

case	beam intensity		time stamp	
	$N_{\text{bunches}}$	[ $10^{10}$ ]	SPS cycle [hh:mm:ss]	BCT [hh:mm:ss]
H, burst ( $-11$ mm)	288	3068.03	08:48:33.735	08:48:53.605
V, burst ( $5.7$ mm)	288	3056.35	08:30:48.135	08:31:08.005
H, regular ( $-13.2$ mm)	288	3071.11	08:57:12.135	08:57:32.005
V, regular ( $3.5$ mm)	288	3039.44	08:27:26.535	08:27:46.405
no scraping	288	2965.18	08:38:57.735	08:39:17.605
no scraping	12	122.575	08:19:16.935	08:19:36.805
H, $-11$ mm	12	122.141	08:17:21.735	08:17:41.605
V, $5.7$ mm	12	115.74	07:28:52.935	07:29:12.805
H, $-11.5$ mm	12	116.972	07:35:36.135	07:35:56.005

Table 4.13: Scraping settings, beam intensities and respective SPS cycles chosen for the present analysis of BLM signals: number of bunches (second column), total beam intensity before scraping (without the background noise, third column), time stamps according to Timber (SPS cycle time stamp, fourth column) and respective BCT timing (fifth column), for referring to BCT signals shown in App. C.

comparison, BLM signals in the LSS1 are quickly analysed, pointing to their good property of linear scaling with number of protons opening to another estimation of the amount of beam scraped during the burst test before dumping, and the FLUKA geometry of the LSS1 is briefly described.

### Analysis of BLM Signals in the LSS1

As already mentioned, the BLM signals in the LSS1 during the burst test are particularly high due to intense secondary particle showers. As already seen in the zoom on that region in Fig. 4.32, many BLMs are very close to saturation or even saturate. As a consequence, for a quantitative benchmark against the BLM signals in the LSS1, a further analysis of the BLM readouts is needed, in order to identify a proper set of measurements, possibly without saturated values.

BCT signals during scraping (see Sec. 4.3.4) are extremely sensitive to the conditions of the beam, including the beam distribution and orbit jittering, the

scraping blade position, speed and tilt angle, as well as to a separate jitter at 50 Hz. All these aspects required to perform averages of BCT signals from SPS cycles characterised by the same blade settings (see Fig. 4.36). On the contrary, BLM signals are less sensitive to the aforementioned aspects; hence, there is no need to average signals from SPS cycles with the same blade settings. Thus, comparisons in absolute values can be done with readouts from single cycles. Table 4.13 lists all those SPS cycles with the main scraping settings from which BLM signals have been taken to be used in the following analysis. For a complete overview on the available BLM signals, see App. E.

Figure 4.45 shows the pattern of BLM signals obtained with different scraping configurations, zoomed on the LSS1 and the DSs at both its ends. For comparison, signals with no scraping for the same beam intensity are also shown. The BLM.11771, at  $s \simeq 560$  m, is the one immediately downstream of the BSHV.11759 scrapers, and the BLM.11904.MDVA, at  $s \simeq 605$  m, is the one immediately downstream of the main beam dump (the LSS1 also hosts the beam dumping system, see Sec. 2.1.1). In all the plots, the BLM patterns in case of no scraping are characterised by the event of a beam dump, with a clear peak at the BLM.11904.MDVA, as obviously expected, no matter the intensity of the dumped beam. On the contrary, their pattern is more detailed in the case of high beam intensities than in the case of low beam intensities.

In the patterns obtained during the test (upper-left frame), the BLM signals in the region between the scrapers and the main dump have the highest readouts, pretty much close to their maximum (see Tab. 4.7). They show signs of saturation, with a trend almost flat. It should be noted that the two BLMs of the regular FODO cell BLM.118 and BLM.119 are close to saturation either, as their calibration factor is one order of magnitude lower than the one of the other BLMs in the LSS1 (see Tab. 4.7). The BLMs downstream of the main dump seem not

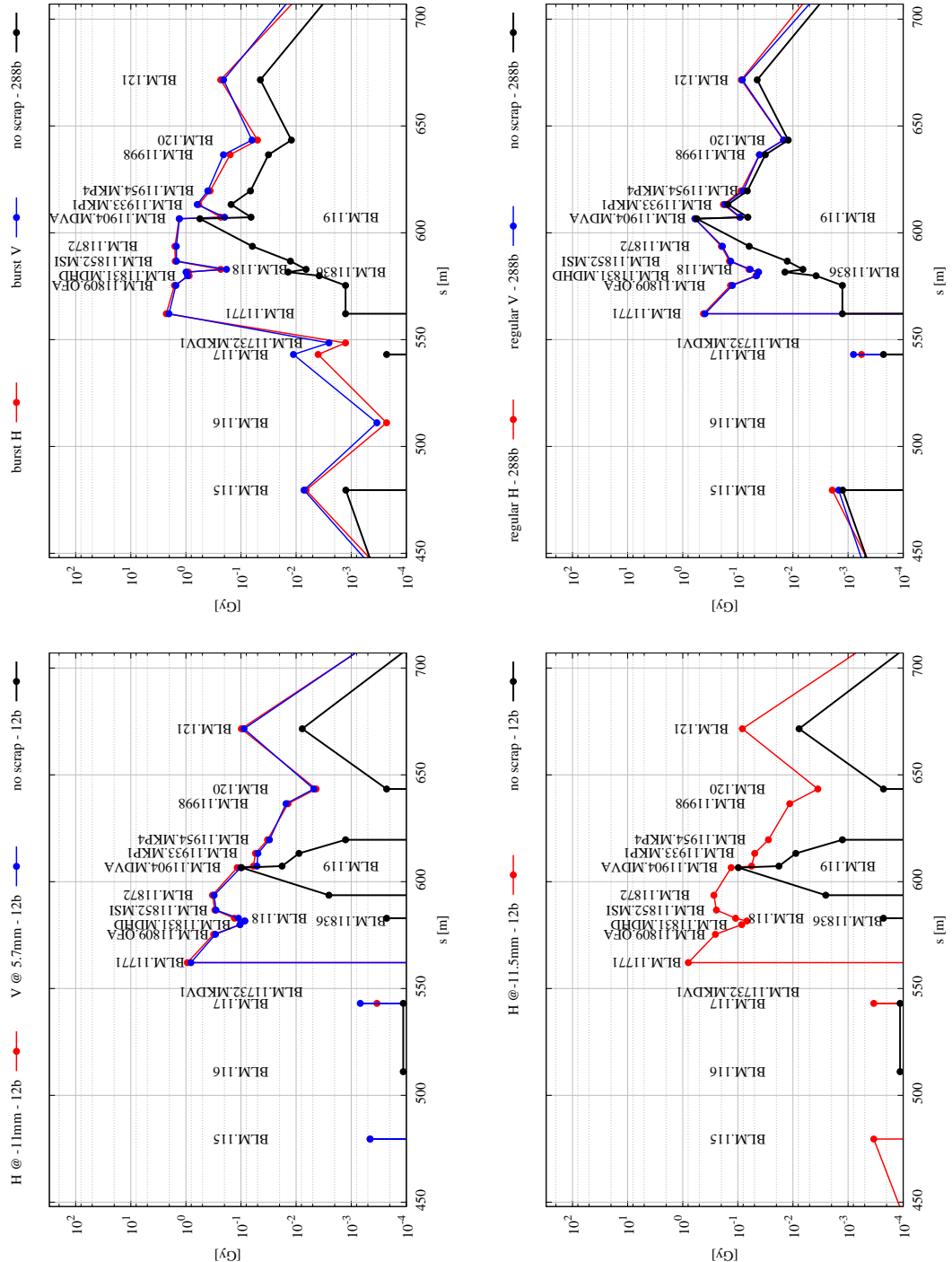


Figure 4.45: Pattern of BLM signals obtained with the blades in different scraping positions, zoomed on the LSS1 and the DSs at both its ends. Top-left frame: signals during burst test of both blades. Top-right frame: signals during regular scraping with each blade. Bottom-left frame: signals during full beam scraping at low beam intensities. Bottom-right frame: signal during scraping with the horizontal blade off the beam centre by  $\sim 500 \mu\text{m}$ . For comparison, the signals with no scraping for the same beam intensity are shown as well.

to saturate, and they have a pattern very similar to the one from a beam dump event (i.e. when no scraping is performed), at the point that some linear scaling could be identified. From the analysis of the BCT signals, it has been concluded that approximately 20–30 % of the beam has been actually scraped during the burst test of the blades (see Tab. 4.12), and the rest has been dumped. This implies that, for these BLMs, the signal due to scraping is somehow comparable to the signal from dump, even though much more intense. This is reasonable, as these BLMs see secondary particle showers leaving the massive objects they are close to, i.e. the main dump TIDV.11892, the quadrupole of the regular FODO cell QDA.11910 and various kickers, with no possibility to disentangle a beam dump event from a scraping event, but for the intensity<sup>8</sup>.

The BLM signals obtained during regular scraping (upper-right frame) are all far from saturation, even though the intensity of the beam is high. Those between the scrapers and the main dump show a distinct component due to scraping. Moreover, the slight difference between signals downstream of the dump, substantially the same for all the involved BLMs, is due to scraping either. It should be noted that the amount of scraped beam is able to trigger such a distinct difference on the BLM signals, also appreciable in logarithmic scale, even though on the order of 1–2 % with respect to the total intensity. Consequently, the BLMs downstream of the dump can shed some light on the intensity that was actually scraped during the burst test.

The lower frames show BLM patterns obtained when scraping low intensity beams, either in case of full beam scraping separately with each blade (lower-left

---

<sup>8</sup>Indeed, in the case of a dump, all the protons hit the entrance face of the dump, pointing downwards (thanks to the sweeping system, with which the dumping system is equipped), thus not towards the BLMs; hence, only a marginal fraction of particles generated in the cascades at large angles may survive these massive elements and reach the BLM. On the contrary, in the case of a scraping event, protons are lost on the mechanical aperture inside these elements, with secondary particles traversing less material to reach the BLMs, and the monitors possibly in the cone of the cascade generated by some lost protons.

frame) or in case of scraping with the horizontal blade off the centre of the beam by  $\sim 500 \mu\text{m}$  (lower-right frame), for which  $\sim 80\%$  of the beam has been scraped. In all these cases, the pattern of the BLM signals are very similar to each other; in particular, the pattern of the BLMs between the scrapers and the main beam dump are somehow different from the one obtained with regular scraping (see upper-right frame), though the signal distinctly comes from scraping; moreover, only the BLM at the dump reads a signal comparable to the one induced by the dump, which is not the case when dealing with high intensity beams. On the contrary, the pattern of the BLMs downstream of the main beam dump are very similar to those seen during regular scraping, and in case of dumping at high intensities.

The plots shown in Fig. 4.45 give indications that signals in the BLMs in the LSS1 may correctly scale linearly with the number of protons, unless close to saturation, as it can be expected from ionisation chambers, even for old devices like the SPS BLMs. Assuming that:

- the BLM signals at full beam scraping of low intensity beams with each blade shown in lower-left frame of Fig. 4.45 are due only to scraping, with no contribution from a beam dump event or any other source of losses. If expressed per proton, this couple of signals can thus be taken as the characteristic footprint of an event of scraping;
- the BLM signals with no scraping at high intensity shown in the upper frames of Fig. 4.45 give a detailed picture of the contribution from a dump event to the BLM signals in the whole LSS1. If normalised per proton, this pattern can be taken as the characteristic footprint of a beam dump event;

the pattern of BLM signals obtained with other scraping settings can be reconstructed from these patterns, with proper weights, proving that BLMs have linear readouts. This would open to the possibility for estimating the amount of beam

actually scraped during the burst test with BLMs. Patterns of signals of BLMs installed in the LSS1 could be thus reconstructed for each scraping position with a linear combination like

$$R_{i,k} = sR_{i,f} + (1 - s)R_{i,d}, \quad (4.6)$$

where  $R_{i,k}$  is the signal read by the  $i$ -th BLM in case of scraping with the blade at position  $k$ , normalised to the beam intensity;  $R_{i,f}$  and  $R_{i,d}$  are the normalised signals in that same BLM for full beam scraping and in case of dump, i.e. the signal for full beam scraping at low intensity shown for each blade in the lower-left frame of Fig. 4.45, and the signal with no scraping at full beam intensity shown in the upper frames of the same figure, respectively;  $s$  is the amount of beam scraped with the blade at the position  $k$ .

Figure 4.46 shows the pattern of BLM signals as measured at different scraping positions and as reconstructed from other BLM signals, shown in Fig. 4.45. The upper frames show how the pattern at full beam scraping at low intensity with each blade can be reconstructed starting from those obtained from regular scraping, barely removing the contribution from beam dump and then compensating for the small portion of beam scraped during regular scraping. The patterns are normalised per beam proton. Even though not perfect, the agreement is remarkable, confirming the assumption on the linearity of BLM signals far from saturation on the number of protons. The lower frames of the same figure show a couple of cases treated with the linear combination of BLM signals as expressed by Eq. 4.6. Both cases deal with the horizontal blade, at regular scraping (left frame) and when scraping with the blade  $\sim 500 \mu\text{m}$  off the beam centre (right frame). Also in these two cases, the agreement between the measurements and the pattern reconstructed with the linear combination expressed by Eq. 4.6 is remarkable.

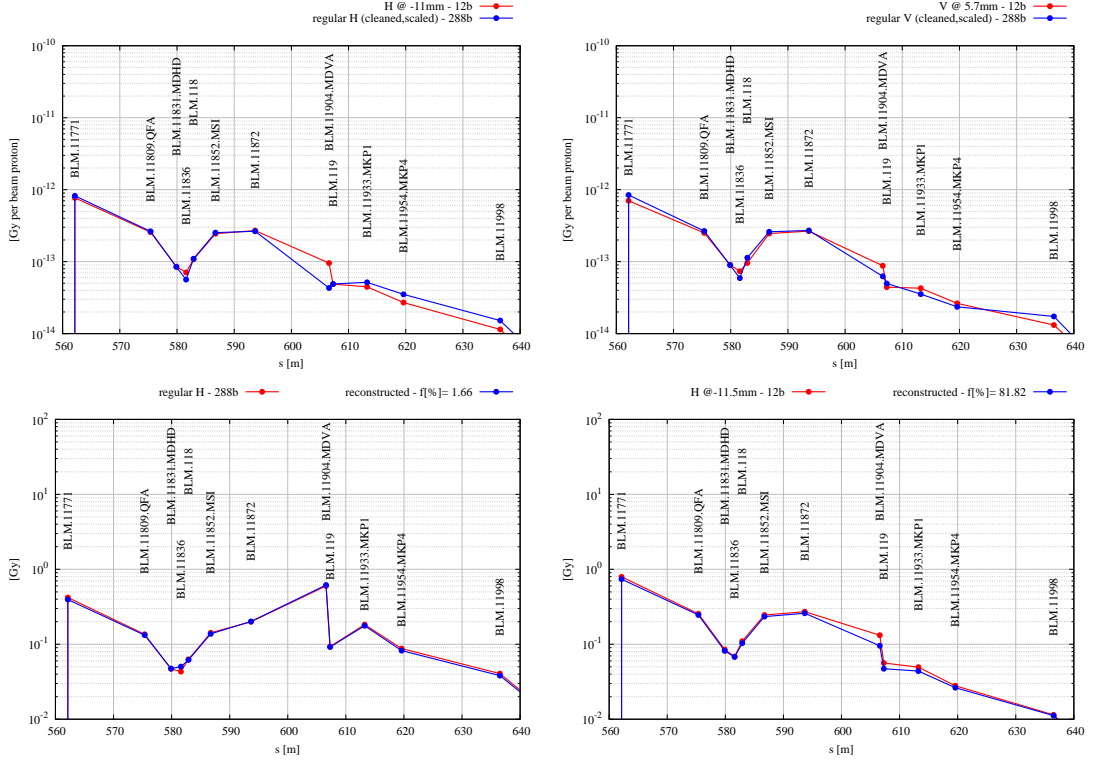


Figure 4.46: Pattern of BLM signals as measured at different scraping positions and as reconstructed from other BLM signals, shown in Fig. 4.45. The shown range of values on the horizontal axis spans over the LSS1 and the DSs at both its ends. Upper frames: pattern of full beam scraping as from measurements at low intensity (red curves) and as reconstructed with signals at regular scraping, cleaned of the component from the beam dump, and compensated for the small amount of beam scraped during regular scraping; the case of the horizontal blade is shown on the left, whereas the case of the vertical blade is shown on the right. The patterns are normalised per beam proton. Lower-left frame: pattern of BLM signals in case of regular scraping as from measurements at high intensity (red curves) and as reconstructed according to Eq. 4.6, i.e. with the signals from full beam scraping at low intensity, weighted by the fraction of beam actually scraped, and from beam dumping at full beam intensity, weighted by the fraction of the dumped beam. The percentage shown in the key represent the amount of beam actually scraped during regular scraping. Lower-right frame: pattern of BLM signals in case of scraping with the horizontal blade  $\sim 500 \mu\text{m}$  off the beam centre as from measurements and as reconstructed, as done for the regular scraping with the same blade. As for the plot on the left, the percentage shown in the key represent the amount of scraped beam.

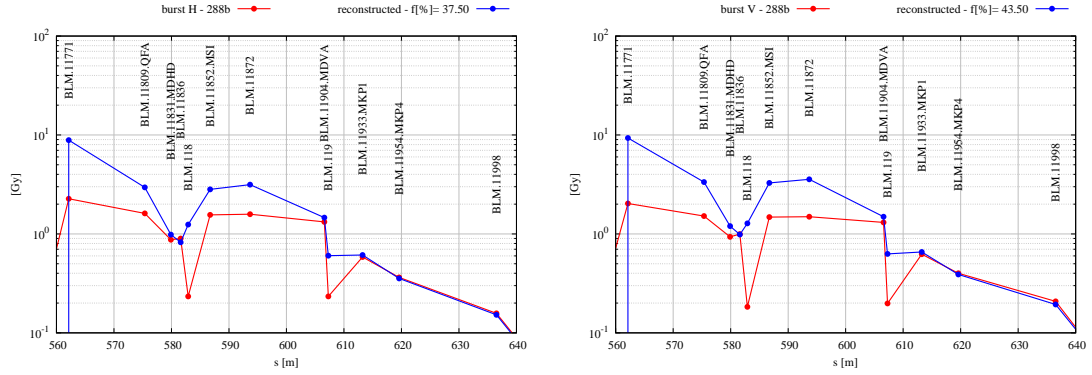


Figure 4.47: Pattern of signals in BLMs located in the LSS1 in case of the burst test of each blade, i.e. when scraping at  $0\sigma$  the beam at full intensity, from direct measurements (red curve) and as reconstructed according to Eq. 4.6, i.e. with the signals from full beam scraping at low intensity and from beam dumping at full intensity shown in Fig. 4.45. The case of the horizontal blade is shown on the left, whereas the case of the vertical blade is shown on the right. The fraction given in the key is the reconstructed amount of scraped beam which allows one to match the signals in the BLMs downstream of the main beam dump, the only ones known to be far from saturation and thus expected to give a readout truly proportional to the amount of beam scraped and dumped.

Given the good properties of linear scaling of the BLM signals, Eq. 4.6 and the signals from full beam scraping at low intensity and from beam dumping at full intensity shown in Fig. 4.45 are then applied to the burst test, in the attempt to estimate the number of protons actually scraped before dumping the beam. Figure 4.47 thus shows the pattern of the BLM signals measured during the burst test, and the reconstructed ones, for each blade. The reconstructed patterns are such that the BLMs downstream of the main beam dump match; the fraction of scraped beam necessary to the matching is indicated in the key. The reconstructed patterns show that all the BLMs between the scraper and the dump saturate, with the exception of one. The reconstructed signal for this BLM matches almost perfectly the measurement, confirming the quality of the result. As a consequence, the reconstructed patterns show the BLM pattern that should have been seen during the burst test in case saturation was not taking place.

Given the good properties of linear scaling of the BLM signals, this method

blade	intensity		mesh [ $\mu\text{m}$ ]	max	
	[%]	[ $10^{13}$ ]		[ $\text{GeV cm}^{-3}$ per $\text{p}^+$ ]	[ $\text{kJ cm}^{-3}$ ]
H	37.5 (20)	1.15 (0.61)	50 x 50	14–16	26–30
			10 x 10	20–25	37–46
V	43.5 (30)	1.33 (0.92)	50 x 50	13–16	28–34
			10 x 10	18–25	38–53

Table 4.14: Summary of amount of beam scraped as estimated via the BLM signals and energy deposition expected in the blade during the burst test. The given intervals on energy deposition consider all the cases of scraping at  $0 \sigma$  shown in Fig. 4.39, for different combinations of tilt angle and speed. The estimations from the BCT signals are given in parentheses. The quoted meshes have a longitudinal stepping of 500  $\mu\text{m}$ .

of estimating the amount of beam scraped during the burst test before dumping seems to be quite robust. The estimations are approximately 80 % and 50 % larger with respect to those obtained with the BCT signals for the horizontal and vertical blade, respectively, with a corresponding increase in the estimated energy deposition. Table 4.14 updates the values given in Tab. 4.12 with the new ones. With respect to the one based on the BCT signals, this method does not suffer neither from the distribution of the beam in the machine nor from the settings of the blade (i.e. speed and tilt angle). It should be noted that the estimation based on the BCT signals suffers from the limited resolution in time of the BCT logging and the limited analogue bandwidth.

The quantitative comparison of energy deposition values in the BLM is presented in the following, after a brief description of the simulation settings and the geometry used. Given the good properties of linear scaling of the BLM signals, only the BLM readouts for full beam scraping at low intensity will be used.

## Simulation Settings

In general, the simulation settings for the quantitative benchmark of the BLM readouts are the same as those presented in Sec. 4.2.1. This involves FLUKA,

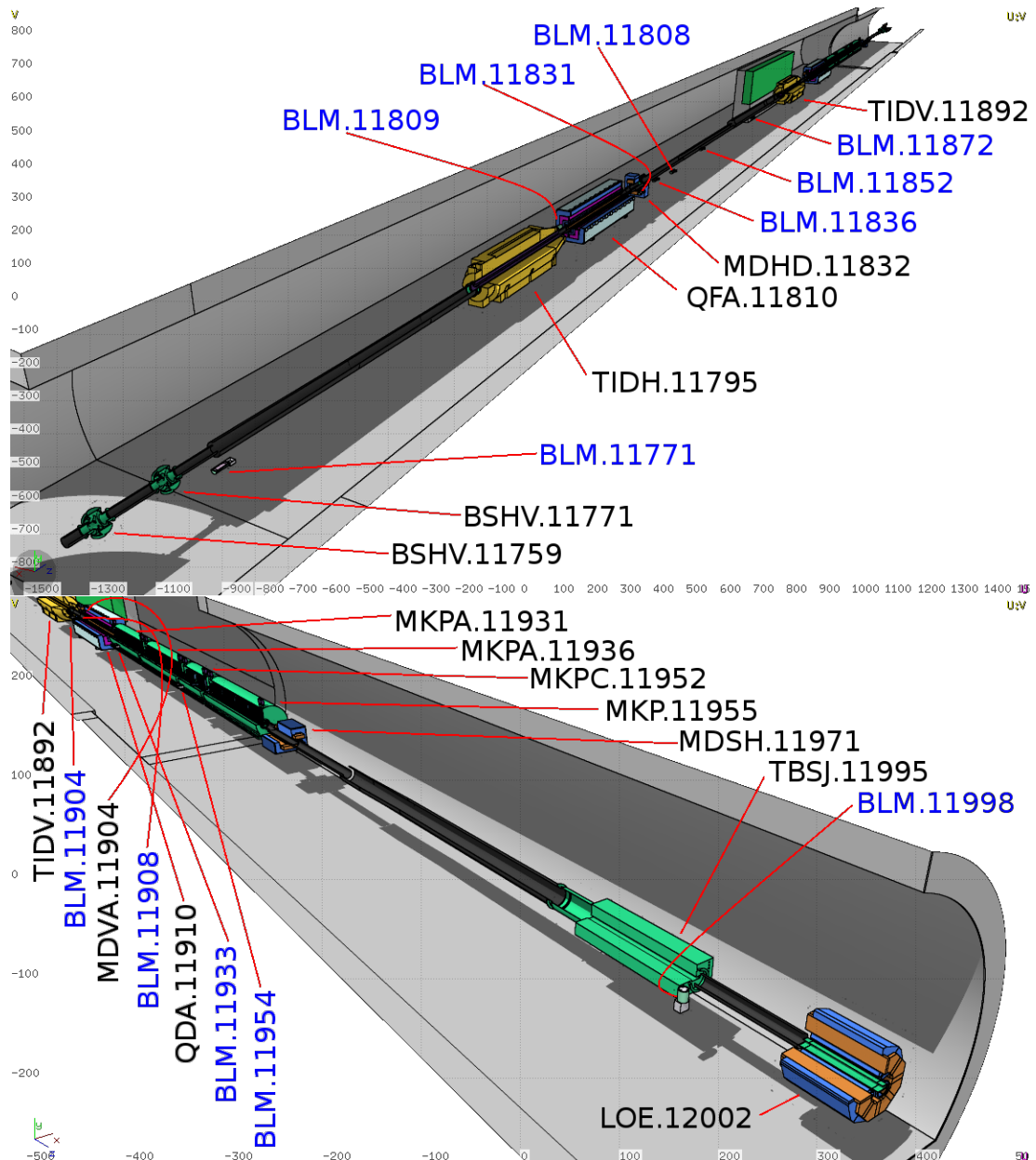


Figure 4.48: 3D rendering with Flair of the whole FLUKA geometry of the LSS1: view from upstream (upper frame) and from downstream (lower frame). The beam always moves from left to right. The scrapers are visible at the upstream edge of the upper frame. BLMs, despite not plainly visible in the geometry, are located usually at beam height. They are indicated as well, labelled in blue.

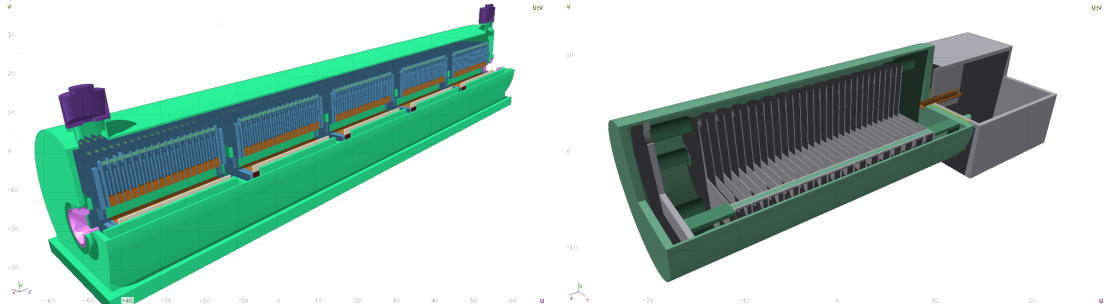


Figure 4.49: 3D rendering with Flair of the FLUKA geometry of the MKPA kicker (left frame) and of the BLM (right frame). As example of the level of detail of the model, the high-voltage plates of each module of the kicker inside the tank have been modelled one by one; the five modules are implemented in the tank using the LATTICE capabilities of FLUKA. The BLM have been modelled in great detail either, down to the single high-voltage plate.

SIXTRACK and the coupling. The only difference is represented by the FLUKA geometry of the SPS LSS1. Indeed, since BLM readouts are sensitive to secondary particle showers, it has been necessary not only to explicitly model the BLMs themselves, but also to extensively develop the FLUKA geometry of the LSS1. In addition to the BSHV.11759 and BSHV.11771 scrapers and the beam-intercepting devices in the LSS5 and the LSS6 already part of the FLUKA geometry used for the calculations presented so far, the geometry of the LSS1 has been developed in great detail, extending from the scrapers to the beginning of the DS downstream of the LSS1. Figure 4.48 shows the 3D rendering with Flair of the FLUKA geometry of the LSS1 used for the studies. The geometry has been assembled with the LB. The effort of the geometry development involved every element shown in the geometry, now also part of the FEDB and available to other users for possible other studies in the future to come.

Figure 4.49 shows the 3D rendering with Flair of the MKPA kicker magnet (left frame), as example of the level of details in the implementation of the geometry. Essential to the results, the BLMs have been explicitly modelled either, and their model is shown in the same figure (right frame). Since measured BLM

gas	volume [cm <sup>-3</sup> ]	density [g cm <sup>-3</sup> ]	mass [g]
nitrogen	1141.1	0.00126	1.4378

Table 4.15: Main characteristics of the region of active gas of the SPS BLMs as modelled in the FLUKA geometry: gas (first column), volume of the region (second column), density of the gas (third column), and mass of gas contained in the volume (fourth column). This last number is essential for the estimation of the BLM signal, since measurements are expressed in Gy.

signals are expressed in Gy, the estimation is performed scoring the energy deposition in the region of active gas inside the monitor, and then taking the ratio to the mass of gas contained in the scoring volume. Table 4.15 summarises the main features of the region of active gas of the SPS BLMs as modelled in the FLUKA geometry.

Concerning physics and particle transport in FLUKA, the only difference with respect to the settings summarised in Sec. 4.2.1 is the increase by an order of magnitude of the transport and production thresholds of the EM part, i.e. electrons and positrons are emitted and transported down to 100 keV, whereas photons are treated down to 10 keV. The increase of these thresholds has been possible since the energy deposition of interest is not the one in extremely small volumes of material, as it was the case for the refined mesh used for the analysis of the scraper blades. Moreover, the use of LPB has been extended to the new massive elements added to the geometry of the LSS1, including the two dumps TIDH.11795 and TIDV.11892, the two main quadrupoles QFA.11810 and QDA.11910, the TBSJ.11995 absorber and the LOE.12002 octupole. LPB is applied to the tunnel walls and the shielding wall next to the TIDV.11892, with much higher thresholds, to gain further CPU time.

The beam distribution used for the simulations is the same as the one used for addressing the effects from the permanent magnetic bump in the LSS1 (see

Sec. 4.2.3). There is only one exception, when the beam sampled for the benchmark against BCT signals (see Sec. 4.3.4) is used to check possible effects due to realistic scraping conditions; these include the speed of the blade, different from the nominal one, and the tilt angle.

The SPS optics is the Q20 one, with the permanent bump in the LSS1 always considered but for one case, used to address the effects due to its presence.

### Quantitative Comparison Against BLM Signals in the LSS1

The aim of this comparison is to have a quantitative benchmark between readouts from BLMs installed in the LSS1 downstream of the tested scrapers and results from the simulations. In particular, the BLM readouts obtained at full beam scraping with low intensity beams are used, as for these values the concerned BLMs have been proven to perform in regime of linear response, and thus measurements are trustworthy, as they are directly proportional to the number of scraped protons. Results from the simulations are estimations of energy deposition in the volume of active gas defined in the FLUKA model of the monitor.

Figure 4.50 shows the quantitative comparison of the signals in the BLMs located in the LSS1 downstream of the scrapers between the measurements at low beam intensity (taken from Fig. 4.45) and the predictions by the simulation, in case of full beam scraping, for each blade. The reference curve for the simulations is the red one, obtained considering the permanent magnetic bump in the LSS1. The agreement between simulation results and measurements is remarkably good for some BLMs, whereas it is poorer for others (anyway, within a factor of 2–3).

As already mentioned in Sec. 4.3.2, the positions of the BLMs along the ring have been deduced from the technical drawings of the SPS [97], and the lattice structure of the accelerator [98]. In some occasions, the drawings showing zooms on specific cells of the SPS LSS1 are not consistent either on the longitudinal

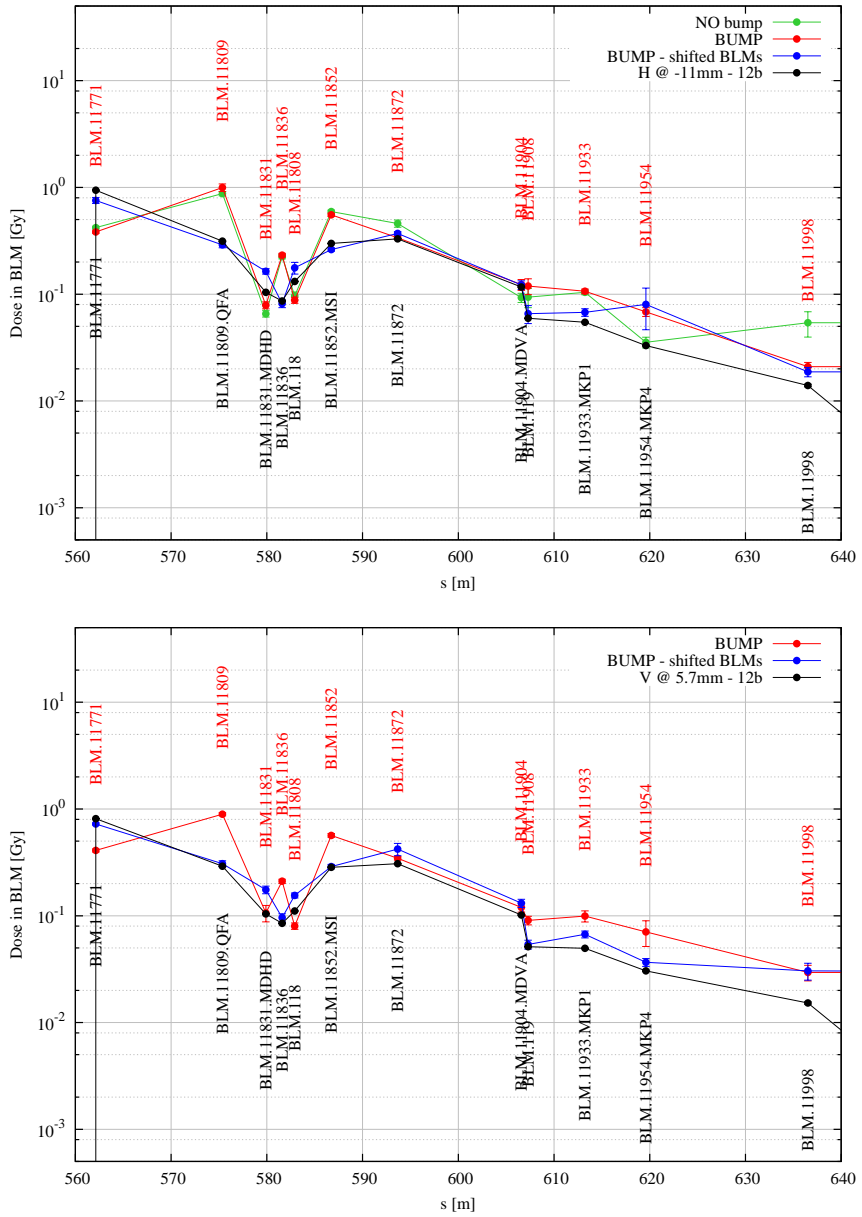


Figure 4.50: Quantitative comparison of the signals in the BLMs located in the LSS1 downstream of the scrapers between the measurements at low beam intensity (black curves, taken from Fig. 4.45) and the predictions by the simulation (coloured curves), in case of full beam scraping. The upper frame shows the case of the horizontal blade, whereas the lower frame shows the case of the vertical blade. The red curves show the simulation results with the BLM in their nominal positions, whereas the blue ones show the effect of a transverse displacement of the monitors in a more favourable position (see Tab. 4.16). The plot for the horizontal blade also shows the results when the permanent magnetic bump in the LSS1 is not considered (green curve). When visible, the errors bars on the measurements refer to the LSB, whereas those on the simulated data refer to the statistical uncertainty only.

BLM	position		displacement [cm]
	reference [cm]	favourable [cm]	
BLM.11771	-45.0	-32.0	13
BLM.11809	22.5	35.5	-13
BLM.11831	-45.0	-32.0	13
BLM.11836	-43.0	-30.0	13
BLM.11808	-45.0	-32.0	13
BLM.11852	-25.0	-38.0	-13
BLM.11872	-35.0	-	0
BLM.11904	-27.5	-	0
BLM.11908	-27.5	-40.5	-13
BLM.11933	-35.0	-48.0	-13
BLM.11954	-37.5	-50.5	-13
BLM.11998	-25.0	-38.0	-13

Table 4.16: BLM transverse positions in the FLUKA geometry. The second column reports the reference BLM positions used in all the simulations, but when monitors are provocatively shifted to more favourable positions, reported in the third column. Both positions are the horizontal transverse displacement with respect to the machine axis, as all the BLMs are installed at beam height. The sign convention is the same as for the local curvilinear reference system used in linear accelerator optics, i.e. a positive value means on the outside of the ring. Displacements, shown in the fourth column, are negative when the BLM is shifted far from the beam, whereas a positive value represent a movement of the monitor closer to the beam.

or on the transverse position of the BLMs. In these situations, priority is given to the detailed drawings. Transversely, the related uncertainty can be similar to the BLM dimensions, whereas longitudinally the related uncertainty can be even larger than the BLM dimensions. It should be kept in mind that the burst test has been carried out at the end of the SPS activity and afterwards the whole LSS1 has been dismounted for important maintenance works; as a consequence, there is no way to resolve the uncertainty due to BLM positioning. In order to address the dependency on the positions of the BLMs and the unavoidable uncertainty, another simulation has been run for each blade, provocatively displacing on purpose the monitors in positions more favourable for the estimation of the

signals, i.e. which would result in improving the agreement with measurements. Displacements are of the order of the transverse outer dimension of the monitor, i.e.  $\sim 13$  cm. Table 4.16 summarises the reference transverse positions of BLMs in the FLUKA geometry and the more favourable ones. Only the two BLMs at the centre of the plots (i.e. BLM.11872 and BLM.11904) have not been moved, since the agreement is already remarkably good. The results obtained with the shifted BLMs are shown by the blue curves in Fig. 4.50. For most of the BLMs upstream of the BLM.11908 included (which is located in the close vicinity of the main beam dump), the agreement becomes extremely good, especially for the BLMs the closest to the scrapers, and with just a couple of monitors giving results off the measurements on the opposite side with respect to those at the reference position (e.g. the signal of the BLM.11831 in its reference position is underestimated with respect to the measurement, whereas in the shifted position is overestimated). BLMs downstream of the BLM.11908 get improved either, even though they suffer a bit from statistics. The comparison between the BLM signals in their reference and shifted positions shows how sensitive is this benchmark on BLM positioning. Nevertheless, despite of the uncertainty on BLM positions, the benchmark can be regarded as extremely good.

The horizontal blade has also been simulated in the case the permanent magnetic bump in the LSS1 is not considered, shown by the green curve in the upper frame of Fig. 4.50. A limited effect can be seen on most of the monitors but those downstream of the main beam dump, i.e. downstream of the BLM.11908, even though the statistics seems to be a bit poor for these monitors. The effect of the permanent magnetic bump in the LSS1 can be thus regarded as secondary to the one due to BLM positioning.

Figure 4.51 shows the effect on the BLM readouts when more realistic scraping settings and beam distribution are considered. In particular, the same settings

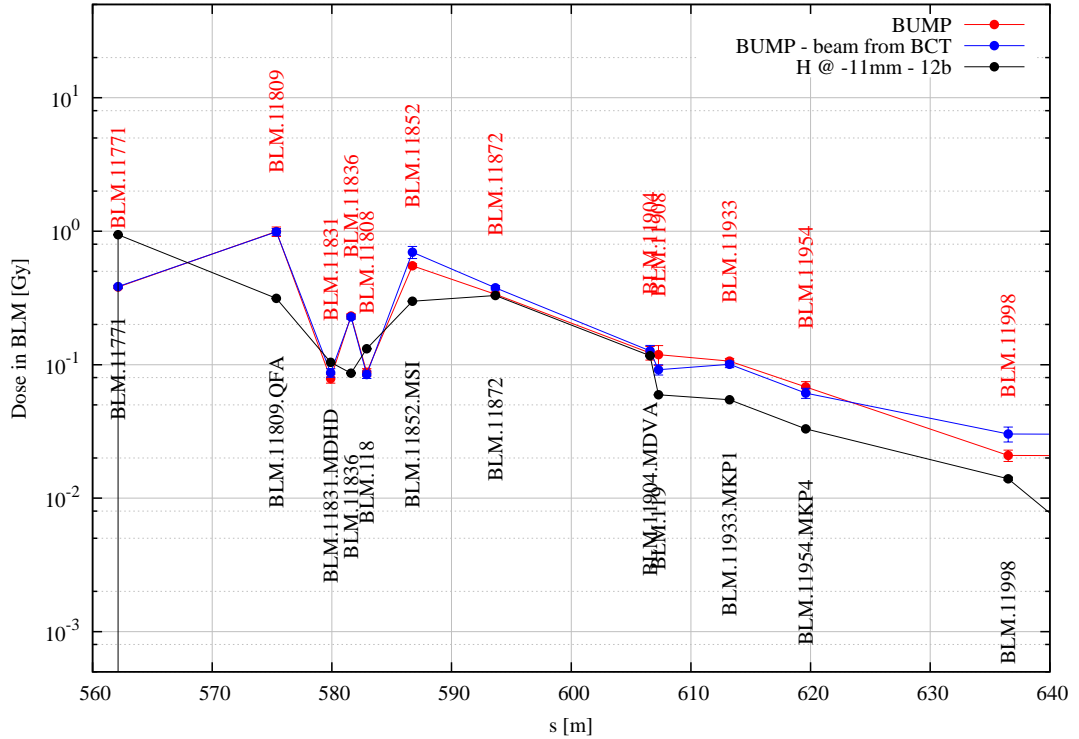


Figure 4.51: Quantitative comparison of the signals in the BLMs located in the LSS1 downstream of the scrapers between the measurements at low beam intensity (black curves, taken from Fig. 4.45) and the predictions by the simulation (coloured curves), when using more realistic scraping settings and beam distribution, in case of full beam scraping. Only the cases for the horizontal blade are shown. In particular, the red curve is the same as the one shown in the upper frame of Fig. 4.50, and it is taken as reference, whereas the blue curve shows the results obtained using the same beam sampled as the one for the benchmark against BCT measurements (see Sec. 4.3.4), and with the blade moving at 60 mm/s and tilted by 4° about the longitudinal axis. Both curves have been obtained considering the permanent magnetic bump in the LSS1 and the BLMs in their reference positions. When visible, the error bars on the measurements refer to the LSB, whereas those on the results from simulation refer to the statistical uncertainty only.

as those in one of the simulations run for the benchmark against the BCT measurements have been chosen, in the attempt to maximise the differences on the beam impact conditions with respect to those considered so far in the benchmark against the BLM readouts, i.e. a broader beam distribution, a blade moving at the slower speed of 60 mm/s and tilted by 4° about the longitudinal axis. Marginal variations can be seen, also on the BLMs downstream of the main beam dump. This proves that, even with quite important changes able to significantly affect the BCT signals (see the upper-left frame of Fig. 4.39), beam impact conditions at the scraper blades are not particularly relevant for the BLM readouts, confirming the stability of BLM signals on actual scraping conditions but for the total number of scraped protons.

#### 4.3.6 Conclusions

In order to verify the high values of energy deposition in the blades of the SPS scrapers predicted by the simulations (e.g. see Fig. 4.6 or Sec. 4.2.6), a beam-based test was carried out at the end of the SPS activity in 2013, scraping LHC beams in the SPS with the most severe settings foreseen by the simulations, i.e. full beam intensity (i.e. 288 bunches, for a total of  $\sim 3 \cdot 10^{13}$  protons) and  $0 \sigma$  scraping. During the test, secondary particle showers generated by the interaction of beam protons with the scraper blades were so intense that the BLM downstream of the tested scraper triggered a beam dump, prematurely stopping the test. Retrieving the timing of the trigger and using BCT readouts at low intensity with the same scraping settings as those of the test allowed the estimation of the number of protons scraped during the test, i.e. 20 % and 30 % of the circulating beam for the horizontal and vertical blade, respectively, corresponding to  $\sim 6.1 \cdot 10^{12}$  and  $\sim 9.2 \cdot 10^{12}$  protons, respectively.

Even though the beam was prematurely dumped, it was possible to damage

the blades. An indirect observation of the damage was possible via the sudden and abrupt degradation of the quality of the vacuum in the MKD dump kickers immediately upstream of the tested scrapers at the moment of the test. The degradation of the vacuum, by some orders of magnitude in terms of pressure, was due to the sublimation of atoms and clusters of atoms induced by the high levels of energy deposition the blades were subject to. Moreover, after the test, a loss in performance of the blades during the regular scraping of beam tails was visible, even though limited. Direct observations of the damage to the blades were possible once the blades were dismounted from the mechanics. Observations of the blades by the naked-eye showed signs of change of crystallographic state on the surface around the edge which scraped the beam. SEM analyses confirmed relevant changes in the porosity of the material, and more quantitative estimations assessed a porosity of  $\sim 30\%$  in the region the most damaged, corresponding to a decrease of the density of the material by the same amount.

BCT signals and BLM readouts were recorded during the burst test and also during other SPS cycles on the same morning of the test. In particular, signals have been collected for different scraping positions at low beam intensities, and for regular scraping at high beam intensities. These were used: to reconstruct the operational conditions of the scraper blades, i.e. speed and tilt angles, at the burst test, and thus to infer energy deposition values which provoked the seen damaged; to have a further estimation of the amount of beam scraped before dumping; and to prove the maturity of the FLUKA–SIXTRACK coupling as simulation tool for the production of reliable results.

The time evolution of the beam current during scraping is extremely sensitive to the distribution of the beam and to the operational conditions of the scraper blades. Beam scans obtained with the scrapers, originally performed to identify the proper position of the blades for the tests, were used to characterise the

beam in machine. Based on this characterisation, the operational conditions of the blade were deduced, comparing the time evolution of the beam intensity during scraping predicted by the simulation with the time evolution of the BCT signals. The comparison has been performed for different scraping positions, to improve the quality of the reconstruction of the operational conditions of the blades. The horizontal blade turned out to move with a speed between 60 mm/s and 80 mm/s, thus lower than the nominal one, and to be tilted by 3–4° about the longitudinal axis (parallel to the direction of the beam). These values of angles are larger than estimations based on considerations about the mechanics of the scrapers. The vertical blade turned out to move with a speed of at most 60 mm/s, and to be almost perfectly aligned (tilt angle much smaller than 0.5°). These outcomes are based on the description of the beam in machine as from the aforementioned scan performed with the scrapers before the test was performed. The description clashes with previous characterisations of LHC beams in the SPS and with measurements of emittance. Thus, these outcomes should be somehow taken “cum grano salis”.

Given these operational conditions of the scraper blades and taking into account the number of protons intercepted before dumping, the energy deposition occurred in the blades during the burst test have been estimated, i.e. 20–24 kJ cm<sup>−3</sup> in the horizontal blade, and 27–37 kJ cm<sup>−3</sup> in the vertical blade. The range of values also depends on the accuracy of the reconstructed operational settings of the blade. These values are clearly above the energy required for graphite to sublimate, i.e. 12.8 kJ cm<sup>−3</sup>, confirming the aforementioned conclusions drawn from the vacuum spikes in the MKDs and the SEM analysis.

Simulations have proved that the loss in performance of the blades during the regular scraping of beam tails seen after the test is not due to the damage induced by the burst test. Alternative explanations to the seen decrease in the number

of scraped protons during regular scraping have been suggested and quantified, i.e. variations of the normalised emittance of the beam in the order of  $0.1 \mu\text{m}$  or drifting of the closed orbit by  $20/50 \mu\text{m}$ .

The pattern of BLM signals along the ring has been used for the qualitative benchmark of the loss maps from simulation. In particular, the loss map generated in case of full beam scraping has been compared to readouts directly taken from the burst test; these are saturated locally at the scrapers, but in the rest of the ring they are below the saturation level, and thanks to the high intensity of the beam, they are maximised, reaching the best quality possible. This comparison can only be qualitative, as loss maps give the average number of protons lost along the ring whereas the BLMs are sensitive to the secondary particle showers started by the lost protons. Nevertheless, the loss map captures the essential characteristics of the pattern of the BLM signals.

A more quantitative benchmark against the BLM readouts has been conducted as well, estimating the energy deposition in the region of the active gas of the BLMs in the LSS1 induced by secondary particle showers during scraping. To perform the simulations for this benchmark, a relevant development of the FLUKA geometry of the LSS1 was necessary, to correctly take into account the development of secondary particle showers. The benchmark is remarkably good, even though it has been proven to suffer from the unavoidable indetermination on the positions of the BLMs in the LSS1.

Preparatory to the benchmark, BLM readouts at different scraping positions were analysed, proving the good properties of the SPS BLMs in linearly scaling signals with the number of lost protons. These analyses allowed for another estimation of the amount of beam scraped during the burst test before dumping the beam, between 80 and 50 % larger than the previous estimations based on the BCT measurements, with an equivalent increase in the estimation of the

maximum energy deposition in the blades induced by the burst test. These new estimations turned out to be quite robust, since BLMs signals are not sensitive to the beam distribution or to actual blade operational settings, but only to the total amount of scraped protons.

The satisfactory benchmark of the simulation tool, i.e. the coupling between FLUKA and SIXTRACK, covered all the observable used to properly characterise the performance of the scraper blades. In particular, the good agreement between the energy deposition values predicted by the simulation and the seen level of damage; between the time profile of the beam intensity during scraping estimated by simulations for different scraping positions and the respective time profile of BCT measurements; between the losses along the ring expected from simulations and the measured pattern of BLM signals along the ring; between the values of energy deposition in the region of active gas of the BLMs foreseen by detailed shower simulations and measured BLM signals prove the solidity of the coupling between FLUKA and SIXTRACK as valuable tool for studies of cleaning performance in circular accelerators.

## 4.4 Conclusions

In the present chapter, the scraping system presently installed in the SPS has been characterised. The characterisation has been carried out in terms of energy deposition in the active material responsible for tail removal, evolution of the beam intensity during scraping, and pattern of losses induced in the ring. The analyses have been performed by means of numerical simulations, combining SIXTRACK (i.e. a code for particle tracking in accelerator lattices) with FLUKA (i.e. a Monte Carlo code for particle–matter interaction). The change of the beam–impact parameter with time during scraping due to the blade sweeping through the beam had to be taken into account to properly describe the cleaning

process; this has been done taking advantage from the geometry capabilities of FLUKA.

Reference results have been obtained with beam at top energy, i.e. at 450 GeV/c, with the SPS Q20 optics and the permanent magnetic bump in the LSS1 taken into account, for a graphite blade perfectly aligned and moving at the nominal speed of 80 mm/s. Moreover, the sampled beam follows a realistic description, featured by double Gaussian distributions with tails more populated than in the case of a simple Gaussian and featured by normalised emittances of  $\sim 2 \mu\text{m}$  and values of  $\sigma_\delta$  of  $2 \cdot 10^{-4}$ .

As expected, simulations have shown that, as consequence of sweeping the blade through the beam, the energy deposition is concentrated in the edge directly facing the scraped protons, smoothing the dependence of values on the original dimensions of the beam. Given the extremely high levels of energy deposition, graphite blades turned out to be more robust than the copper ones, allowing for higher beam currents in the SPS, relevant in view of the brighter beams foreseen for the luminosity upgrade of the LHC. Nevertheless, full beam scraping (i.e. at  $0 \sigma$ ) at full beam intensity already with Nominal LHC beam parameters remains anyhow prohibitive also for graphite, with values as high as  $\sim 27 \text{ GeV cm}^{-3}$  per proton, corresponding to  $140 \text{ kJ cm}^{-3}$  per bunch train of Nominal LHC beams, prohibitive as far as the robustness of the scraper blade is concerned. The case of scraping at  $0 \sigma$  is more an accident scenario rather than an operational one, as in case of beam injection into the LHC only the tails are scraped off, and, in case the scrapers are used as a tool to characterise the profile of the circulating beam, diagnostics is usually not performed at full beam intensity.

The beam intensity decreases with time during scraping; it takes approximately 1000–1500 turns, corresponding to 23–34 ms, to graphite blades to fully

attenuate the beam below the 1 % level. In particular, the profile at the beginning is dominated by the beam distribution and the speed of the blade, whereas once the blade has reached the centre of the beam on the axis of the movement a regime with an exponential attenuation is found, which depends only on the characteristics of the blade (e.g. density and inelastic interaction length of the material, and length of the blade), on the betatron tune and on the aperture profile inside the machine.

Secondary protons are emitted as a consequence of nuclear inelastic interactions in the blade. An average of 0.8 secondary protons is emitted and lost in the ring per intercepted proton; out of this, an average of  $2.9 \cdot 10^{-2}$  protons per intercepted proton is lost in the DS immediately downstream of the scraper, and an average of  $5.2 \cdot 10^{-2}$  protons per intercepted proton is lost in the rest of the machine but in the LSS where the scraper is installed. Protons lost in the DS have an energy larger than 100 GeV, whereas those lost in the rest of the ring have an energy larger than 435 GeV. Locally at the scraper proton losses are mostly due to inelastic and single diffractive scattering, whereas in the rest of the machine losses are mainly due to elastic and MCS, and occasionally by single diffractive scattering. The DS immediately downstream of the scrapers are in a transition region.

Simulations have shown very soft dependencies of these observables when more realistic operational conditions are considered, i.e. when addressing the effects due to the presence of the magnetic bump in the LSS1 or by the fact of performing scraping at the end of the ramp instead of at flat top. The only exception is the maximum energy deposition in the case of energy ramping, as it is decreased by  $\sim 15 \%$ .

Even though the scraper blades are very short devices and can thus be considered as always aligned, the effects of blade tilting were systematically addressed,

considering angles larger than what can be reasonably expected by mechanical considerations [90] but in agreement with what reconstructed from BCT measurements, and thus maximising effects. Simulations showed no impact on the observables of interest but for energy deposition, with the maximum being raised up by a factor of 2 in the worst case, for the considered range of angles. In addition, the case of a tilt by a positive angle about the longitudinal plane lowers the maximum value of energy deposition by a factor of 2, but much longer scraping times, even up to a factor of 6 with respect to the case of a perfectly aligned blade.

In order to verify the values of energy deposition predicted by the simulations, a beam-based test was carried out at the end of the SPS activity in 2013, scraping LHC beams in the SPS with the most severe settings foreseen by the simulations, i.e. full beam intensity (i.e. 288 bunches, for a total of  $\sim 3 \cdot 10^{13}$  protons) and  $0\sigma$  scraping. Indirect and direct observations proved that the blades were damaged, with emission of atoms and clusters of atoms, even though the beam was prematurely dumped due to too high losses at the scrapers. In particular, blade porosity was estimated on the basis of SEM images to  $\sim 30\%$  in the region the most damaged, corresponding to a decrease of the density of the material by the same amount. Independent estimations of the amount of beam actually scraped concluded that the maximum energy deposition generated during the burst test is higher than the heat required by graphite to locally sublimate by a factor between 2 and 4 even though the beam was prematurely dumped. These estimations have been possible thanks to the quantitative benchmark of the time profile of the beam intensity predicted by the simulations and the time profile measured by the BCT, and to the analysis of measured BLM signals. In particular, the benchmark against the BCT measurements also allowed the reconstruction of the actual speed and tilt angle of the blades.

After the test, a loss in performance of the blades during the regular scraping of beam tails was visible, even though limited. Further analyses and simulations showed that this change in the performance should not be due to the generated damage but to other sources, e.g. a systematic small variation in the normalised emittance of the beam or a small drift in the beam closed orbit.

BCT signals and BLM readouts recorded during the burst test and also during other SPS cycles on the same morning of the test were used to carry out a quantitative benchmark of the FLUKA–SIXTRACK coupling. The benchmark can be regarded as satisfactory even though the unavoidable uncertainties on the beam actually in machine and the position of the BLMs, proving the solidity of the coupling between FLUKA and SIXTRACK as valuable tool for studies of cleaning performance in circular accelerators.

# Chapter 5

## Characterisation of the Upgraded SPS Scraping System

In the framework of the LIU activities, a new design of the SPS scraping system, alternative to the existing one, has been proposed [48]. The concept is based on a long, static absorber block towards which the beam is steered for scraping by means of a magnetic bump (see Sec. 2.2.2). By design, the new system is expected to have several advantages over the existing one (see Sec. 2.2.3).

This chapter describes the performance of the upgraded system, to highlight its assets and liabilities. The outcomes are then used to compare the upgraded system with the existing one, to show how the new design gives improved endurance and performance.

As for the existing design (see Chap. 4), the characterisation of the upgraded system is carried out in terms of:

1. energy deposition in the active material responsible for tail removal. This is relevant to estimate the the induced thermal loads and stresses;
2. time evolution of the beam intensity during scraping. This is used to assess the typical time-scales required to accomplish scraping;

3. pattern of losses induced in the ring. This is used to identify locations with high losses, where potential issues of ageing of the insulation in magnet coils or of material activation may arise.

The analyses are performed by means of numerical simulations, combining SIXTRACK, a code for particle tracking in accelerator lattices (see Sec. 3.2), with FLUKA, a Monte Carlo code (see Sec. 3.1). The former is used to simulate the dynamics of the beam in the SPS, whereas the latter is used to simulate the interaction of the beam with the scraper blades. The combination of the two (see Sec. 3.3) is necessary, since the analysed device is a multi-turn cleaning system, implying that any estimation related to cleaning must take into account the dynamics of the beam in the accelerator. Moreover, the distance between the beam closed orbit and the absorber block changes with time during scraping, due to the raising of the bump; this has to be taken into account in the simulation, since it affects the estimation of the energy deposition in the absorber block and the time evolution of the beam intensity during scraping. For this reason, the possibility of changing the magnetic settings of elements has been implemented in SIXTRACK (see Sec. 3.2.3) and used in the simulations to simulate the rising of the magnetic bump (see Sec. 3.1.2).

The chapter is structured in four sections. Section 5.1 presents a first set of results, to address the dependence of energy deposition and time evolution of the beam intensity on absorber length and speed of raising the bump, two parameters relevant to the design of the system. The dependence on possible beam-absorber misalignments is also explored, as this might be a concern from the operational point of view. A simplified version of the coupling between FLUKA and SIXTRACK has been used, the only one available at the time of these first studies, with the most relevant simplification being that the rising of the bump is emulated by moving the absorber towards the beam. Consequently, while

the predicted loss pattern cannot be regarded as precise enough (and thus it is not shown), dependencies of energy deposition and time evolution of the beam intensity on absorber length, speed of raising the bump, and beam–absorber misalignments are consistent. An asset of the upgraded system clearly shown by the results presented is the almost perfectly linear scaling of the time profile of the beam intensity, which determines the time required for scraping, with the speed of raising the magnetic bump. This is due to the deployment of a long absorber block, which implies a high probability for a proton to undergo a nuclear inelastic event and thus being absorbed already at the first passage (see Sec. 2.2.3).

Section 5.2 updates the outcomes from Sec. 5.1, removing the emulation of the rising of the bump by the opposite movement of the absorber towards the beam, and actually simulating the rising of the magnetic bump by means of dynamic kicks in **SIXTRACK** (see Sec. 3.2.3). Removing this simplification, higher values of energy deposition are found, since, during the rising of the bump, the beam approaches the scraper with a decreasing impact angle, until the parallelism condition is attained, and the pattern of peak energy deposition turns out to be very similar to the one obtained when the absorber is moved towards the beam with a fixed tilt angle (see the parametric study on possible beam–absorber misalignments, presented in Sec. 5.1). As a matter of fact, the explicit simulation of the rising of the bump is relevant for the determination of the peak energy deposition in the static absorber, and minor effects are found also in the total energy load and in the evolution of the beam intensity during scraping.

Section 5.3 gives the complete picture of both the horizontal and vertical upgraded scraping systems. Results are shown in terms of energy deposition in the absorber block, typical values of energy loss per single passage in the absorber classified on the basis of the event undergone by the surviving proton, time evolution of the beam intensity during scraping and losses along the ring.

In order to carry out the studies, the mature version of the coupling between FLUKA and SIXTRACK has been used (see Sec. 3.3), particularly targeted to the generation of loss maps. Results show that the static absorber block of the vertical system is more loaded than the one of the horizontal system, by a factor of almost 2, with  $10.5 \text{ GeV cm}^{-3}$  per proton, i.e.  $120 \text{ kJ cm}^{-3}$  per bunch train of the 2012 Maximum LIU beam parameters (see Tab. 1.5). Each system requires  $\sim 1200$  turns (i.e.  $\sim 30$  ms) to fully achieve scraping, with no substantial difference between the two systems. An average of 0.11 protons per beam proton are lost in the ring, most of them in the DS and arc immediately downstream of the absorbers.

In Sec. 5.4 an extensive comparison between the results obtained for the existing scraping system and for the one proposed for upgrade is given, pointing out similarities and differences, and stressing assets and liabilities. In case of full beam scraping at full beam intensity energy deposition values in both systems are much higher than the energy required to locally lead graphite to the sublimation point. Nevertheless, the upgraded system profits from the longer absorber, and energy deposition values are a factor of 2 lower than those found for the existing system. Other assets of the upgraded system over the existing one, which are consequences of the deployment of an absorber longer than the blades, are:

- almost perfectly linear scaling of the time required for scraping with the speed of the bump, as in a single passage protons have a high probability to be absorbed in the scraper or being kicked onto an orbit resulting in a loss in the mechanical aperture of the machine. This allows a greater control of the time required for scraping;
- losses in the ring decreased by a factor of 2, but locally downstream of the device.

In addition to all these benefits, the design of the upgraded system is intrinsically

more flexible than the one of the existing system (see Sec. 2.2.3). On the other hand, the existing system is extremely simple, whereas the upgraded design is more complex, making use of several devices, i.e. magnets and absorbers. In addition, due to its simplicity, short times of intervention and conditioning are expected for the existing system, which is not the case for the upgraded one.

As for the results presented in the previous chapter, error bars in results from FLUKA, when visible, refer only the statistical error. Moreover, evaluations of energy deposition are performed in adiabatic assumptions, i.e. without simulating heat diffusion during the scraping process. As reasonably expected, this assumption gives slightly overestimated results, which can be regarded as conservative.

All the results presented in this chapter are original; this is the first time a multi-turn cleaning system based on a magnetic bump is analysed and characterised in terms of energy deposition, time evolution of the beam intensity during cleaning and losses induced in the ring.

### 5.0.1 Simulation Settings

All the results presented in this chapter have been obtained by coupling FLUKA to SIXTRACK (see Sec. 3.3), but contrary to what is done for the present system, thoroughly studied with the mature version of the coupling, the studies presented here reflect the development of the simulation tool, since relevant dependencies on design parameters have been spot with intermediate versions.

The thin lens model of the SPS lattice structure is given in input to SIXTRACK, loading the SPS Q20 optics (see Sec. 2.1.1). The optics file has been obtained with MADX, slicing the thick lens model of the SPS lattice structure with the `teapot` algorithm [88] (see Sec. 4.2.1). The aperture model of the machine is taken from the MADX database on `afs`, as for the lattice structure and optics. Protons of any energy above the FLUKA transport threshold are fed back

to SIXTRACK.

The settings of FLUKA have been kept the same for all the cases treated in the chapter. The geometry consists only of the absorber block in graphite,  $1.67 \text{ g cm}^{-3}$  in density. Contrary to what has been undertaken for the present system, neither has any other beam-intercepting device been explicitly modelled in the FLUKA geometry nor beam line elements downstream of the scrapers been modelled. PRECISIO settings are used, which imply in particular a transport threshold of protons at 100 keV (see Sec. 3.1.3). Single Coulomb scattering is switched on nearby boundaries between materials, to better describe the exit angle of beam particles which do not undergo any nuclear interaction in the absorber. A couple of Cartesian meshes covering the whole absorber or just a transverse portion of it have been used to estimate the energy deposition, all different among each other by the stepping on the transverse directions, with  $50 \mu\text{m}$  being the smallest one, but for the results presented in Sec. 5.3, for which a  $10 \mu\text{m}$  stepping has been chosen, as done for the analysis of the scraping system presently installed (see Sec. 4.2, for instance). The same longitudinal stepping is kept, i.e. 2.5 cm.

The tracked beam is given a 2D Gaussian distribution on both transverse planes, matched to the machine linear optics, and a 1D Gaussian distribution in momentum. Simulations have been performed at flat top, i.e. 450 GeV/c. As for the present system, the change in the relative distance between the absorber and the beam centre during scraping is expected to smooth the dependence of energy deposition values on beam spot size, and thus on beam emittance. For this reason, priority has been given to the beam parameters featured by the highest bunch population; since most of the studies have been carried out when LIU beam parameters from 2012 were still valid (see Tab. 1.5), the Maximum LIU beam parameters have been considered. It should be kept in mind that, while energy deposition results per bunch train scale linearly with the bunch population, peak

energy deposition values per beam proton roughly scale with  $\sqrt{\epsilon}$ , where  $\epsilon$  is the normalised emittance, since, due to the beam sweeping, the pattern of the energy deposition retains a memory of the original spot size only on the non-cleaning plane. This scaling sticks only to the betatron contribution to the beam spot size, ignoring the one from the momentum distribution of beam particles, which accounts for some percent.

At the start of the simulation, the relative beam-absorber distance is  $5 \sigma$ , and it is decreased to reach  $0 \sigma$ , hence performing full beam scraping, as this is the most demanding in terms of energy deposition, and also the fastest in achieving acceptable statistics. The simulation goes on after the closed orbit has reached the edge of the absorber block, moving it further inside the absorber, to fully get rid of possible de-bunching protons.

## 5.1 Preliminary Studies

In this section, a set of preliminary studies is presented, focussed only on energy deposition in the absorber block and time evolution of the beam intensity during scraping. Results obtained for the baseline, i.e. a graphite absorber block 1 m in length and the magnetic bump raised with a speed of  $0.002 \sigma$  per turn (see Sec. 2.2.2), are compared to a couple of other relevant cases, i.e. with the rising of the bump 10 times faster with respect to the baseline, i.e.  $0.02 \sigma$  per turn, and with an absorber twice as long with respect to the baseline, i.e. 2 m. These studies have been performed to assess dependencies on relevant parameters of design, i.e. speed of bump and length of the absorber. In addition, a sensitivity analysis on the beam impact angle is presented either, to check how relevant possible misalignments can be. In principle, the use of a four-bumpers scheme gives enough flexibility to provide perfect alignment between the circulating beam and the absorber block. Nevertheless, misalignments can always take place, and

the flexibility of the bump may be limited by the local clearance available to the beam. Results presented here are focussed on the horizontal scraping system only.

### 5.1.1 Simulation Settings

All the cases presented in this section have been carried out with a version of the FLUKA–SIXTRACK coupling (see Sec. 3.3) simpler than that available at the time of writing:

- the rising of the magnetic bump has been simulated not by explicitly changing the kicks of the involved magnets in SIXTRACK, but moving the absorber block in the opposite direction, i.e. towards the beam, with the same speed as the bump. Effects deriving from this assumption are shown in Sec. 5.2, with the use of dynamic kicks implemented in SIXTRACK (see Sec. 3.2.3);
- tracking is performed in 4D, i.e. without activating the longitudinal dynamics of the beam, as, at the time of the simulations, the coupling was not yet mature for handling the dynamics on the longitudinal plane. Effects due to the inclusion of the 6D tracking on results are shown in Sec. 5.2;
- the aperture check is performed online during tracking, but no linear interpolation of the trajectory of the lost proton is performed to better estimate the loss position (see Sec. 3.2.2). This assumption has no impact on the results shown, as it is just a refinement of the estimation of the loss location, and it does not affect energy deposition results and time evolution of the beam intensity.

In addition to the simulation settings already described in Sec. 5.0.1, the thin lens model of the SPS lattice structure has been obtained with three slices for

each magnetic element, but five for the main bending magnets. No dipole edges have been introduced. As already mentioned in Sec. 4.2.2, this assumption is expected to have negligible effects, due to the relatively small number of revolutions typically simulated (i.e. few thousands) and due to the fact that the optics is re-matched by MADX after slicing, before creating the files in input to SIXTRACK.

### 5.1.2 Results

In the following, results for the baseline are given and compared to those in the case of a longer absorber and a faster rising of the bump, to assess dependencies on these two design parameters. In these cases, the absorber is always parallel to the circulating beam. Afterwards, the focus is moved to the parametric study as a function of the impact angle, to assess consequences of possible misalignments.

#### The Baseline and the Variation of Key Design Parameters

Figure 5.1 shows the pattern of energy deposition in the static absorber of the upgraded scrapers for the baseline, for a longer absorber block and for a faster rising of the bump. Values, normalised to the Maximum LIU beam parameters (see Tab. 1.5), are above the energy required for graphite to reach the sublimation temperature, i.e.  $12.8 \text{ kJ cm}^{-3}$  (see Tab. 4.2). Values for the longer absorber are lower than those for the baseline, reflecting the fact that protons are intercepted over a longer distance, decreasing the spatial density of inelastic events and thus diluting the pile-up of secondary particle showers (even though they do not dominate). For the faster bump, the pattern is steeper, with the maximum value getting higher, even though not significantly. While on the cleaning plane the energy deposition is collapsed on the very first layers of material which intercepts the beam, on the non-cleaning plane the energy deposition map reflects the beam

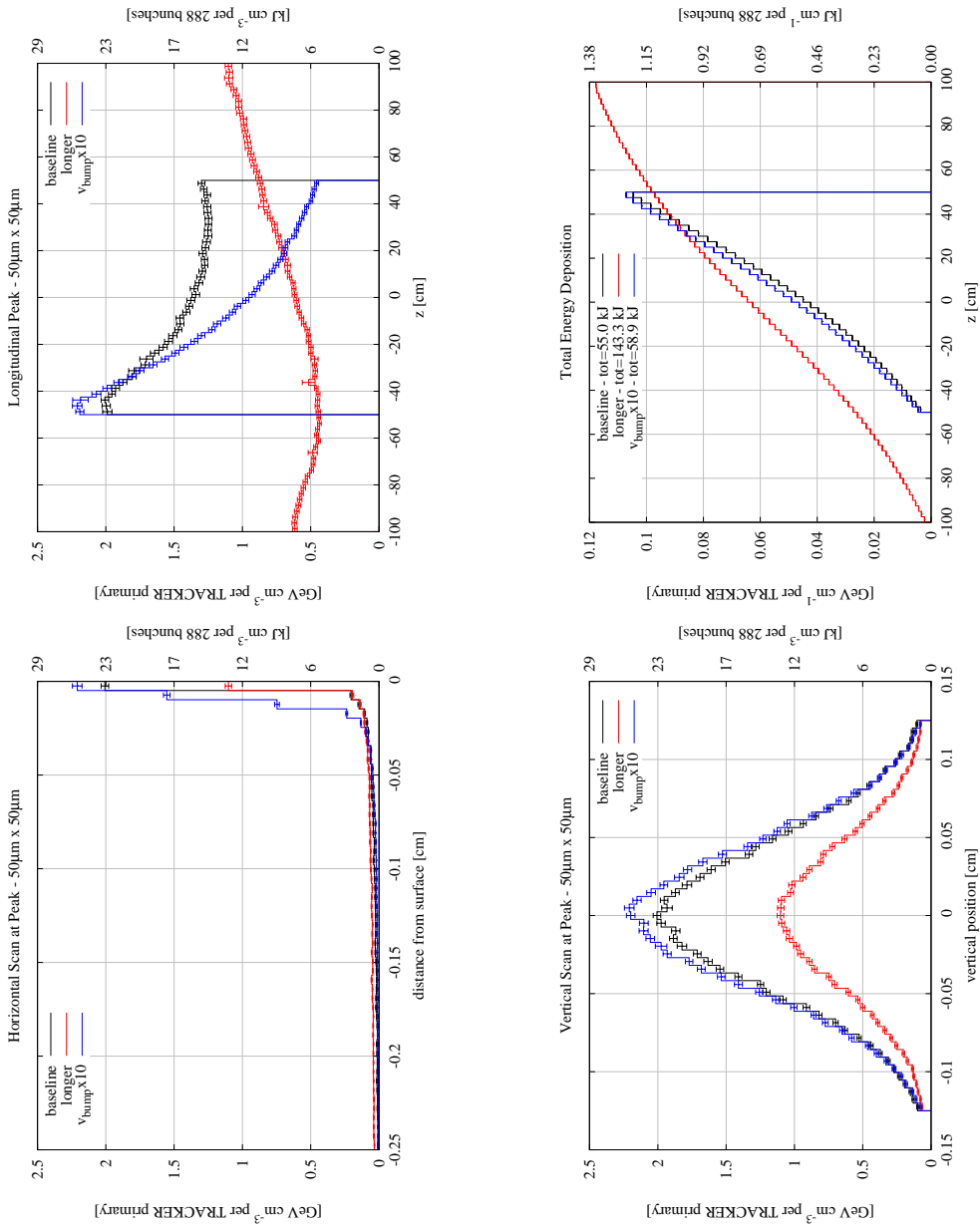


Figure 5.1: Energy deposition in the static absorber block of the upgraded SPS scrapers when scraping at  $0 \sigma$ , for the baseline (black curves), in case of an absorber twice as long as the one of the baseline, i.e. of 2 m in length (red curves), and in case of a speed of the bump ten times larger than the one of the baseline, i.e.  $0.02 \sigma$  per turn (blue curves). The upper-left frame shows the longitudinal pattern of the peak energy deposition, whereas the upper-right frame shows the longitudinal pattern of the total energy deposition. The lower frames show the horizontal (left frame) and vertical (right frame) scans of the energy deposition map at the maximum (see longitudinal pattern of the peak). The magnetic bump is raised by  $0.002 \sigma$  per turn but for the faster bump. Results are obtained simulating the horizontal absorber only, and are scaled on the right vertical axis to a total beam intensity of  $7.2 \cdot 10^{13}$  protons.

distribution. In fact, a FWHM of  $\sim 1$  mm can be seen in the vertical scan, compatible with the beam vertical  $\sigma$  of  $\sim 460 \mu\text{m}$  (see Tab. 2.4). In the horizontal scan, only the case of the faster rising of the bump is actually different from the others, with a smoother pattern, due to the greater average depth at which protons interact with the absorber. The total energy deposition reflects the further development of electromagnetic showers in the case of the longer absorber, which gets a load 2.5 times higher.

Figure 5.2 shows the evolution of the beam intensity during scraping. Contrary to any profile obtained with the present system (see Fig. 4.10 for instance), no exponential attenuation regime is seen, confirming the expectation that a single passage through the absorber is enough to absorb most of the protons (see Sec. 2.2.3). Thus, the profile of the beam intensity depends mainly on the speed of the bump, i.e. on the speed of the beam sweeping. As further proof, the profile obtained with the faster bump, if enlarged by the same factor as the one by which the speed is increased, gets quite close to the one of the baseline. The case of the longer absorber shows that, in terms of time required for scraping, a longer absorber does not help, since the probability that a proton is absorbed in one passage increases only by 10 %.

### Parametric Study with Beam Impact Angle

In the following, effects on the energy deposition and on the time evolution of the beam intensity due to a possible misalignment between the absorber block and the beam orbit are shown. A couple of angles are considered, i.e.  $15 \mu\text{rad}$ , similar to a beam  $\sigma$  in angle (see Tab. 2.4), and  $100 \mu\text{rad}$ , taken as usual precision of alignment of an object of this length. The beam  $\sigma$  in angle is  $\sqrt{\gamma\epsilon}$ , where  $\epsilon$  is the geometrical emittance of the beam and  $\gamma$  is defined by linear accelerator optics

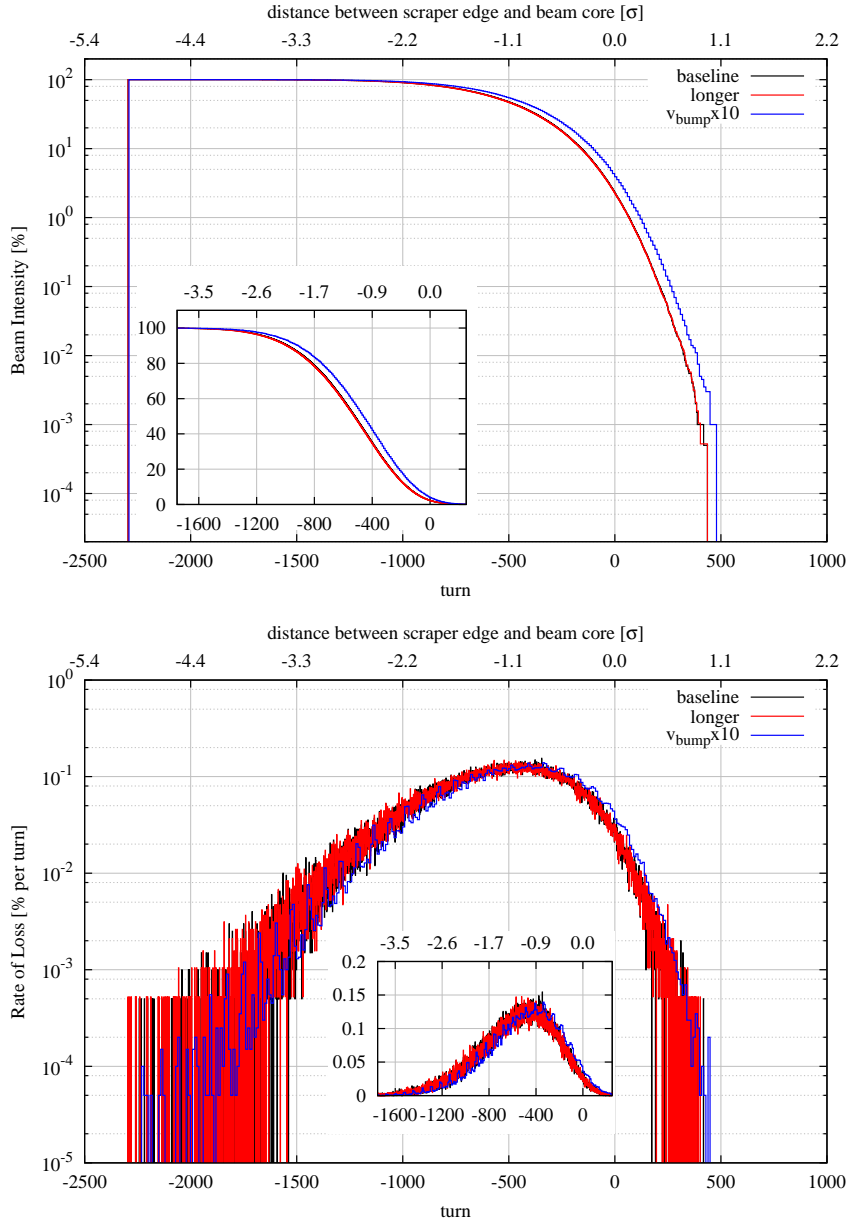


Figure 5.2: Evolution of the beam intensity (upper frame) and rate of intercepted protons (lower frame) when scraping at  $0 \sigma$  with the upgraded SPS scrapers, for the baseline (black curves), in case of an absorber twice as long as the one of the baseline, i.e. of 2 m in length (red curves), and in case of a speed of the bump ten times larger than the one of the baseline, i.e.  $0.02 \sigma$  per turn (blue curves). The curves obtained in the case of the faster bump are artificially enlarged by a factor of 10 in number of turns, to highlight how linear the scaling with the speed of the bump is. The zooms are focussed on the moment when most of the beam is actually scraped. The magnetic bump is raised by  $0.002 \sigma$  per turn, but for the faster bump. Results are obtained simulating the horizontal absorber. The origin of the two horizontal axes corresponds to the moment when the centre of the closed orbit is perfectly on the edge of the absorber.

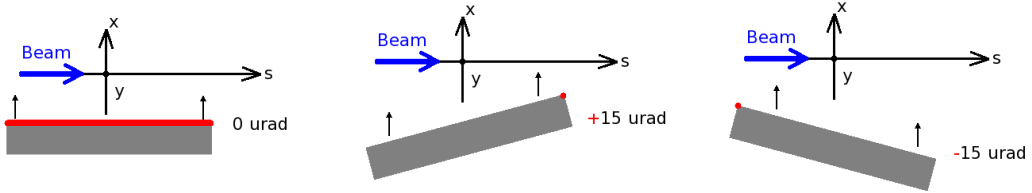


Figure 5.3: Sign convention for misalignment studies: perfect alignment between the absorber and the beam closed orbit (left frame); misalignment by a positive angle (central frame); misalignment by a negative angle (right frame). The red line and spot indicate the location in the absorber where the maximum energy deposition is expected.

as (see Eq. A.6)

$$\gamma = \frac{1 + \alpha^2}{\beta},$$

where  $\beta$  is the betatron function and  $\alpha$  its longitudinal derivative (see Eq. A.5).

The sign convention follows the one shown in Fig. 5.3.

Figure 5.4 compares the pattern of energy deposition in the static absorber block of the upgraded scrapers for the baseline with different cases of misalignment between the absorber and the beam. As it can be seen, the misalignment angle plays a major role in concentrating values of peak energy deposition at the beginning or at the end of the absorber, depending on the sign of the angle. As expected, higher values are found for larger misalignment angles, even though the scaling is not linear. No qualitative change in the transverse distribution is seen. Totals are larger for negative angles than for the positive ones since a larger fraction of secondary particle showers are started at the beginning of the absorber and develop through it.

Figure 5.5 shows the evolution of the beam intensity for the same cases. No major changes are seen with misalignment, meaning that a possible misalignment about the transverse axis of the non-cleaning plane does not imply a loss of performance. Nonetheless, being based on a magnetic bump generated by a four-bumpers scheme, there is some flexibility in modifying the beam angle at

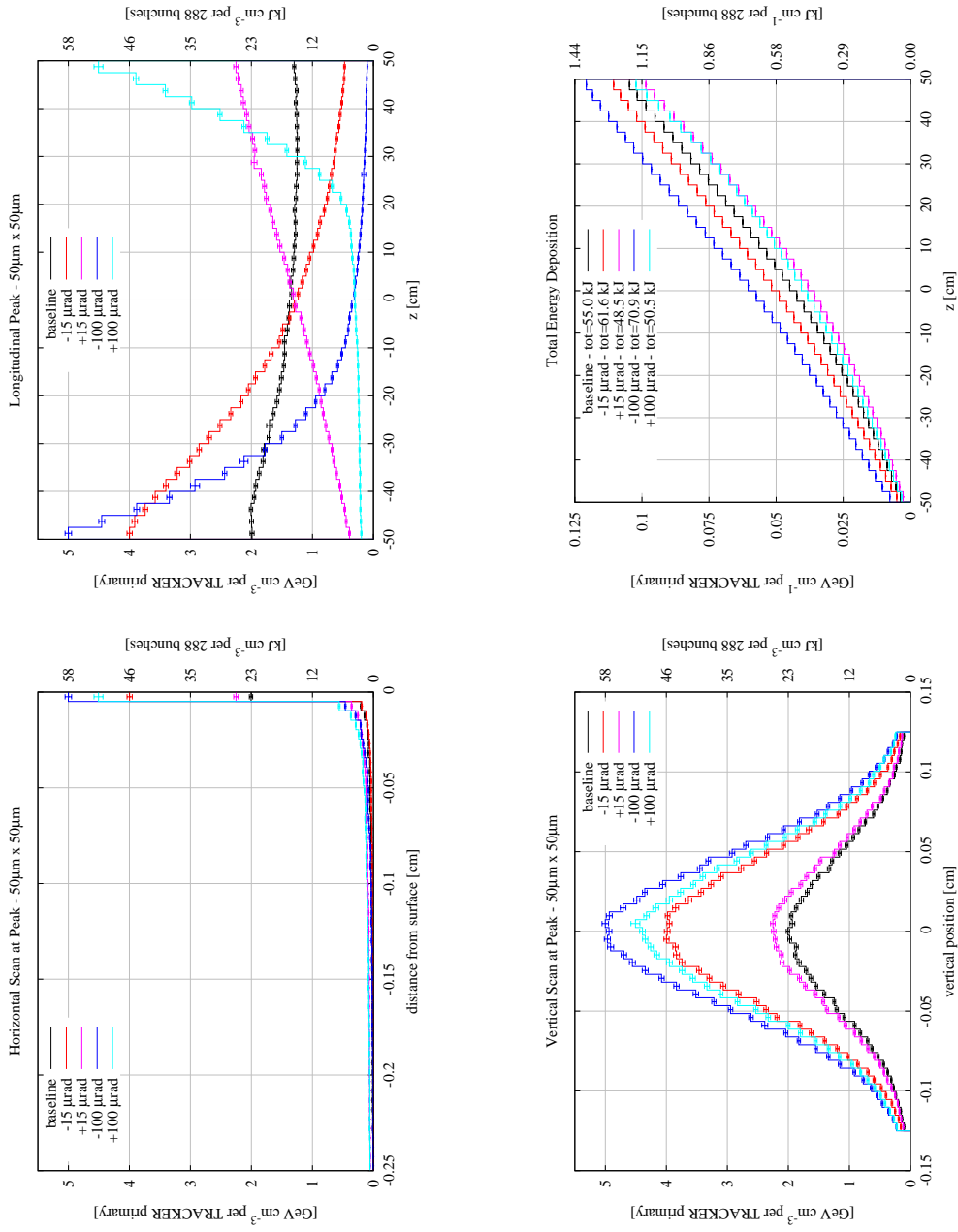


Figure 5.4: Energy deposition in the static absorber block of the upgraded SPS scrapers when scraping at  $0 \sigma$ , for the baseline (black curves, the same as those shown in Fig. 5.1 with the same colour) and for four different beam impact angles. The upper-left frame shows the longitudinal pattern of the peak energy deposition, whereas the upper-right frame shows the longitudinal pattern of the total energy deposition. The lower frames show the horizontal (left frame) and vertical (right frame) scans of the energy deposition map at the maximum (see longitudinal pattern of the peak). The magnetic bump is raised by  $0.002 \sigma$  per turn. Results are obtained simulating the horizontal absorber, and are scaled on the right vertical axis to a total beam intensity of  $7.2 \cdot 10^{13}$  protons.

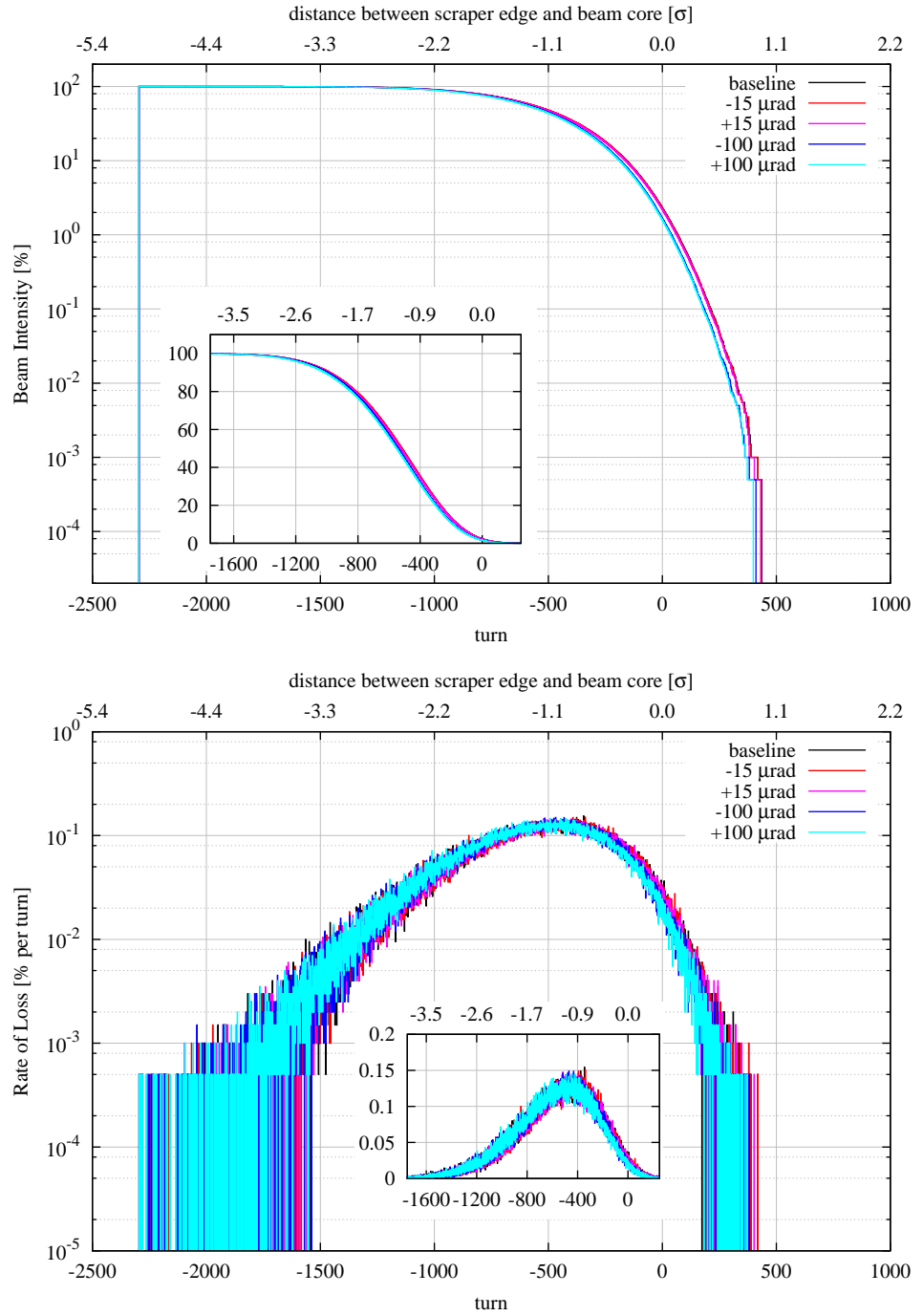


Figure 5.5: Evolution of the beam intensity (upper frame) and rate of intercepted protons (lower frame) when scraping at  $0 \sigma$  with the upgraded SPS scrapers, for the baseline (black curves, the same as those shown in Fig. 5.2 with the same colour) and for four different beam impact angles. The zooms are focussed on the moment when most of the beam is actually scraped. The magnetic bump is raised by  $0.002 \sigma$  per turn. Results are obtained simulating the horizontal absorber. The origin of the two horizontal axes corresponds to the moment when the closed orbit is perfectly on the edge of the absorber.

the absorber, compensating possible misalignments, as far as enough clearance to the beam is guaranteed.

### 5.1.3 Conclusions

This first set of results, even though not explicitly obtained by simulating the rising of the magnetic bump but moving the absorber block in the opposite direction with the same speed as the one of the bump, has shown that peak values of energy deposition in the absorber are in the order of a few  $\text{GeV cm}^{-3}$  per beam proton in case of a Gaussian beam with a normalised emittance of  $2.5 \mu\text{m}$ , i.e. the one foreseen by the Maximum LIU beam parameters (see Tab. 1.5), those with the largest bunch population among the LIU ones available at the time of the simulations. If the full train of 288 bunches is considered,  $\sim 20 \text{ kJ cm}^{-3}$  are found. A clear asset of the upgraded system is the almost perfectly linear scaling of the time profile of the beam intensity, which determines the time required for scraping, with the speed of raising the magnetic bump. This is due to the deployment of a long absorber block, which implies a high probability for a proton to undergo a nuclear inelastic event and thus be absorbed already at the first passage.

The use of an absorber longer than the baseline turns out to be beneficial for the energy deposition, whereas negligible effects can be seen on the time required for scraping. Similarly, possible misalignments imply a local intensification of energy deposition at the beginning or end of the absorber quite important, depending on the misalignment angle, but with no loss in performance concerning time required for scraping.

## 5.2 Results with Dynamic Kicks

In this section, results for the baseline already presented and discussed in Sec. 5.1 are updated, removing the approximation of emulating the rising of the bump with moving the absorber block in the opposite direction; on the contrary, the actual rising of the bump is simulated in **SIXTRACK**. The closed orbit is thus moved towards the absorber, which is kept at a fixed position, this way scraping the beam against it as foreseen to happen in reality. The rising of the magnetic bump is simulated in **SIXTRACK** by means of dynamic kicks (see Sec. 3.2.3).

The same exact beam as the one used for the results presented in Sec. 5.1 has been tracked, in order to allow direct comparisons. It should be noted that the beam has a 1D Gaussian distribution in momentum, with  $\sigma_\delta = 5.25 \cdot 10^{-4}$ , as from the Maximum LIU beam parameters from 2012 (see Tab. 1.5). Such a large value of  $\sigma_\delta$  leads to sampling a fraction of the beam with an energy deviation larger than the acceptance of the RF bucket, i.e.  $\sim 0.37$  GeV (see Sec. 2.1.2). This energy deviation corresponds to  $1.58 \sigma_\delta$ , and the fraction of protons outside this level is  $\sim 11\%$ . If for 4D tracking this has no relevant effect, in case of 6D tracking some beam protons debunch even without having interacted with the absorber block. Small effects are visible in the time profile of the beam intensity during scraping shown in the present section. The full analyses presented in Sec. 5.3 consider a beam distribution properly cut in momentum to avoid sampling protons which de-bunch. Nevertheless, results presented here do not lose validity due to this approximation.

### 5.2.1 Simulation Settings

The same simulation settings as those used for the results shown in Sec. 5.1 have been deployed here as well (see Secs. 5.0.1 and 5.1.1), with the exception of the technique for emulating the rising of the magnetic bump. While previously the

absorber block has been artificially moved towards the beam with a movement opposite to the one obtained with the bump, here the rising of the magnetic bump has been explicitly simulated in **SIXTRACK** by means of dynamic kicks (see Sec. 3.2.3). Consequently, the static absorber block in the **FLUKA** geometry has been positioned and tilted to follow the beam closed orbit at the nominal settings of the bump (see Tab. 2.4).

The rising of the bump has been simulated varying the kick of the involved bumpers; these are listed in Tab. 2.5, along with their nominal kicks<sup>1</sup>. The simulations start with the closed orbit off the edge of the absorber by  $5\sigma$ , corresponding to applying a kick equalling 91.7 % and 82.0 % of the nominal one, for the horizontal and vertical bumps, respectively.

In the following, results obtained with the horizontal scraping system are shown. The vertical system has not been studied, as its behaviour and the respective variations are not expected to be different. In fact, the rising of the two bumps is performed with the same speed, and the beam sizes on the non-cleaning plane are similar (see Tab. 2.4).

### 5.2.2 Results

Figure 5.6 shows the pattern of energy deposition in the static absorber block of the upgraded SPS scrapers. The case considered is the baseline design, with different simulation settings. The black curves are the results obtained with 4D tracking in **SIXTRACK**, when the absorber is moved towards the beam (as in Fig. 5.1), shown as reference. Additionally, the green curves include the effect from a misalignment angle of  $-15\ \mu\text{rad}$  (already shown in Fig. 5.4 by the red curves), presented here as a further reference for comparison. The red and blue

---

<sup>1</sup>The bumpers are modelled in the file describing the lattice structure of the SPS in input to **SIXTRACK** by thin lens dipole kicks, with type 1 and  $-1$  for the horizontal and the vertical bumpers, respectively.

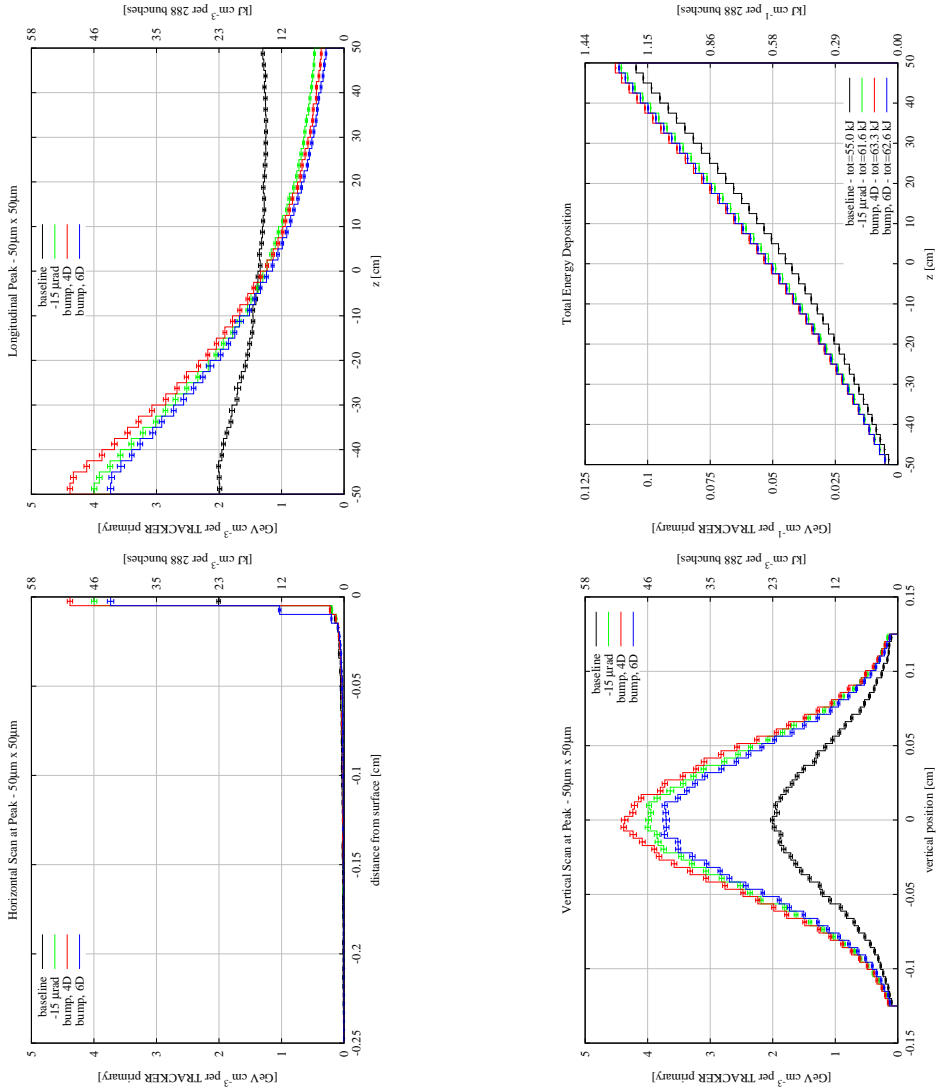


Figure 5.6: Energy deposition in the static absorber block of the upgraded SPS scrapers when scraping at  $0 \sigma$  for the baseline. The black curves are those already shown in Fig. 5.1 (with the same colour), obtained with 4D tracking in SIXTRACK and emulating the rising of the bump with the opposite movement of the absorber block towards the beam; on the contrary, the red and blue curves have been obtained raising the bump in SIXTRACK, with the tracking performed as given in the key of the plot. The green curves represent the case of a misalignment of  $-15 \mu\text{rad}$  already shown in Fig. 5.4 (red curves), obtained with 4D tracking and moving the block towards the beam. The upper-left frame shows the longitudinal pattern of the peak energy deposition, whereas the upper-right frame shows the longitudinal pattern of the total energy deposition. The lower frames show the horizontal (left frame) and vertical (right frame) scans of the energy deposition map at the maximum (see longitudinal pattern of the peak). The magnetic bump is raised by  $0.002 \sigma$  per turn. Results are obtained simulating the horizontal absorber, and are scaled on the right vertical axis to a total beam intensity of  $7.2 \cdot 10^{13}$  protons.

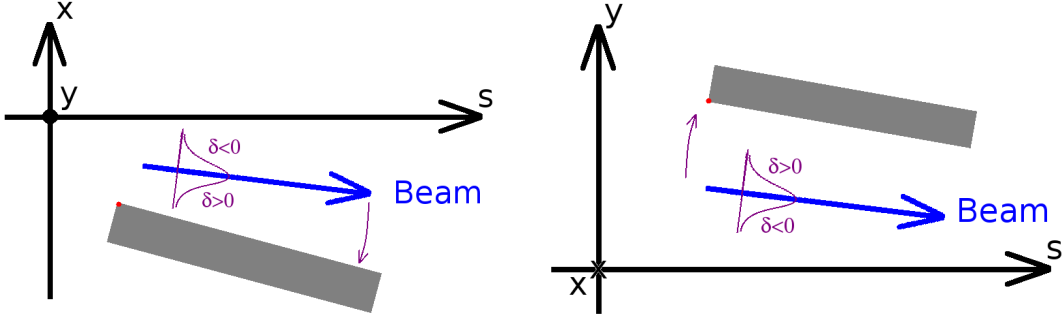


Figure 5.7: During the rising of the magnetic bump, the beam is moved towards the static absorber blocks. Since the closed orbit at the absorber blocks is not flat, i.e. it is not parallel to the longitudinal axis, the closed orbit is changed not only in position, but also in angle while ramping the bumpers up. The horizontal scraping system is shown on the left, whereas the vertical one is shown on the right, for which the low value of the dispersion function (see Tab. 2.4) makes actually negligible dispersive effects.

curves are results obtained raising the magnetic bump, with the 4D and 6D tracking in SIXTRACK, respectively.

As it can be seen, the cases with the actual rising of the bump are very similar to the previous one with the misalignment angle. The reason is that during the rising of the bump not only is the beam moved towards the static absorber, but its angle is also increased, towards the nominal value (see Tab. 2.4) corresponding to the final condition of being parallel to the absorber (see Fig. 5.7). In fact, the beam closed orbit at the absorber is not flat, i.e. parallel to the longitudinal axis, and its angle scales during the rising of the bump (see Sec. 2.2.2), similarly to its position. Thus, for most of the time, the beam impacts the absorber with a certain angle, reaching the parallel condition only at the very end of the rising of the bump, when the closed orbit coincides with the edge of the absorber. It should be kept in mind that  $15 \mu\text{rad}$  is the angular  $\sigma$  of the beam (see Tab. 2.4).

Values in case of the 6D tracking are lower than those for the 4D tracking, since the longitudinal motion transversely spreads the impact position of protons, leading them to impact the absorber at larger transverse positions. In fact, the

profile of the horizontal scan of the energy deposition in case of 6D tracking is smoother than the one obtained with 4D tracking, with a significantly higher value in the second bin from the surface, due to larger impact parameters.

Figure 5.8 shows the time evolution of the beam intensity for the same cases (the same colour coding is applied). The curves obtained when the bump is raised are rather close to those obtained when the absorber is moved towards the beam, showing that this assumption does not introduce any major artifact in the simulation in this respect. The slight delay in the cases when the magnetic bump is raised (visible in the zoom of the upper frame) is due to non-linearities introduced by the sextupoles in the bump region, which end up in a not linear rising of the bump itself (see Sec. 3.2.3). The faster cleaning in case of 6D tracking is due to the longitudinal dynamics, which moves particle ellipses in phase space, bringing them to the side of the absorber from the opposite one. Finally, the curve I obtain from 6D tracking changes shape at  $\sim -250$  turns. This is due to a de-bunching of the protons present in the sampled beam. These protons fail to intercept the absorber until the closed orbit (i.e. the beam centre) is extremely close to it.

### 5.2.3 Conclusions

With respect to Sec. 5.1, results for the baseline are updated here improving the representation of the magnetic bump in the simulation; in fact, the rising of the bump is not emulated with the opposite movement of the absorber block, but with dynamic kicks in SIXTRACK (Sec. 3.2.3).

The analysis of the energy deposition presented in this section shows that values in the absorber are higher when the rising of the bump is actually simulated than when it is simply emulated with the opposite movement of the absorber towards the beam. In particular, during the rising of the bump the beam approaches

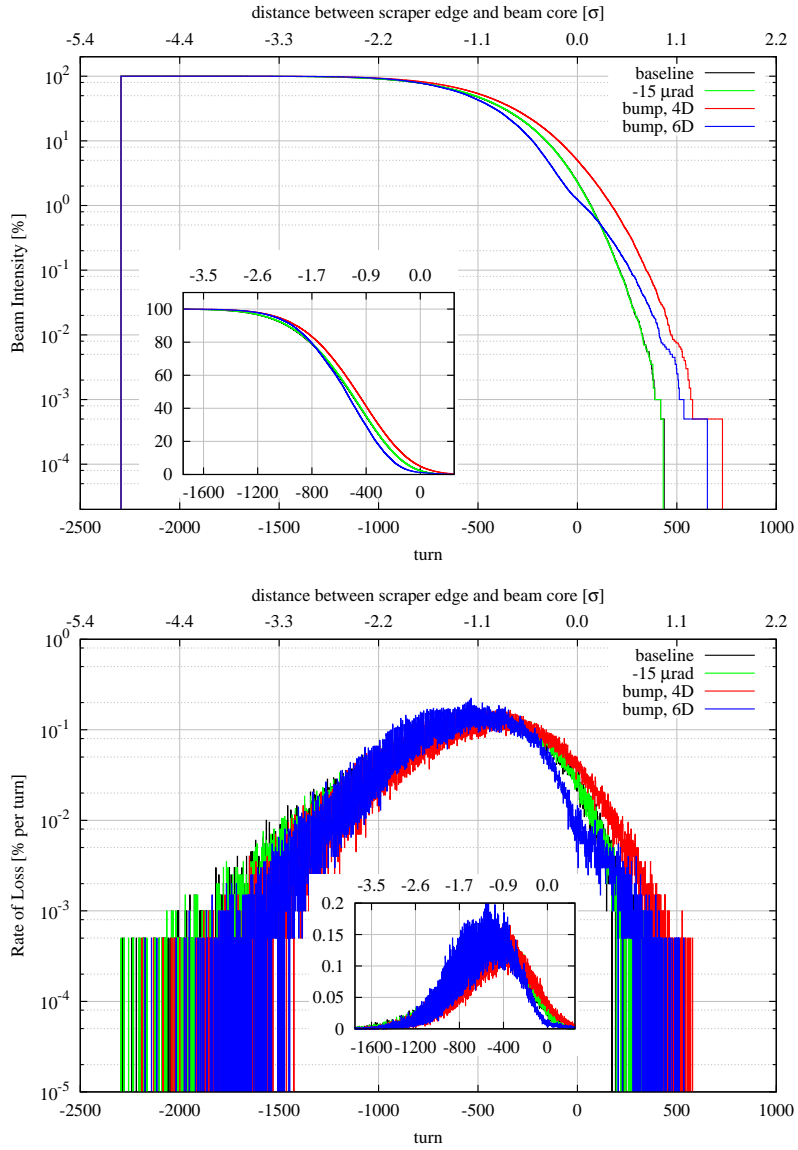


Figure 5.8: Evolution of the beam intensity (upper frame) and rate of intercepted protons (lower frame) when scraping at  $0 \sigma$  with the upgraded SPS scrapers, for the baseline. The black curves are those already shown in Fig. 5.2, obtained with 4D tracking in SIXTRACK and emulating the rising of the bump with the opposite movement of the absorber block towards the beam, whereas the red and blue curves have been obtained raising the bump in SIXTRACK, performing the tracking as given in the key of the plot. The green curves represent the case of a misalignment of  $-15 \mu\text{rad}$  already shown in Fig. 5.5 (red curves), obtained with 4D tracking and moving the block towards the beam. The zooms are focussed on the moment when most of the beam is actually scraped. The magnetic bump is raised by  $0.002 \sigma$  per turn. Results are obtained simulating the horizontal absorber. The origin of the two horizontal axes corresponds to the moment when the closed orbit is perfectly on the edge of the absorber.

the scraper with a decreasing impact angle, until the parallelism condition is attained. For this reason, the pattern of peak energy deposition turns out to be very similar to the one obtained when the absorber is moved towards the beam with a fixed tilt angle, equal to the angular  $\sigma$  of the beam. Moreover, the longitudinal dynamics lowers peak energy values slightly, since it leads protons to hit the absorber with transverse positions larger than those when no longitudinal dynamics is applied, smoothing the gradient of energy deposition on the plane of cleaning.

The evolution of the beam intensity in case the rising of the bump is actually simulated does not significantly differ from the one when the rising of the bump is emulated with the opposite movement of the absorber towards the beam. Nevertheless, the presence of sextupoles in the region of the bump has an impact on the time evolution of the beam intensity, as the bump is actually raised in a not perfectly linear way. Moreover, the longitudinal dynamics has an effect in speeding up the beam scraping.

As a matter of fact, the explicit simulation of the rising of the bump is relevant for the determination of the peak energy deposition in the static absorber, and minor effects are found also in the total energy load and in the evolution of the beam intensity during scraping.

### 5.3 Full Analysis

In the present section, the baseline of the upgraded SPS scrapers is fully analysed and characterised for  $0 \sigma$  scraping, i.e. for the case the most challenging in terms of energy deposition in the absorber and causing the highest losses in the ring. Both the horizontal and the vertical systems are here presented, with the latter being shown for the first time. Moreover, typical values of energy loss per single passage through the absorber are given for the most relevant interactions undergone by

beam protons (as done for the present system, see Sec. 4.2.2). The picture is completed by loss maps.

### 5.3.1 Simulation Settings

The settings of these simulations are very similar to those reported in Sec. 5.0.1.

The main differences are:

- bending magnets are sliced in three and not in five. Moreover, dipole edges have been introduced;
- aperture markers at locations corresponding to the entrance and exit faces of the quadrupoles and dipoles in their thick lens description have been inserted on purpose, for the aperture model in thin lenses to best suit the one in thick lenses, especially at transitions;
- the rising of the magnetic bump is explicitly simulated in SIXTRACK by means of dynamic kicks (see Sec. 3.2.3), as done in Sec. 5.2;
- the trajectory of lost protons is linearly interpolated at aperture restrictions (see Sec. 3.2.2), to get a better estimation of the loss point;
- a more refined mesh for estimating the energy deposition is here used, compatible with the one deployed in most of the analyses about the system presently installed, shown in Chap. 4. The mesh is  $10 \mu\text{m} \times 10 \mu\text{m} \times 2.5 \text{ cm}$  (horizontal times vertical times longitudinal), whereas in this chapter a mesh  $50 \mu\text{m} \times 50 \mu\text{m} \times 2.5 \text{ cm}$  has been used so far.

The settings for FLUKA are identical to those used so far. In particular, neither any other beam-intercepting device has been explicitly modelled in the FLUKA geometry nor beam line elements downstream of the scrapers have been modelled.

The sampled beam is identical to the one used so far, but for a cut at  $1.58 \sigma_\delta$  in momentum, corresponding to the height of the RF bucket, i.e.  $\sim 0.37$  GeV (see Sec. 2.1.2). This has been applied to avoid sampling protons out of the RF acceptance and thus de-bunching since the start of the simulations, since the studies here presented have been performed in 6D.

### 5.3.2 Results

Figure 5.9 shows the pattern of the energy deposition in the static absorber block of the upgraded SPS scrapers for the baseline, both for the horizontal and the vertical systems. Since the simulated scenario is the same, the two absorbers get a very similar total energy deposition, with almost identical patterns, as expected. The patterns of energy deposition density are qualitatively the same. The peak energy deposition has a decreasing profile, due to the rising of the bump. In fact, while raising the bump, the beam impacts the absorber with a decreasing angle, reaching the parallel condition only when the closed orbit, i.e. the centre of the beam, coincides with the edge of the absorber. This leads to a concentration of the energy deposition in the region of the upstream face. On the plane of cleaning, it is collapsed on the very first layers of material (the horizontal absorber is hit on the side of positive  $x$  values, whereas the vertical absorber is hit from below, see Fig. 5.7), whereas on the plane of non-cleaning the profiles retain the memory of the original dimension of the beam.

Important differences are seen on actual values. The peak energy deposition in the absorber of the vertical system is higher than in the one of the horizontal system; this is due to the fact that the quadrupole upstream of both absorbers is a de-focussing one (see Fig. 2.11), de-focussing the beam on the horizontal plane and focussing it on the vertical plane. This implies that, while rising the magnetic bump, protons impact the absorber with smaller angles in the case of

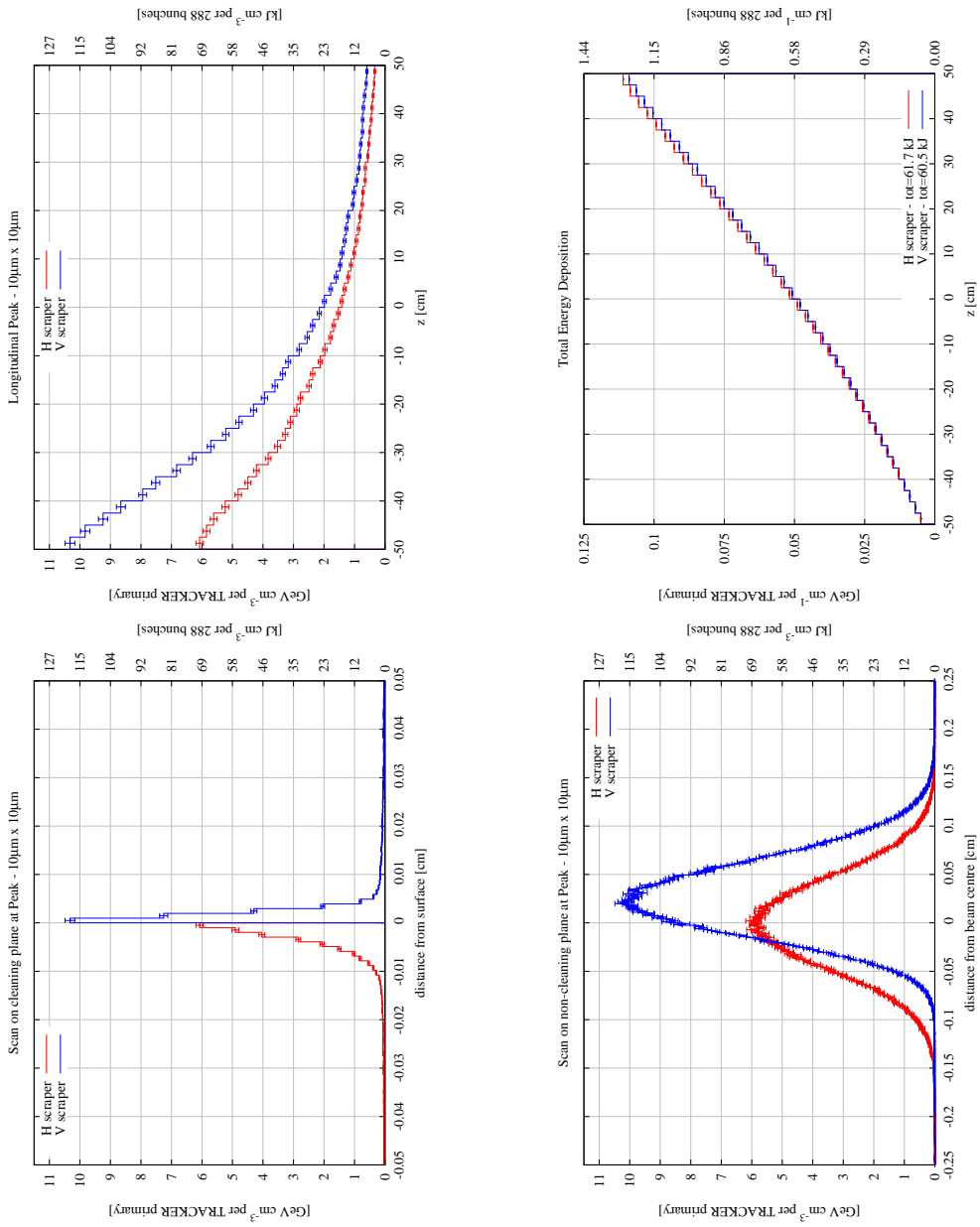


Figure 5.9: Energy deposition in the static absorber block of the upgraded SPS scrapers when scraping at  $0 \sigma$  for the baseline, in case of the horizontal (red curves) and vertical (blue curves) systems. The upper-left frame shows the longitudinal pattern of the peak energy deposition, whereas the upper-right frame shows the longitudinal pattern of the total energy deposition. The lower frames show the scans of the energy deposition map on the cleaning (left frame) and on the non-cleaning (right frame) planes. The scans are given at the location of the maximum (see longitudinal pattern of the peak). Tracking in SIXTRACK is performed in 6D and the rising of the bump is simulated by means of dynamic kicks (see Sec. 3.2.3), with a speed of  $0.002 \sigma$  per turn. Results are scaled on the right vertical axis to a total beam intensity of  $7.2 \cdot 10^{13}$  protons.

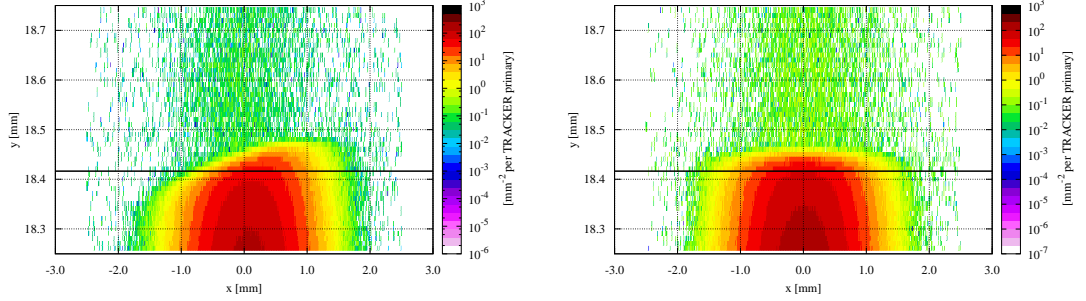


Figure 5.10: Fluence of beam protons at the entrance face of the absorber of the vertical scraping system, in case sextupoles are switched on (left frame) or off (right frame). The map collapses many turns. The black line represents the lower edge of the absorber.

the vertical absorber than in the case of the horizontal one, leading to concentrate the energy deposition even more on the surface. In fact, the scan on the cleaning plane shows a profile in the case of the vertical absorber steeper than in the case of the horizontal absorber.

The scan of the energy deposition on the non-cleaning plane in the case of the vertical absorber is off the beam centre. This is due to the presence of sextupoles in the region of the bump (see Fig. 2.11). Figure 5.10 shows the map of the fluence of beam protons at the entrance face of the vertical absorber, in case sextupoles are switched on or off. As it can be seen, a clear asymmetry at impact onto the absorber is seen when sextupoles are powered. Moreover, the same sextupoles are responsible for generating an energy distribution on the non-cleaning plane slightly smaller than the actual beam size (by  $\sim 15\%$ , i.e. from  $\sim 460\ \mu\text{m}$  from optics, see Tab. 2.4, down to  $\sim 400\ \mu\text{m}$ ), somehow rubbing out the memory of the original spot size.

It should be noted that the peak energy deposition in the horizontal absorber is 1.5 times higher than the one shown in Fig. 5.6 in case of 6D tracking and rising of the bump, since an increased resolution has been used here, i.e.  $10\ \mu\text{m} \times 10\ \mu\text{m}$  (horizontal times vertical stepping) instead of  $50\ \mu\text{m} \times 50\ \mu\text{m}$ . The longitudinal

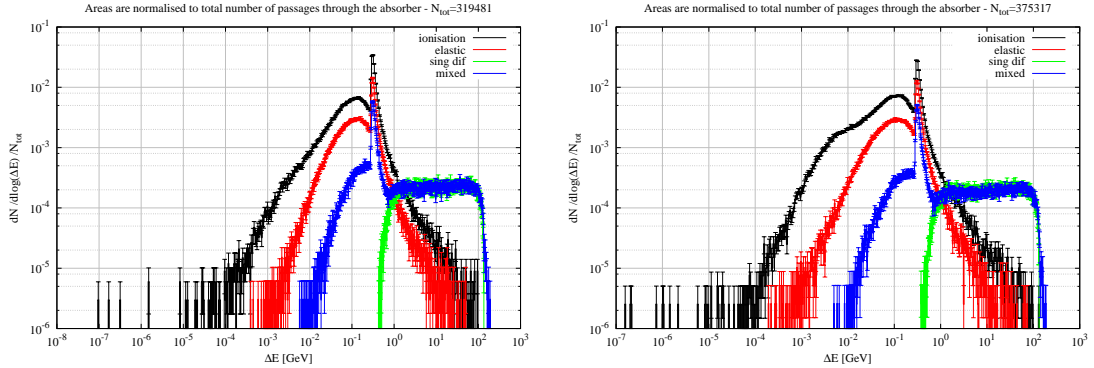


Figure 5.11: Distribution of the energy loss in the static absorber block of the upgraded SPS scrapers per single proton passage when scraping at  $0\sigma$ , according to the most relevant event undergone by the traversing proton surviving the interaction (“deep” inelastic interactions are thus excluded). Results for the horizontal absorber are shown in the left frame, whereas those for the vertical absorber are shown in the right frame. “Mixed” events refer to all passages for which a proton undergoes more than one elastic or single diffractive event or both. All the distributions are normalised to the total number of passages through the absorber.

stepping of the mesh has been kept at 2.5 cm.

Figure 5.11 shows the distribution of the energy loss in the static absorber block of the upgraded SPS scrapers per single proton passage when scraping at  $0\sigma$ , according to the most relevant event undergone by the traversing proton surviving the interaction. One can note the pronounced ionisation peak at  $\sim 310$  MeV and its Landau tail (see Sec. 1.4.3). For protons traversing the whole length of the absorber, an average value of  $\sim 390$  MeV from the Bethe–Bloch formula is found, confirming that surviving protons travel most of the length of the absorber for each single passage. Considering that the bucket height of the SPS is  $\sim 370$  MeV (see Sec. 2.1.2), a fraction of protons surviving the impact on the absorber block may debunch. Single diffractive scattering is responsible for substantial energy losses per single passage, above few GeV, as visible in the figure.

Figure 5.12 shows the evolution of the beam intensity and the number of

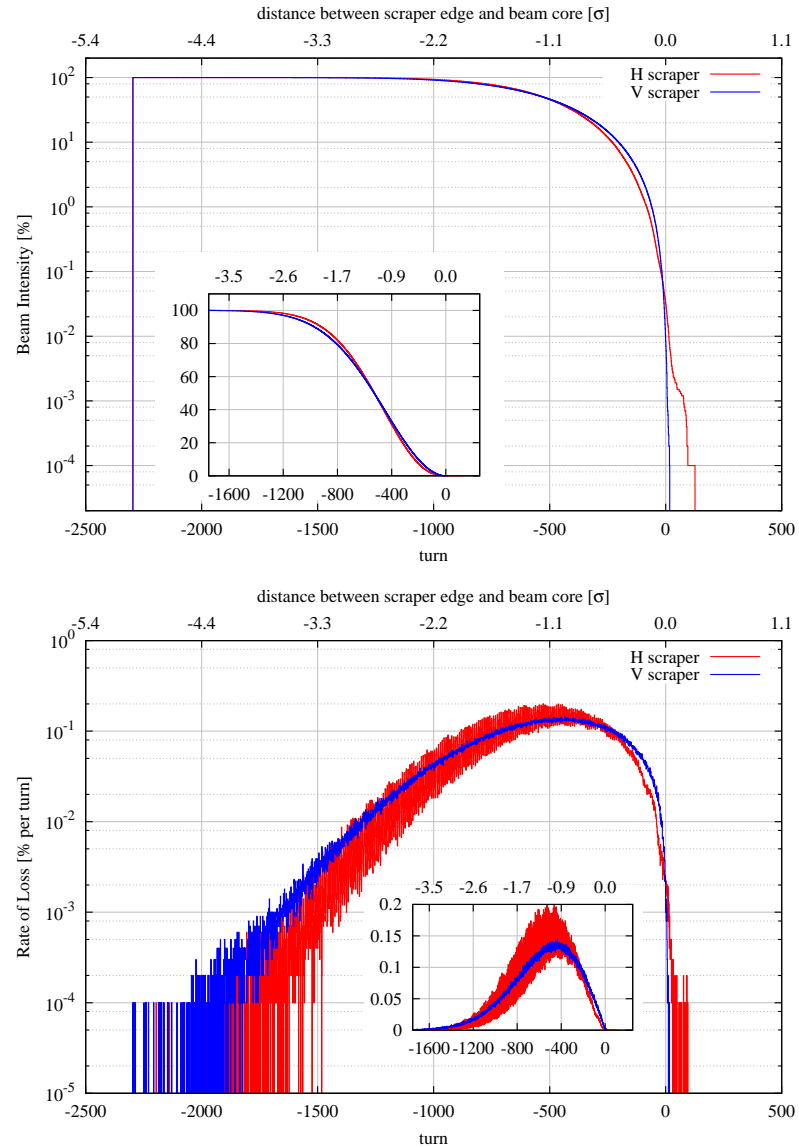


Figure 5.12: Evolution of the beam intensity (upper frame) and rate of intercepted protons (lower frame) when scraping at  $0 \sigma$  with the upgraded SPS scrapers for the baseline, in case of the horizontal (red curves) and vertical (blue curves) systems. The zooms in linear scale are focussed on the moment when most of the beam is scraped off. Tracking in SIXTRACK is performed in 6D and the rising of the bump is simulated by means of dynamic kicks (see Sec. 3.2.3), with a speed of  $0.002 \sigma$  per turn. The origin of the two horizontal axes corresponds to the moment when the closed orbit is perfectly on the edge of the absorber.

intercepted protons per each turn. As expected, there are no major differences between the two systems, and both require  $\sim 1200$  turns (i.e.  $\sim 30$  ms) to fully achieve scraping. In particular, the profiles for the horizontal system display a tiny, longer tail, due to de-bunching protons. In fact, these protons start to debunch after a non-destructive interaction in the absorber, i.e. an interaction resulting in a loss of energy larger than the bucket height but not leading the proton to be lost in the absorber or in the mechanical aperture of the machine. Given the relatively large module of the dispersion function at the absorber (5 % of the maximum value found in the arc, see Fig. 2.2) and being negative (see Tab. 2.4), these protons circulate on the left of the closed orbit whereas the absorber sits on the right (see Fig. 5.7); consequently, the magnetic bump must be raised above its nominal settings in order to intercept them. On the contrary, the vertical system does not suffer from this effect, as the vertical dispersion at the absorber is more than one order of magnitude smaller than the one at the horizontal absorber. Losses per turn have larger variations for the horizontal system than for the vertical one due to oscillations of the beam centre, larger on the horizontal plane than in the vertical one because of the dispersion.

Figure 5.13 shows the pattern of proton losses along the SPS ring. No major differences in the patterns are seen, with most of the losses localised in the DS and in the arc immediately downstream of the absorbers. The total number of losses differs slightly between the two systems, due to the more grazing impact in case of the vertical system, implying an increased leakage from the absorber.

Figure 5.14 relates the losses along the ring with the last event undergone by the lost protons in the absorber. Given the length of the absorber, it is quite unlikely that a proton leaves it after having experienced only ionisation and MCS.

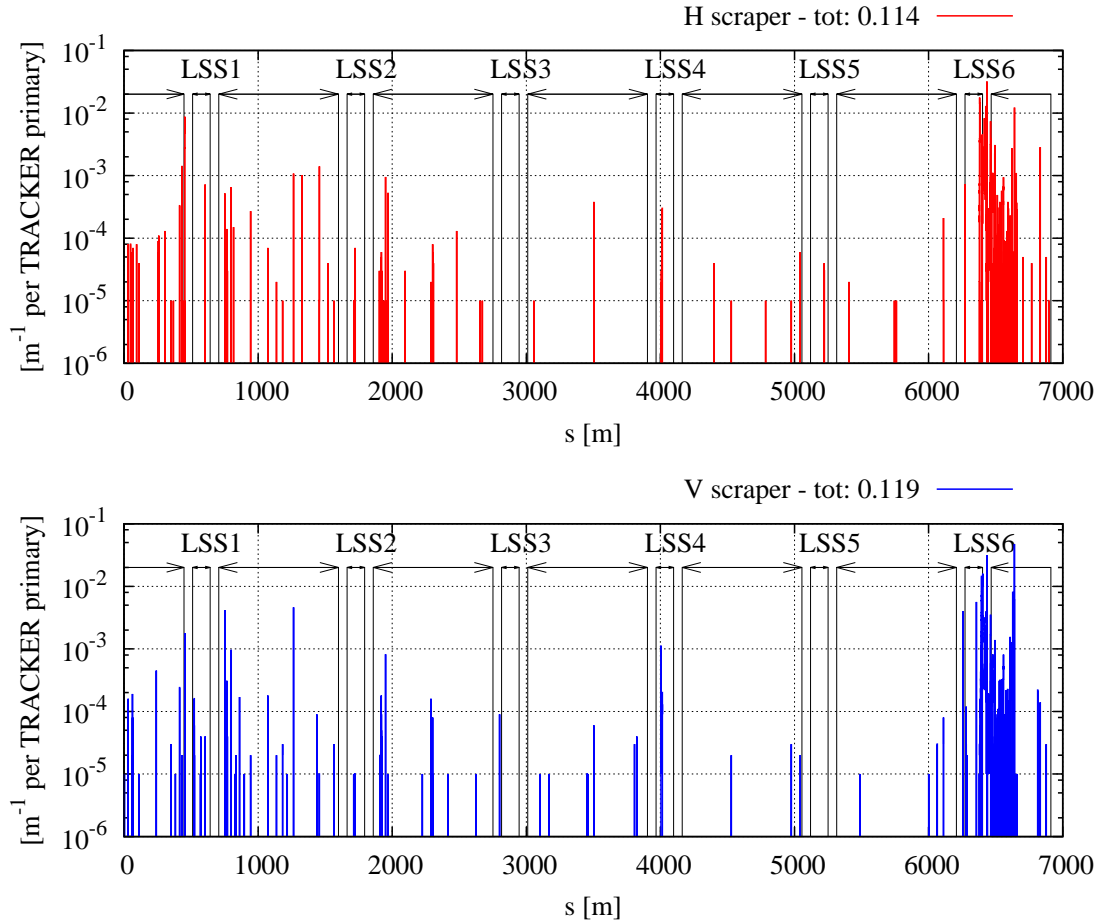


Figure 5.13: Pattern of proton losses along the SPS ring when scraping at  $0 \sigma$  with the upgraded SPS scrapers for the baseline, in case of the horizontal (red curve, upper frame) and vertical (blue curve, lower frame) systems. The totals in the key of the plot report the average number of protons lost per beam proton. A lower momentum cut at 300 GeV/c has been applied, to avoid being dominated by secondary protons produced in the absorber, which are mainly lost in the absorber itself and in its vicinity. Tracking in SIXTRACK is performed in 6D and the rising of the bump is simulated by means of dynamic kicks (see Sec. 3.2.3), with a speed of  $0.002 \sigma$  per turn.

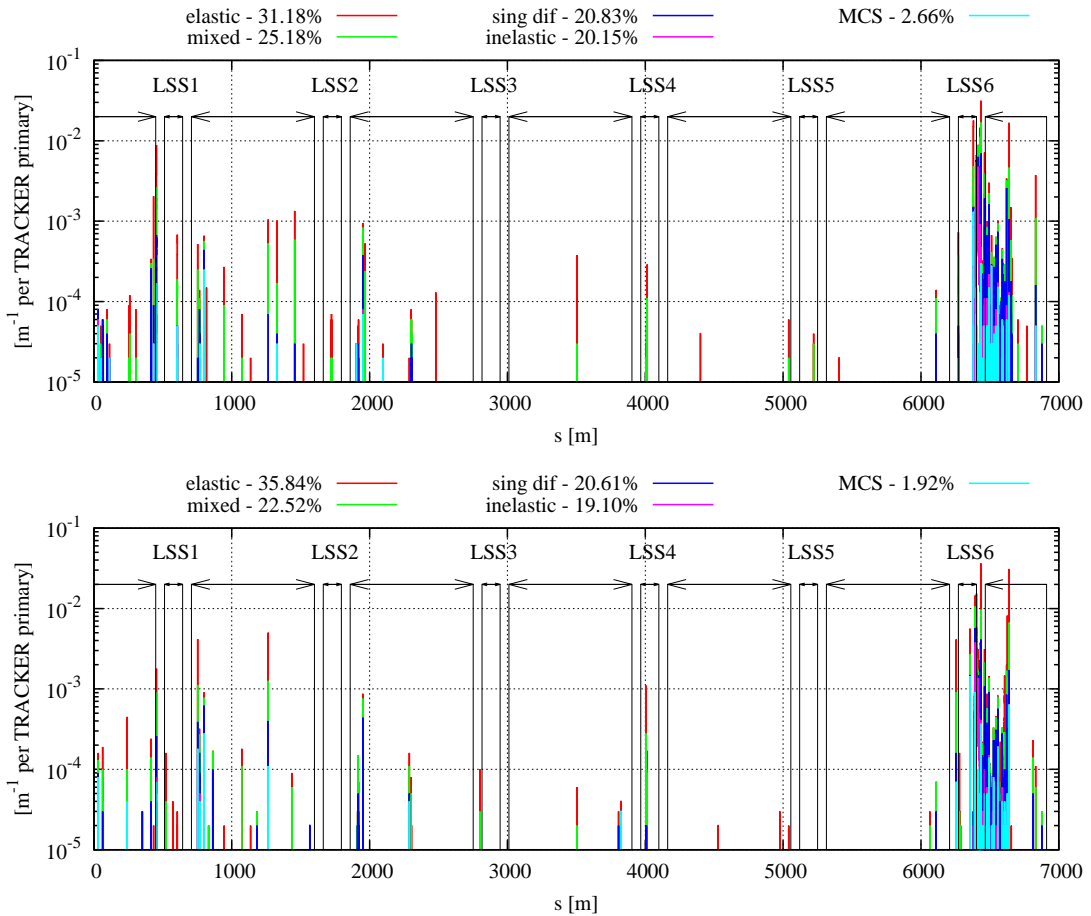


Figure 5.14: Pattern of proton losses along the SPS ring when scraping at  $0 \sigma$  with the upgraded SPS scrapers for the baseline, in case of the horizontal (upper frame) and vertical (lower frame) systems, with colour codes distinguishing the last event that the lost proton underwent in the absorber block. It should be noted that MCS and ionisation follow any discrete event. A lower momentum cut at 300 GeV/c has been applied. For each event type, the percentage refers to the protons lost everywhere in the SPS ring. Histograms are added on top of each other, starting from MCS up to elastic scattering.

### 5.3.3 Conclusions

The baseline of the upgraded scrapers has been fully characterised in terms of energy deposition, time evolution of the beam intensity and losses in the ring. Both the horizontal and the vertical systems have been considered. The case of  $0 \sigma$  scraping has been analysed, as it is the most challenging one in terms of energy deposition and losses in the ring. Maximum LIU beam parameters (see Tab. 1.5) have been used.

The static absorber block of the vertical system is more loaded than the one of the horizontal system, by a factor of almost 2, due to the polarity of the upstream magnet, focussing on the vertical plane.  $10.5 \text{ GeV cm}^{-3}$  per proton are found, corresponding to  $120 \text{ kJ cm}^{-3}$  per bunch train. This is a factor of 6 higher than the first estimation of  $20 \text{ kJ cm}^{-3}$  per bunch train (see Fig. 5.1). This large increase is given by the different plane of cleaning (which accounts for the aforementioned factor of 2, see Fig. 5.9), by the explicit simulation of the rising of the bump (which accounts for another factor of 2, see Fig. 5.6), and by the more refined mesh used to estimate the energy deposition (which accounts for another factor 1.5, see Figs. 5.6 and 5.9). Due to the change of distance between the closed orbit and the absorber block, energy deposition is collapsed on the face scraping the beam, whereas on the non-cleaning plane the distribution of energy deposition reflects the beam spot size.

Each system requires  $\sim 1200$  turns (i.e.  $\sim 30$  ms) to fully achieve scraping, with no substantial difference between the two systems. Approximately 0.11 protons per beam proton are lost in the ring, most of them in the DS and arc just downstream of the absorbers.

## 5.4 Comparison with the Existing System

In this section a comparison between the existing system, analysed in Chap. 4, and the proposed upgrade, analysed in this chapter, is given, summarising results already shown in this thesis and stressing assets and liabilities of the two systems. The comparison is mainly focussed on  $0 \sigma$  scraping, i.e. full beam scraping, as this is the most challenging operational setting in terms of energy deposition (and consequently thermo-mechanical stresses) and losses induced in the ring. In particular, results shown in Sec. 4.2.2 for the existing system are compared to results shown in Sec. 5.3 for the upgraded system. Results for the existing system have been obtained considering a speed of the blade of 80 mm/s (see Sec. 2.2.1) and a Gaussian beam with a normalised emittance of  $1 \mu\text{m}$ , a value very close to the LIU BCMS beam parameters, the most challenging ones among those assumed by the LIU project at the time of writing (see Tab. 1.5). On the other hand, results for the upgraded system have been obtained considering a bump speed of  $0.002 \sigma$  per turn (see Sec. 2.2.2) and a Gaussian beam with a normalised emittance of  $2.5 \mu\text{m}$ , which belongs to the beam parameter set with the largest bunch population among the LIU ones (see Tab. 1.5), assumed as reference by the LIU project at the time of the studies.

The absorber of the upgraded system is much longer (see Sec. 2.2.2) than the blade of the present system (see Sec. 2.2.1), i.e. by a factor of 100. As a consequence, basically only one passage is needed to remove a proton from the beam, making the upgraded system less sensitive to multi-turn effects (see Sec. 2.2.3). For the same reason, less beam protons are expected to survive the impact on the absorber, resulting in less losses along the ring. Moreover, despite the development of electromagnetic showers, energy is absorbed over a larger volume of material, lowering the energy deposition density.

### 5.4.1 Energy Deposition

For both the system presently installed in the SPS and the upgraded one, the relative position of the centre of the beam to the absorbing material changes with time; as a consequence, the energy deposition is collapsed on the very first layers of material intercepting the beam. The present system is swept through the beam with a movement orthogonal to the plane of cleaning; consequently, the energy deposition is concentrated on the non-cleaning plane (see Figs. 4.7 and 4.8). On the contrary, the bump of the upgraded system is raised on the same plane of cleaning, concentrating the energy deposition on the cleaning plane. For both systems, the distribution of the energy deposition on the other plane keeps memory of the original beam dimension. This allows a very rough scaling of maximum energy deposition density with  $\sqrt{\beta\epsilon}$ , where  $\beta$  is the optics betatron function at the device and  $\epsilon$  the geometrical emittance. This scaling sticks only to the betatron contribution to the beam spot size, ignoring that from the momentum distribution of beam particles, which accounts only for some percent.

Values of energy deposition expected in the absorber of the upgraded system are lower than those in the blades of the system presently installed. In fact, 30–35 GeV cm<sup>−3</sup> per beam proton are found in the case of the blades of the present system (see Fig. 4.7), whereas a maximum value of 10–11 GeV cm<sup>−3</sup> per beam proton is found in the case of the upgraded system (see Fig. 5.9). Scaling the latter from the superseded Maximum LIU normalised emittance to 1  $\mu$ m with  $\sqrt{\epsilon}$ , 16–17 GeV cm<sup>−3</sup> are found, a factor of roughly 2 lower than the expectation for the system presently installed. The lower values of peak energy deposition are due to the larger length of the absorber, allowing dilution over a longer distance, despite the development of secondary particle cascades, which cannot take place in the blade of the system presently installed.

No matter which system is analysed, all these values of energy deposition are

system	$\epsilon_N$ [ $\mu\text{m}$ ]	[ $\text{GeV cm}^{-3}$ ]	Max	
			LIU BCMS [ $\text{kJ cm}^{-3}$ ]	LIU Nominal [ $\text{kJ cm}^{-3}$ ]
present	1	30–35	240–280	220–260
upgraded	2.5	10–11	130–140	120–130

Table 5.1: Maximum energy deposition in the blade of the SPS scraping system presently installed and in the long absorber block of the proposed upgrade, as foreseen by the simulations. Full beam scraping, i.e. at  $0 \sigma$ , of a Gaussian beam is considered. Values per proton are given in column three, and they are taken from Fig. 4.7 for the system presently installed and from Fig. 5.9 for the upgraded system; the normalised emittances considered in sampling the beam for the simulations are reported in column two. The values per proton beam are scaled to LIU beam parameters (see Tab. 1.5), i.e.  $1.3 \mu\text{m}$  of normalised emittance and  $2 \cdot 10^{11}$  protons per bunch in case of LIU BCMS, and  $2.1 \mu\text{m}$  of normalised emittance and  $2.3 \cdot 10^{11}$  protons per bunch in case of LIU Nominal. The scaling  $\sqrt{\epsilon}$  with the normalised emittance is considered.

extremely high, and if the full train of 288 bunches with any bunch population among those foreseen by any of the beam parameter set reported in Tab. 1.5 is considered, they are well above the energy required to locally bring graphite to the sublimation point, i.e.  $12.8 \text{ kJ cm}^{-3}$  (see Tab. 4.2). Table 5.1 compares the maximum energy deposition values found by the simulation for both systems, scaled to both LIU Nominal and BCMS beam parameters (see Tab. 1.5), presently considered by the LIU project.

The speed of the scraper blade has a net effect on the energy deposition, as visible in Fig. 4.1; in fact, the higher the speed of the blade, the larger the volume hit by beam protons and thus the larger the portion of the blade where energy is mainly deposited. In the case of the upgraded system, the speed of the magnetic bump does not offer a mitigation action as far as energy deposition is concerned, as visible in Fig. 5.1. On the other hand, increasing the length of the active material decreases values of energy deposition in the absorber of the upgraded system, as visible in Fig. 5.1, since the proton track-length is diluted over a longer distance.

Tilting of the blade and of the static absorber have relevant effects on the patterns of energy deposition, further loading the portion of material which directly sees the beam. In particular, maximum values are increased by a factor of  $\sim 2$  in the case of the present system (see Fig. 4.21) and by a factor larger than 2 for the upgraded system (see Fig. 5.4), for the range of angles considered in the simulations. It should be noted that, while for the present system there is no way to change the beam-impact conditions, the upgraded system, being based on a magnetic bump, offers more flexibility in compensating possible misalignments. This compensation may be limited by the actual shape of the bump, since the beam must be granted enough clearance.

Most of the time, a proton going through the blades of the present system undergoes simple ionisation and MCS (see Fig. 4.9), with very limited energy loss, whereas in the case of the upgraded system other mechanisms of interaction (i.e. nuclear reactions) become more relevant in a single passage (see Fig. 5.11), with more important energy losses (in case of diffractive events) or the removal of the beam particle (for “deep” inelastic events). This is a clear effect due to the length of the intercepting devices.

### 5.4.2 Profile of Beam Intensity

The most relevant asset of the upgraded system is the almost perfectly linear scaling of the time required for scraping with the speed of the bump, as visible in Fig. 5.2. This asset is a clear consequence of the larger length of the absorber, which increases the probability that a proton is absorbed in the intercepting material in only one passage, implying that the time for scraping is determined by the rapidity in ramping the magnets and not by the characteristics of the device actually intercepting the beam. On the contrary, given the length of the blades, the performance of the present system in terms of time required for

scraping is limited by the speed of the blade, and most of all by its length, given the exponential attenuation of the beam intensity with time seen as soon as the blade reaches the core of the beam, as visible in Fig. 4.10. Nevertheless, with the settings considered in this thesis, i.e. a blade of graphite of  $1.83 \text{ g cm}^{-3}$  of density, 1 cm in length and moving at 80 mm/s (see Sec. 2.2.1), and a static absorber of graphite of  $1.67 \text{ g cm}^{-3}$ , 1 m in length and with a bump raised at the rhythm of  $0.002 \sigma$  per turn (see Sec. 2.2.2), both systems achieve full beam scraping in 1000–1200 turns (i.e.  $\sim 25$ –30 ms).

In most of the analysed cases, the presence of a tilt angle does not significantly influence the time required for scraping, for both the system presently installed (see Fig. 4.23) and the upgraded one (see Fig. 5.5). The only exception is represented by a tilt angle about the longitudinal axis for the present system, which dramatically increases the time required to fully accomplish  $0 \sigma$  scraping, i.e. specifically by a factor of 5. The benchmark presented in Sec. 4.3.4 and in particular Fig. 4.39 show that this can actually happen in reality, and only a re-alignment of the device can improve the performance. On the other hand, the upgraded system, being based on a magnetic bump implemented with a four-bumpers scheme, offers much more flexibility.

As far as time required for scraping is concerned, the absorber of the upgraded system is already sufficiently long, and a further increase of its length does not improve the performance. This is due to the fact that in case of a 2 m-long absorber the probability that a proton is absorbed in one passage increases only by 10 %. On the other hand, increasing the length of the absorber helps in diluting energy deposition values (as already discussed). On the contrary, the thickness of the blade plays an important role on the time required for scraping, as shown by Fig. 4.10, if the curve for copper is used as representative of the case of a graphite blade with a length increased by the ratio between the inelastic

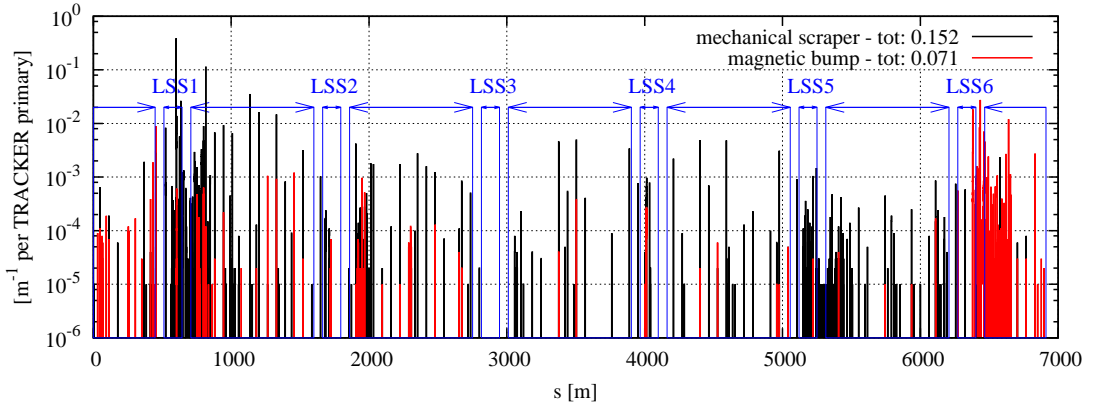


Figure 5.15: Pattern of proton losses along the SPS ring when scraping at  $0\sigma$  with the scraping system presently installed, located in the SPS LSS1 (black curve), and with the upgraded one, located in the LSS6 (red curve). Results have been obtained applying a lower momentum cut at  $440\text{ GeV}/c$ , not to be heavily dominated by losses in the DS and arc immediately downstream of the scrapers. The comparison is done for the horizontal systems only.

interaction lengths of copper and graphite, i.e.  $\sim 3\text{ cm}$ .

### 5.4.3 Losses

Figure 5.15 compares the losses induced in the ring by the system presently installed and by the upgraded one. For both, the horizontal scraping system is considered. A lower momentum cut at  $440\text{ GeV}/c$  has been applied (corresponding to  $\delta \sim 2\%$ ), not to be heavily dominated by losses in the DS and arc immediately downstream of the scrapers. In general, the two patterns show similar characteristics, still with a loss concentration in the DS and in the arc immediately downstream of the systems. The total number of losses per beam proton are reported in the key of the plot. In total, the upgraded system generates losses in the ring a factor of 2 lower than that generated with the system presently installed.

#### 5.4.4 Additional Remarks

As already mentioned in Sec. 2.2.3, the upgraded system is more complex than the one presently installed. In fact, instead of a thin blade and the respective mechanics for being swept through the beam, it requires the installation of dipole magnets, for generating the magnetic bumps, and the absorber blocks. In case of serious damage, the exchange of the blade is much simpler and faster operation than exchanging a long absorber block. Moreover, the opening of a magnetic bump locally decreases the clearance available to the beam. On the other hand, a magnetic bump with a four–bumpers scheme allows full flexibility in controlling the conditions of beam impact, even though this has to cope with ensuring that the beam is given enough clearance.

# Chapter 6

## Conclusions

In view of the upgrade in luminosity of the LHC, beams brighter than those available to present in the machine are foreseen, with unprecedented beam emittances and bunch populations. As a consequence, beams become more destructive and uncontrolled losses more dangerous. In the framework of the LIU project, aimed at upgrading the LHC injection chain to achieve the desired beam parameters, the protection devices installed along the entire LHC injection chain are under revision, in order to verify their effectiveness and mechanical stability. Among them, this thesis is focussed on the SPS scraping system.

The SPS scrapers are part of a series of systems aimed at protecting the LHC during beam transfer, when the LHC collimation system cannot offer adequate protection by design. In fact, this is located in specific regions of the ring far from where injection takes place; moreover, it is a multi-turn cleaning system, implying that not all beam particle phases are intercepted in one turn. While all other injection protection systems protect the LHC against beams mis-steered by magnet faults during beam transfer, the SPS scrapers provides injection in the LHC with halo cleaning, fundamental to prevent magnet quench at injection. They are a multi-turn, “fast” cleaning system, meaning that they interact with

the beam only for a short time, i.e. a few hundred ms, immediately before extraction. Since the active part of the device is inserted in the path of the beam at a given moment in the accelerator cycle, energy deposition is concentrated in the very first layers of material in contact with the beam, exposing it to damage levels in case of accidental interception of the beam core.

A new SPS scraping system design has been proposed for the LIU era. While the present system is made of a graphite blade swept through the beam at the desired scraping position on each plane of cleaning, the proposed upgrade is based on a long, static absorber block in graphite, against which the beam is scraped by means of a magnetic bump. An absorber block and a magnetic bump is envisaged per cleaning plane. The key point of the upgraded system is the use of a long absorber made of a light material like graphite to clean the beam, with immediate benefit on the energy deposition in the intercepting device, since energy is deposited over a larger volume. Other assets that the new design is expected to have are improved control on the time required for cleaning and reduction of losses induced in the ring and operational flexibility, even though the design is more complex. In addition, since no mechanical component is present, the system is not subject to wear.

In this thesis, I have characterised both the system presently in use and the upgraded one in terms of energy deposition in the absorbing medium, time required for cleaning and losses in the machine. The analyses have been performed by means of extensive numerical simulations. FLUKA, i.e. a Monte Carlo code for particle transport in matter, has been combined with SIXTRACK, a tracking code for single particle beam dynamics. The former is used to properly describe the interaction of the beam with the intercepting device, whereas the latter is used to take into account the beam dynamics during scraping. I have significantly extended the functionalities of the coupling tool to cover all the needs required

for the work presented in this thesis, namely:

- I have extended the FLUKA–SIXTRACK coupling to be used in any possible tracking configuration, in particular 6D tracking (thus including longitudinal dynamics) with a thin lens description of the SPS ring, following the standards of LHC collimation studies [83];
- I have implemented in FLUKA the possibility of moving portions of the geometry, allowing one to explicitly simulate the sweeping of the blades of the system presently installed;
- I have implemented in SIXTRACK the possibility to vary the kick of elements in the accelerator structure, allowing one to explicitly simulate the rising of the magnetic bump used to scrape the beam in the upgraded design. Moreover, I have restored and extended the online aperture check, native to SIXTRACK. All this is fundamental to properly estimate energy deposition values in the intercepting device, time profile of the beam intensity during cleaning and losses induced in the ring.

I carried out all the code development with the most general approach, so that tools are now available for studying any other device and ring.

I have extensively analysed the scraping system presently installed in the SPS and the one foreseen for upgrade, and the outcomes have been used to compare the two. In particular, the analyses have quantitatively confirmed all the assets that the upgraded design is expected to have in comparison to the system presently installed, thanks to the deployment of a light absorber, much longer than the blade.

I have shown that, due to the relative movement of the absorber and the circulating beam, the distribution of the energy deposition in both systems is concentrated on the very first layers of material intercepting the beam on the

plane of the movement, whereas it keeps a memory of the original beam dimension on the other plane. With nominal settings, maximum values expected in the graphite absorber of the upgraded system are lower than those in the graphite blades of the existing system, by a factor 2. Nevertheless, no matter which system is analysed, the energy density deposited in case of full beam scraping (i.e. at  $0\sigma$ ) with full bunch trains (i.e. 288 bunches) of any population considered in this thesis, is extremely high, and values of the order of some tens or even hundreds of  $\text{kJ cm}^{-3}$  are found, well above the threshold required to locally bring graphite to the sublimation point. This scenario is somewhat extreme, as the scrapers are operationally used to intercept only the tails of the beam (i.e. few %), and low intensity beams are used in case of beam scans.

I have shown that one of the most relevant assets of the upgraded system is the almost perfect linear scaling of the time required for scraping with the speed of the bump. The time required for scraping is not limited by the capability of the intercepting device in removing beam particles, as it happens for the blades of the system presently installed, but by the speed of raising the bump, controlled by the powering of the bumpers. Nevertheless, with nominal settings, the existing system achieves scraping over a time interval of 75–150 ms, which fits operational requirements.

I have shown that another advantage of the upgraded system over the one presently installed is the reduction of losses induced in the ring. In fact, these are a factor of 2 lower than those generated by the present system. The loss patterns of the two systems have similar characteristics, with most of the losses (i.e. protons with an energy larger than 300 GeV) mainly concentrated in the DS and the arc immediately downstream of the scraping system.

It should be kept in mind that the upgraded system is more complex than the one presently installed in terms of required hardware. In fact, instead of

a thin blade and the respective mechanics for being swept through the beam, the upgraded system requires the installation of dipole magnets, for generating the magnetic bumps, and the absorber blocks. In case of serious damage, the exchange of the blade is an operation much simpler and more rapid than the exchange of a long absorber block. Moreover, the opening of a magnetic bump locally decreases the clearance available to the beam. On the other hand, a magnetic bump with a four-bumpers scheme allows some flexibility in controlling the conditions of beam impact, provided that the beam is given enough clearance in the region of the bump. These have an important effect on the load on the intercepting material. In fact, I have shown that a tilt angle between the circulating beam and the intercepting device can increase the energy deposition by a factor of 2 in the most loaded point of the active material, for the explored range of angles.

In order to verify the reliability of the analyses I presented, I have carried out a benchmark of the simulation tool against measurements with beam. An endurance test of the present scraping system has been performed at the end of the SPS activity in 2013, with the aim of stressing the scraper blades with the worst conditions envisaged by the simulation. The tested blades were actually damaged, as SEM analyses revealed local changes in the porosity of the blade, evidence of sublimation of the material, as expected by the simulation. The benchmark did not concern only energy deposition results, but also the time profile of the beam intensity while scraping and the BLM signals in the region of the scraper, recorded during the test and its setup. The comparison of simulation results against beam intensity measurements allowed to reconstruct the settings of the scraping system during the test, whereas the comparison against BLM measurements offered a further opportunity to benchmark the FLUKA-SIXTRACK coupling. Since the beam was prematurely dumped before being fully scraped,

the two sets of measurements were independently used to estimate the amount of beam scraped before dump, obtaining comparable results.

This thesis is the first extensive analysis of the SPS scraping system, both in its configuration presently installed and in its proposed design for possible upgrade for the LIU era. This thesis is also the first analysis and comparison of collimation systems with varying beam-impact conditions during cleaning, and the results and outcomes here presented can be used as reference for studying similar devices in other machines. Moreover, this thesis is the first extensive use and benchmark of the FLUKA-SixTRACK coupling. This simulation tool has been developed in the most general way, to be used for any accelerator ring and device under study. It is the first simulation tool for halo cleaning studies in circular machines which allows one to properly deal with changing conditions of impact on the beam-intercepting device.

# Appendix A

## Notes on Linear Accelerator Physics

It is beyond the purpose of this appendix to give a comprehensive overview of the physics of high energy accelerators, for which the reader is addressed to more complete reference textbooks, e.g. Refs. [41, 65]. On the contrary, I briefly recall here the most important concepts and mathematical expressions of linear accelerator physics, as reference for the most recurrent ones in this thesis.

Linear accelerator physics deals with circular accelerators made only of elements generating linear magnetic fields, i.e. dipoles and quadrupoles. In case of no coupling between the horizontal, vertical and longitudinal planes, the equations of motion of beam particles in the accelerator ring can be solved independently, and the solutions on each plane can be singularly used. The mathematical formalism is based on a local, curvilinear reference system (see left frame of Fig. A.1), going through the whole machine on its axis. The system is right-handed, with  $s$  being the longitudinal coordinate, going through the ring;  $x$  the horizontal coordinate, pointing outwards of the ring; and  $y$  the vertical coordinate, pointing upwards.

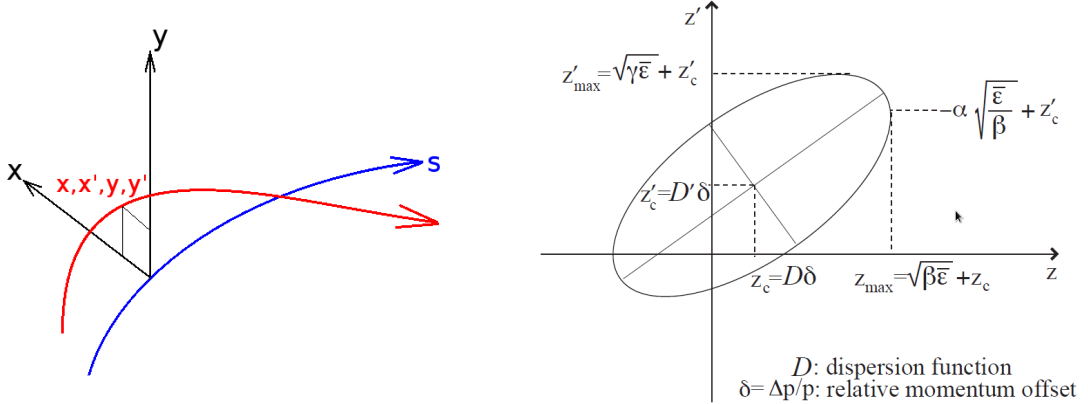


Figure A.1: Left frame: curvilinear reference system, with the possible trajectory of a beam particle (red line) and the respective transverse coordinates at the indicated location. Right frame: motion of a beam particle in the transverse phase space [102]. Particles move along betatron ellipses like the shown one, off-centred due to the momentum offset of the particle.

## A.1 Particle Coordinates, Motion and Optics Functions

In each location along the accelerator ring, a particle is identified by six coordinates, which can be grouped in couples. Four of them identify beam particles in their motion on the transverse planes, i.e.  $x-x'$  and  $y-y'$ . The non-primed variables are the transverse positions, whereas the primed variables mark the particle directions with respect to the transverse axes – actually,  $x'$  and  $y'$  are the derivatives with  $s$  of the horizontal and vertical position, i.e.  $x' = dx/ds$  and  $y' = dy/ds$ . Two other coordinates are used to describe particles in their longitudinal motion (i.e. on the plane parallel to the motion of the beam): the relative momentum offset  $\delta$  and the lag  $\sigma$  with respect to the synchronous particle (for instance, see Eq. 3.1 for the definition of the lag used in SIXTRACK). In particular, the relative momentum offset is defined as

$$\delta = \frac{p - p_0}{p_0}, \quad (\text{A.1})$$

where  $p$  is the momentum of the particle and  $p_0$  the one of the synchronous particle. The synchronous particle is the one circulating with the correct energy, and thus it sees the electric field of the accelerating RF cavities always with the same phase. In a synchrotron, all beam particles but the synchronous one perform oscillations on the two transverse planes, due to the magnetic structure of the accelerator, and on the longitudinal plane, due to the electric field in the RF cavities. Thus, the six variables describing each particle oscillate either, turn by turn and along the whole ring.

The transverse displacement  $z$  and direction  $z'$  (where  $z$  indicates both  $x$  and  $y$ ) of a particle is the sum of two components, i.e. the betatron and the synchrotron ones

$$z = z_\beta + z_s; \quad (\text{A.2})$$

$$z' = z'_\beta + z'_s. \quad (\text{A.3})$$

Unlike the betatron one, the synchrotron component is dependent on the momentum of the particle.

The betatron displacement and direction oscillate following an ellipse in the  $z$ – $z'$  phase space (see the right frame of Fig. A.1), mathematically expressed by

$$\gamma z_\beta^2 + 2\alpha z_\beta z'_\beta + \beta z'_\beta^2 = \bar{\epsilon}_z. \quad (\text{A.4})$$

The ellipse is identified by the three Courant–Snider optical functions (also called Twiss parameters), i.e. the betatron function  $\beta(s)$ , its longitudinal derivative

$$\alpha(s) = -\frac{1}{2} \frac{d\beta}{ds}, \quad (\text{A.5})$$

and

$$\gamma(s) = \frac{1 + \alpha(s)^2}{\beta(s)}. \quad (\text{A.6})$$

As it can be seen, only two of them are actually independent from each other, whereas  $\gamma(s)$  can be derived from the other two. They are continuous functions of the position in the accelerator ring  $s$ , and they are determined uniquely by the lattice structure of the accelerator<sup>1</sup>; moreover, they are independent of the beam energy. In particular, the  $\beta$ -function is related to the beam envelope, i.e. to the beam dimensions. The phase of the betatron oscillation along the ellipse can be expressed as

$$\phi_{z,\beta}(t) = 2\pi Q_z t + \phi_{z,\beta,0}, \quad (\text{A.7})$$

where  $Q_z$  is the number of betatron oscillations in one turn or “betatron tune”,  $\phi_{z,\beta,0}$  is the initial phase, and  $t$  is the turn number. The term on the right-hand side of Eq. A.4 is a constant of motion, i.e. the single-particle emittance. Its unit of measurement is the same as the one of length, most commonly expressed in  $\mu\text{m}$  or  $\text{nm}$ . It is proportional to the volume in phase space taken by the motion of the particle.

In order to avoid exciting resonances and thus lose beam, the betatron tune must be non-integer; moreover, the horizontal and vertical betatron tunes  $Q_x$  and  $Q_y$  should satisfy the following relation

$$nQ_x + mQ_y \neq p,$$

where  $n$ ,  $m$  and  $p$  are integer numbers [41].

The synchrotron contribution to the particle displacement and direction can

---

<sup>1</sup>In case of transfer lines, the Twiss parameters along the beam line are determined not only by the lattice structure of the line, but also by the value of the parameters at the beginning of the line (initial conditions). On the contrary, in case of a circular accelerator, the need for initial conditions to the Twiss parameters is replaced by the requirement that they must be continuous functions and match after one turn.

be expressed by

$$z_s = D(s) \delta; \quad (\text{A.8})$$

$$z'_s = D'(s) \delta, \quad (\text{A.9})$$

where  $\delta$  is the normalised momentum offset (see Eq. A.1), and  $D(s)$  and  $D'(s)$  are the dispersion function and its derivative with  $s$ , i.e.  $D'(s) = dD/ds$ . They have the same properties as those of the Twiss parameters.  $\delta$  oscillates following the longitudinal motion about the synchronous particle. In case of oscillations of small amplitude, i.e. for those particles not far from the synchronous one in longitudinal phase space, the motion follows an ellipse, as it happens for the betatron component, with a synchrotron phase that can be expressed as

$$\phi_s(t) = 2\pi Q_s t + \phi_{s,0}, \quad (\text{A.10})$$

where, similarly to the betatron motion,  $Q_s$  is the number of longitudinal oscillations in one turn or “longitudinal tune” and  $\phi_{s,0}$  is the initial phase.

As shown by Eqs. A.2 and A.3 and by the right frame of Fig. A.1, the turn-by-turn motion of any beam particle in the transverse plane is given by the superposition of the betatron motion, which leads the particle to move along the ellipse identified by the Twiss parameters, and the synchrotron motion, which off-centres ellipses in phase space and makes them oscillate. In general, the betatron motion is much faster than the longitudinal one. For example, the betatron tunes of the SPS are 20.13 and 20.18 on the horizontal and vertical planes (see Sec. 2.1.1, respectively, whereas the synchrotron tune is  $5.95 \cdot 10^{-3}$  (see Tab. 2.1).

## A.2 Statistical Quantities

Statistical quantities can be used to describe the beam as an ensemble of particles. In general, these quantities are root mean square (rms) values calculated on particle coordinates; for instance, the rms beam size  $\sigma_z$  and divergence  $\sigma_{z'}$  of the beam are the rms values of particle positions and directions.

Similarly, the rms emittance  $\epsilon$  is the rms value of the single-particle emittances, and the rms relative momentum offset  $\sigma_\delta$  is the rms value of the relative momentum offsets (see Eq. A.1) of beam particles. These can be used to express the rms beam size and divergence of the beam as

$$\sigma_z = \sqrt{\sigma_{z,\beta}^2 + \sigma_{z,s}^2} = \sqrt{\epsilon\beta + (D\sigma_\delta)^2}; \quad (\text{A.11})$$

$$\sigma_{z'} = \sqrt{\sigma_{z',\beta}^2 + \sigma_{z',s}^2} = \sqrt{\epsilon\gamma + (D'\sigma_\delta)^2}, \quad (\text{A.12})$$

where the betatron and synchrotron contributions, explicitly indicated in the middle term of the equations by the subscripts  $\beta$  and  $s$ , are summed in quadrature, reflecting the linear combination on the transverse displacement and direction (see Eqs. A.2 and A.3). Likewise, the momentum spread of the beam  $\sigma_p$  can be expressed in terms of the rms relative momentum offset  $\sigma_\delta$  as

$$\sigma_p = p_0 \sigma_\delta, \quad (\text{A.13})$$

where  $p_0$  is the momentum of the synchronous particle.

The emittance can be seen as the temperature of beam particles in the reference system moving with the beam [41]. As a consequence of Liouville's theorem, it stays constant with time if the dynamics of the beam particles is subject to conservative forces, which is the case for the Lorentz force imparted by magnetic elements [41].

The optical quality of a photon beam from a synchrotron light source is characterised by the spectral brightness, which is the six-dimensional density of the photon beam in phase space [41]

$$\mathcal{B} = \frac{\dot{N}_{\text{ph}}}{4\pi^2 \sigma_x \sigma_{x'} \sigma_y \sigma_{y'} \frac{d\epsilon}{\epsilon}},$$

where  $\dot{N}_{\text{ph}}$  is the photon flux per unit relative energy bandwidth  $d\epsilon/\epsilon$ , and  $\sigma_x \sigma_y$  and  $\sigma_{x'} \sigma_{y'}$  are the area and divergence of the photon beam at generation, respectively. These take into account both the emittance of the lepton beam generating the photons and the diffraction-limited photon emittance [41].

Similarly, the concept of brightness can also be applied to charged particle beams [5]; its formulation in four dimensions can be written as [103]

$$\mathcal{B} = \frac{I}{\pi^2 \epsilon_x \epsilon_y},$$

where  $I$  is the particle current or longitudinal particle density, and  $\epsilon_x$  and  $\epsilon_y$  are the horizontal and vertical rms emittances, respectively. As a matter of fact, while the emittance has the physical meaning of a volume occupied in phase space, brilliance has the “inverse” physical meaning, i.e. the one of a density in phase space.

### A.3 The Floquet's Transformations and the Normalised Phase Spaces

The Floquet's transformations allow one to transform real particle coordinates  $z_\beta$  and  $z'_\beta$ , free of the synchrotron contribution, into normalised ones  $\xi$  and  $\xi'$

$$\xi = \frac{z_\beta}{\sqrt{\epsilon \beta}}; \quad (\text{A.14})$$

$$\xi' = \frac{z_\beta \alpha + z'_\beta \beta}{\sqrt{\epsilon \beta}}, \quad (\text{A.15})$$

where  $\beta$  and  $\alpha$  are the Twiss parameters introduced in the previous section. The normalised coordinates keep the same meaning as the one of the real coordinates. In the normalised phase space, the betatron motion along the ellipse become the more simple motion along a circle, e.g.

$$\xi = n_\beta \cos \phi_{z,\beta};$$

$$\xi' = n_\beta \sin \phi_{z,\beta}.$$

where  $n_\beta$  is the normalised betatron amplitude, and it can be calculated from the normalised coordinates as

$$n_\beta = \sqrt{\xi^2 + \xi'^2}, \quad \text{with} \quad n_\beta \in [0 : \infty). \quad (\text{A.16})$$

Using the normalised betatron amplitude, the single-particle emittance can be rewritten as

$$\overline{\epsilon_z} = n_\beta^2 \epsilon, \quad (\text{A.17})$$

and the maximum values of the betatron coordinates can be expressed as (see the right frame of Fig. A.1)

$$z_{\beta,\max} = n_{\beta} \sigma_{z,\beta}; \quad (\text{A.18})$$

$$z'_{\beta,\max} = n_{\beta} \sigma_{z',\beta}, \quad (\text{A.19})$$

where the betatron contribution to the rms beam size and divergence has been used (see Eqs. A.11 and A.12).

Similarly, the normalised synchrotron amplitude  $n_{\delta}$  can be defined as

$$n_{\delta} = \frac{\delta}{\sigma_{\delta}}, \quad \text{with} \quad n_{\delta} \in [0 : \infty), \quad (\text{A.20})$$

where the rms normalised momentum offset has been used; the synchrotron transverse position and direction (see Eqs. A.8 and A.9) as

$$z_s = D n_{\delta} \sigma_{\delta}; \quad (\text{A.21})$$

$$z'_s = D' n_{\delta} \sigma_{\delta}, \quad (\text{A.22})$$

where the dispersion function and its derivative have been used.

## A.4 Normalised Emittance

The single-particle emittance decreases as the particle energy is increased during acceleration. This is due to the fact that the electric field of the RF system is parallel to the beam direction, accelerating particles longitudinally, and not transversely; as a consequence, particles get more forward directed, decreasing the maximum angle in the betatron oscillations and consequently the maximum betatron transverse position.

Together with the single-particle emittance, the rms emittance shrinks down with beam energy. A value of rms emittance can be defined, which remains constant during acceleration. This is the normalised emittance  $\epsilon_N$ , related to the rms emittance as follows

$$\epsilon = \frac{\epsilon_N}{\beta_r \gamma_r}, \quad (\text{A.23})$$

where  $\beta_r \gamma_r$  is the relativistic reduced momentum of the beam. Sometimes the rms emittance is referred to as the “geometrical” emittance.

The shrinking down of the geometrical emittance is reflected on the transverse beam size and divergence, which shrinks down according to Eqs. A.11 and A.12.

# Appendix B

## Limits of Energy Deposition in Copper and Graphite

This appendix shows how the limits on the energy deposition in copper and graphite reported in Tab. 4.2 have been calculated.

### B.1 Copper

The heat necessary for local melting is taken as ultimate limit of energy deposition in copper. This is the sum of the heat necessary to reach the melting temperature and the heat of fusion (or latent heat). The former is obtained integrating the curve of the heat capacity of copper, shown in Fig. B.1, with the following equation

$$\Delta E = \int_{T_{\text{low}}}^{T_{\text{high}}} c(T) \, dT, \quad (\text{B.1})$$

where  $\Delta E$  is the energy to be calculated,  $T_{\text{low}}$  and  $T_{\text{high}}$  are the extremes of integration, i.e. the ambient temperature (293.15 K) and the melting temperature ( $\sim 1100$  °C), respectively, and  $c(T)$  the specific heat at constant pressure. The integral is computed numerically, using the trapezoidal rule, over the whole range

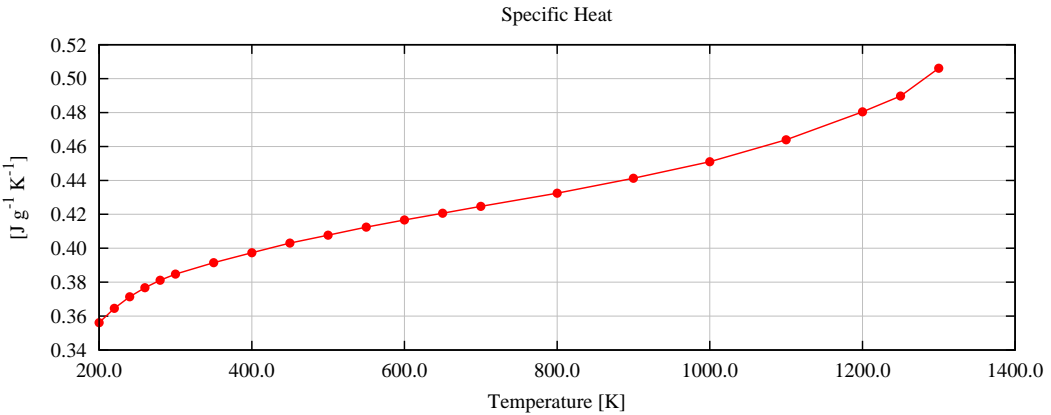


Figure B.1: Specific heat at constant pressure of copper as a function of temperature [104].

of temperatures. A value of  $3.9 \text{ kJ cm}^{-3}$  is found. It should be noted that the calculation is performed in adiabatic assumptions, i.e. the heat has no time to diffuse.

Taking into account a value of heat of fusion of  $1.9 \text{ kJ cm}^{-3}$ , a total value of energy density required to locally melt copper of  $5.8 \text{ kJ cm}^{-3}$  is found, and is taken as ultimate limit.

## B.2 Graphite

The heat necessary for locally starting sublimation is taken as ultimate limit of energy deposition in graphite. This is calculated barely as the heat necessary to reach the sublimation temperature, integrating the curve of the heat capacity of graphite, shown in Fig. B.2, with Eq. B.1, as done in the case of copper (see previous section). The extremes of integration are the ambient temperature (293.15 K) and the sublimation temperature at atmospheric pressure ( $\sim 3600^\circ\text{C}$ ), used as lower and upper extreme, respectively. A value of  $12.8 \text{ kJ cm}^{-3}$  is found, and is taken as ultimate limit.

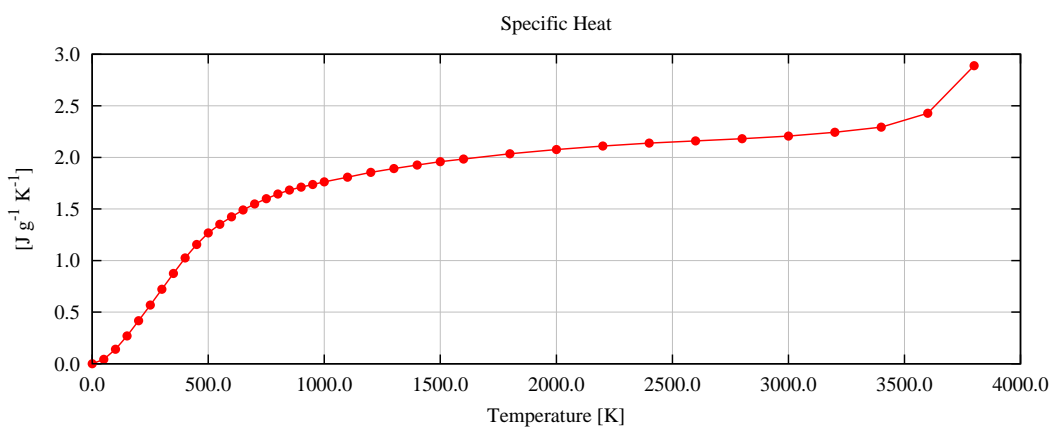


Figure B.2: Specific heat at constant pressure of graphite [105] as a function of temperature. The curve for the specific type of graphite used for the blades of the existing scrapers is shown, i.e. Steinemann R4550.

# Appendix C

## Averaging BCT Signals

In this appendix I report the procedure followed to calculate the normalised and averaged BCT signals shown in Fig. 4.36 and the respective amount of beam scraped, shown in Fig. 4.38. The procedure is illustrated in particular for the calculation of the uncertainties.

The algebra on the BCT signals presented in this appendix is necessary to obtain curves more stable than a single BCT measurement. In fact, BCT signals are extremely sensitive to beam distribution, possible closed orbit drifts and actual scraping settings (i.e. position, speed and tilt angle of the blade); in addition, cycle-by-cycle variations may be present. Moreover, as visible in Figs. C.2 through C.13, which show all the BCT measurements considered for the analysis presented in Sec. 4.3.4, a jitter at 50 Hz is constantly present in all the signals.

In this appendix, the process to get to the normalised and averaged BCT signals is first given, with a detailed explanation of the error propagation. Then the amount of scraped beam is derived and the associated uncertainties explained. Afterwards, basic formulæ for some simple statistics about a set of values and for the propagation of uncertainties are recalled for reference, as they are used throughout the appendix. Finally, all the bare BCT signals used to derive the normalised and averaged profiles shown in Fig. 4.36 are reported.

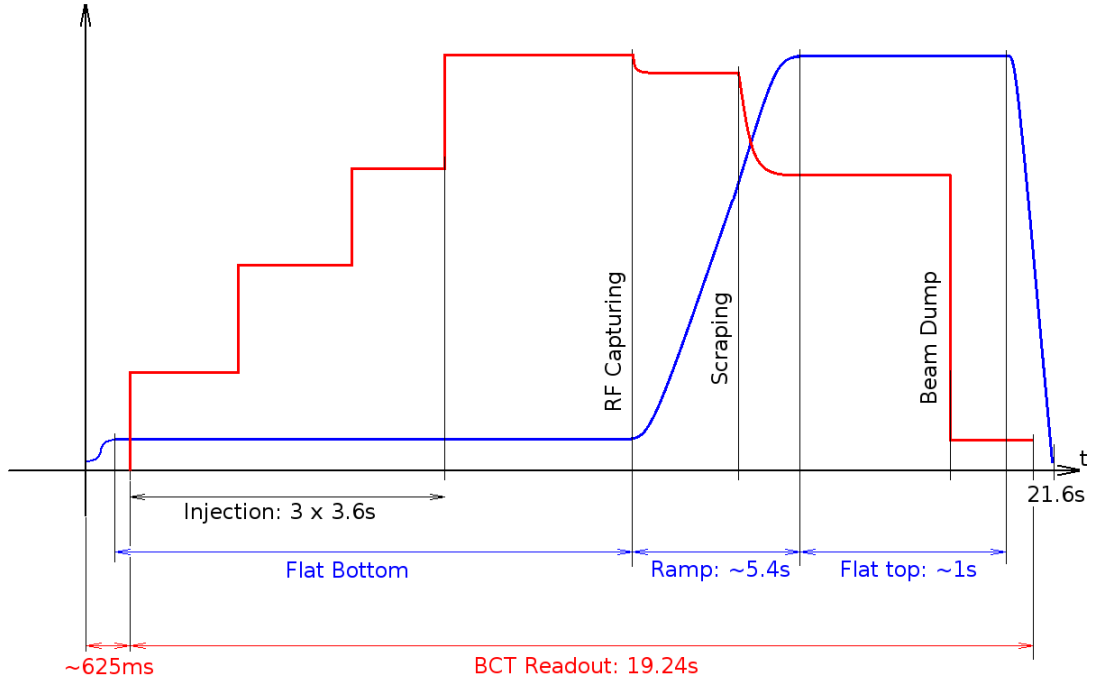


Figure C.1: Example of SPS cycle with BCT timing explicitly indicated. The red curve shows the profile of beam current in the SPS, whereas the blue curve represents the magnetic cycle. The most important events during the SPS cycles and their relevant timing are indicated. The axes are not in scale, to highlight all the essential characteristics of the patterns.

The algebra presented in this appendix is coded in a program used to analyse the bare BCT signals.

## C.1 Normalisation and Averaging of BCT Signals

Figure C.1 sketches a typical SPS cycle, where the timing of the BCT has been explicitly indicated. Axes are not in scale, to highlight all the essential characteristics of the pattern. The total length of the cycle is given by the magnetic cycle of the accelerator, indicated by the blue curve, covering flat bottom, ramping up, flat top and ramping down, for a total duration of 21.6 s. The red curve shows an example of pattern of the beam current read by the BCT. It starts immediately

from the first injection, delayed by  $\sim 625$  ms with respect to the beginning of the SPS cycle, and it lasts for 19.24 s. This example in particular is characterised by four consecutive injections from the PS, losses at RF capturing just before starting the ramp, losses due to scraping and the beam dump at the end of the flat top. A background signal remains at the end. In the following, I indicate as a “BCT signal” the whole set of values recorded by the monitor during a single SPS cycle.

In order to get to the normalised BCT signals shown in Fig. 4.36 starting from the bare ones  $I(t)$ , the following steps are taken (with reference to Fig. C.1):

1. the background noise  $\mu_{\text{bg}}$  present after the beam dump is subtracted to the bare signal  $I(t)$

$$\tilde{I}(t) = I(t) - \mu_{\text{bg}}; \quad (\text{C.1})$$

2. the signal without background noise  $\tilde{I}(t)$  is normalised to the intensity immediately before scraping  $\mu_i$

$$i(t) = \frac{\tilde{I}(t)}{\mu_i}; \quad (\text{C.2})$$

3. the average over  $N_M$  independent BCT normalised signals  $i(t)$  with the same scraper position is calculated

$$\langle i(t) \rangle = \frac{\sum_{N_M} i(t)}{N_M}. \quad (\text{C.3})$$

Due to the presence of the jitter, the background signal and the intensity before scraping are calculated with averages over  $N$  consecutive readouts in the same BCT signal, to get more stable values. Table C.1 lists all the time intervals considered to compute the averages. Some basic statistics is performed either, to get the standard deviations  $\sigma$  of values in each time interval and the error on the

action		time intervals [ms]
H scraping	before	17200–17400
	after	17750–17950
V scraping	before	17450–17650
	after	17900–18100
dump	after	19140–19240

Table C.1: Time intervals (BCT timing) used for computing the average beam intensity before and after scraping, and after dump.

mean  $\epsilon_\mu$ , with the formulæ given in Sec. C.3. In particular, the standard deviation computed before and after scraping is used as measure of the uncertainty from the jitter, to be associated to each value of the bare signal  $I(t)$ , whereas the error on the mean value of the background is used as uncertainty on the background noise, when calculating uncertainties of signals without background.

The propagation of uncertainties through normalisation and averaging of BCT signals is treated as follows:

1. a constant uncertainty  $\sigma_I$  is associated to each value  $I(t)$  of the bare BCT signal. The uncertainty is not assigned the LSB, since the jitter is dominating; on the contrary, it is obtained from the standard deviations associated to the average intensity before and after scraping, taking their average, i.e.

$$\sigma_I = \frac{\sigma_i + \sigma_f}{2}. \quad (\text{C.4})$$

The standard deviation associated to the background noise is not used here, since the most interesting part of the BCT signal is the one affected by scraping;

2. a constant uncertainty  $\sigma_{\tilde{I}}$  is associated to each value  $\tilde{I}(t)$  of the BCT signal cleaned of the background noise. Since the evaluation of the noise is obtained with a subset of points from the bare BCT signal, the uncertainty

$\sigma_{\tilde{I}}$  is calculated from the uncertainty of the bare BCT signal  $\sigma_I$  and the error on the estimation of the background noise  $\epsilon_{\mu_{\text{bg}}}$  (see Sec. C.3), using the formula of the propagation of uncertainties in the case of difference of correlated variables shown in Tab. C.2, according to the definition of  $\tilde{I}(t)$  (see Eq. C.1)

$$\sigma_{\tilde{I}} = \sigma_I + \epsilon_{\mu_{\text{bg}}}; \quad (\text{C.5})$$

3. since the normalised BCT profile  $i(t)$  is obtained taking the ratio between the BCT signal cleaned of the background  $\tilde{I}(t)$  and the average intensity before scraping  $\mu_b$  (see Eq. C.2), the associated uncertainty  $\sigma_i$  is obtained using the formula for the ratio of correlated variables reported in Tab. C.2

$$\frac{\sigma_i(t)}{i(t)} = \frac{\sigma_{\tilde{I}}}{\tilde{I}(t)} + \frac{\sigma_{\mu_b}}{\mu_b}; \quad (\text{C.6})$$

4. finally, the uncertainty associated to the average normalised BCT signal  $\sigma_{\langle i \rangle}$  is calculated from the definition of  $\langle i(t) \rangle$  (see Eq. C.3)

$$\sigma_{\langle i \rangle}^2(t) = \frac{\sum_{N_M} \sigma_i^2(t)}{N_M}, \quad (\text{C.7})$$

keeping in mind that the normalised BCT signals  $\langle i(t) \rangle$  are fully uncorrelated with each other.

The whole procedure does not consider the dispersion of the values of the normalised signals  $i(t)$  used to compute the average  $\langle i(t) \rangle$  for a given time  $t$ . As a consequence, the standard deviation on the normalised values is also computed as

$$\sigma_{\langle i \rangle, d}^2(t) = \frac{\sum_{N_M} [i(t) - \langle i(t) \rangle]^2}{N_M}. \quad (\text{C.8})$$

In all the figures of Sec. 4.3.4, the error bars show the maximum between  $\sigma_{\langle i \rangle}(t)$  and  $\sigma_{\langle i \rangle, d}(t)$ .

## C.2 Amount of Scraped Beam

Figure 4.38 shows the beam scans obtained from the normalised and averaged BCT signals  $\langle i(t) \rangle$  shown in Fig. 4.36, calculating the amount of scraped beam  $R$  for each scraping position. This is the difference between the normalised beam intensity before and after scraping, normalised again to the normalised intensity before scraping. As done for the bare BCT signals in order to get fully rid of the signal jittering, the averages before and after scraping  $\mu_{\langle i \rangle, b}$  and  $\mu_{\langle i \rangle, a}$  (see Sec. C.3), respectively, are taken, using the same time intervals as those shown in Tab. C.1. The uncertainties associated to these two average values are the error on the mean, i.e.  $\epsilon_{\mu_{\langle i \rangle, b}}$  and  $\epsilon_{\mu_{\langle i \rangle, a}}$  (see Sec. C.3). The uncertainty associated to the amount of scraped beam  $\sigma_R$  is obtained with the propagation of uncertainties of uncorrelated variables applied to the mean normalised beam intensity before and after scraping, i.e. (referring to Sec. C.3)

$$R = \frac{\mu_{\langle i \rangle, b} - \mu_{\langle i \rangle, a}}{\mu_{\langle i \rangle, b}};$$

$$\left( \frac{\sigma_R}{R} \right)^2 = \frac{\epsilon_{\mu_{\langle i \rangle, b}}^2 + \epsilon_{\mu_{\langle i \rangle, a}}^2}{(\mu_{\langle i \rangle, b} - \mu_{\langle i \rangle, a})^2} + \left( \frac{\epsilon_{\mu_{\langle i \rangle, b}}}{\mu_{\langle i \rangle, b}} \right)^2.$$

## C.3 Basic Statistics Formulæ

Given a set of data  $I(t)$ , e.g the bare signal from a BCT made of  $N$  consecutive readouts, the mean value  $\mu$ , the standard deviation of the data  $\sigma$  and the error on the average  $\epsilon_\mu$  are computed as

$$\mu = \frac{\sum_{t_{\min}}^{t_{\max}} I(t)}{N};$$

$$\sigma^2 = \frac{\sum_{t_{\min}}^{t_{\max}} [I(t) - \mu]^2}{N - 1};$$

$$\epsilon_\mu^2 = \frac{\sigma^2}{N}.$$

definition	uncorrelated	correlated
$q = x \pm y$	$(\delta q)^2 = (\delta x)^2 + (\delta y)^2$	$\delta q \leq \delta x + \delta y$
$q = xy$ or $q = x/y$	$\left(\frac{\delta q}{q}\right)^2 = \left(\frac{\delta x}{x}\right)^2 + \left(\frac{\delta y}{y}\right)^2$	$\frac{\delta q}{ q } \leq \frac{\delta x}{ x } + \frac{\delta y}{ y }$

Table C.2: Propagation of uncertainties [106]: mathematical definition of the variable  $q$  dependent on  $x$  and  $y$  (first column), and respective mathematical expressions for the calculation of the uncertainty on values of  $q$  based on the uncertainties on values of  $x$  and  $y$  in case these are fully uncorrelated, i.e. they are independent variables (second column), and in all other cases (third column).

## C.4 Basic Formulæ for the Propagation of Uncertainties

In the following, the basic formulæ for the propagation of uncertainties are reported [106]. When combining two random variables  $x$  and  $y$  in a new random variable  $q$ , the uncertainty  $\delta q$  on the values of the new variable depends on the uncertainties  $\delta x$  and  $\delta y$  on the values of the starting variables. This dependence can be mathematically expressed based on the definition of  $q$ , depending on the degree of correlation between  $x$  and  $y$ . Table C.2 summarises the most common cases, used in this appendix.

## C.5 BCT Readouts

In the following, all the bare BCT signals used for computing the normalised and averaged signals presented in Fig. 4.36 are shown, zoomed on the moment of scraping. Signals are grouped according to the scraping position of each blade. The bare BCT signals are shown in the left frames, whereas the normalised ones are shown in the right frames, together with their average. The error bars in the averaged normalised signals refer to the maximum between the error propagation and the dispersion of the normalised signals.

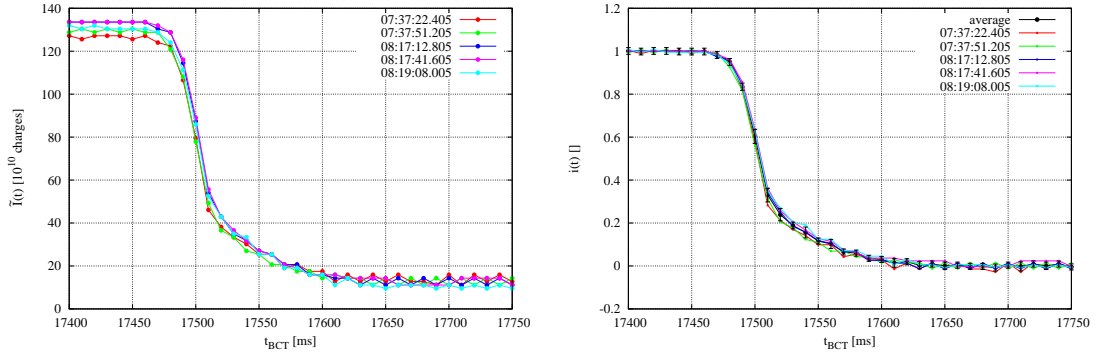


Figure C.2: BCT signals when scraping at  $-11$  mm (i.e. full beam scraping) with the horizontal blade of the BSHV.11759 scraper.

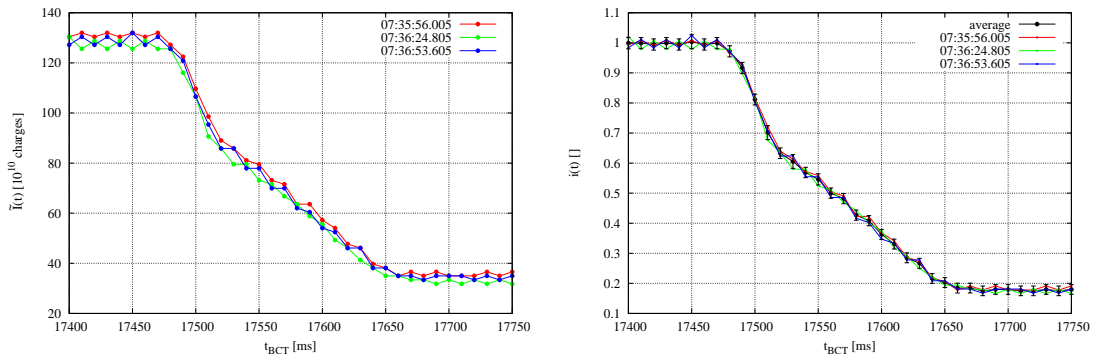


Figure C.3: BCT signals when scraping at  $-11.5$  mm with the horizontal blade of the BSHV.11759 scraper.

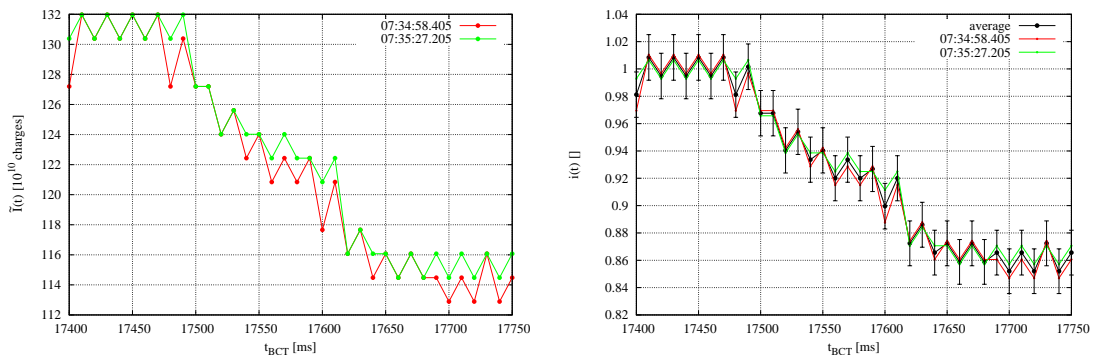


Figure C.4: BCT signals when scraping at  $-12.5$  mm with the horizontal blade of the BSHV.11759 scraper.

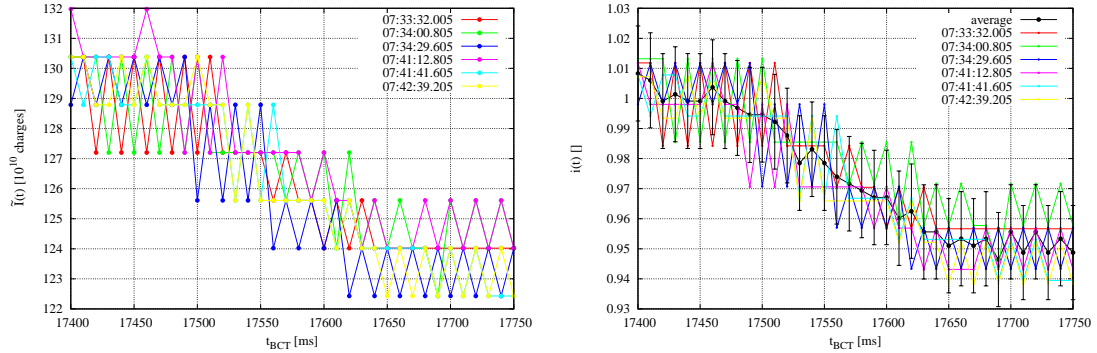


Figure C.5: BCT signals when scraping at  $-13$  mm with the horizontal blade of the BSHV.11759 scraper.

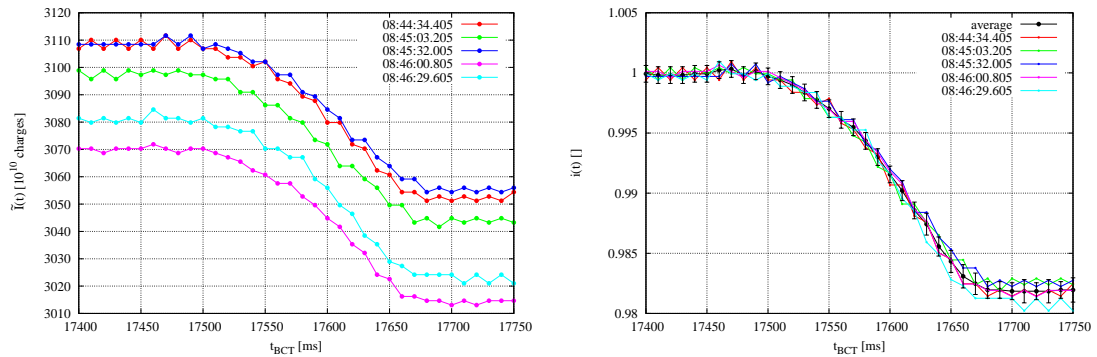


Figure C.6: BCT signals at  $-13.2$  mm (i.e. regular scraping) with the horizontal blade of the BSHV.11759 scraper before the burst test.

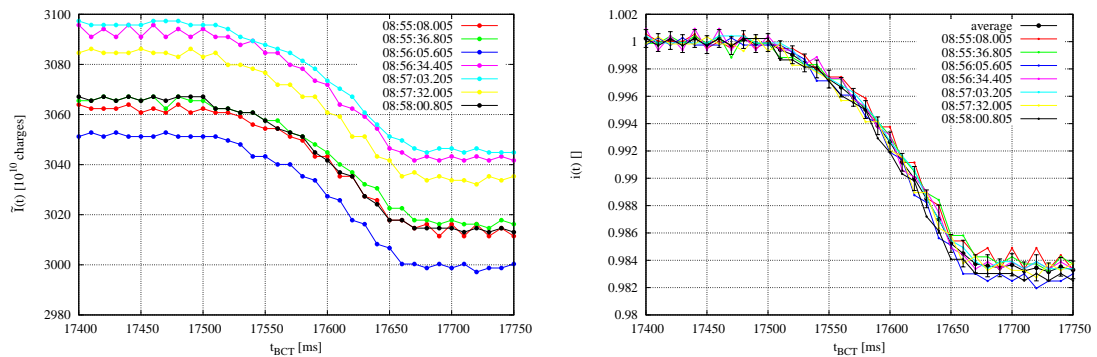


Figure C.7: BCT signals at  $-13.2$  mm (i.e. regular scraping) with the horizontal blade of the BSHV.11759 scraper after the burst test.

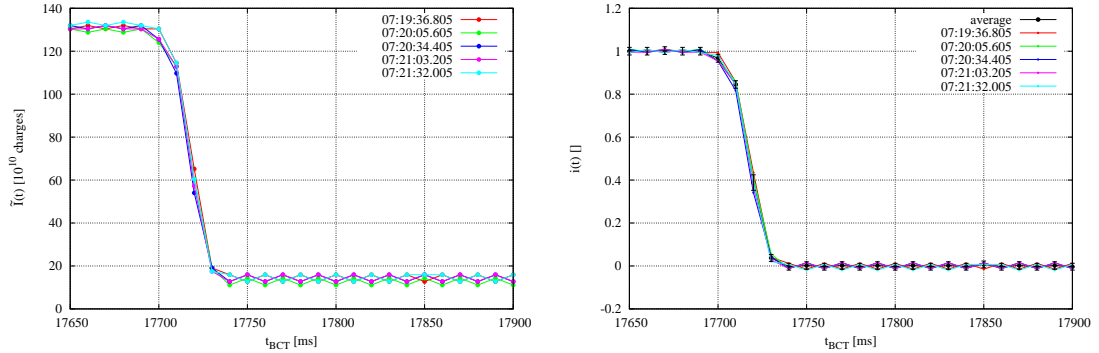


Figure C.8: BCT signals when scraping at 6.2 mm with the vertical blade of the BSHV.11759 scraper.

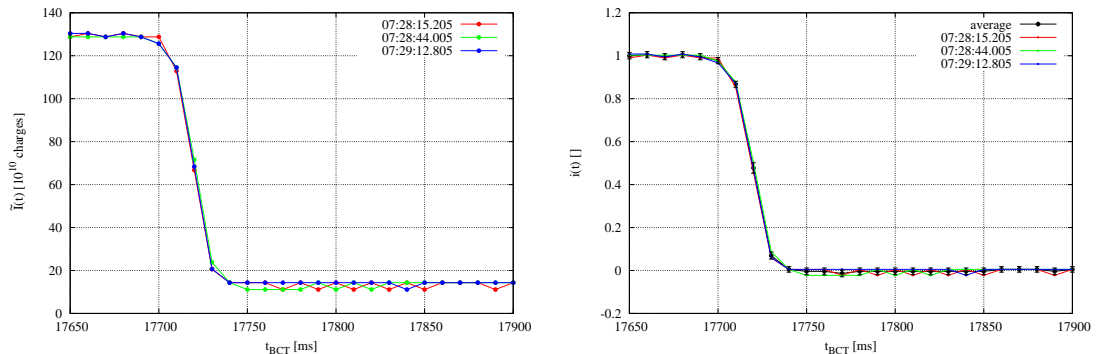


Figure C.9: BCT signals when scraping at 5.7 mm (i.e. full beam scraping) with the vertical blade of the BSHV.11759 scraper.

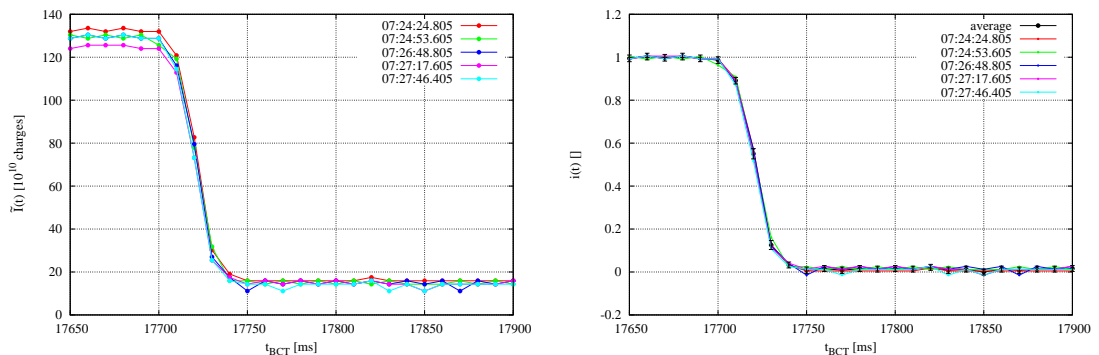


Figure C.10: BCT signals when scraping at 5.6 mm with the vertical blade of the BSHV.11759 scraper.

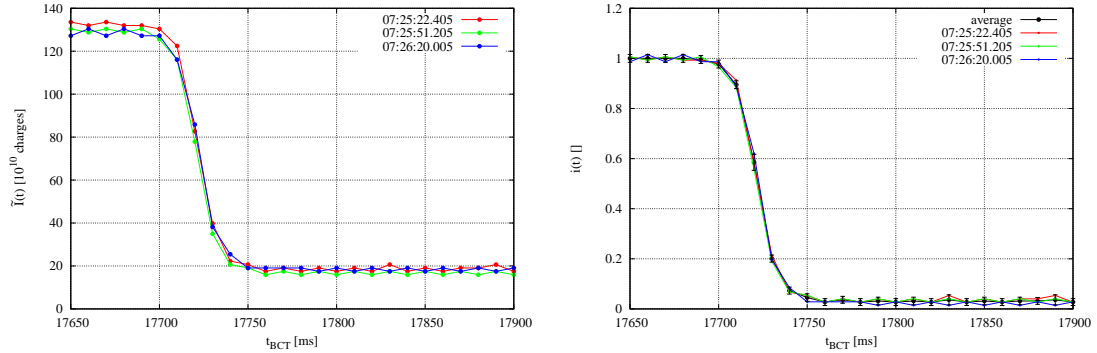


Figure C.11: BCT signals when scraping at 5.5 mm with the vertical blade of the BSHV.11759 scraper.

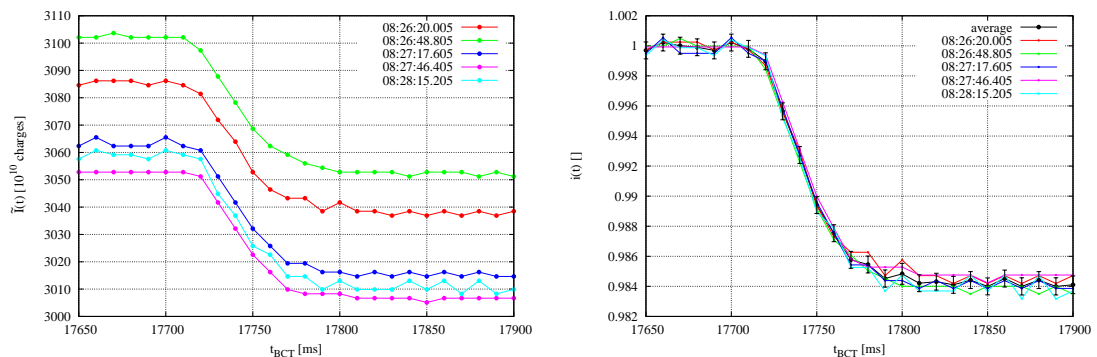


Figure C.12: BCT signals at 3.5 mm (i.e. regular scraping) with the vertical blade of the BSHV.11759 scraper before the burst test.

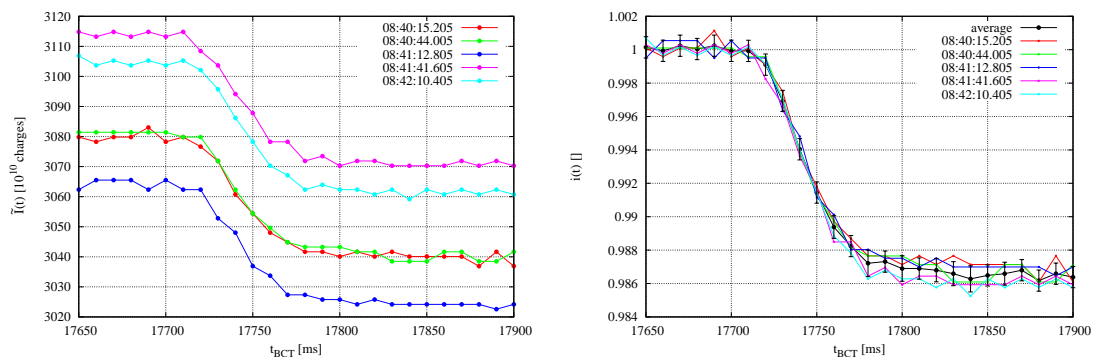


Figure C.13: BCT signals at 3.5 mm (i.e. regular scraping) with the vertical blade of the BSHV.11759 scraper after the burst test.

# Appendix D

## Amount of Scrapped Beam

Knowing the analytical expression of the beam distribution (on both transverse planes and in momentum) and the scraper settings, it is possible to quantitatively predict the amount of beam scraped on each plane. In the present appendix, I recall the analytical expressions of the beam distributions used for the analyses presented in Chaps. 4 and 5, and I calculate the respective amount of scraped beam. I derive the expressions of the amount of beam not seeing the blade, which is the complement to 1 of the amount of scraped beam. Beforehand, the difference between pure betatron and combined betatron–momentum cleaning is shown, as this is relevant for the SPS scraper blades and thus enters the analytical expressions here derived.

### D.1 Origin of Combined Betatron–Momentum Cleaning

From linear accelerator optics [41, 65] (see App. A), the maximum transverse position  $z_{\max}$  ( $z$  represents either the horizontal position  $x$  or the vertical one  $y$ ) of a particle at a certain location in a synchrotron is given by the sum of

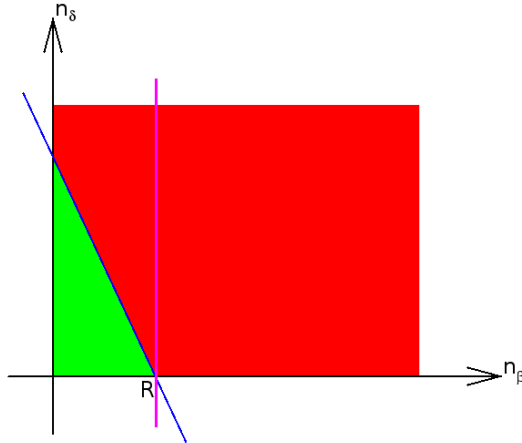


Figure D.1: Schematics of combined betatron–momentum cleaning as seen in the  $n_\beta$ – $n_\delta$  plane. The blue line represents the limiting condition for a beam particle to get intercepted by a device set at  $R \sigma_{z,\beta}$  off the beam centre, expressed by Eq. D.1. The magenta line represents the setting of the intercepting device. The red portion of the plane represents the population of beam particles going to be intercepted, whereas the green part represents the population which never sees the intercepting device.

the maximum contribution from the betatron and synchrotron parts,  $z_{\beta,\max}$  and  $z_{s,\max}$  (see Eq. A.2 and the right frame of Fig. A.1), respectively, i.e.

$$z_{\max} = z_{\beta,\max} + z_{s,\max} = n_\beta \sigma_{z,\beta} + n_\delta \sigma_{z,s},$$

where the normalised betatron amplitude  $n_\beta$  (see Eq. A.16) and the normalised synchrotron amplitude  $n_\delta$  (see Eq. A.20) of the particle have been used, together with the betatron and synchrotron contribution to the rms beam size, i.e.  $\sigma_{z,\beta}$  and  $\sigma_{z,s}$ , respectively (see Eq. A.11).

When a beam–intercepting device is inserted at a distance  $z_R = R \sigma_{z,\beta}$  from the beam centre, all the particles with a maximum transverse position larger than  $z_R$  interact, sooner or later, with the device, being possibly lost. The limit condition when the maximum transverse position of the particle is equal to the

setting of the device can be thus expressed as

$$n_\beta \sigma_{z,\beta} + n_\delta \sigma_{z,s} = R \sigma_{z,\beta}.$$

From the above equation, it can be inferred that for any value of normalised betatron amplitude  $n_\beta$  there exists a value of normalised synchrotron amplitude  $n_\delta$  such that the particle is anyway intercepted by the device. The value of  $n_\delta$  is given by

$$n_\delta = \frac{\sigma_{z,\beta}}{\sigma_{z,s}} (R - n_\beta). \quad (\text{D.1})$$

This implies that the device performs a combined betatron–momentum cleaning, since  $n_\beta$  and  $n_\delta$  are coupled. Equation 4.4 states the same, explicitly expressing  $\sigma_{z,\beta}$  and  $\sigma_{z,s}$ . Equation D.1 represents a simple line in the plane  $n_\beta$ – $n_\delta$  (see Fig. D.1), with slope

$$m = -\frac{\sigma_{z,\beta}}{\sigma_{z,s}}.$$

The blue line in Fig. D.1 graphically represents the condition expressed by Eq. D.1; thus, after a sufficiently large number of turns in the accelerator, all the beam particles above the blue line (i.e. in the red portion of space in Fig. D.1) are intercepted by the device, whereas those below the blue line (i.e. in the green portion of space in Fig. D.1) do not see the intercepting device at all.

Depending on the slope of the curve, i.e. on the value of  $m$ , a different level of combined cleaning is performed, and thus a different amount of beam is removed for the same beam distribution. If  $\sigma_{z,\beta} \gg \sigma_{z,s}$ , typically because the dispersion function is small, then pure betatron cleaning is performed, as  $\lim_{\sigma_{z,s} \rightarrow 0} m = -\infty$ , and the blue curve in Fig. D.1 collapses onto the magenta one; in this case, all the beam particles on the right of the magenta curve are removed, no matter the value of their momentum, i.e.  $n_\delta$ .

In conclusion, combined betatron–momentum cleaning is performed if dispersive effects are important, reflected in a synchrotron contribution to the rms beam size comparable to the betatron one.

## D.2 Expected Amount of Surviving Beam

The amount of beam  $I_C(R)$  not seeing the intercepting device set at the position  $R \sigma_{z,\beta}$  can be predicted by the integral in Eq. 4.5, here reported

$$I_C(R) = \int_0^R \text{pdf}_\beta(n_\beta) \, dn_\beta \int_0^{n_{\delta,\max}} \text{pdf}_\delta(n_\delta) \, dn_\delta, \quad (\text{D.2})$$

where  $\text{pdf}_\beta(n_\beta)$  and  $\text{pdf}_\delta(n_\delta)$  are the distributions of the normalised betatron amplitude on the transverse plane  $z$  and the normalised synchrotron amplitude on the longitudinal plane, respectively;  $n_{\delta,\max}$  is the upper limit of integration on the longitudinal plane. In case of combined betatron–momentum cleaning,  $n_{\delta,\max}$  is given by Eq. D.1, and it sets the coupling between  $n_\beta$  and  $n_\delta$ , that must be taken into account in the integration. Otherwise, for pure betatron cleaning,  $n_{\delta,\max}$  is  $\infty$ .

In the following, the integral stated in Eq. D.2 is analytically solved in case of pure betatron cleaning and in case of combined betatron–momentum cleaning, for a couple of beam distributions. The mathematics is focussed on the estimation of the amount of beam  $I_C(R)$  that does not see the intercepting device. To get the respective amount of cleaned beam  $I_S(R)$ , i.e. scraped off, it is just needed to calculate the complement of  $I_C(R)$  to 1, i.e.

$$I_S(R) = 1 - I_C(R). \quad (\text{D.3})$$

Beforehand, a reminder on Gaussian distributions is given.

### D.2.1 Reminder on Gaussian Distributions

In this section, a brief summary of Gaussian and Gaussian-related pdfs is presented, as these are the distributions used in Chaps. 4 and 5

#### 1D Gaussian PDF

With “1D Gaussian” pdf I refer to a Gaussian distribution in one dimension

$$\text{pdf}(p) = \frac{1}{\sqrt{2\pi}\sigma} \exp \left[ -\frac{p^2}{2\sigma^2} \right],$$

where  $p$  is the independent variable,  $\sigma$  its standard deviation and the mean of the distribution is 0. This distribution is considered here as it has been used for spreading in momentum beam particles sampled for tracking. The pdf of the modulus of the normalised coordinate, i.e.  $\delta = |p/\sigma|$ , is

$$\text{pdf}(\delta) = \sqrt{\frac{2}{\pi}} \exp \left[ -\frac{\delta^2}{2} \right], \quad (\text{D.4})$$

and its cumulative pdf is given by

$$F(\Delta) = \int_0^\Delta \text{pdf}(\delta) d\delta = \int_0^\Delta \sqrt{\frac{2}{\pi}} \exp \left[ -\frac{\delta^2}{2} \right] d\delta = \text{erf} \left[ \frac{\Delta}{\sqrt{2}} \right], \quad (\text{D.5})$$

where the error function erf has been used

$$\text{erf}(x) = \frac{2}{\sqrt{\pi}} \int_0^x e^{-t^2} dt. \quad (\text{D.6})$$

#### 2D Gaussian PDF

With “2D Gaussian” pdf I refer to a Gaussian distribution in two dimensions

$$\text{pdf}(\xi, \xi') = \frac{1}{2\pi\sigma^2} \exp \left[ -\frac{\xi^2 + \xi'^2}{2\sigma^2} \right], \quad (\text{D.7})$$

where both the independent variables  $\xi$  and  $\xi'$  have the same standard deviation  $\sigma$ . In case of  $\sigma = 1$ , this pdf can be used to describe a Gaussian beam in the normalised betatron phase space (see Sec. A.3). The beam distribution in (non-normalised) phase space is still Gaussian. The above pdf can be rewritten in terms of the normalised betatron amplitude  $n_\beta$  and phase  $\phi_{z,\beta}$  (see Eq. A.16) as

$$\begin{aligned} \text{pdf}(\xi, \xi') d\xi d\xi' &= \frac{1}{2\pi} \exp \left[ -\frac{\xi^2 + \xi'^2}{2} \right] d\xi d\xi' \\ &= \frac{1}{2\pi} \exp \left[ -\frac{n_\beta^2}{2} \right] n_\beta dn_\beta d\phi_{z,\beta} = \text{pdf}(n_\beta, \phi_{z,\beta}) dn_\beta d\phi_{z,\beta}, \end{aligned} \quad (\text{D.8})$$

where the performed change of coordinates from the normalised ones  $\xi-\xi'$  to normalised amplitude-phase  $n_\beta-\phi_{z,\beta}$  has been performed, profiting from the fact that it coincides to a change of variables from a Cartesian coordinate system to a polar one.  $\text{pdf}(n_\beta, \phi_{z,\beta})$  can be separated in its components, with the one in normalised amplitude given by

$$\text{pdf}(n_\beta) = n_\beta \exp \left[ -\frac{n_\beta^2}{2} \right], \quad (\text{D.9})$$

and the one in phase being constant, i.e.  $\text{pdf}(\phi_{z,\beta}) = 1/2\pi$ . Its cumulative distribution is given by

$$\begin{aligned} F(N_\beta) &= \int_0^{N_\beta} \text{pdf}(n_\beta) dn_\beta = \int_0^{N_\beta} n_\beta \exp \left[ -\frac{n_\beta^2}{2} \right] dn_\beta = -\exp \left[ -\frac{n_\beta^2}{2} \right]_0^{N_\beta} \\ &= 1 - \exp \left[ -\frac{N_\beta^2}{2} \right] \end{aligned} \quad (\text{D.10})$$

## Double 2D Gaussian PDF

With “double 2D Gaussian” pdf I refer to a distribution obtained with a linear combination of two 2D Gaussian distributions (see Eq. D.7), such that the integral

is 1, and each component has its own value of standard deviation. This pdf can be written as

$$\text{pdf}(\xi, \xi') = \frac{I_1}{2\pi\sigma_1^2} \exp \left[ -\frac{\xi^2 + \xi'^2}{2\sigma_1^2} \right] + \frac{(1 - I_1)}{2\pi\sigma_2^2} \exp \left[ -\frac{\xi^2 + \xi'^2}{2\sigma_2^2} \right], \quad (\text{D.11})$$

where  $\xi$  and  $\xi'$  are the independent variables;  $I_1$  and  $1 - I_1$  are the weights applied to the first and second Gaussians, respectively, so that the integral of the pdf is 1; and  $\sigma_1$  and  $\sigma_2$  are the respective standard deviations. The standard deviations can be expressed in terms of a common one and two magnification factors, i.e.  $\sigma_1 = f_1\sigma$  and  $\sigma_2 = f_2\sigma$ . In case  $\xi$  and  $\xi'$  are the normalised betatron coordinates,  $\sigma$  can be set to 1, and the same pdf can be expressed in terms of normalised betatron amplitude  $n_\beta$  and phase  $\phi_{z,\beta}$  (similarly to Eqs. D.8, but paying attention to the weights  $I_1$  and  $1 - I_1$  and to the magnification factors  $f_1$  and  $f_2$ ) as

$$\text{pdf}(n_\beta, \phi_{z,\beta}) = \frac{I_1}{2\pi f_1^2} n_\beta \exp \left[ -\frac{n_\beta^2}{2f_1^2} \right] + \frac{(1 - I_1)}{2\pi f_2^2} n_\beta \exp \left[ -\frac{n_\beta^2}{2f_2^2} \right]. \quad (\text{D.12})$$

As done in the case of the 2D Gaussian distribution, the part depending only on the normalised betatron amplitude  $n_\beta$  can be separated from the one of the betatron phase  $\phi_z$ , and the resulting pdf is (similarly to Eq. D.9)

$$\text{pdf}(n_\beta) = I_1 \frac{n_\beta}{f_1^2} \exp \left[ -\frac{n_\beta^2}{2f_1^2} \right] + (1 - I_1) \frac{n_\beta}{f_2^2} \exp \left[ -\frac{n_\beta^2}{2f_2^2} \right], \quad (\text{D.13})$$

and its cumulative distribution (similarly to Eq. D.10) as

$$F(N_\beta) = 1 - I_1 \exp \left[ -\frac{N_\beta^2}{2f_1^2} \right] - (1 - I_1) \exp \left[ -\frac{N_\beta^2}{2f_2^2} \right] \quad (\text{D.14})$$

### D.2.2 Pure Betatron Cleaning

As already mentioned, in case of pure betatron cleaning, the upper limit of integration  $n_{\delta,\max}$  on the longitudinal part of the integral in Eq. D.2 is independent of  $n_{\beta}$ . Consequently, the longitudinal and betatron part of the integral can be solved separately. Considering the entire domain of  $n_{\delta}$ , i.e.  $[0 : \infty)$  (see Sec. A.3), the integral of the longitudinal part is 1, and the integral on the betatron part coincides with the cumulative pdfs given in Eq. D.10, for a single 2D Gaussian distribution, and in Eq. D.14, for a double 2D Gaussian distribution, where  $N_{\beta}$  has to be changed with  $R$ , i.e. the transverse position at which the scraper is set, in units of rms beam size  $\sigma_{z,\beta}$  (only the betatron component). In particular, the value shown by the light blue curves in Fig. 4.39 is exactly given by the latter of the quoted equations, using the parameters listed in Tab. 4.10, with  $R$  depending on the scraping position of the blade.

### D.2.3 Combined Betatron–Momentum Cleaning

As already mentioned, in case of combined betatron–momentum cleaning, the upper limit of integration  $n_{\delta,\max}$  in the longitudinal part of the integral in Eq. D.2 depends on  $n_{\beta}$ , and it is expressed by Eq. D.1. Hence, the integral in Eq. D.2 can be rewritten as

$$I_C(R) = \int_0^R \text{pdf}_{\beta}(n_{\beta}) dn_{\beta} \int_0^{m(R-n_{\beta})} \text{pdf}_{\delta}(n_{\delta}) dn_{\delta}.$$

Consequently, the longitudinal and betatron part of the integral cannot be solved separately; on the contrary, the longitudinal part must be solved first, and then the betatron part. Depending on the analytical expression of  $\text{pdf}_{\delta}(n_{\delta})$ ,  $I_C(R)$  has a different mathematical expression for the same  $\text{pdf}_{\beta}(n_{\beta})$ .

In the following, a single component of a double 2D Gaussian distribution (see

Eq. D.13) is always considered as distribution on the betatron transverse plane  $z$ , i.e.

$$\text{pdf}_\beta(n_\beta) = I \frac{n_\beta}{f^2} \exp \left[ -\frac{n_\beta^2}{2f^2} \right]. \quad (\text{D.15})$$

In this way, the algebra is performed only on one component, as the other one follows accordingly, changing  $I$  into  $1 - I$  and  $f$  into the magnification factor of the second component. Similarly, the case of a Gaussian distribution is obtained setting  $I = f = 1$ . For the longitudinal plane, two different distributions are considered, i.e. a simple 1D Gaussian (see Eq. D.4)

$$\text{pdf}_\delta(n_\delta) = \sqrt{\frac{2}{\pi}} \exp \left[ -\frac{n_\delta^2}{2} \right], \quad (\text{D.16})$$

corresponding to the case in which beam particles are given only a momentum spread (i.e. no distribution in lag with respect to the synchronous particle), distributed as a Gaussian, and a 2D Gaussian (see Eq. D.9)

$$\text{pdf}_\delta(n_\delta) = n_\delta \exp \left[ -\frac{n_\delta^2}{2} \right], \quad (\text{D.17})$$

corresponding to the case in which beam particles are given both a momentum spread and a distribution in lag with respect to the synchronous particle. It should be kept in mind that the domain of  $n_\beta$  and  $n_\delta$  is

$$n_\beta, n_\delta \in [0 : \infty).$$

## Momentum Distribution: 1D Gaussian

In case the beam is distributed in momentum according to a 1D Gaussian pdf (see Eq. D.4), the integral on the longitudinal part is

$$\begin{aligned} \int_0^{m(R-n_\beta)} \text{pdf}_\delta(n_\delta) dn_\delta &= \int_0^{m(R-n_\beta)} \sqrt{\frac{2}{\pi}} \exp\left[-\frac{n_\delta^2}{2}\right] dn_\delta = \\ &= \text{erf}\left[\frac{n_\delta}{\sqrt{2}}\right]_0^{m(R-n_\beta)} = \text{erf}\left[\frac{m(R-n_\beta)}{\sqrt{2}}\right]. \end{aligned}$$

This expression can then be inserted in  $I_C(R)$  (see Eq. D.2)

$$I_C(R) = \int_0^R I \frac{n_\beta}{f^2} \exp\left[-\frac{n_\beta^2}{2f^2}\right] \text{erf}\left[\frac{m(R-n_\beta)}{\sqrt{2}}\right] dn_\beta,$$

where a single component of a double 2D Gaussian distribution (see Eq. D.13) has been used for describing the betatron part. If analytically solved [107], this integral can be written as

$$I_C(R) = A \left[ B F(n_\beta) + G(n_\beta) \right]_0^R, \quad (\text{D.18})$$

where

$$A = I; \quad (\text{D.19})$$

$$B = -\frac{fm}{\sqrt{f^2m^2+1}} \exp\left[-\frac{m^2R^2}{2(f^2m^2+1)}\right]; \quad (\text{D.20})$$

$$F(n_\beta) = \text{erf}\left[\frac{f^2m^2(n_\beta - R) + n_\beta}{f\sqrt{2(f^2m^2+1)}}\right]; \quad (\text{D.21})$$

$$G(n_\beta) = -\exp\left[-\frac{n_\beta^2}{2f^2}\right] \text{erf}\left[\frac{m(R-n_\beta)}{\sqrt{2}}\right]. \quad (\text{D.22})$$

The following are the evaluations of  $F(n_\beta)$  and  $G(n_\beta)$  in  $R$  and in 0

$$F(R) = \operatorname{erf} \left[ \frac{R}{f\sqrt{2(f^2m^2 + 1)}} \right]; \quad F(0) = \operatorname{erf} \left[ -\frac{f^2m^2R}{f\sqrt{2(f^2m^2 + 1)}} \right]; \quad (\text{D.23})$$

$$G(R) = 0; \quad G(0) = -\operatorname{erf} \left[ \frac{mR}{\sqrt{2}} \right]. \quad (\text{D.24})$$

The value shown by the magenta lines in Fig. 4.39 is exactly given by the above equation, using the parameters listed in Tab. 4.10 for the double Gaussian distributions of the betatron part, with  $R$  depending on the scraping position of the blade in units of  $\sigma_{z,\beta}$ .

### Momentum Distribution: 2D Gaussian

In case the beam is distributed in momentum according to a 2D Gaussian pdf (see Eq. D.17), the integral on the longitudinal part is

$$\begin{aligned} \int_0^{m(R-n_\beta)} \operatorname{pdf}_\delta(n_\delta) dn_\delta &= \int_0^{m(R-n_\beta)} n_\delta \exp \left[ -\frac{n_\delta^2}{2} \right] dn_\delta = \\ &= -\exp \left[ \frac{-n_\delta^2}{2} \right]_0^{m(R-n_\beta)} = 1 - \exp \left[ -\frac{m^2(R-n_\beta)^2}{2} \right]. \end{aligned}$$

This expression can then be inserted in  $I_C(R)$  (see Eq. D.2)

$$I_C(R) = \int_0^R I \frac{n_\beta}{f^2} \exp \left[ -\frac{n_\beta^2}{2f^2} \right] \left\{ 1 - \exp \left[ -\frac{m^2(R-n_\beta)^2}{2} \right] \right\} dn_\beta,$$

where a single component of a double 2D Gaussian distribution (see Eq. D.13) has been used for describing the betatron part. If analytically solved [107], this integral can be written as

$$I_C(R) = T(n_\beta) \Big|_0^R - A \left[ BF(n_\beta) + G(n_\beta) \right]_0^R,$$

where

$$T(n_\beta) = -I \exp \left[ -\frac{n_\beta^2}{2f^2} \right]; \quad (\text{D.25})$$

$$A = \frac{I}{f^2 m^2 + 1} \exp \left[ -\frac{m^2 R^2}{2} \right]; \quad (\text{D.26})$$

$$B = \frac{f m^2 R \sqrt{\pi}}{\sqrt{2(f^2 m^2 + 1)}} \exp \left[ \frac{f^2 m^4 R^2}{2(f^2 m^2 + 1)} \right]; \quad (\text{D.27})$$

$$F(n_\beta) = \operatorname{erf} \left[ \frac{f^2 m^2 (n_\beta - R) + n_\beta}{f \sqrt{2(f^2 m^2 + 1)}} \right]; \quad (\text{D.28})$$

$$G(n_\beta) = -\exp \left[ \frac{n_\beta f^2 m^2 (R - 0.5 n_\beta) - 0.5 n_\beta^2}{f^2} \right]. \quad (\text{D.29})$$

As it can be seen, the solution can be expressed as difference between the pure component from the double Gaussian  $T(n_\beta)$  and a portion very similar to the one found in the case of a 1D Gaussian distribution in momentum (see Eq. D.18). In particular, the expressions for  $A$  and  $B$  in the present case are more complex than those previously found (see Eqs. D.19 and D.20), even though it is possible to recognise common parts. The expression of  $F(n_\beta)$  is identical to the one obtained in case of the 1D Gaussian distribution (see Eq. D.21), whereas in the expression of  $G(n_\beta)$  the argument of the exponential function is more complicated than in the case of 1D Gaussian distribution in momentum (see Eq. D.22), and the part with the error function completely disappears. The following are the evaluations of  $T(n_\beta)$  and  $G(n_\beta)$  in  $R$  and in 0

$$T(R) = -I \exp \left[ -\frac{R^2}{2f^2} \right]; \quad T(0) = -I; \quad (\text{D.30})$$

$$G(R) = -\exp \left[ -\frac{R^2}{2f^2} (1 - f^2 m^2) \right]; \quad G(0) = -1. \quad (\text{D.31})$$

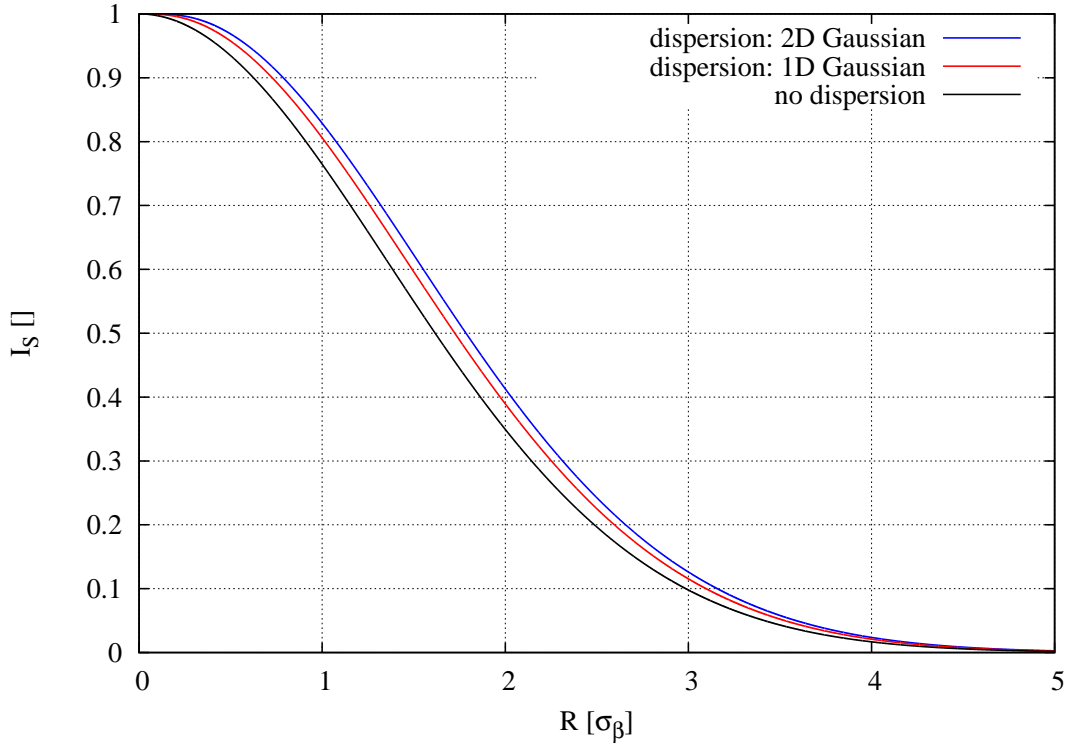


Figure D.2: Fraction of beam stopped by an intercepting device as a function of its cleaning position  $R \sigma_{z,\beta}$ . In particular, the case of the horizontal blade of the BSHV.11759 scraper and the beam distributed according to a double Gaussian on the betatron part with parameters reported in Tab. 4.10 for the horizontal plane, is shown. The black curve is obtained for pure betatron cleaning (i.e. when dispersive effects are not taken into account), whereas the red and the blue curves are obtained in case of combined betatron–momentum cleaning, with a momentum distribution as indicated by the key. The value of  $\sigma_\delta$  used in the plot is the one reported in Tab. 4.10.

### Comparison

Figure D.2 shows the fraction of beam  $I_C(R)$  stopped by an intercepting device as a function of its cleaning position  $R \sigma_{z,\beta}$ . In particular, the case of the horizontal blade of the BSHV.11759 scraper and the beam distributed according to a double Gaussian on the betatron part (see Eq. D.13) with parameters reported in Tab. 4.10 for the horizontal plane is shown. As it can be seen, dispersion effects lead to clean fractions of beam larger than what expected with pure betatron cleaning.

## Appendix E

### Collection of BLM Signals

In this appendix, all the BLM signals collected for the scraping positions reported in Tab. 4.13 are reported. For all the sets of signals, a plot with the overview on the entire ring (in the upper frames) and the zoom on the LSS1 downstream of the BSHV.11759 scrapers included (in the lower frames) are given. No error bars are shown, for the sake of clarity. For reference, the calibration factors are listed in Tab. 4.7. Given the large number of BLM sets available when no scraping is performed with a high intensity beam (i.e.  $\sim 3 \cdot 10^{13}$  protons), the sets have been split in two.

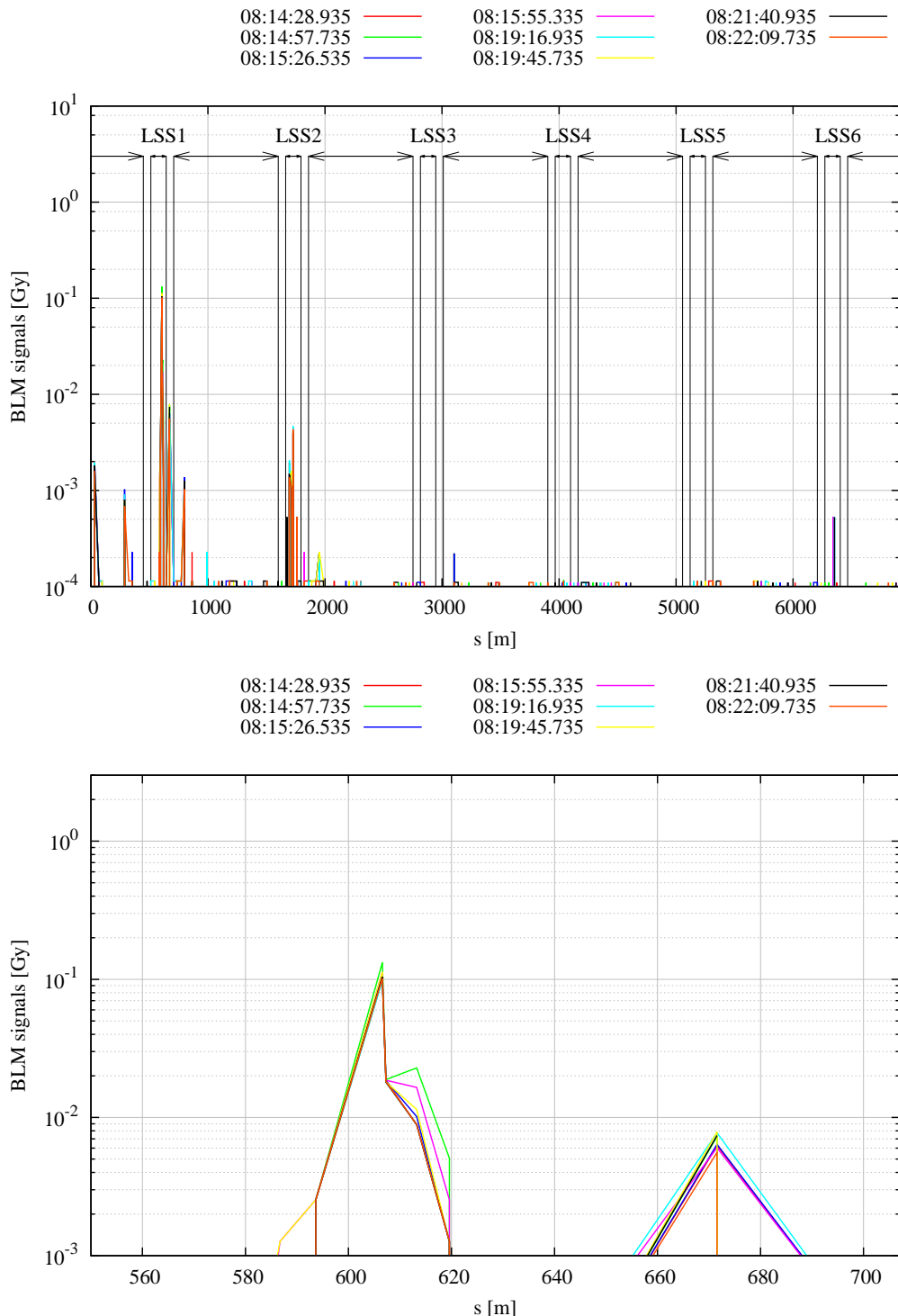


Figure E.1: BLM signals when no scraping is performed with a low intensity beam (i.e.  $\sim 10^{12}$  protons).

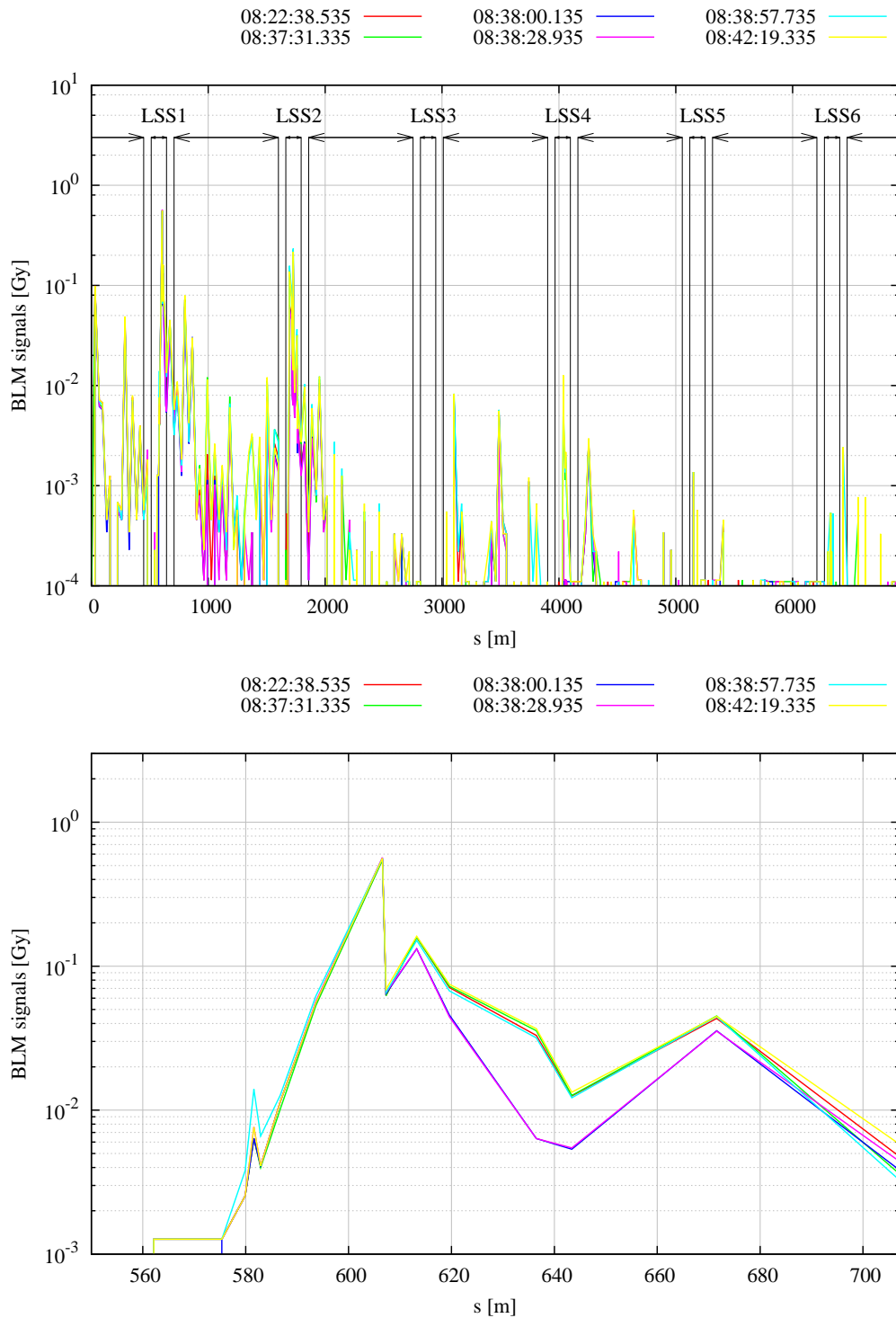


Figure E.2: First set of BLM signals when no scraping is performed with a high intensity beam (i.e.  $\sim 3 \cdot 10^{13}$  protons).

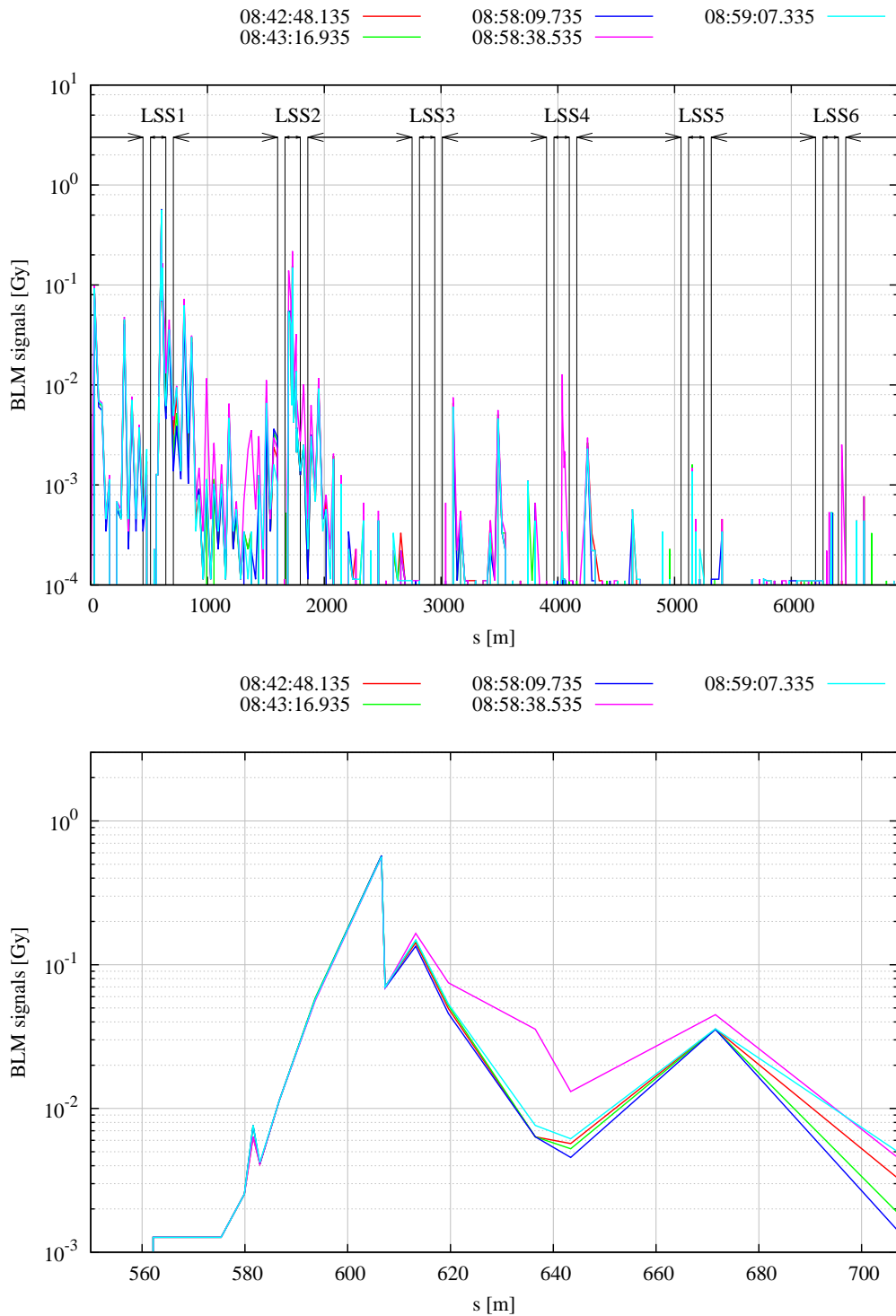


Figure E.3: Second set of BLM signals when no scraping is performed with a high intensity beam (i.e.  $\sim 3 \cdot 10^{13}$  protons).

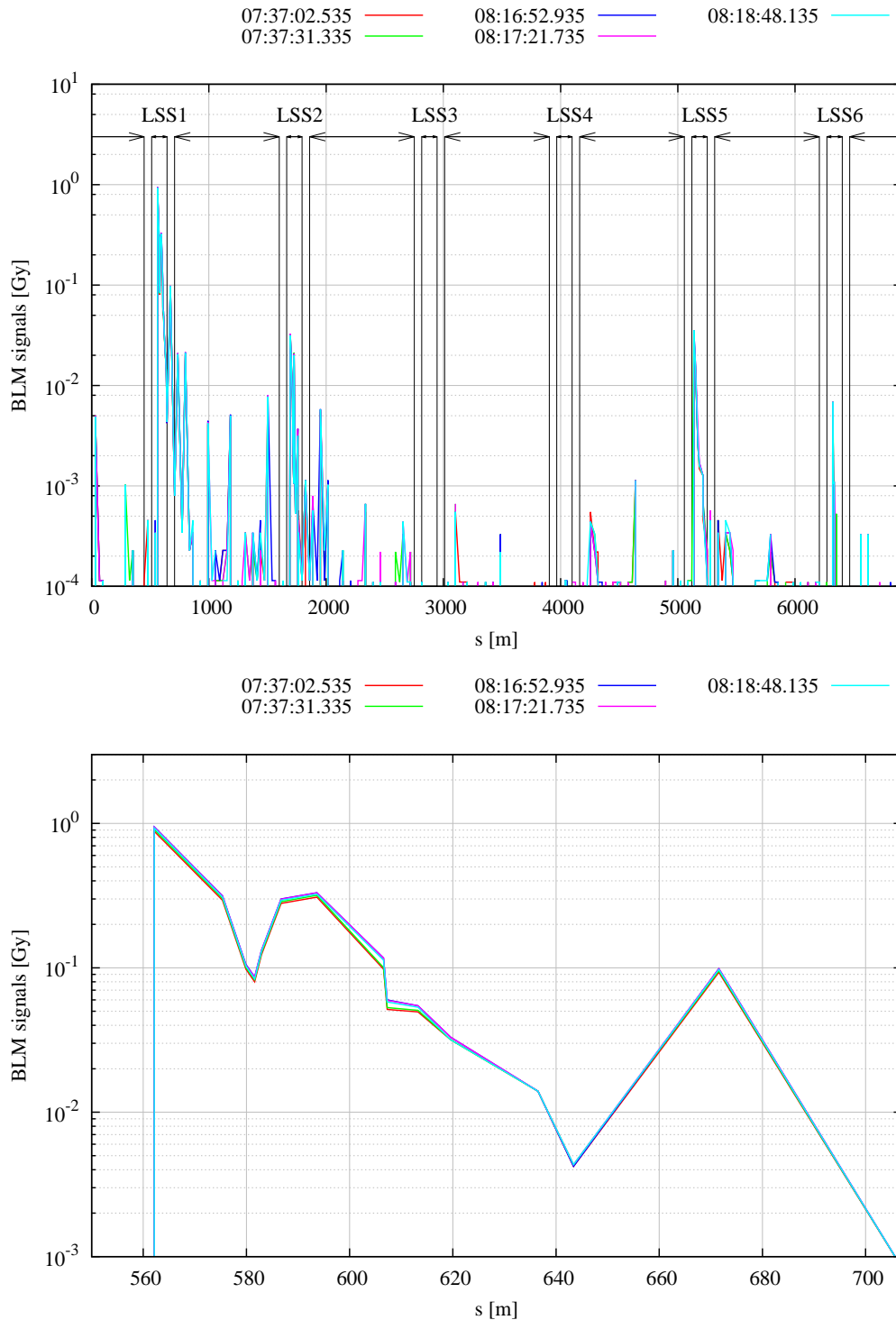


Figure E.4: BLM signals when scraping with the horizontal blade of the BSHV.11759 scraper at  $-11$  mm (i.e. full beam scraping), with a low intensity beam (i.e.  $\sim 10^{12}$  protons).

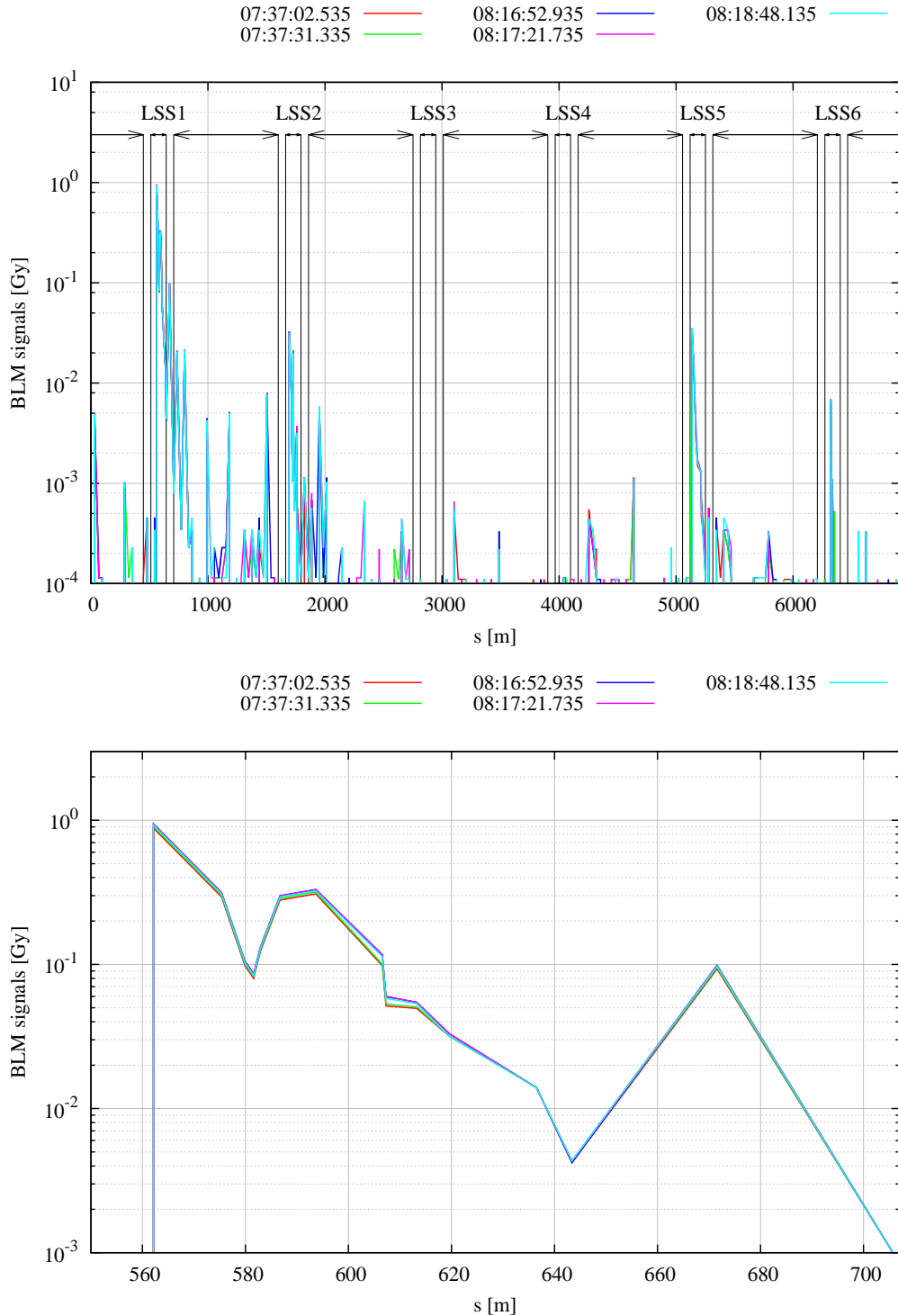


Figure E.5: BLM signals when scraping with the horizontal blade of the BSHV.11759 scraper at  $-11.5$  mm (i.e.  $\sim 500 \mu\text{m}$  off the centre of the beam), with a low intensity beam (i.e.  $\sim 10^{12}$  protons).

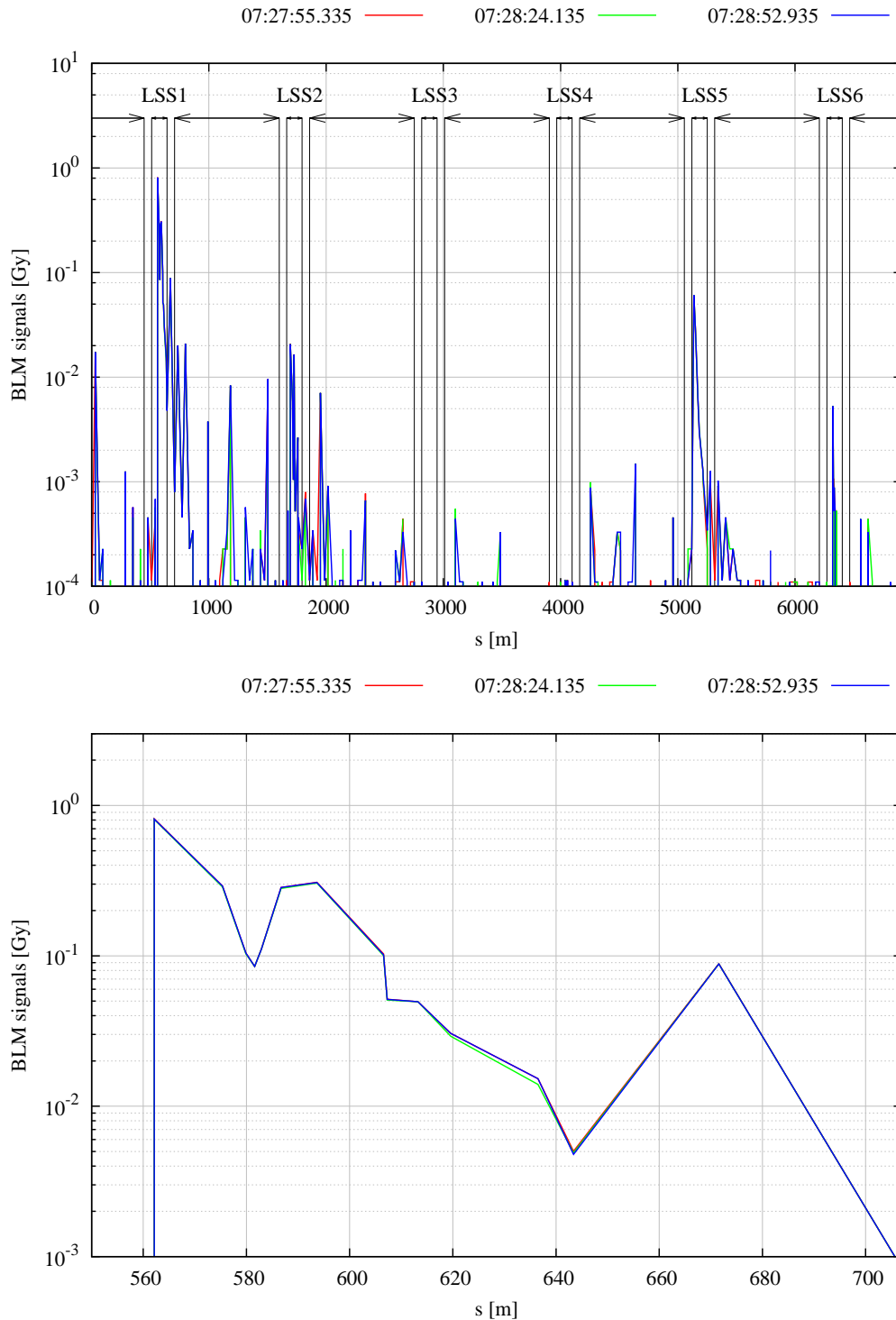


Figure E.6: BLM signals when scraping with the vertical blade of the BSHV.11759 scraper at 5.7 mm (i.e. full beam scraping), with a low intensity beam (i.e.  $\sim 10^{12}$  protons).

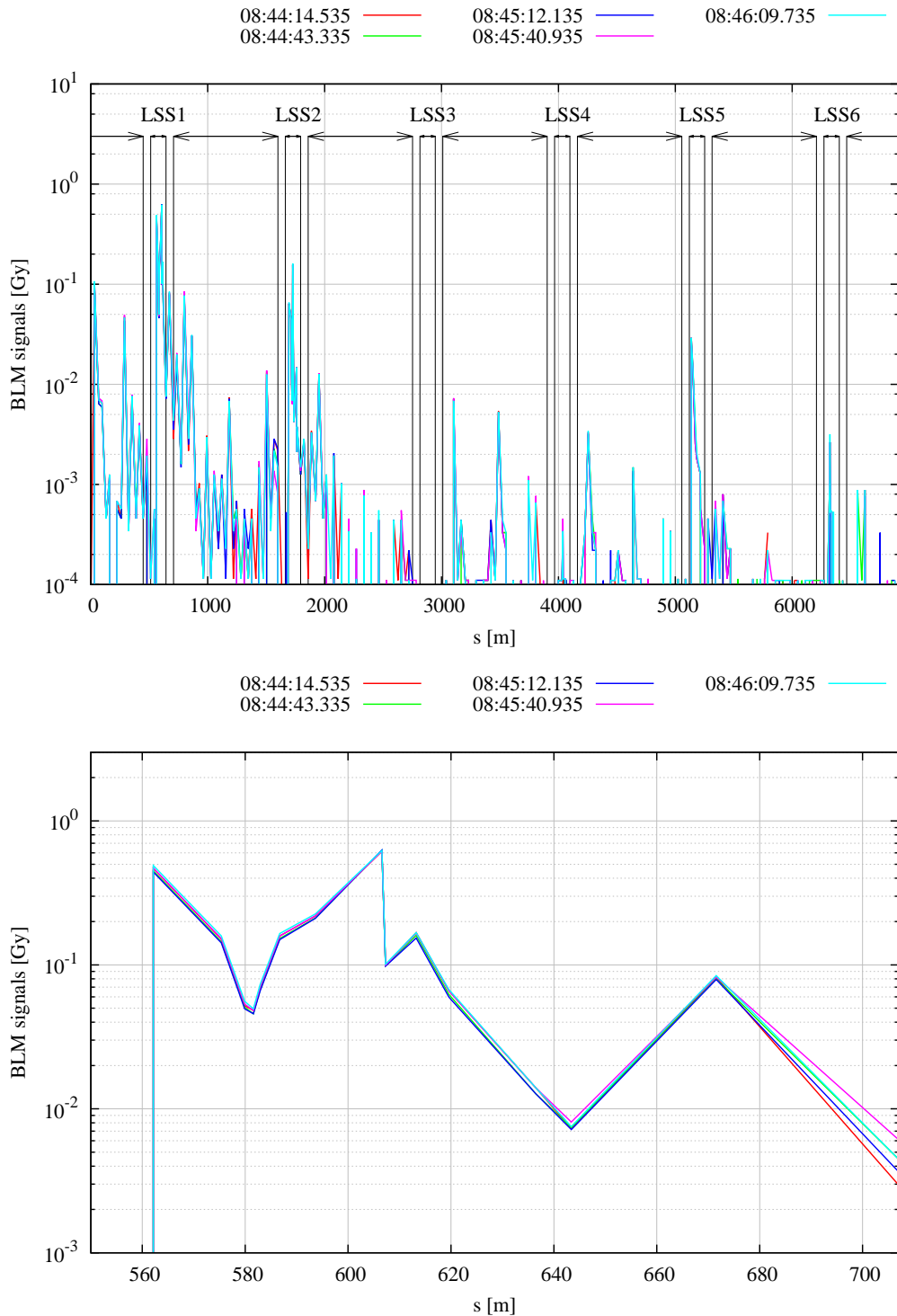


Figure E.7: BLM signals when scraping with the horizontal blade of the BSHV.11759 scraper at  $-13.2$  mm (i.e. regular scraping), with a high intensity beam (i.e.  $\sim 3 \cdot 10^{13}$  protons), before the burst test of the blade.

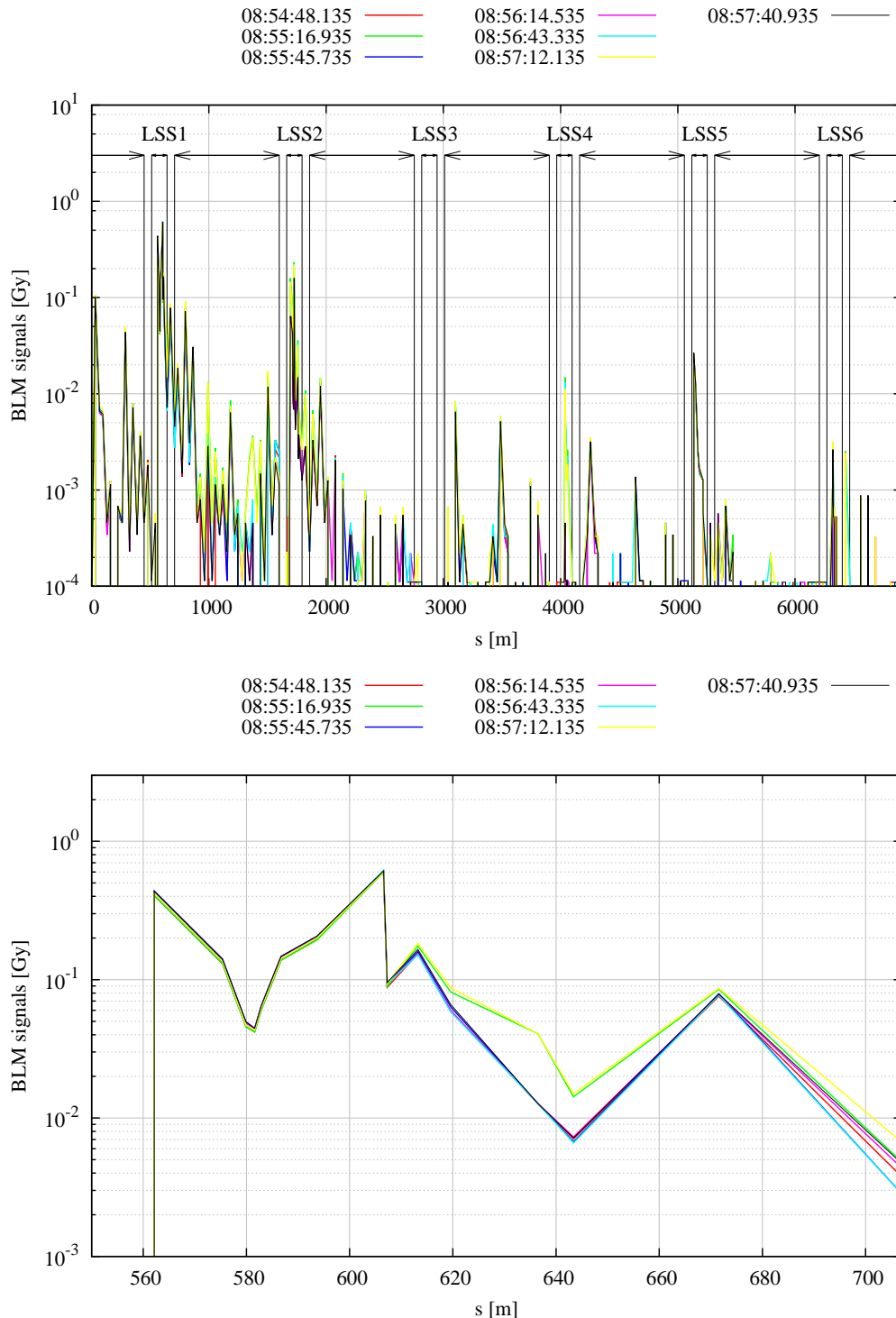


Figure E.8: BLM signals when scraping with the horizontal blade of the BSHV.11759 scraper at  $-13.2$  mm (i.e. regular scraping), with a high intensity beam (i.e.  $\sim 3 \cdot 10^{13}$  protons), after the burst test of the blade.

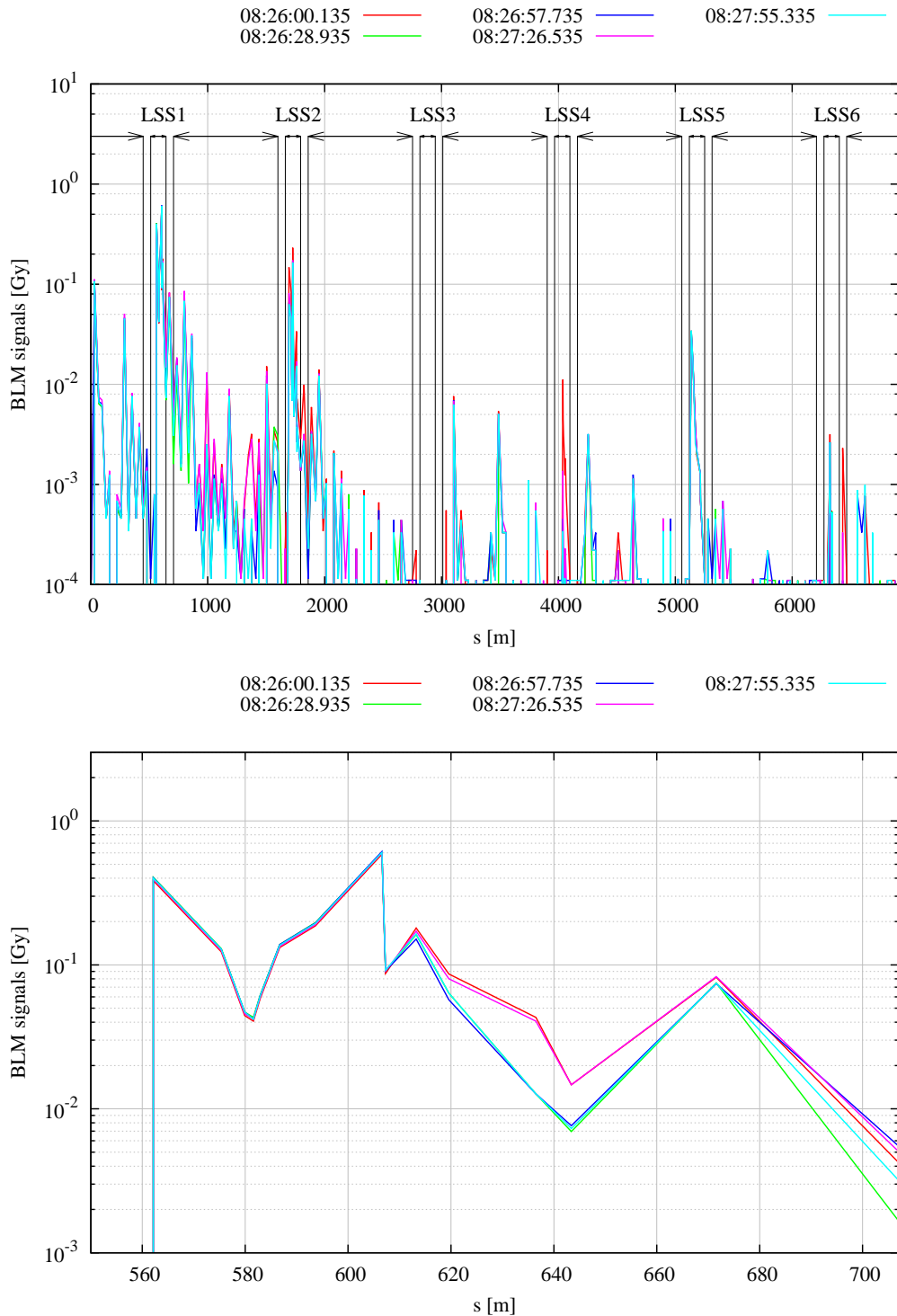


Figure E.9: BLM signals when scraping with the vertical blade of the BSHV.11759 scraper at 3.5 mm (i.e. regular scraping), with a high intensity beam (i.e.  $\sim 3 \cdot 10^{13}$  protons), before the burst test of the blade.

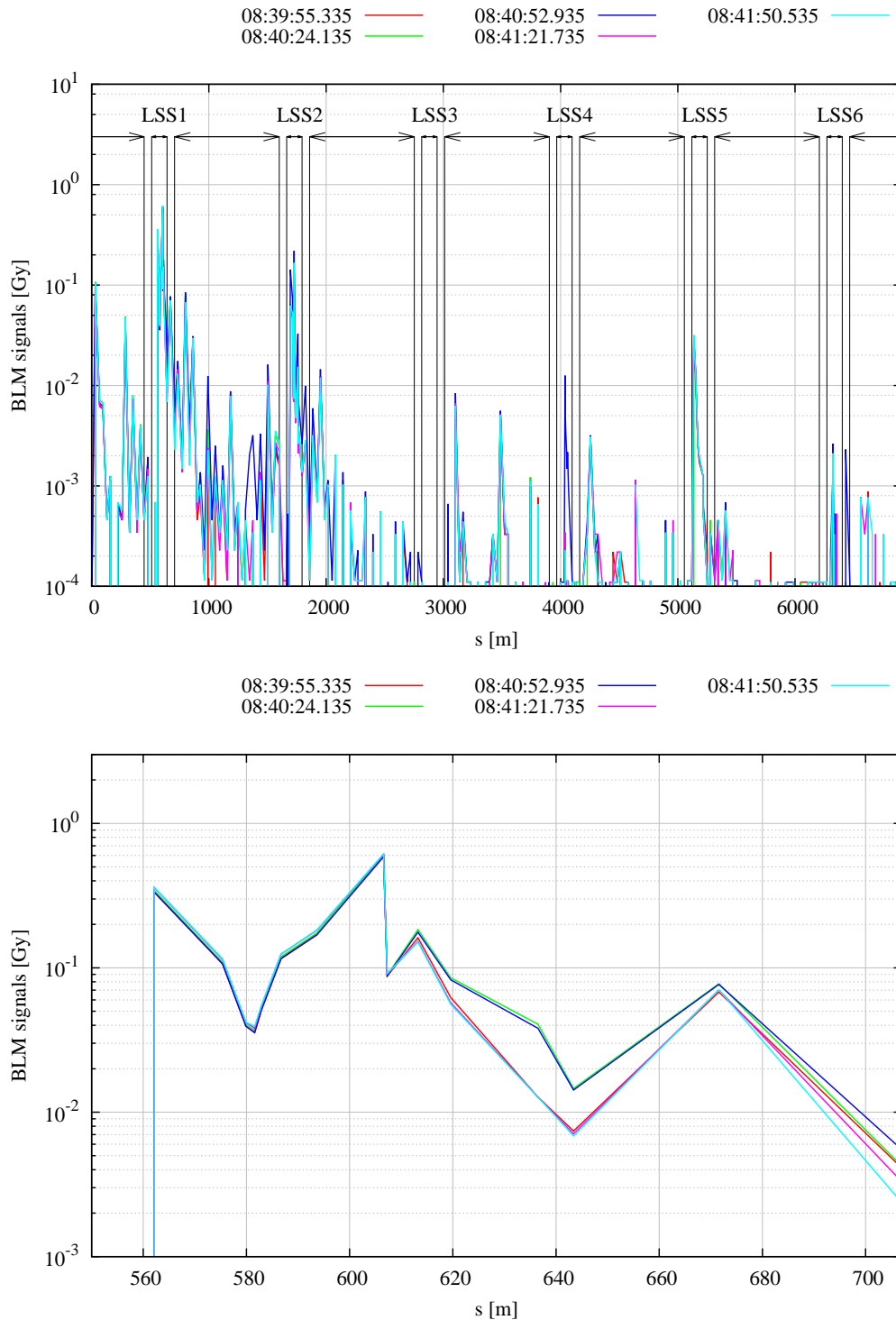


Figure E.10: BLM signals when scraping with the vertical blade of the BSHV.11759 scraper at 3.5 mm (i.e. regular scraping), with a high intensity beam (i.e.  $\sim 3 \times 10^{13}$  protons), after the burst test of the blade.

# Bibliography

- [1] K. Johnsen. CERN Intersecting Storage Rings (ISR). *Proc. Nat. Acad. Sci. USA*, **70**:619–626, 1973. <http://www.pnas.org/content/70/2/619.full.pdf>.
- [2] L.R. Evans. *The Proton–Antiproton Collider*. John Adams’ Lecture. CERN, Geneva, 1988. Delivered at CERN, Nov 25<sup>th</sup> Nov, 1987, <http://cds.cern.ch/record/186337/files/CERN-88-01.pdf>.
- [3] D.W. Kerst et al. Attainment of Very High Energy by Means of Intersecting Beams of Particles. *Phys. Rev.*, **102**:590–591, Apr 1956. <http://link.aps.org/doi/10.1103/PhysRev.102.590>.
- [4] G.K. O’Neill. Storage–ing Synchrotron: Device for High-Energy Physics Research. *Phys. Rev.*, **102**:1418–1419, Jun 1956. <http://link.aps.org/doi/10.1103/PhysRev.102.1418>.
- [5] A.W. Chao et al. *Handbook of Accelerator Physics and Engineering*; 2<sup>nd</sup> ed. World Scientific, Singapore, 2013.
- [6] W. Herr and B. Muratori. Concept of Luminosity. In *CAS - CERN Accelerator School: Intermediate Course on Accelerator Physics*, pages 361–378, Zeuthen, Germany, Sep 2003. <http://dx.doi.org/10.5170/CERN-2006-002.361>.
- [7] W. Herr. Particle Colliders and Concept of Luminosity. Presentation at the CERN Accelerator School, Introductory level – Oct, 28<sup>th</sup>–Nov, 9<sup>th</sup> 2012, [http://zwe.web.cern.ch/zwe/CAS2012/lectures/Granada\\_luminosity.pdf](http://zwe.web.cern.ch/zwe/CAS2012/lectures/Granada_luminosity.pdf).
- [8] O. Brüning, P. Collier, P. Lebrun, S. Myers, R. Ostojic, J. Poole, and P. Proudlock. *LHC Design Report - Vol. 1*. Number CERN-2004-003-V-1. CERN, Geneva, 2004. <http://dx.doi.org/10.5170/CERN-2004-003-V-1>.
- [9] The ATLAS Collaboration. The ATLAS Experiment at the CERN Large Hadron Collider. *J. Instrum.*, **3**:S08003, 2008. [http://iopscience.iop.org/1748-0221/3/08/S08003/pdf/1748-0221\\_3\\_08\\_S08003.pdf](http://iopscience.iop.org/1748-0221/3/08/S08003/pdf/1748-0221_3_08_S08003.pdf).

- [10] The CMS Collaboration. The CMS Experiment at the CERN Large Hadron Collider. *J. Instrum.*, **3**:S08004, 2008. [http://iopscience.iop.org/1748-0221/3/08/S08004/pdf/1748-0221\\_3\\_08\\_S08004.pdf](http://iopscience.iop.org/1748-0221/3/08/S08004/pdf/1748-0221_3_08_S08004.pdf).
- [11] The ALICE Collaboration. The ALICE Experiment at the CERN LHC. *J. Instrum.*, **3**:S08002, 2008. [http://iopscience.iop.org/1748-0221/3/08/S08002/pdf/1748-0221\\_3\\_08\\_S08002.pdf](http://iopscience.iop.org/1748-0221/3/08/S08002/pdf/1748-0221_3_08_S08002.pdf).
- [12] The LHCb Collaboration. The LHCb Detector at the CERN LHC. *J. Instrum.*, **3**:S08005, 2008. [http://iopscience.iop.org/1748-0221/3/08/S08005/pdf/1748-0221\\_3\\_08\\_S08005.pdf](http://iopscience.iop.org/1748-0221/3/08/S08005/pdf/1748-0221_3_08_S08005.pdf).
- [13] L. Rossi and O. Brüning. High Luminosity Large Hadron Collider - A description for the European Strategy Preparatory Group. Technical Report CERN-ATS-2012-236, CERN, Geneva, Aug 2012. <https://cds.cern.ch/record/1471000/files/CERN-ATS-2012-236.pdf>.
- [14] V.D. Shiltsev. High Energy Particle Colliders: Past 20 Years, next 20 Years and Beyond. Technical Report FERMILAB-PUB-12-100-APC, FermiLab, Batavia, May 2012. <http://lss.fnal.gov/archive/2012/pub/fermilab-pub-12-100-apc.pdf>.
- [15] Statement by the ATLAS collaboration about findings of the Higgs Boson at the CERN LHC: <http://www.atlas.ch/news/2012/latest-results-from-higgs-search.html>.
- [16] Statement by the CMS collaboration about findings of the Higgs Boson at the CERN LHC: <http://cms.web.cern.ch/news/observation-new-particle-mass-125-gev>.
- [17] A. Siemko. Safeguarding the Superconducting Magnets. *CERN Courier*, Aug 2013.
- [18] M.N. Wilson. *Superconducting Magnets*. Oxford Univeristy Press, 1987.
- [19] M. Benedikt, P. Collier, V. Mertens, J. Poole, and K. Schindl. *LHC Design Report - Vol. 3*. Number CERN-2004-003-V-3. CERN, Geneva, 2004. <http://dx.doi.org/10.5170/CERN-2004-003-V-3>.
- [20] LHC performance and statistics: <http://lhc-statistics.web.cern.ch/LHC-Statistics>.
- [21] HL-LHC website: [hilumilhc.web.cern.ch](http://hilumilhc.web.cern.ch).
- [22] The HiLumi LHC Collaboration. HL-LHC Preliminary Design Report. Technical Report CERN-ACC-2014-0300, Nov 2014. <http://cds.cern.ch/record/1972604>.

- [23] L. Rossi. LHC Upgrade Plans: Options and Strategy. Technical Report CERN-ATS-2011-257, CERN, Geneva, Dec 2011. <https://cds.cern.ch/record/1407911/files/CERN-ATS-2011-257.pdf>.
- [24] LIU website: [espace.cern.ch/liu-project](https://espace.cern.ch/liu-project).
- [25] K. Hanke et al. Status of the LIU Project at CERN. In *Proceedings of IPAC14*, number THPME070, Dresden, Germany, Jun 2014. <http://accelconf.web.cern.ch/AccelConf/IPAC2014/papers/thpme070.pdf>.
- [26] S. Fartoukh. Achromatic telescopic squeezing scheme and application to the LHC and its luminosity upgrade. *Phys. Rev. ST Accel. Beams*, **16**:111002, Nov 2013. <http://link.aps.org/doi/10.1103/PhysRevSTAB.16.111002>.
- [27] L. Arnaudon et al. Linac4 Technical Design Report. Technical Report CERN-AB-2006-084; CARE-Note-2006-022-HIPPI, CERN, Geneva, Dec 2006. <http://project-spl.web.cern.ch/project-spl/documentation/l4tdr.pdf>.
- [28] R. Garoby et al. Status and Plans for the Upgrade of the LHC Injectors. In *Proceedings of IPAC13*, number THPWO077, Shanghai, China, May 2013. <http://accelconf.web.cern.ch/accelconf/ipac2013/papers/thpwo077.pdf>.
- [29] B. Auchmann, G.E. Steele, and A. Verweij. Quench and Damage Levels for Q4 and Q5 Magnets new Point 6. Technical Report EDMS document 1355063, CERN, Geneva, Feb 2014.
- [30] V. Kain, K. Vorderwinkler, J. Ramillon, R. Schmidt, and J. Wenninger. Material Damage Test with 450 GeV LHC-Type Beam. In *Proceedings of PAC05*, pages 1607–1609, Knoxville, USA, May 2005. <http://accelconf.web.cern.ch/accelconf/p05/PAPERS/RPPE018.pdf>.
- [31] Tommasini, D. Dielectric Insulation and High-Voltage Issues. In *CAS - CERN Accelerator School: Specialised Course on Magnets*, pages 335–355, Bruges, Belgium, Jun 2009. <http://arxiv.org/pdf/1104.0802.pdf>.
- [32] Fessia, P. Analysis of Possible Options for Quadrupoles and Dipole in Cleaning Insertions. Technical Report CERN-ACC-2014-0013, CERN, Geneva, Gen 2014. <https://cds.cern.ch/record/1644780/files/CERN-ACC-2014-0013.pdf>.
- [33] Fessia, P. Review of Radiation Resistance of Cold Magnets and Status of IR7 Warm Magnets, Jun 2013. Presentation at the 24<sup>th</sup> “Collimation Upgrade Specification Meeting”, Jun, 21<sup>st</sup> 2013 <http://lhc-collimation-upgrade-spec.web.cern.ch/>

LHC-Collimation-Upgrade-Spec/Files/meetings/24/PFessia\_MQW-MBW.pdf.

- [34] J. Beringer et al. [Particle Data Group Collaboration]. Review of Particle Physics. *Phys. Rev. D*, **86**:010001, 2012.
- [35] K.S. Krane. *Introductory Nuclear Physics*. J. Wiley and Sons, 1987.
- [36] A. Ferrari and P.R. Sala. The Physics of High Energy Reactions. Technical Report ATL-PHYS-97-113, ATL-GE-PN-113, CERN, Geneva, Sep 1997. <http://cds.cern.ch/record/682497/files/phys-97-113.pdf>.
- [37] P.R. Sala, A. Ferrari, A. Fassò, and J. Ranft. FLUKA: a Multi-Particle Transport Code. Number CERN-2005-10, INFN/TC\_05/11, SLAC-R-773, 2005.
- [38] T.T. Böhlen et al. The FLUKA Code: Developments and Challenges for High Energy and Medical Applications. *Nuclear Data Sheets*, **120**:211–214, Jun 2014.
- [39] M.J. Berger. *PSTAR: Stopping-power and range tables for protons*. NIST, Gaithersburg, MD, 2002.
- [40] E. Métral et al. Transverse Impedance of LHC Collimators. In *Proceedings of PAC07*, number WEOAC03, Albuquerque, New Mexico, US, Jun 2007. <http://accelconf.web.cern.ch/accelconf/p07/PAPERS/WEOAC03.pdf>.
- [41] H. Wiedemann. *Particle Accelerator Physics; 3<sup>rd</sup> ed.* Springer, Berlin, 2007.
- [42] L. Palumbo, V.G. Vaccaro, and M. Zobov. Wake Fields and Impedance. In *CAS - CERN Accelerator School: 5<sup>th</sup> Advanced Accelerator Physics Course*, pages 331–390, Rhodes, Greece, Oct 1993. <http://cds.cern.ch/record/276437>.
- [43] D.P. McGinnis. The Design of Beam Pickup and Kickers. In *6<sup>th</sup> Beam Instrumentation Workshop*, pages 64–85, Vancouver, BC, Canada, Oct 1994. [http://ab-dep-bdi-em.web.cern.ch/ab-dep-bdi-em/uploads/Main.UsefulPublications/beam\\_inst\\_94.pdf](http://ab-dep-bdi-em.web.cern.ch/ab-dep-bdi-em/uploads/Main.UsefulPublications/beam_inst_94.pdf).
- [44] V.E. Balakin, A.V. Novokhatsky, and V.P. Smirnov. VLEPP: Transverse Beam Dynamics. In *12<sup>th</sup> International Conference on High Energy Accelerators*, pages 119–120, Fermi National Accelerator Laboratory, Batavia, Illinois, US, Aug 1983.
- [45] P. Fork. Lecture Notes on Beam Instrumentation and Diagnostics, Mar 2013. JUAS - Joint University Accelerator School – Jan, 7<sup>th</sup>–Mar, 14<sup>th</sup> 2013, <https://indico.cern.ch/event/218284/contribution/186/material/slides/1.pdf>.

- [46] R.W. Aßmann et al. The final collimation system for the LHC. In *Proceedings of EPAC06*, number LHC-Project-Report-919, Edinburgh, UK, Jul 2006.
- [47] C. Bracco. *Commissioning Scenarios and Tests for the LHC Collimation System*. PhD thesis, EPFL, Lausanne, 2009. <https://cds.cern.ch/record/1174254/files/EuCARD-DIS-2009-004.pdf>.
- [48] O. Mete et al. Feasibility Studies in View of a New LIU-SPS Scraping System. Technical Report CERN-ACC-NOTE-2013-0016, CERN, Geneva, Sep 2013. <https://cds.cern.ch/record/1599049/files/LIU-SPS-ScrapingSystem-CERN-ACC-NOTE-2013-0016-20131001.pdf>.
- [49] F. Schmidt. SIXTRACK Version 4.2.16: Single Particle Tracking Code Treating Transverse Motion with Synchrotron Oscillations in a Symplectic Manner; User's Reference Manual. Technical Report CERN-SL-94-56; CERN-SL-94-56-AP, CERN, Geneva, Sep 1994. <http://cds.cern.ch/record/269474>.
- [50] G. Ripken and F. Schmidt. A Symplectic Six-Dimensional Thin-Lens Formalism for Tracking. Technical Report CERN-SL-95-12. CERN-SL-95-12-AP. DESY-95-063, CERN, Geneva, Apr 1995. <http://cds.cern.ch/record/281283>.
- [51] SIXTRACK website: <http://sixtrack.web.cern.ch/SixTrack>.
- [52] A. Mereghetti, V. Boccone, F. Cerutti, R. Versaci, and V. Vlachoudis. The FLUKA LineBuilder and Element Data Base: Tools for Building Complex Models of Accelerator Beam Lines. In *Proceedings of IPAC12*, number WEPPD071, New Orleans, Louisiana, USA, May 2012. <http://accelconf.web.cern.ch/AccelConf/IPAC2012/papers/WEPPD071.pdf>.
- [53] Twiki of the LineBuilder: <https://twiki.cern.ch/twiki/bin/view/FlukaTeam/FlukaLineBuilder>.
- [54] F. Cerutti, S. Gilardoni, A. Mereghetti, P. Schoofs, and V. Vlachoudis. Scrapers in the SPS: Estimation of Cleaning Performances and Thermal Loads. Technical Report in publication, CERN, Geneva.
- [55] S. Redaelli, R. Aßmann, and G. Robert-Démolaize. LHC Aperture and Commissioning of the Collimation System. In *Proceedings of the 2<sup>nd</sup> LHC Project Workshop*, pages 268–276, CERN, Geneva, Switzerland, Jan 2005. [http://cds.cern.ch/record/987839/files/cham-xiv-8\\_03.pdf](http://cds.cern.ch/record/987839/files/cham-xiv-8_03.pdf).
- [56] H. Burkhardt and R. Schmidt. Intensity and Luminosity after Beam Scraping. Technical Report CERN-AB-2004-032-ABP, CERN, Geneva, Jul 2004. <http://cds.cern.ch/record/777311/files/ab-2004-032.pdf>.

- [57] G. Arduini and H. Burkhardt. Transverse Tail Scraping in the SPS for Clean LHC Injection. Technical Report EDMS document 772782, CERN, Geneva, Feb 2006.
- [58] *The 300 GeV Programme*. Number CERN/1050. CERN, Geneva, 1972. <http://cds.cern.ch/record/104068/files/CM-P00077738-e.pdf>.
- [59] CNGS website: <http://proj-cngs.web.cern.ch/proj-cngs>.
- [60] I. Efthymiopoulos et al. HiRadMat: a New Irradiation Facility for Material Testing at CERN. In *Proceedings of IPAC11*, number TUPS058, San Sebastián, Spain, Sep 2011. <http://accelconf.web.cern.ch/AccelConf/IPAC2011/papers/TUPS058.pdf>.
- [61] High-Radiation to Materials (HiRadMat) Facility of CERN/SPS. <https://espace.cern.ch/hiradmat-sps/Wiki%20Pages/Home.aspx>.
- [62] W. Scandale. UA9 Status Report for 2011. Technical Report CERN-SPSC-2011-037. SPSC-SR-092, CERN, Geneva, Oct 2011. <http://cds.cern.ch/record/1392395/files/SPSC-SR-092.pdf>.
- [63] Holzer, B.J. Beam Optics and Lattice Design for Particle Accelerators. In *CAS - CERN Accelerator School: Course on High Power Hadron Machines*, number CERN-2013-001, pages 171–206, Bilbao, Spain, May 2011. <http://arxiv.org/pdf/1303.6514.pdf>.
- [64] E. Shaposhnikova. Lessons from SPS studies in 2010. In *Proceedings of the Chamonix 2011 Workshop on LHC Performance*, pages 359–365, Chamonix, France, Jan 2011. [https://cds.cern.ch/record/1353880/files/EC\\_9\\_05.pdf](https://cds.cern.ch/record/1353880/files/EC_9_05.pdf).
- [65] S.-Y. Lee. *Accelerator physics*; 3<sup>rd</sup> ed. World Scientific, Singapore, 2012.
- [66] H. Bartosik, G. Arduini, and Y. Papaphilippou. Optics Considerations for Lowering Transition Energy in the SPS. In *Proceedings of IPAC11*, number MOPS012, San Sebastián, Spain, Sep 2011. <http://accelconf.web.cern.ch/AccelConf/IPAC2011/papers/MOPS012.pdf>.
- [67] H. Bartosik et al. Experimental Studies with Low Transition Energy Optics in the SPS. In *Proceedings of IPAC11*, number MOPS010, San Sebastián, Spain, Sep 2011. <http://accelconf.web.cern.ch/AccelConf/IPAC2011/papers/MOPS010.pdf>.
- [68] H. Bartosik et al. Increasing Instability Thresholds in the SPS by Lowering Transition Energy. In *Proceedings of IPAC12*, number WEPPR072, New Orleans, Louisiana, USA, May 2012. <http://accelconf.web.cern.ch/AccelConf/IPAC2012/papers/WEPPR072.pdf>.

- [69] MADX website: <http://mad.web.cern.ch/mad>.
- [70] H. Bartosik. Private communication.
- [71] F.M. Velotti. Private communication.
- [72] Cornelis, K. Beam Losses in SPS, Nov 2013. Presentation at the “Joint LIU-LAGUNA Review: Need for SPS Collimation System”, Nov, 21<sup>st</sup> 2013 <http://indico.cern.ch/event/277677/contribution/2/material/slides/0.pptx>.
- [73] M. Donze. Private communication.
- [74] Dale R. Bettine. *The Art and Science of Managing the Engineer*. Xlibris Corporation, 2010.
- [75] S. Roesler, R. Engel, and J. Ranft. The Monte Carlo event generator DPMJET-III. In *Proc. Monte Carlo 2000 Conference, Lisbon, October 23–26 2000, A. Kling, F. Barão, M. Nakagawa, L. Távora, P. Vaz eds., Springer-Verlag*, Berlin, Germany, 2000.
- [76] Vlachoudis, V. FLAIR: A Powerful But User Friendly Graphical Interface For FLUKA. In *Proc. Int. Conf. on Mathematics, Computational Methods and Reactor Physics (M&C 2009)*, Saratoga Springs, New York, USA, 2009. [http://www.fluka.org/flair/Flair\\_MC2009.pdf](http://www.fluka.org/flair/Flair_MC2009.pdf).
- [77] Twiki of the FLUKA–SIXTRACK coupling: <https://twiki.cern.ch/twiki/bin/view/FlukaTeam/CouplingSVNRepositories>.
- [78] SVN repository of the FLUKA–SIXTRACK coupling code (CERN credentials required): [http://svn.cern.ch/repos/fluka\\_coupling](http://svn.cern.ch/repos/fluka_coupling).
- [79] SVN repository of SIXTRACK at: <http://svn.cern.ch/guest/SixTrack>.
- [80] A. Mereghetti et al. SIXTRACK–FLUKA Active Coupling for the Upgrade of the SPS Scrapers. In *Proceedings of IPAC13*, number WEPEA064, Shanghai, China, May 2013. <http://accelconf.web.cern.ch/AccelConf/IPAC2013/papers/WEPEA064.pdf>.
- [81] R. De Maria et al. Recent Developments and Future Plans for SIXTRACK. In *Proceedings of IPAC13*, number MOPWO028, Shanghai, China, May 2013. <http://accelconf.web.cern.ch/AccelConf/IPAC2013/papers/mopwo028.pdf>.
- [82] Twiki of the FLUKAIO protocol: [twiki.cern.ch/twiki/bin/view/FlukaTeam/FlukaIO](https://twiki.cern.ch/twiki/bin/view/FlukaTeam/FlukaIO).

- [83] G. Robert-Demolaize et al. A New Version of SIXTRACK with Collimation and Aperture Interface. In *Proceedings of PAC05*, number FPAT081, Knoxville, Tennessee, USA, Jul 2005. <http://accelconf.web.cern.ch/AccelConf/p05/PAPERS/FPAT081.PDF>.
- [84] R. Bruce and P.D. Hermes. Private communication.
- [85] G.E.P. Box and M.E. Muller. A Note on the Generation of Random Normal Deviates. *The Annals of Mathematical Statistics*, **29**(2):610–611, Jun 1958. <http://dx.doi.org/10.1214/aoms/1177706645>.
- [86] N. Holden. Development of the ICOSIM Program and Application to Magnetised Collimators in the LHC. Technical Report CERN-AB-Note-2008-054, CERN, Geneva, Dec 2008. <http://cds.cern.ch/record/1151294>.
- [87] R.W. Aßmann et al. Collimation of Heavy Ion Beams in LHC. In *Proceedings of EPAC04*, number LHC-Project-Report-766, Lucerne, Switzerland, Jul 2004.
- [88] H. Burkhardt, R. De Maria, M. Giovannozzi, and T. Risselada. Improved TEAPOT Method and Tracking with Thick Quadrupoles for the LHC and its Upgrade. (MOPWO027), May 2013.
- [89] L.N. Drøsdal et al. SPS Scraping and LHC Transverse Tails. In *Proceedings of IPAC13*, number MOPWO032, Shanghai, China, May 2013. <http://accelconf.web.cern.ch/AccelConf/IPAC2013/papers/mopwo032.pdf>.
- [90] J.C. Moyroud and R. Folch. Cumul de Jeux - Angle de la Lame Graphite. Technical Report EDMS document 1454838, CERN, Geneva, Dec 2014.
- [91] <http://lhc-logging.web.cern.ch/lhc-logging/timber>.
- [92] F. Léaux and G. Arnau Izquierdo. Microscopic Observations of Irradiated Graphite Scraper Blades. Technical Report EDMS document 1339153, CERN, Geneva, Feb 2014.
- [93] link to CERN elogbook, shift with the SPS scrapers burst test (CERN credentials required): <https://ab-dep-op-elogbook.web.cern.ch/ab-dep-op-elogbook/elogbook/secure/eLogbook.php?lgbk=50&date=20130216&shift=1>.
- [94] O.E. Berrig et al. CERN-SPS Wire Scanner Impedance and Wire Heating Studies. Technical Report CERN-BE-2014-006, CERN, Geneva, Sep 2014. <https://cds.cern.ch/record/1972478/files/CERN-BE-2014-006.pdf>.
- [95] L. Jensen. Private communication.

[96] M. Stockner and C.W. Fabjan. *Beam Loss Calibration Studies for High Energy Proton Accelerators*. PhD thesis, Vienna, Tech. U., Vienna, 2007. Presented on 27 Nov 2007.

[97] CERN Drawing Directory - website: <http://edms-service.web.cern.ch/edms-service/CDD>.

[98] J. Emery. Private communication.

[99] S. Cettour Cavé. Private communication.

[100] L.N. Drøsdal. Private communication.

[101] R. Losito. Private communication.

[102] V. Previtali. *Performance Evaluation of a Crystal-Enhanced Collimation System for the LHC*. PhD thesis, EPFL, Lausanne, 2010. [http://infoscience.epfl.ch/record/149810/files/EPFL\\_TH4794.pdf](http://infoscience.epfl.ch/record/149810/files/EPFL_TH4794.pdf).

[103] J. Buon. Beam Phase Space and Emittance. (LAL-RT-90-15-REV. LAL-RT-92-03), Feb 1992. <https://cds.cern.ch/record/242313>.

[104] G. K. White and S. J. Collocott. Heat Capacity of Reference Materials: Cu and W. *JPCRD*, **13**:1251–1257, 1984. <http://www.nist.gov/data/PDFfiles/jpcrd263.pdf>.

[105] F.L. Maciariello. Private communication.

[106] J.R. Taylor. *An Introduction to Error Analysis: The Study of Uncertainties in Physical Measurements*. University Science Books, 2 sub edition, 1996.

[107] Wolfram Mathematica Online Integrator: <http://integrals.wolfram.com/index.jsp>.